MEASURING PROTON SPIN POLARIZABILITIES WITH POLARIZED COMPTON SCATTERING

A Dissertation Presented

by

PHILIPPE PAUL MARTEL

Submitted to the Graduate School of the
University of Massachusetts Amherst in partial fulfillment
of the requirements for the degree of

DOCTOR OF PHILOSOPHY

February 2013

Physics

MEASURING PROTON SPIN POLARIZABILITIES WITH POLARIZED COMPTON SCATTERING

A Dissertation Presented

by

PHILIPPE PAUL MARTEL

Approved as to style and content by:

Rory Miskimen, Chair

Barry Holstein, Member

David Kawall, Member

Paul Lahti, Member

Donald Candela, Department Chair
Physics

ACKNOWLEDGMENTS

First of all I'd like to thank my advisor, Rory Miskimen, without whom none of this would have been possible. For over a decade now you've been a mentor and a friend, helping to guide me along this path. For first hiring me as an undergraduate, supporting me when I was unsure about graduate school, helping me to prepare for the Quals, and assisting in wading through this analysis, thank you. I sincerely appreciate the respect, trust, and encouragement you've given me all these years. Thanks also go to my other committee members, Barry Holstein, David Kawall, and Paul Lahti, for their help in getting all of this done, as well as to the secretaries and everyone else in the UMass Physics Department for many years of guidance.

I'd like to thank Dave Hornidge for bringing us on board for this great experiment and trusting in a graduate student you didn't know to work on this task. Thanks also for all the support, invitations to give talks, and friendly discussions that you've provided. Additionally I want to thank Hans-Jürgen Arends, Michael Ostrick, Andreas Thomas, and the rest of A2, for welcoming me into the collaboration with open arms and making me feel at home. Thanks are also due to Barbara Pasquini for the use of, and help with, the dispersion code, and similarly to Irakli Keshelashvili and Dominik Werthmueller for the use of, and help with, the calibration software.

This journey to a physics Ph.D. has been a long one, with many supporting characters along the way. As I can't possibly list you all, know that even if you're not mentioned here my thanks to you are no less sincere. Thanks to my undergraduate physics classmates (and roommates), Kazem Edmond, Josh Reusch, Jasper McChesney, and Steve Healy, for many late nights doing homework, drinking an unhealthy

amount of caffeinated soda, and occasionally giving up on the homework to watch a movie instead.

To my friends on the UMass Fencing team, notably Chris Borzumato, Sam Horenstein, and Chris Mock, thanks for all the crazy times we had. It's honestly a bit of a surprise that I made it through undergrad with all of you. However, you kept me grounded, you kept me sane (in a sense), and we certainly had a lot of fun. Too bad we'll never play Diplomacy again.

Once in graduate school, I owe at least half of my success to German Colón, Stefan Dickert, and Preema Pais. Without the three of you (and Emily Thompson, though we only took one class together) I never would have survived that year of insanity or passed the Quals. Next to the last two weeks of writing this, those hours we spent in the lounge working were the hardest of my life. At least we had calzones.

Before coming to MAMI for this experiment, I also spent two and a half years working at TUNL/HIγS down at Duke University. I'm very thankful for the opportunities afforded me there by Henry Weller and Mohammad Ahmed. The array of what I learned from you, as well as from Mark Spraker, Dick Prior, and many others, made me an experimental physicist. Those tools have helped me every step along the way, and I'll be forever grateful. I would also like to thank Seth Henshaw, Brent Purdue, and Sean Stave, both for helping the new student and his girlfriend (neither of whom you had ever met) move into their apartment, and for all the great times we shared down there. I wouldn't trade those late nights in the lab, cabling up detectors or building some target holder in the shop, for anything.

The time my wife and I spent in Mainz would not have been the same without Pauline Hall Barrientos, Cristina Collicott, Evie Downie, and Duncan Middleton (as well as the Canadian summer students). You became our family, and we'll never forget our experiences out there. You've all also been very supportive of my work, always willing to help with analysis and AcquRoot questions.

Obviously none of this would have been possible without my family. Thanks to my in-laws for making me feel like one of the family, and for helping us out upon returning from Germany. I don't know what we would have done without you. I'm deeply thankful for the constant love and support that my grandparents have given, and the encouragement and drive that my aunts and uncles have provided; you all inspire me to push ever onward, while giving me the confidence to do so. Thanks go to my brothers, who had the unfortunate task of following me in school and receiving many 'Oh, you're Phil's brother' comments. Since we're rather separated in ages I've always tried to set a good example, and that's been part of my drive for many years. Along the way you've both grown up into amazing men, and I have no doubt that you'll both achieve things beyond comparison.

Trying to properly thank my parents is almost as hard as writing this thesis, and just as important. Everything I've done, and everything I am, is due to you. I hope you both realize just how amazing you are. You're loving, supportive, trusting, and honest. You've always left me confident that whatever I choose to do in life is ok, while still driving me to always reach for the stars. When I'd fall you were always there, not to judge, but to pick me back up. I could not have achieved this without you. For all that you've done for me, and for all that you are, thank you Mom and Dad. I love you both very much.

Lastly, I want to thank my wife Sherri. You've traveled this crazy path with me since before graduate school. From Amherst, to Durham, to Mainz, and back, you've been there for me. Without your constant love and support I would have drifted off this path long ago. Without your amazing culinary abilities I'd be eating macaroni and cheese. Without your smile and laughter I wouldn't want to get up in the morning. You make me a better person every day, you mean the world to me, and I could not be happier about spending the rest of my life with you. I love you more than words could ever express.

ABSTRACT

MEASURING PROTON SPIN POLARIZABILITIES WITH POLARIZED COMPTON SCATTERING

FEBRUARY 2013

PHILIPPE PAUL MARTEL

B.Sc., UNIVERSITY OF MASSACHUSETTS, AMHERST

M.Sc., UNIVERSITY OF MASSACHUSETTS, AMHERST

Ph.D., UNIVERSITY OF MASSACHUSETTS, AMHERST

Directed by: Professor Rory Miskimen

Polarized nuclear Compton scattering on a proton target provides a test of low energy QCD. The beam-target asymmetries of a circularly polarized Bremsstrahlung photon beam on a transversely polarized butanol target (Σ_{2x}) and on a longitudinally polarized butanol target (Σ_{2z}), and the beam asymmetry of a linearly polarized Bremsstrahlung beam on an unpolarized hydrogen target (Σ_3) are sensitive to the proton spin polarizabilities, third order terms in the energy expansion of the Compton scattering amplitude. This experiment consisted of the Σ_{2x} measurement, both just below and above two-pion threshold.

TABLE OF CONTENTS

LIST OF TABLES

Table **Page**

LIST OF FIGURES

Figure **Page**

CHAPTER 1

MOTIVATION FOR COMPTON SCATTERING

The interaction of light with matter is described by various processes at different energies. The primary type of matter this work is focused on is that of individual protons (or a hydrogen atom). However, there is a significant contribution of carbon that must also be accounted for.

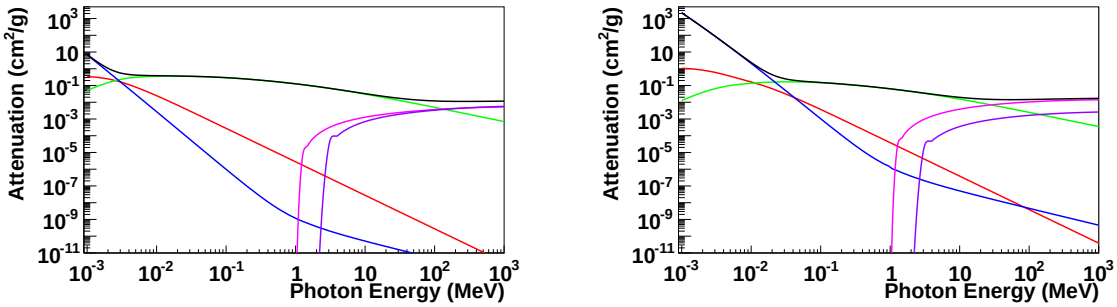

(a) Hydrogen (b) Carbon

Figure 1.1: Electromagnetic interactions for hydrogen and carbon. Lines are photoelectric absorption (blue), coherent (Rayleigh) scattering (red), incoherent (atomic Compton) scattering (green), pair production in nuclear field (magenta), pair production in electron field (purple), and their total (black).[1]

Figure 1.1 shows some of the processes, and their relative strengths, for hydrogen and carbon. At low photon energies (below 3 keV for hydrogen, 20 keV for carbon) the dominating process is the photoelectric effect, where the photon is absorbed by the atom followed by the ejection of an electron. Above this energy atomic Compton scattering becomes more prominent. In this process the photon transfers some of its energy to an orbital electron, allowing it to break free of the atom, while the photon

retains some of its energy as it scatters away. At higher energies, the photon can interact with the nuclear or electron fields and produce a particle/anti-particle pair (typically electron/positron). Conveniently named, pair production requires a photon energy above the combined rest mass of the pair (1.022 MeV for electron/positron). For hydrogen this becomes the dominant process above 80 MeV, and for carbon above 26 MeV.[1]

1.1 Compton Scattering

There are also other processes, such as coherent scattering (elastic scattering off of the atom itself), pion photoproduction (similar to pair production), and photodisintegration (knocking a neutron or proton out of the nucleus). However, the process involved in this study is nuclear Compton scattering (henceforth simply called Compton scattering), where the photon scatters off of the nucleus. For hydrogen, this is scattering off of a single proton

$$\gamma(q) + p(p) \rightarrow \gamma(q') + p(p') \tag{1.1}$$

where q and q' represent the initial and final four-momenta of the photon, respectively, and p and p' represent the initial and final four-momenta of the proton, respectively.

1.1.1 Born Terms

The amplitude of this Compton scattering process can be expanded in terms of the photon energy, where the zeroth order term gives the typical Thomson scattering off of a point-like charged particle of a given mass. Using the notation and derivation of Levchuk and L'vov[2], the zeroth order Hamiltonian has the form

$$H_{\text{eff}}^{(0)} = \frac{\vec{\pi}^2}{2m} + e\phi \tag{1.2}$$

where m is the mass, e is the electric charge, and

$$\vec{\pi} = \vec{p} - e\vec{A} \tag{1.3}$$

is a covariant momentum in which $\vec{p}$ is the momentum and $\vec{A}$ is the vector potential. The Hamiltonian at first order is dependent upon the anomalous magnetic moment, κ, of the nucleon.

$$H_{\text{eff}}^{(1)} = -\frac{e(1+\kappa)}{2m}\,\vec{\sigma}\cdot\vec{H} - \frac{e(1+2\kappa)}{8m^2}\,\vec{\sigma}\cdot\left[\vec{E}\times\vec{\pi} - \vec{\pi}\times\vec{E}\right] \tag{1.4}$$

These two terms together are the so-called Born terms, and represent the external degrees of freedom of the nucleon. At photon energies below 20 MeV approximately, the photon can only access these external degrees of freedom.[3]

1.1.2 Scalar Polarizabilities

At higher energies, the internal degrees of freedom start to play a role. The second order in the energy expansion contains the scalar polarizabilities

$$H_{\text{eff}}^{(2)} = -4\pi\left[\frac{1}{2}\alpha_{E1}\vec{E}^2 + \frac{1}{2}\beta_{M1}\vec{H}^2\right] \tag{1.5}$$

where α_{E1} and β_{M1} are the electric and magnetic polarizability. These terms represent the internal response of the nucleon to an applied electric or magnetic field, respectively.[4] This can be visualized by imagining the nucleon containing, in addition to the constituent quarks, a sea of virtual charged pions popping in and out of existence. Applying an electric field across the nucleon, as shown in Figure 1.2, will induce a current in this cloud, separating the positive from the negative pions, and physically 'stretching' the nucleon in the direction of the field. Applying a magnetic field across the nucleon, as shown in Figure 1.3, will also induce a current in the cloud,

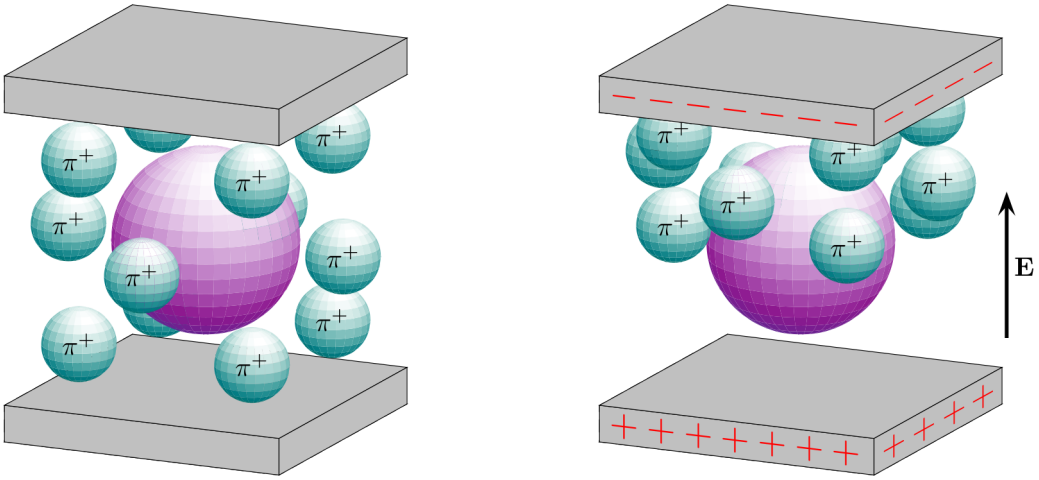

(a) Electric field off (b) Electric field on

Figure 1.2: Nucleon response to electric field[5]

creating a diamagnetic moment that directly opposes the paramagnetic moment of the constituent quarks.

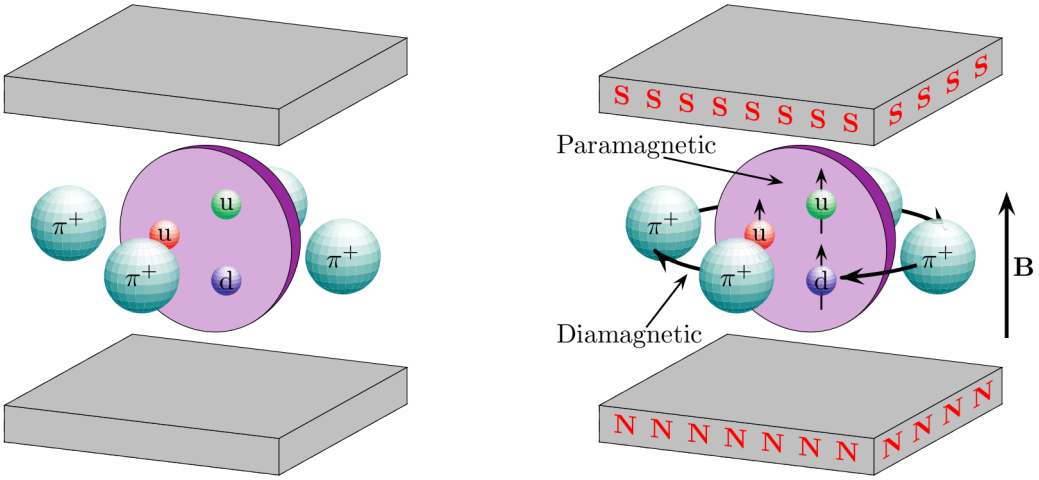

(a) Magnetic field off (b) Magnetic field on

Figure 1.3: Nucleon response to magnetic field[5]

A large number of Compton scattering experiments have taken place on unpolarized proton targets since the 1950's, many of which can be utilized to extract

the electric and magnetic polarizabilities. A very thorough discussion of these experiments is given by Grießhammer *et al.*[6] The principle in extracting the scalar polarizabilities is a comparison between the theoretical curves produced using only the Born terms, versus using a Low Energy Expansion (LEX), or using a Dispersion Relation (DR).[7] The LEX calculation[8][9] provides an expression for the cross section as

$$\left(\frac{d\sigma}{d\Omega}\right) = \left(\frac{d\sigma}{d\Omega}\right)_{Born} - \omega\omega' \left(\frac{\omega'}{\omega}\right)^2 \frac{e^2}{m} \left[\frac{\alpha+\beta}{2}\left(1+\cos\theta\right)^2 + \frac{\alpha-\beta}{2}\left(1-\cos\theta\right)^2\right] \quad (1.6)$$

Dispersion relations will be discussed in more detail in subsubsection 1.1.3.3. The difference between these theories is shown in Figure 1.4a.[10] While the LEX and DR curves are identical below approximately 90 MeV, they both differ from the Born curve. Above 90 MeV all of their behaviors become noticeably different.

The current Particle Data Group (PDG) values for these polarizabilities were the result of an experiment by Olmos de León *et al.* at MAMI.[11] This experiment used the A2 tagged photon beam of 55-165 MeV with an array of TAPS detectors covering the angular range of 59-155°, as shown in Figure 1.4b. Their results, along with DR curves of clear agreement, are shown in Figure 1.4. With their data they extracted the following values for α_{E1} and β_{M1}:

$$\alpha_{E1} = \left[11.9 \pm 0.5\,(\text{stat}) \mp 1.3\,(\text{syst})\right] \times 10^{-4}\,\text{fm}^3 \quad (1.7)$$

$$\beta_{M1} = \left[1.2 \pm 0.7\,(\text{stat}) \pm 0.3\,(\text{syst})\right] \times 10^{-4}\,\text{fm}^3 \quad (1.8)$$

In addition to their own extraction of the scalar polarizabilities, their analysis combined results from three previous experiments:

- Federspiel *et al.*, 32-72 MeV at 60 and 135°[12]
- MacGibbon *et al.*, 70-100 MeV at 90 and 135°[10]

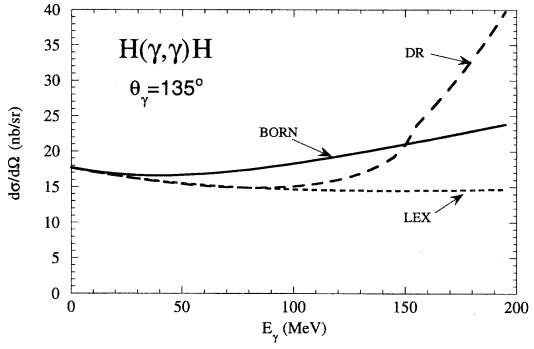

(a) Theory Curves[10]

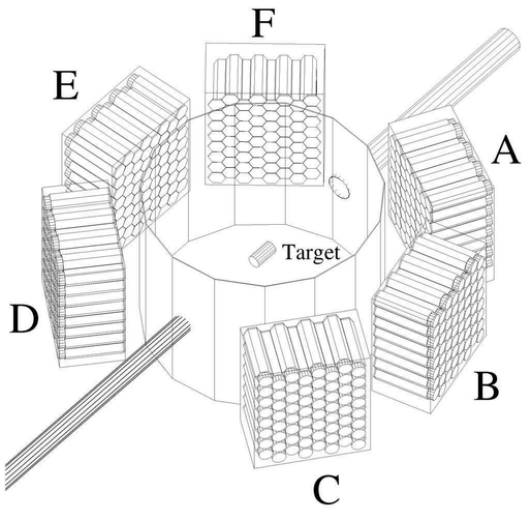

(b) TAPS setup[11]

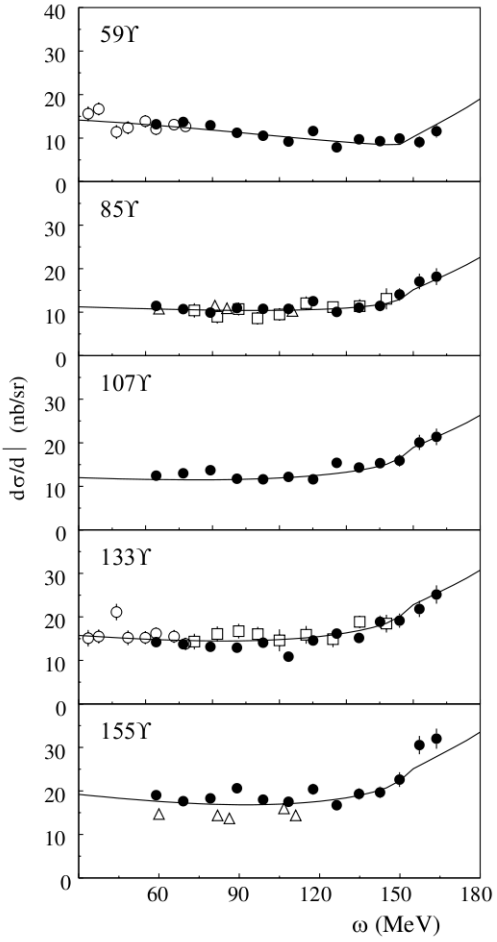

(c) Cross sections[11]

Figure 1.4: Alpha and beta measurement. (a) Curves with various theoretic predictions: Born terms only, Low Energy Expansion (LEX), or dispersion calculation.[10] (b) Setup from TAPS/MAMI measurement.[11] (c) Results from TAPS/MAMI measurement.[11]

- Zieger *et al.*, 98-132 MeV at 180°[13]

and performed a global fit with all of these data points. This fit also utilized a constraint given by the Baldin[14] (or BL, for Baldin-Lapidus[15]) sum rule

$$\alpha + \beta = \frac{1}{2\pi^2} \int_{\omega_0}^{\infty} \frac{\sigma_{\text{tot}}(\omega)}{\omega^2} d\omega \tag{1.9}$$

Their error contour plot, provided here in Figure 1.5, shows the constraints the various experiments, as well as the sum rule, bring to the fit. Their results from that analysis

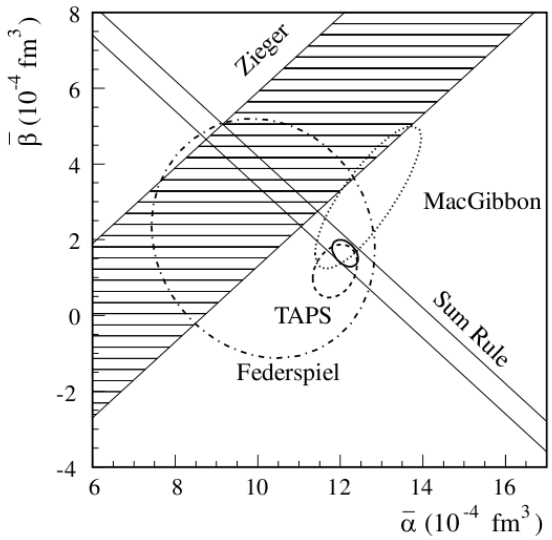

Figure 1.5: Alpha and beta results. Global fit for α_{E1} and β_{M1}, showing their TAPS data, Federspiel *et al.*[12], MacGibbon *et al.*[10], and Zieger *et al.*[13] (whose measurement at 180° provides a measurement of $\alpha_{E1}-\beta_{M1}$ only, giving the hashed region).[11]

then provided the following global fit (and current PDG) values:

$$\alpha_{E1} = [12.1 \pm 0.3\,(\text{stat}) \mp 0.4\,(\text{syst}) \pm 0.3\,(\text{mod})] \times 10^{-4}\,\text{fm}^3 \tag{1.10}$$

$$\beta_{M1} = [1.6 \pm 0.4\,(\text{stat}) \pm 0.4\,(\text{syst}) \pm 0.4\,(\text{mod})] \times 10^{-4}\,\text{fm}^3 \tag{1.11}$$

Their re-evaluation[11] of the Baldin sum rule is also important

$$\alpha_{E1} + \beta_{M1} = (13.8 \pm 0.4) \times 10^{-4}\,\text{fm}^3 \tag{1.12}$$

as this was used in the dispersion calculations for the sensitivity studies outlined in this dissertation, along with the difference between the two polarizabilities

$$\alpha_{E1} - \beta_{M1} = [10.5 \pm 0.9\,(\text{stat} + \text{syst}) \pm 0.7\,(\text{mod})] \times 10^{-4}\,\text{fm}^3 \tag{1.13}$$

It should be noted, however, that recent calculations using Baryon Chiral Perturbation Theory (BχPT) by Lensky and Pascalutsa[16], and Chiral Effective Field Theory (χEFT) by Grießhammer *et al.*[6], both exhibit similar discrepancies with the PDG values.

1.1.3 Spin Polarizabilities

At third order in the energy expansion the vector, or spin, polarizabilities appear:

$$H_{\text{eff}}^{(3)} = -4\pi\Bigg[\frac{1}{2}\gamma_{E1E1}\vec{\sigma}\cdot(\vec{E}\times\dot{\vec{E}}) + \frac{1}{2}\gamma_{M1M1}\vec{\sigma}\cdot(\vec{H}\times\dot{\vec{H}}) - \gamma_{M1E2}E_{ij}\sigma_i H_j + \gamma_{E1M2}H_{ij}\sigma_i E_j\Bigg] \tag{1.14}$$

These describe a coupling of the proton spin with an applied electric or magnetic field.[4] Although the visualization is not as good as that for α_{E1} or β_{M1}, this coupling can be thought of as causing a precession of the nucleon spin with respect to the applied field, analogous to a classical Faraday effect.[5] Unlike the scalar polarizabilities, the four proton spin polarizabilities have not been individually measured. Several experiments have provided values for various linear combinations of the SPs, notably the forward spin polarizability:

$$\gamma_0 = -\gamma_{E1E1} - \gamma_{E1M2} - \gamma_{M1E2} - \gamma_{M1M1} = (-1.0 \pm 0.08)\times 10^{-4}\,\text{fm}^4[17][18] \tag{1.15}$$

and the backward spin polarizability:

$$\gamma_\pi = -\gamma_{E1E1} - \gamma_{E1M2} + \gamma_{M1E2} + \gamma_{M1M1} = (-38.7 \pm 1.8)\times 10^{-4}\,\text{fm}^4[19] \tag{1.16}$$

It should be noted that this value for the backward spin polarizability is the sum of the dispersive part and the π^0-pole term, $\gamma_\pi^{\pi^0-\text{pole}} = -46.7\times 10^{-4}\,\text{fm}^4$[20]. Without this term, it would be

$$\gamma_\pi^{\text{disp}} = (8.0 \pm 1.8) \times 10^{-4}\,\text{fm}^4[4] \tag{1.17}$$

1.1.3.1 Forward Spin Polarizability

The measurement of the forward spin polarizability, γ_0, comes from a set of two experiments of the GDH Collaboration. The primary goal of these experiments was to measure the Gerasimov, Drell, Hearn (GDH) sum rule integral

$$\frac{2\pi^2\alpha_e\kappa^2}{M^2} = \int_{\omega_0}^{\infty} \frac{\sigma_{3/2}(\omega) - \sigma_{1/2}(\omega)}{\omega} d\omega \tag{1.18}$$

where ω is the photon energy, κ is the anomalous magnetic moment, M is the nucleon mass, and σ is the total photo-absorption cross section. The designation of $\sigma_{3/2}$ and $\sigma_{1/2}$ comes from the fact that the measurement of the GDH integral requires a circularly polarized photon beam with a longitudinally polarized proton target. The total photo-absorption cross section when the helicity of the beam and the polarization of the target are parallel is $\sigma_{3/2}$, and when the helicity of the beam and the polarization of the target are anti-parallel is $\sigma_{1/2}$. The collaboration divided this measurement into two steps, first from 200 to 800 MeV at MAMI, and second from 700 MeV to 1.8 GeV at ELSA. Both labs used detectors with nearly 4π sr coverage, DAPHNE at MAMI, and the appropriately named 'GDH-Detector'[21] at ELSA, both supplemented by forward detectors. A frozen spin target, similar to that used in this dissertation's experiment, provided the polarized target. The combined differences in total photo-absorption cross sections are shown in Figure 1.6.[18]

A similar relation to the GDH sum rule exists, relating γ_0 to these differences in total photo-absorption cross sections:

$$\gamma_0 = -\frac{1}{4\pi^2} \int_{\omega_0}^{\infty} \frac{\sigma_{3/2}(\omega) - \sigma_{1/2}(\omega)}{\omega^3} d\omega \tag{1.19}$$

which simultaneously allowed for a determination of the forward spin polarizability. That analysis resulted in the number given in Equation 1.15.

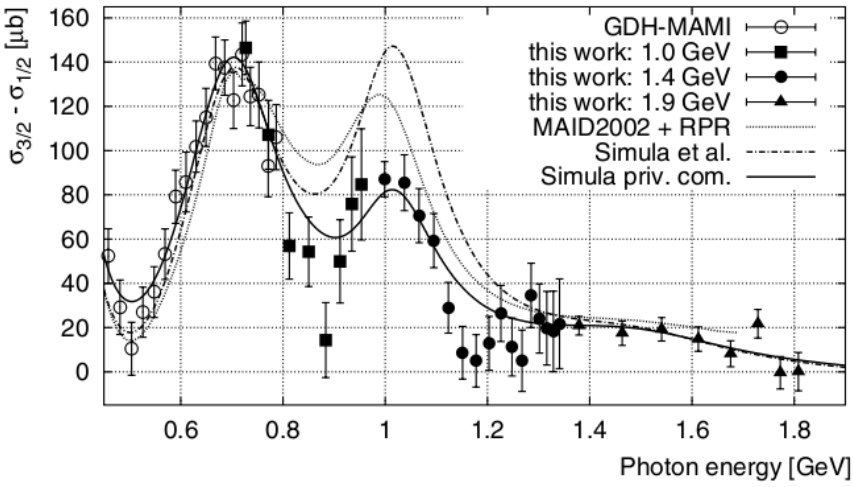

Figure 1.6: Measurement of the GDH sum rule and the forward spin polarizability. Determined by the difference between parallel and anti-parallel photo-absorption cross sections for circularly polarized photons scattering from a longitudinally polarized target.[18]

1.1.3.2 Backward Spin Polarizability

The backward spin polarizability, γ_π, was determined with a dispersive analysis of back-angle Compton scattering at MAMI, with a single large NaI detector at 136°, and a forward wall (SENECA)[19]. Their plot, reproduced here in Figure 1.7, shows their cross sections compared with other data sets from Saskatoon[22], LEGS[23][24], and LARA[25][26]. The result for γ_π used here, as given in Equation 1.16, is from their fit to these data sets, arguing in the process that the LEGS data set appears to be inconsistent with their data as well as previous measurements of γ_π. The data set from the LEGS collaboration[24] also measured two other linear combinations of the spin polarizabilities

$$\gamma_{13} = -\gamma_{E1E1} + \gamma_{E1M2} \tag{1.20}$$

$$\gamma_{14} = -\gamma_{E1E1} - 2\gamma_{M1M1} - \gamma_{E1M2} \tag{1.21}$$

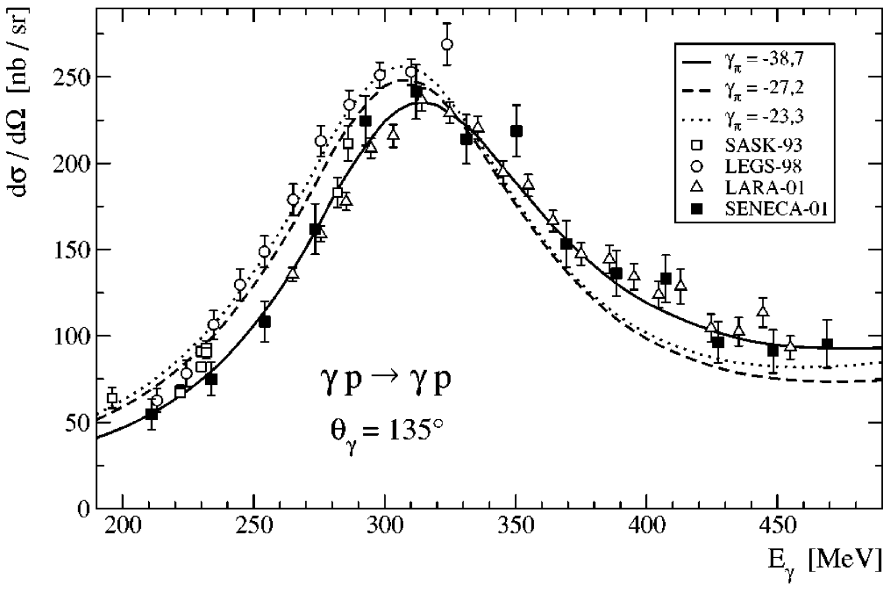

Figure 1.7: Measurement of the backward spin polarizability. Determined by back-angle Compton scattering compared to other data-sets, showing fits for various values of the backward spin polarizability.[19]

1.1.3.3 Theoretical Predictions

The interaction of light with point-like charged particles is well described by quantum electrodynamics (QED), but introducing these internal degrees of freedom into the proton requires the use of quantum chromodynamics (QCD) which describes the strong interactions of quarks and gluons. While perturbative QCD works very well at high energies, the coupling constant becomes so large at low energies that the quarks and gluons can not be used as the relevant degrees of freedom. At the limit where the masses of the lighter quarks (up and down) go to zero there is a decoupling of left- and right-handed quarks, leading to what's called chiral symmetry. It's known, however, that this symmetry must be spontaneously broken in nature, which leads to the existence of three mass-less Goldstone bosons coinciding with the pion mesons.[27] Additionally one can include the strange quark which, while much heavier than the up or down quark, is still much lighter than the charm, bottom, or top quarks. In this setting there are then five additional Goldstone bosons coinciding with the kaon

and eta mesons (neglecting the eta prime). With the masses of the lighter quarks and these mesons being non-zero chiral symmetry is explicitly broken, but since they are still relatively small compared to baryon and other meson masses, it remains an approximate symmetry of QCD with an expansion parameter given by the pion mass.[28]

This framework, derived by Weinberg[29] and expanded upon by Gasser and Leutwyler[30][31], is called Chiral Perturbation Theory (χPT) or with the inclusion of the nucleon itself as a degree of freedom, called Heavy Baryon χPT (HBχPT). To additionally include the delta resonance as another degree of freedom, the mass splitting between the nucleon and Δ becomes another parameter in the power counting scheme. This method is called the small scale expansion (SSE).[32] To get around a loss of manifest Lorentz invariance in HBχPT, the infrared regularization (IR) scheme of Becher and Leutwyler[33] can be used to examine Lorentz invariant χPT.[34]

Another method for studying the polarizabilities is that of dispersion relations. For Compton scattering, with initial photon and proton four-momenta of q and p, going to final photon and proton four-momenta of q' and p', respectively, the Lorentz invariant Mandelstam variables are

$$s = (q+p)^2 \tag{1.22}$$

$$t = (q-q')^2 \tag{1.23}$$

$$u = (q-p')^2 \tag{1.24}$$

where s is then the square of the center-of-mass energy, and t is the square of the momentum transfer. Two combinations of these variables

$$s+t+u = 2M^2 \tag{1.25}$$

$$\nu = \frac{s-u}{4M} \tag{1.26}$$

are also invariant, where M is the proton mass.[35] The T matrix for Compton scattering can then be defined by six independent structure functions $A_i(\nu, t)$, $i = 1, \ldots, 6$, which are functions of two of these variables, ν and t, and where

$$\mathrm{Re}A_i(\nu, t) = A_i^B(\nu, t) + \frac{2}{\pi}\mathcal{P}\int_{\nu_{\mathrm{thr}}}^{\infty} d\nu' \frac{\mathrm{Im}_s A_i(\nu', t)}{\nu'^2 - \nu^2} \tag{1.27}$$

Due to the asymptotic behavior of A_i as $\nu \to \infty$ at a fixed value for t, it turns out that A_1 and A_2 do not converge. One way to cause them to converge is to subtract off versions of them at $\nu = 0$ and at fixed t.[36]

$$\mathrm{Re}A_i(\nu, t) = A_i^B(\nu, t) + \left[A_i(0, t) - A_i^B(0, t)\right] + \frac{2}{\pi}\nu^2\mathcal{P}\int_{\nu_{\mathrm{thr}}}^{\infty} d\nu' \frac{\mathrm{Im}_s A_i(\nu', t)}{\nu'(\nu'^2 - \nu^2)} \tag{1.28}$$

The subtraction constants $A_i(0, t) - A_i^B(0, t)$ can be determined by yet another subtraction, this time at $t = 0$, resulting in another set of subtraction constants

$$a_i = A_i(0, 0) - A_i^B(0, 0) \tag{1.29}$$

These constants, however, are directly related to the scaler polarizabilities by

$$\alpha_{\mathrm{E1}} = -\frac{1}{4\pi}(a_1 + a_3 + a_6) \tag{1.30}$$

$$\beta_{\mathrm{M1}} = \frac{1}{4\pi}(a_1 - a_3 - a_6) \tag{1.31}$$

the spin polarizabilities by

$$\gamma_{\mathrm{E1E1}} = \frac{1}{8\pi M}(a_2 - a_4 + 2a_5 + a_6) \tag{1.32}$$

$$\gamma_{\mathrm{M1M1}} = -\frac{1}{8\pi M}(a_2 + a_4 + 2a_5 - a_6) \tag{1.33}$$

$$\gamma_{\mathrm{E1M2}} = \frac{1}{8\pi M}(a_2 - a_4 - a_6) \tag{1.34}$$

$$\gamma_{\mathrm{M1E2}} = -\frac{1}{8\pi M}(a_2 + a_4 + a_6) \tag{1.35}$$

and to the forward and backward spin polarizabilities by[4]

$$\gamma_0 = \frac{1}{2\pi M} a_4 \tag{1.36}$$

$$\gamma_\pi = -\frac{1}{2\pi M}(a_2 + a_5) \tag{1.37}$$

The a_2 term in γ_π is the π^0-pole term that was mentioned for Equation 1.17.

Various theoretical values for these polarizabilities are predicted by some of these theories, as shown in Table 1.1, compiled together by Drechsel *et al.*[37]

	$O(p^3)$	$O(p^4)$	$O(p^4)$	LC3	LC4	SSE	BGLMN	HDPV	KS	DPV
γ_{E1}	-5.7	-1.4	-1.8	-3.2	-2.8	-5.7	-3.4	-4.3	-5.0	-3.8
γ_{M2}	1.1	0.2	0.7	0.7	0.8	.98	0.3	-0.01	-1.8	0.5
γ_{E2}	1.1	1.8	1.8	0.7	0.3	.98	1.9	2.1	1.1	1.6
γ_{M1}	-1.1	3.3	2.9	-1.4	-3.1	3.1	2.7	2.9	3.4	2.9
γ_0	4.6	-3.9	-3.6	3.1	4.8	.64	-1.5	-0.7	2.3	-1.1
γ_π	4.6	6.3	5.8	1.8	-0.8	8.8	7.7	9.3	11.3	7.8

Table 1.1: Values for the spin polarizabilities. $O(p^n)$ are Chiral Perturbation Theory (χPT) calculations.[38][39][40] LC3 and LC4 are $O(p^3)$ and $O(p^4)$ Lorentz invariant χPT calculations, respectively.[34] SSE is a Small Scale Expansion calculation.[38] The remaining four are all dispersion relation calculations.[41][42][43][37] Of particular note are the HDPV[42] results, which will be used as the basis for this study.

Given the wide range of values depicted in Table 1.1, a measurement of the spin polarizabilities would provide a useful tool in helping to validate (or invalidate) one, or some, of these theories. The experiment discussed in this thesis is the first component of a Compton scattering program measuring beam-target asymmetries (circularly polarized beam with either a transversely or longitudinally polarized target) and the beam asymmetry (linearly polarized beam with an unpolarized target). These experiments will access the higher order terms in the energy expansion of Equation 1.14, and allow for the extraction of the proton spin polarizabilities.

1.2 Polarized Compton Scattering Asymmetries

This dissertation presents the results of the first of these Compton scattering asymmetry measurements, that of a circularly polarized photon beam on a transversely polarized target.

$$\Sigma_{2x} = \frac{\sigma^R_{+x} - \sigma^L_{+x}}{\sigma^R_{+x} + \sigma^L_{+x}} = \frac{N^R_{+x} - N^L_{+x}}{N^R_{+x} + N^L_{+x}} \tag{1.38}$$

where σ^R_{+x} and σ^L_{+x} represent the cross sections for a positive transversely polarized target with a right and left helicity beam, respectively. The benefit of calculating an asymmetry is that the terms to relate the cross section to the number of events observed, N, divide out between the numerator and denominator. This will be discussed at length in chapter 6. This set of Compton scattering can be visualized by Figure 1.8.

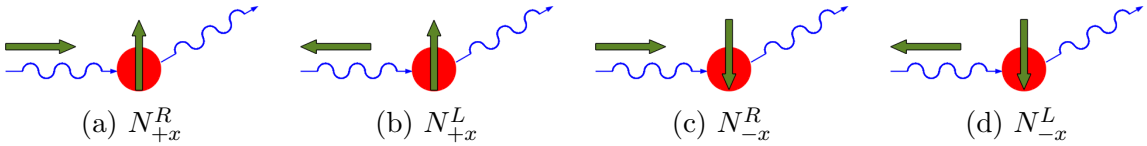

(a) N^R_{+x} (b) N^L_{+x} (c) N^R_{-x} (d) N^L_{-x}

Figure 1.8: Orientations for Compton scattering with a transversely polarized target and a circularly polarized photon beam. The arrow on the left of each represent the beam helicity, and the arrow on the right of each represents the target polarization direction.

In the future a similar experiment will be performed with a longitudinally polarized proton target and a circularly polarized beam, giving the asymmetry

$$\Sigma_{2z} = \frac{\sigma^R_{+z} - \sigma^L_{+z}}{\sigma^R_{+z} + \sigma^L_{+z}} = \frac{N^R_{+z} - N^L_{+z}}{N^R_{+z} + N^L_{+z}} \tag{1.39}$$

where σ^R_{+z} and σ^L_{+z} represent the cross sections for a positive longitudinally polarized target with a right and left helicity beam, respectively. This set of Compton scattering can be visualized by Figure 1.9.

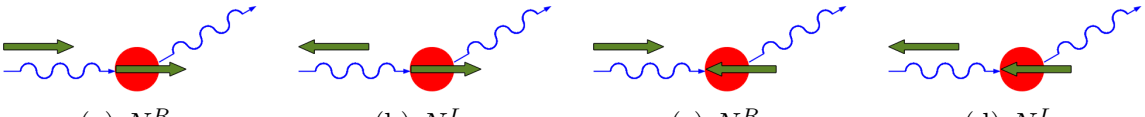

(a) N^R_{+x} (b) N^L_{+x} (c) N^R_{-x} (d) N^L_{-x}

Figure 1.9: Orientations for Compton scattering with a longitudinally polarized target and a circularly polarized photon beam. The arrow on the left of each represent the beam helicity, and the arrow on the right of each represents the target polarization direction.

Due to parity, it is also trivial to see from the figures that:

$$\sigma^R_{-x} = \sigma^L_{+x} \tag{1.40}$$

$$\sigma^L_{-x} = \sigma^R_{+x} \tag{1.41}$$

$$\sigma^R_{-z} = \sigma^L_{+z} \tag{1.42}$$

$$\sigma^L_{-z} = \sigma^R_{+z} \tag{1.43}$$

for a given energy, theta, and phi.

In the near future the collaboration at MAMI will begin a measurement with a linearly polarized beam on an unpolarized proton target, giving the asymmetry

$$\Sigma_3 = \frac{\sigma_\parallel - \sigma_\perp}{\sigma_\parallel + \sigma_\perp} = \frac{N_\parallel - N_\perp}{N_\parallel + N_\perp} \tag{1.44}$$

where $\sigma_\parallel$ and $\sigma_\perp$ represent the cross sections for an unpolarized target with a linearly polarized beam parallel and perpendicular to the scattering plane, respectively. This set of Compton scattering can be visualized by Figure 1.10.

1.2.1 Sensitivity

To study the sensitivities of the proton spin polarizabilities on nuclear Compton scattering a fixed-t dispersion analysis code[4] was used to generate tables of cross

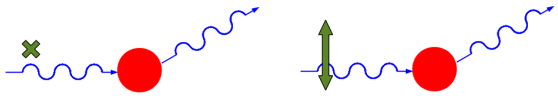

(a) $N_{\perp}$ (b) $N_{\parallel}$

Figure 1.10: Orientations for Compton scattering with a linearly polarized photon beam. The green 'X' on the left plot represents the polarization of the beam as perpendicular to the paper, whereas the arrow on the right represents the polarization of the beam as parallel to the paper.

sections for various values of the polarizabilities. This was done for the three experimental runs, Σ_{2x}, Σ_{2z}, and Σ_3, at a beam energy of 290 MeV. Using the construction of γ_0 and γ_π given in Equation 1.15 and Equation 1.17, respectively, the spin polarizabilities can be written in a basis of γ_{E1E1}, γ_{M1M1}, γ_0, and γ_π. From this basis one unknown spin polarizability is varied while the other is kept fixed. This gives an indication for what each asymmetry is more sensitive to. Given the fact that α, β, γ_0, and γ_π are all used in this dispersion code to produce these cross sections, it's important at each point to allow them to vary about their experimental errors. Figure 1.11a to Figure 1.13b show the results of this method of sensitivity testing, where each band represents a different value of either γ_{E1E1} or γ_{M1M1}, while the width of the band derives from allowing the other polarizabilities to vary. The clear separation of bands in Figure 1.11a compared to Figure 1.11b demonstrates the sensitivity of the transverse target asymmetry to γ_{E1E1}. The opposite effect is seen in both Figure 1.12a compared to Figure 1.12b and Figure 1.13a compared to Figure 1.13b, which demonstrate the sensitivity of the longitudinal target asymmetry and beam asymmetry to γ_{M1M1} A more detailed study of these sensitivities is provided in Appendix A, where the case for this set of experiments was made based not just on this ability to distinguish between the bands of different polarizabilities, but in running a full χ^2 fit with all of the expected data and extracting all four spin polarizabilities both with and without the use of additional constraints.

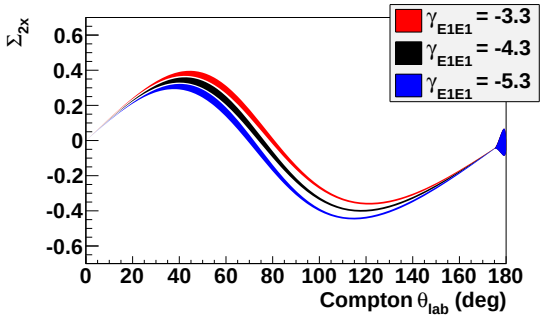

(a) Vary γ_{E1E1}, fix γ_{M1M1}

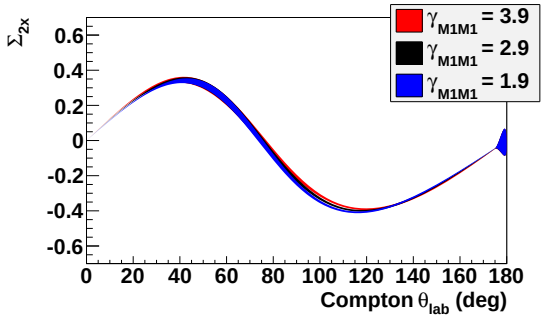

(b) Fix γ_{E1E1}, vary γ_{M1M1}

Figure 1.11: Theoretical Compton scattering asymmetries with a transversely polarized target and a circularly polarized photon beam. The bands represent the spread about these values by varying α, β, γ_0, and γ_π by their errors.

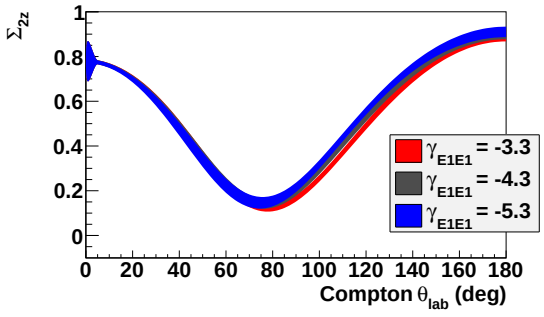

(a) Vary γ_{E1E1}, fix γ_{M1M1}

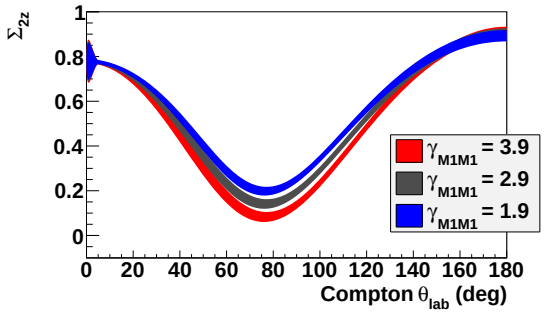

(b) Fix γ_{E1E1}, vary γ_{M1M1}

Figure 1.12: Theoretical Compton scattering asymmetries with a longitudinally polarized target and a circularly polarized photon beam. The bands represent the spread about these values by varying α, β, γ_0, and γ_π by their errors.

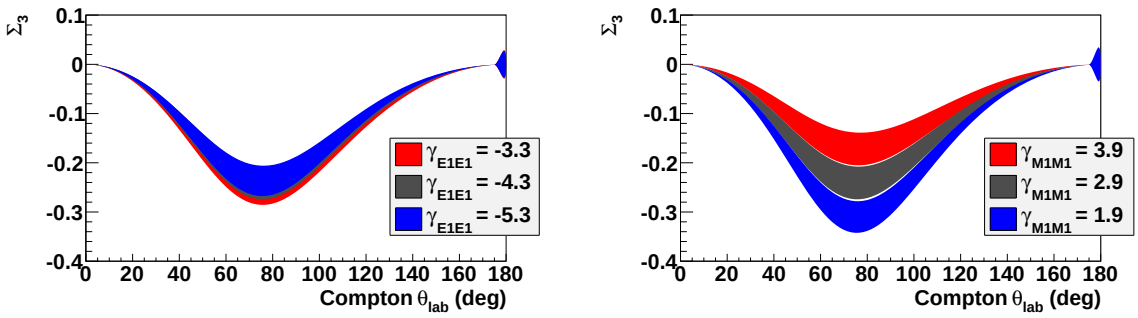

(a) Vary γ_{E1E1}, fix γ_{M1M1}

(b) Fix γ_{E1E1}, vary γ_{M1M1}

Figure 1.13: Theoretical Compton scattering asymmetries with an unpolarized target and a linearly polarized photon beam. The bands represent the spread about these values by varying α, β, γ_0, and γ_π by their errors.

CHAPTER 2

EXPERIMENT

The Mainz Microtron is a continuous wave (CW) electron accelerator located at the Johannes Gutenberg University in Mainz, Germany. The facility is part of the Institute for Nuclear Physics (Institut für Kernphysik, or KPH), and includes four experimental halls: A1 (Electron Scattering), A2 (Tagged Photons), A4 (Parity Violation), and X1 (X-rays).

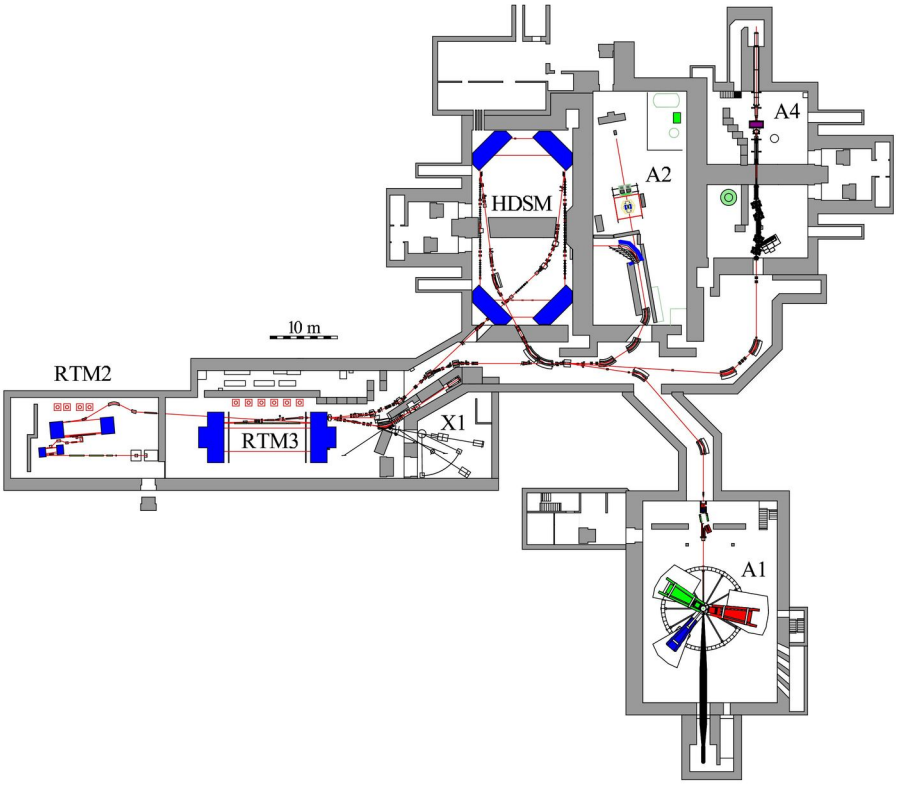

Figure 2.1: MAMI facility floor-plan, with the various microtrons and experimental halls[44]

2.1 MAMI Accelerator

The accelerator is actually composed of four individual microtrons: three Race-track Microtrons (RTMs) and one Harmonic Double Sided Microtron (HDSM), described in subsection 2.1.3 and subsection 2.1.4, respectively. The initial injector linac provides a 3.97 MeV electron beam which can be ramped up to 14.86 MeV with RTM1, then up to 180 MeV with RTM2, then up to 883 MeV with RTM3, and finally up to 1604 MeV with the HDSM.

2.1.1 History of MAMI

The design and construction of the facility started in 1975 with a goal of reaching e^- beam energies around 800 MeV. This was achieved in several stages, with the first (MAMI-A1) beginning operation in March 1979 using RTM1 and a Van-de-Graff injector. After some initial testing, experiments began taking data in November 1979. With the addition of RTM2 the second stage (MAMI-A2) ran from July 1983 until October 1987. The final upgrade of the original plan was the installation of RTM3 between 1987 and 1990. At this time a need was also expressed for a better injector with improved stability, resulting in the Van-de-Graff being replaced by a 3.97 MeV linac. This stage (MAMI-B) has been running since August 1990, with the first experiment taking place in the A2 hall in April 1991. In 1999 the demand arose to further increase the beam energy to 1.5 GeV. To maintain the integrity of the well running facility, an upgrade was agreed upon that would minimize the impact by utilizing already available space and performing a large component of the construction in parallel with MAMI-B beam-time. The HDSM was then built in what had been the X1 hall, allowing it to be closed off from the rest of the facility while beam was delivered to the remaining halls. This final stage (MAMI-C) was brought on-line in December 2006, with the first experiment taking place in the A1 hall in February 2007.[45]

2.1.2 Polarized Source

In addition to an unpolarized beam produced with a simple thermionic electron gun, MAMI can provide a polarized beam by striking a GaAsP (III-V semiconductor) cathode with circularly polarized laser light, producing longitudinally polarized photoelectrons. This process of optical pumping in solids was first noted in Si[46], and later applied to GaAs[47][48]. The polarized light is provided by a pulsed Ti:Sapphire laser. With an initial linear polarization, the light is converted into circularly polarized light by way of a quarter-wave plate, a birefringent material with a specific thickness that results in a 90° retardation of the phase for light transmitted along one axis as opposed to light transmitted along the perpendicular axis. If the plane of polarization of the incoming light is oriented at 45° with respect to the optical axis of this material, the parallel and perpendicular components of the transmitted light are equal, resulting in circular polarization. In the MAMI setup the quarter-wave plate is in the form of a Pockels cell, where a flip of the voltage polarity across the cell changes the optic axis of the material, thereby flipping both the helicity of the transmitted laser light and the electron beam polarization between parallel and anti-parallel. This is done with a frequency of approximately 1 Hz, which helps to reduce systematic effects in the analysis.[49]

The polarization of the electron beam is measured with a Mott polarimeter, shown in Figure 2.2.[50] The process is based on Mott scattering, where an asymmetry between the $\pm\hat{y}$ directions is observed for an electron, traveling in the $\hat{z}$ direction and polarized in the $\pm\hat{x}$ direction, scattered from a thin gold foil.[52] Since the electron beam is initially polarized in the direction of motion this measurement must occur after a spin rotation. This is performed with a Wien filter which utilizes a magnetic field perpendicular to an electric field, both of which are perpendicular to the beam direction. Properly chosen fields produces the desired spin rotation without deflecting the beam.[53]

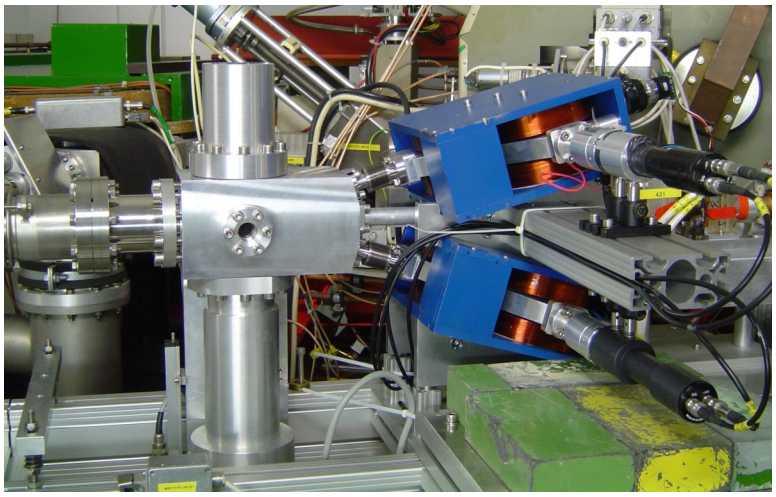

Figure 2.2: MAMI Mott polarimeter. The electron beam enters from the left, and the scattered electrons (up or down) are bent by dipole magnets, contained in the blue boxes, into detectors.[51]

2.1.3 Racetrack Microtron

A microtron is an accelerator that recirculates the beam through the same linac multiple times. One version of this is the racetrack microtron (RTM), appropriately named given its shape, as shown in Figure 2.3. An RTM consists of a single linac

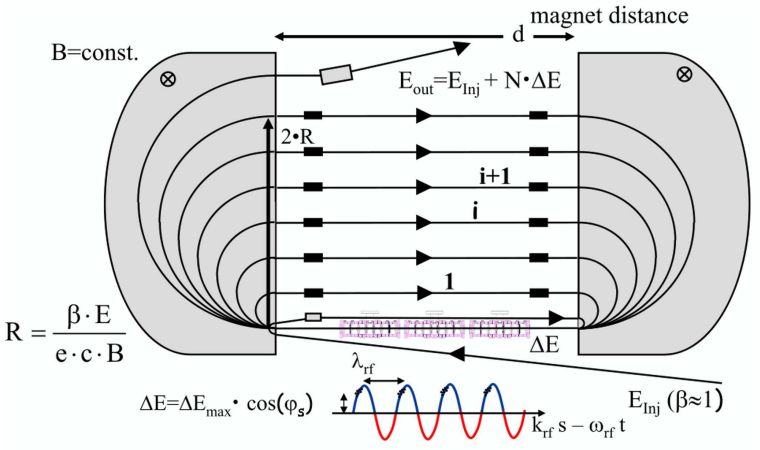

Figure 2.3: Racetrack Microtron[54]

placed between two large dipole magnets. The magnetic field of the dipoles is chosen such that the electrons from both the initial injection as well as each post-linac pass

will bend 180° into one of many exit lines. From there the electrons travel into the second dipole and again bend 180°, following the same radius of curvature since the magnetic field is the same as in the first dipole. The electrons therefore pass back into the linac to be accelerated. The linac uses a radio frequency klystron to alternate the potentials of a series of standing wave cavities, causing a well timed bunch of electrons to accelerate in each section. The increase in energy of an electron through the linac is given by Equation 2.1

$$\Delta E = \frac{ec^2 B}{2\pi\nu_{rf}} \tag{2.1}$$

where e is the electric charge, c is the speed of light, B is the magnetic field, and ν_{rf} is the frequency of the klystrons ($\nu_{rf} = c/\lambda_{rf} = 2.45$ GHz).[54] The values for the three RTMs can be found in Table 2.1.

Accelerating a polarized electron beam this way, however, has the unfortunate tendency to destroy the polarization. As the electrons pass through the dipole magnets their spin will tend to precess about the magnetic field with a frequency proportional to the cyclotron frequency. Another reason for the installation of the Wien filter noted in subsection 2.1.2 was to ensure that the polarization is purely longitudinal upon arrival in an experimental hall. By selecting a specific initial spin rotation angle, determined by the desired final beam energy, the spin direction ends up parallel to the beam direction after performing the known number of turns in each microtron.[53]

2.1.4 Harmonic Double Sided Microtron

RTM3 allows MAMI-B to reach electron energies of 883 MeV, which was sufficient for this experiment, which only required an electron beam energy of 450 MeV. In general, however, reaching 1.6 GeV posed challenges in addition to those noted in subsection 2.1.1. Each successive RTM is significantly larger, requiring larger magnetic fields and/or larger dipole magnets to bend the more energetic beam appropriately.

The field of RTM3 is already close to the upper limit of iron core magnets. So for a 1.6 GeV beam a dipole magnet of the same strength would have to be 5.4 times the size of an RTM3 dipole, which are already 450 metric tons (or tonnes) a piece. Instead, a double sided microtron was constructed with an arrangement, as shown in Figure 2.4, of two linacs and four dipole magnets. This setup requires each dipole to bend the beam by only 45°, thereby reducing the size them individually.[54]

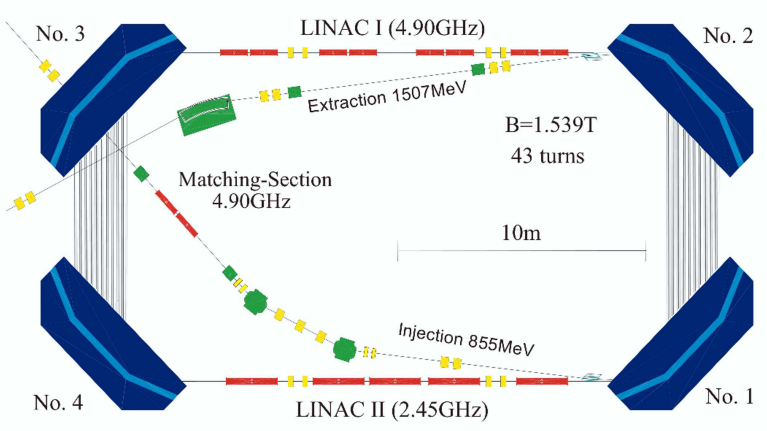

Figure 2.4: Harmonic Double Sided Microtron[54]

	RTM1	RTM2	RTM3	HDSM
Injection E (MeV)	3.97	14.86	180.0	855
Extraction E (MeV)	14.86	180.0	855	1508
Mag. Field (T)	0.1026	0.555	1.2842	1.53-0.95
ΔE per Cycle (MeV)	0.599	3.24	7.5	16.58-13.66
Number of Cycles	18	51	90	43

Table 2.1: Microtron parameters

2.2 A2 (Tagged Photon) Hall

In the A2 hall, where this experiment was run, the electron beam passes through a 10 μm copper foil, radiating Bremsstrahlung (German for 'braking radiation') photons with energies up to the initial electron beam energy. If the electron beam is

longitudinally polarized, the radiated photon will be circularly polarized.[55] The photon polarization is determined via QED by

$$P_\gamma = P_e \frac{4E_\gamma E_e - E_\gamma^2}{4E_e^2 - 4E_\gamma E_e + 3E_\gamma^2} \tag{2.2}$$

where E_γ is the energy of the photon, and where E_e and P_e are the energy and polarization of the electron beam, respectively.[56] For a 450 MeV electron beam, the ratio of the photon to electron polarization is given by the curve in Figure 2.5. After

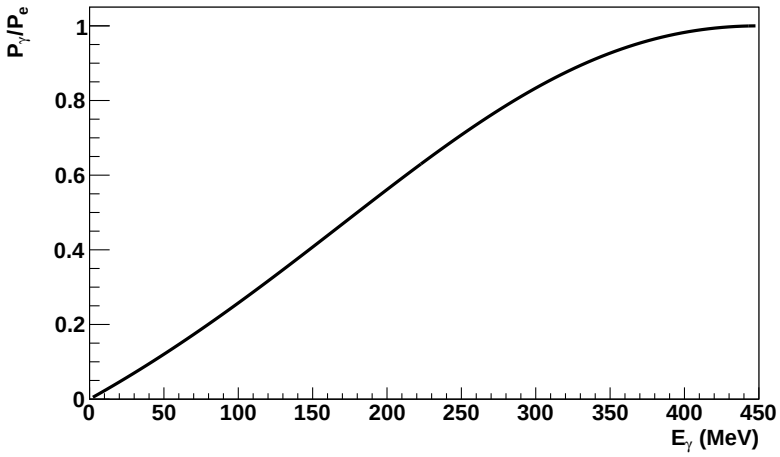

Figure 2.5: Ratio of circular photon polarization to longitudinal electron polarization for a 450 MeV electron beam

being produced, the photon continues straight through a lead collimator of variable diameter (here chosen as 2.5 mm) while the electron enters the Glasgow Photon Tagger.

2.2.1 Tagger

In the tagger the electron's path is bent by a large dipole magnet, as shown in Figure 2.6. The magnetic field is specifically chosen for the electron beam energy such that the electrons that do not radiate passing through the foil are bent into a beam dump. Those that do radiate lose energy in the process and will bend with

a smaller radius of curvature, with most of them hitting a ladder of 353 plastic scintillator detectors on the focal plane, as shown in Figure 2.6. Each scintillator

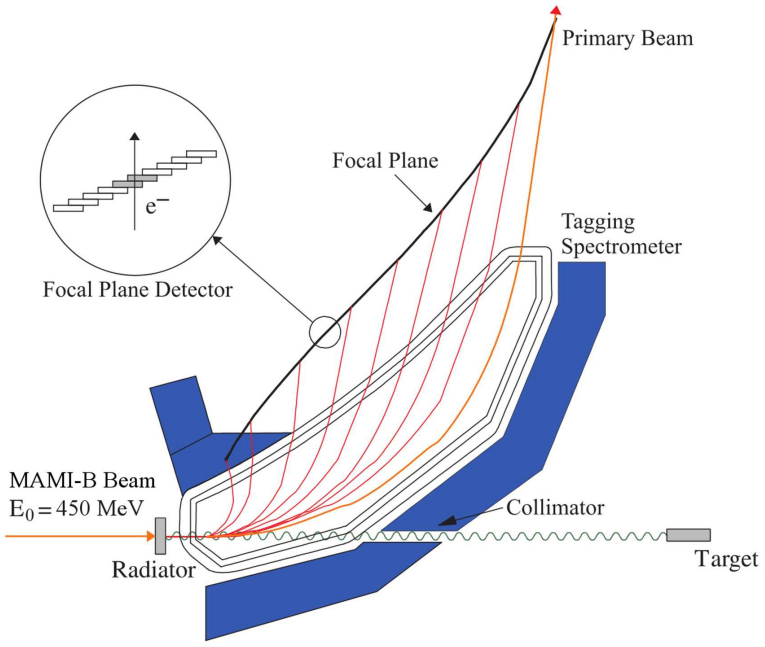

Figure 2.6: Glasgow photon tagger. After the electron beam enters from the left and strikes the radiator, the Bremsstrahlung photon continues to the right, while the electron is bent by the spectrometer magnet.[55]

is approximately 2 cm wide, 8cm long, 2 mm thick, and coupled to an individual detector. The scintillators are overlapped and electronically paired, so that a 'hit' requires two sequential detectors to fire, reducing accidental events. Because of this pairing there is then one fewer channel, for a total of 352. The specific channel hit coincides with an electron energy (for a given magnetic field) which determines the energy of the radiated, or tagged, photon through energy conservation.[57]

$$E_\gamma = E_e - E_{\text{tagg}} \tag{2.3}$$

The distribution of energies follows the expected Bremsstrahlung distribution, as shown in Figure 2.7.

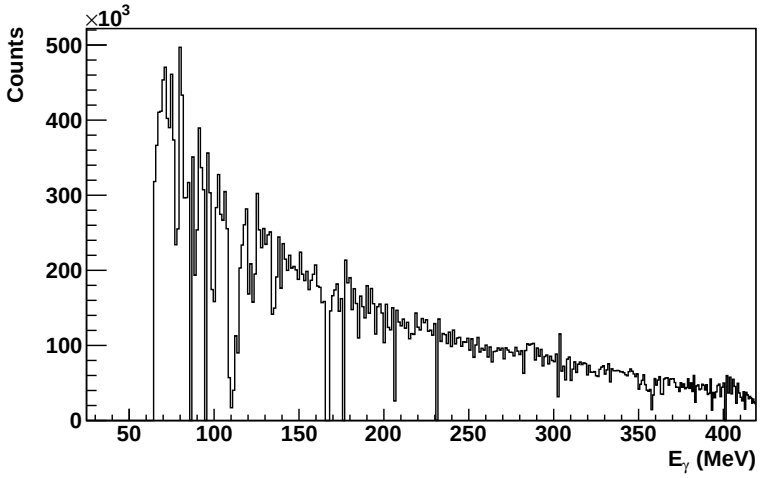

Figure 2.7: Bremsstrahlung distribution of photon energies

2.2.2 Targets

After collimation, the Bremsstrahlung photon beam travels 8.25 m in the A2 hall before striking a target. Two targets were utilized in this experiment, the polarized butanol target, and a carbon target used for background subtraction.

2.2.2.1 Butanol Target

While polarization of electrons is relatively easy, polarization of protons is considerably more difficult. With a 2.5 T magnet at a temperature of 1 K, proton polarizations will only achieve about 0.25%, while electron polarizations will reach about 92%. To obtain a highly polarized source of protons, this experiment utilizes the process of Dynamic Nuclear Polarization (DNP). The simplistic, albeit incomplete in this instance, description of DNP is given by the Solid-State Effect (SSE).[58] If a target of protons surrounded by free radicals is placed in the same 2.5 T magnetic field at a temperature of 1 K, the electron spins will align in the direction of the field. If the target is then exposed to microwaves with a frequency of $\nu = \nu_e - \nu_p$, where ν_e and ν_p are the Larmor frequencies of electrons and protons respectively, spin-flips between the electrons and protons will transfer the polarization to the protons over time.[59] For 2.5 T the Larmor frequencies are

$$\nu_e = \frac{\mu_e B}{\pi\hbar} = \frac{9.285 \times 10^{-24}\,\mathrm{J\,T^{-1}} \cdot 2.5\,\mathrm{T}}{3.14 \cdot 1.055 \times 10^{-34}\,\mathrm{J\,s}} = 70.04\,\mathrm{GHz} \tag{2.4}$$

$$\nu_p = \frac{\mu_p B}{\pi\hbar} = \frac{1.411 \times 10^{-26}\,\mathrm{J\,T} \cdot 2.5\,\mathrm{T}}{3.14 \cdot 1.055 \times 10^{-34}\,\mathrm{J\,s}} = 106.4\,\mathrm{MHz} \tag{2.5}$$

where μ_e and μ_p are the magnetic moments of the electron and proton, respectively. The polarization of the proton can also be reversed by simply adjusting the frequency to $\nu = \nu_e + \nu_p$, thereby populating the other level in the hyperfine splitting.

To maintain this polarization the target would have to remain in the magnetic field and be continuously pumped with microwaves, which is impractical for many physics applications due to the large size of the polarizing magnet. To get around this issue, the setup for this experiment uses a Frozen Spin Target (FST)[60], which has a ^{3}He/^{4}He dilution refrigerator that can achieve temperatures of 25 mK, shown in Figure 2.8. The target material, composed of beads of frozen butanol (C_4H_9OH)

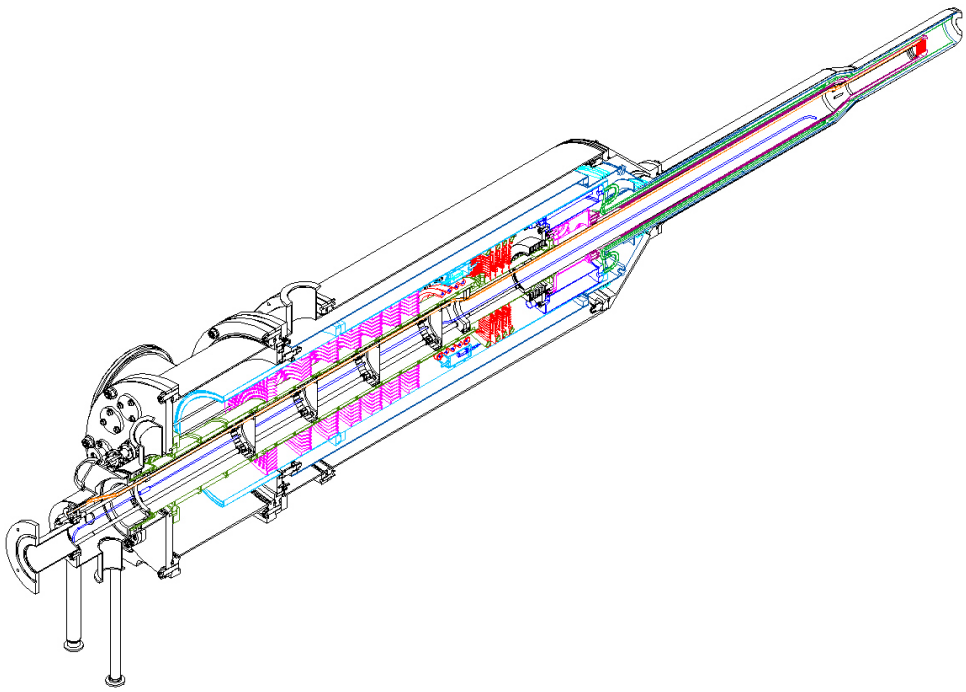

Figure 2.8: Frozen Spin Target cryostat. The photon beam enters from the bottom left and strikes the target in the red section at the top right.[61]

shown in Figure 2.9, is surrounded by a ^{3}He/^{4}He bath. It's first cooled down to ap-

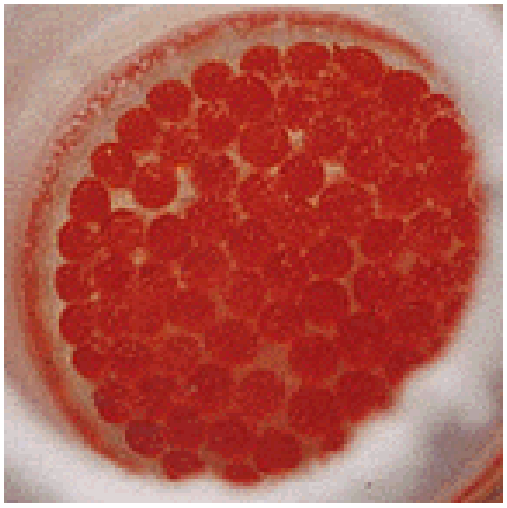

(a) Butanol Beads

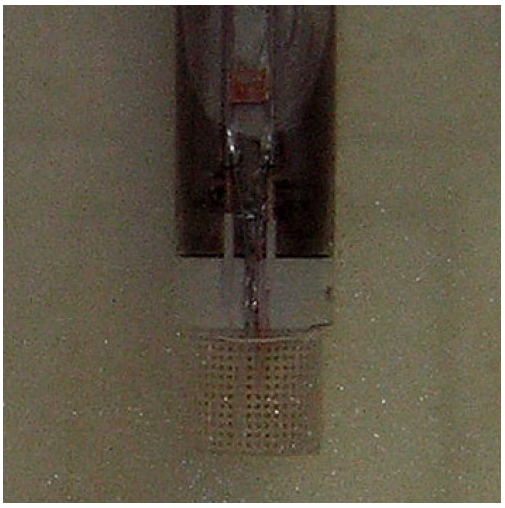

(b) Target Holder

Figure 2.9: Butanol target. Butanol beads (left) are enclosed in the white holder attached to the end of the target insert (right). The holes in the holder allow for the flow of ^{3}He/^{4}He. Also visible (right) are the leads for the NMR coil.

proximately 0.2 K, and then inserted into the 2.5 T polarizing magnet. Microwaves just above (or below) the electron Larmor frequency are pumped into the target, polarizing the protons. Once the desired (or maximum) nuclear polarization is reached, the microwaves are turned off and the cryostat lowers the temperature to 25 mK, 'freezing' the spins in place. To help maintain the polarization as long as possible a much smaller 'holding coil', located within the shells of the cryostat, is energized. Although its field of 0.6 T is much weaker than the polarizing magnet, it's sufficient to achieve relaxation times on the order of 1000 hours, with maximum polarizations above 90%.[61] To measure the target polarization a Nuclear Magnetic Resonance (NMR) coil is placed close to the target material. Coupling between the spins of the target and the coil itself affects the inductance of the coil when the frequency is swept through the proton Larmor frequency. By measuring this effect both in thermal equilibrium (a so called TE measurement) and in frozen spin mode, the polarization of the protons can be determined. This is done at the beginning and end of each

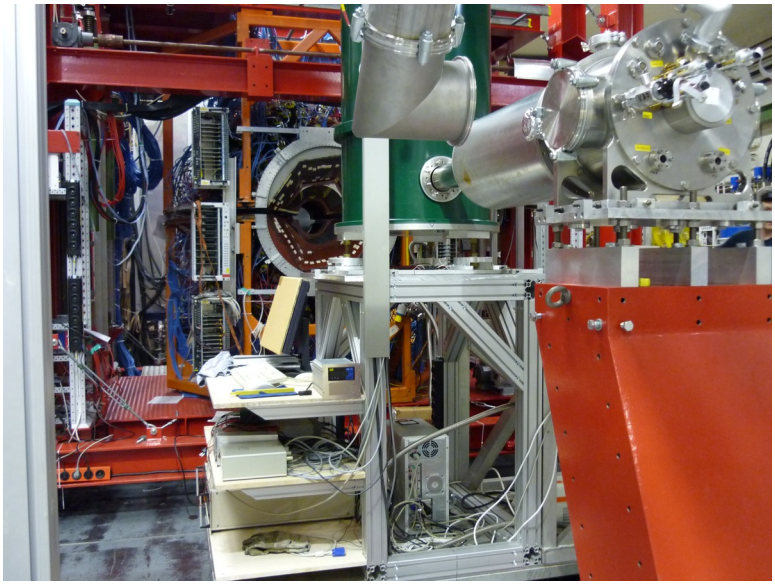

Figure 2.10: Frozen Spin Target. The dilution refrigerator is shown on the right with the polarizing magnet (green) placed over its nose. Visible in the background is the Crystal Ball detector system which is swapped with the polarizing magnet during running.

polarization period, and by extrapolating between these two measurements the polarizations for each run can be determined based on the time they occurred during this period. These measurements and the resulting table of polarization values were handled by Sebastian Schrauf.

2.2.2.2 Carbon Target

Since the target is not a 'simple' proton target, the inclusion of carbon, oxygen, and helium all contribute to the background in the experiment. In addition to the background from pion photoproduction off of the proton (discussed in section 4.4), this target allows for both coherent (interacting with the atom itself) and incoherent (interacting, and knocking out, a proton from the atom) versions of Compton scattering and pion photoproduction off of these additional atoms. Separate runs were taken with a specifically chosen carbon target, shown in Figure 2.11, to account for this. The density and length chosen for the target matches its total number of nucleons

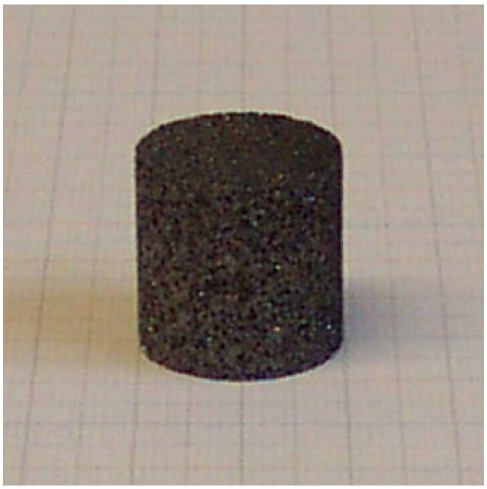

Figure 2.11: Carbon foam target. With a density of 0.55 g/cc the total number of nucleons in the carbon target matches the number of non-hydrogen nucleons in the butanol target.

with the total number of 'heavy' (non-hydrogen) nucleons in the butanol target (plus helium mixture). This was determined in the following way.

The length of the target cell is given as $L_T = 2.0\,\mathrm{cm}$, and the butanol filling factor is given as $F = 0.6$. From these, the effective length of butanol in the target can be calculated by

$$L_{Bu} = L_T \times F = 2.0\,\mathrm{cm} \times 0.6 = 1.2\,\mathrm{cm} \tag{2.6}$$

and the effective length of the helium in the bath surrounding the target by

$$L_{He} = (L_T \times (1 - F)) + 0.2\,\mathrm{cm} = (2.0\,\mathrm{cm} \times 0.4) + 0.2\,\mathrm{cm} = 1.0\,\mathrm{cm} \tag{2.7}$$

The extra 0.2 cm in the effective length of the helium in the target accounts for the additional helium in the cryostat downstream of the target cell. Additional parameters of the materials are given in Table 2.2.

Note that the number of nucleons for butanol has two numbers, 74 and 64. 74 is the total number of nucleons per butanol molecule. However, only the non-hydrogen nucleons are considered for the subtraction. Since butanol is C_4H_9OH, this gives 4

Material	ρ (density, $\frac{\text{g}}{\text{cm}^3}$)	M (molar mass, $\frac{\text{g}}{\text{mol}}$)	N (nucleons per unit)
Butanol	0.94	74.1	74 (64 non H)
Helium	0.14	4.0	4
Carbon	0.55	12.01	12

Table 2.2: Material parameters for butanol and carbon targets

carbon atoms (each with 12 nucleons) and 1 oxygen atom (with 16 nucleons), for a total of 64 nucleons. The area number density (molar) of butanol in the target is

$$n_{Bu} = \frac{L_{Bu} \times \rho_{Bu} \times N_{Bu}}{M_{Bu}} = \frac{1.2\,\text{cm} \times 0.94\,\frac{\text{g}}{\text{cm}^3} \times 64\,\text{nucleons}}{74.1\,\frac{\text{g}}{\text{mol}}} = 0.97\,\frac{\text{mol (nucleons)}}{\text{cm}^2} \tag{2.8}$$

and the area number density (molar) of helium in the target is

$$n_{He} = \frac{L_{He} \times \rho_{He} \times N_{He}}{M_{He}} = \frac{1.0\,\text{cm} \times 0.14\,\frac{\text{g}}{\text{cm}^3} \times 4\,\text{nucleons}}{4.0\,\frac{\text{g}}{\text{mol}}} = 0.14\,\frac{\text{mol (nucleons)}}{\text{cm}^2} \tag{2.9}$$

The total area number density (molar) of the frozen spin target is then

$$n = n_{Bu} + n_{He} = 1.11\,\frac{\text{mol (nucleons)}}{\text{cm}^2} \tag{2.10}$$

and setting the area number density (molar) of the carbon target equal to this result, the desired length of the carbon target is found from the reverse equation:

$$L_C = \frac{n_C \times M_C}{\rho_C \times N_C} = \frac{1.11\,\frac{\text{mol (nucleons)}}{\text{cm}^2} \times 12.01\,\frac{\text{g}}{\text{mol}}}{0.55\,\frac{\text{g}}{\text{cm}^3} \times 12\,\text{nucleons}} = 2.02\,\text{cm} \tag{2.11}$$

Since the length is only 1% larger than the length of the target cell this was deemed an ideal choice for a background target, and the material (called PocoFoam) was purchased from Poco Graphite.[62] The density of the carbon foam was also

measured at MAMI with a result slightly below the expected value, at $\rho_C = 0.53\,\frac{\mathrm{g}}{\mathrm{cm}^3}$. Using this value the length should be

$$L_C = \frac{n_C \times M_C}{\rho_C \times N_C} = \frac{1.11\,\frac{\text{mol (nucleons)}}{\mathrm{cm}^2} \times 12.01\,\frac{\mathrm{g}}{\mathrm{mol}}}{0.53\,\frac{\mathrm{g}}{\mathrm{cm}^3} \times 12\,\text{nucleons}} = 2.10\,\mathrm{cm} \tag{2.12}$$

which is a 4% difference, approximately.

By matching the target nucleons this way, the carbon target runs can be subtracted directly from the butanol target runs, after taking into account different running times and beam currents. Since the carbon target is inserted into the same cryostat, the subtraction also removes any contribution from the windows, and/or shells, of the cryostat. Secondary interactions between the final state particles and the target material they travel through also remain similar to those in the butanol target, as the shape and density are comparable.

2.2.3 Detectors

When the photon beam strikes the target, a system of detectors is used to determine the final state particles. This system is shown in Figure 2.12, and is described in the following sections.

2.2.3.1 Crystal Ball

The Crystal Ball (CB), shown in Figure 2.13, is a calorimeter that was constructed at the Stanford Linear Accelerator (SLAC) in the 1970's. Proposed in 1974, mere months before the J/ψ was discovered, it ran at SLAC from 1974 until 1982, performing many of the first measurements of the J/ψ. At this point it was moved to DESY where it ran from 1982 until 1987 measuring bottom quarks, among other things. After an eight year stint in storage it was put back into use at Brookhaven measuring baryon resonances from 1995 until 2002, at which point it was moved to its present location in the A2 hall at MAMI.[64] The CB is composed of 672 NaI

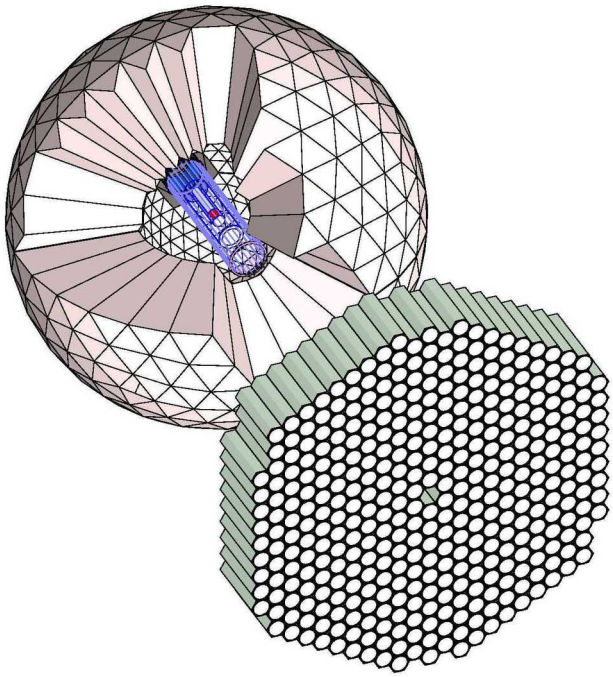

Figure 2.12: Detector systems in the A2 hall. The spherical object shown is the Crystal Ball (with the target cell, particle identification detectors, and multiwire proportional chambers shown in the cutout). The plane of cylinders is the Two Arms Photon Spectrometer.

crystals optically coupled to individual photo-multiplier (PMT) tubes. Each crystal is, however, optically decoupled from one another.

Each crystal, as shown in Figure 2.14, is a 40.6 cm long truncated triangular pyramid. The triangular sides at the top of the pyramid (inner surface of the detector) are 5.1 cm wide and at the bottom of the pyramid (outer surface of the detector) are 12.7 cm wide. A group of nine crystals form a minor triangle, a group of four minor triangles form a major triangle, and twenty major triangles form an icosahedron. This segmentation is shown in Figure 2.15 and Figure 2.16. The CB covers a polar angular range of 21° to 159°, and almost the entire azimuthal angular range except for a small section between the two separate hemispheres of the CB. It provides an energy resolution of 3-4% within the region of interest, a polar angular resolution

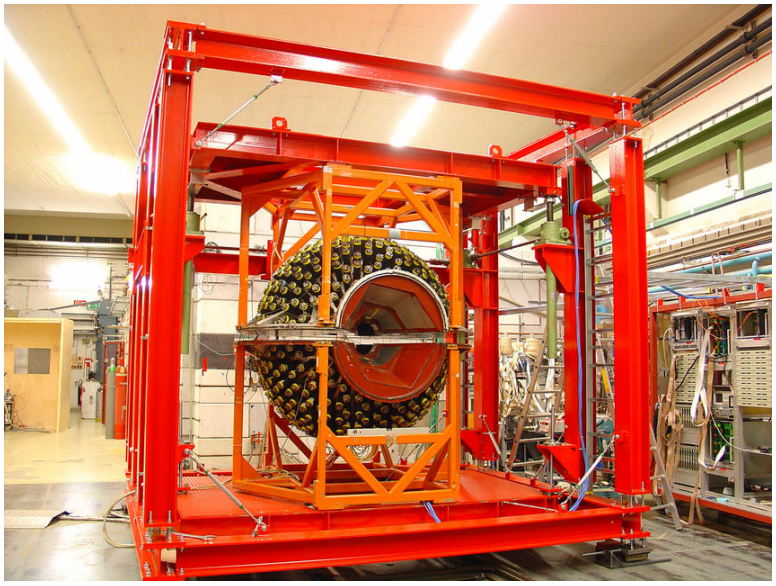

Figure 2.13: Crystal Ball NaI detector. The detector is shown in its frame along with attendant photomultiplier tubes (PMTs) but without cables.[63]

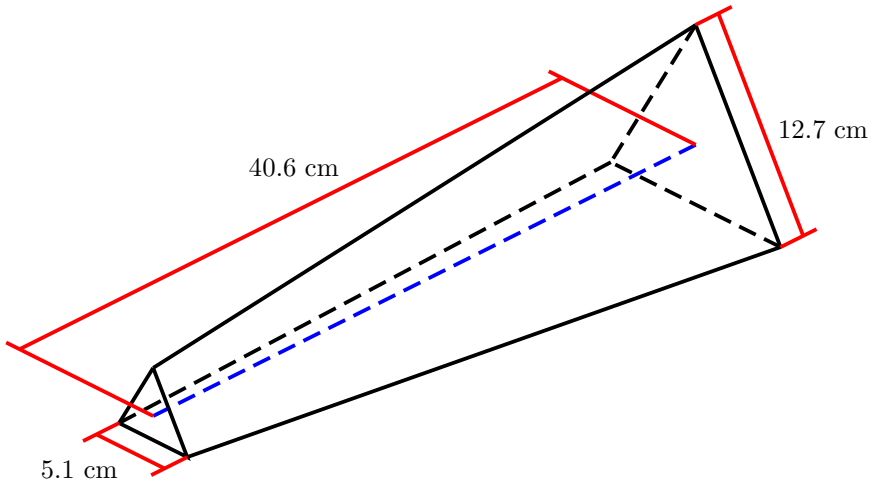

Figure 2.14: NaI crystal

of 3°, and an azimuthal angular resolution equal to the polar resolution divided by $\sin\theta$.[65]

Three additional detectors located in the beamline bore of the CB, a particle identification detector (PID) and two multiwire proportional chambers (MWPCs),

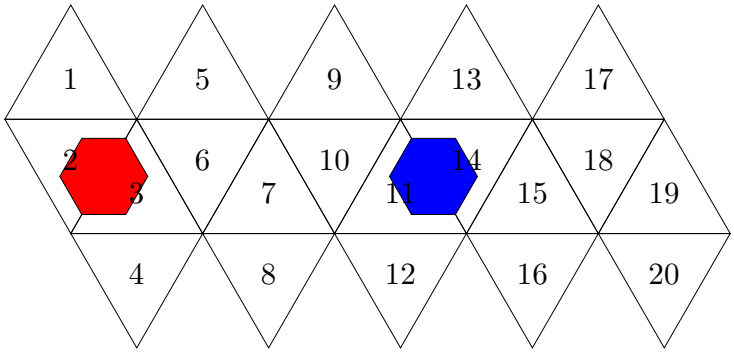

Figure 2.15: Crystal Ball major segmentation. The blue and red spots represent the sections that were removed for the incoming and outgoing photon beams, respectively.

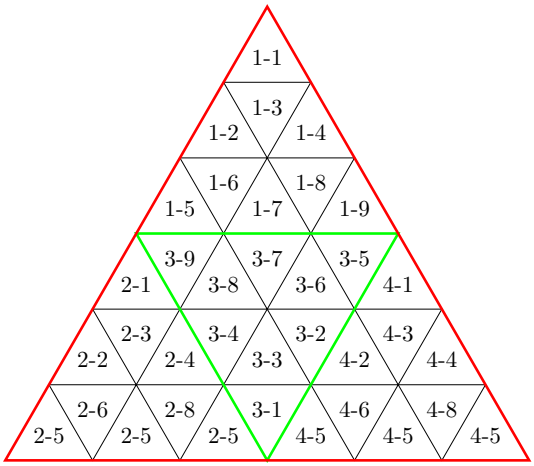

Figure 2.16: Crystal Ball minor segmentation. The green triangle separates the four minor triangles, and the black triangles separate each individual crystal.

are used for charged particle detection. As it's useful to describe these as all part of one system, in the future 'NaI' will refer specifically to the Crystal Ball NaI detectors, whereas 'CB' will refer to the collection of NaI, PID, and MWPCs.

2.2.3.2 PID

The PID, as shown in Figure 2.17, is a group of 24 plastic scintillator paddles, 500 mm long, 15.3 mm wide, and 4 mm thick, arranged in a cylinder parallel to the beam

with an inner diameter of 116.5 mm. Each detector therefore subtends 15° in ϕ, and

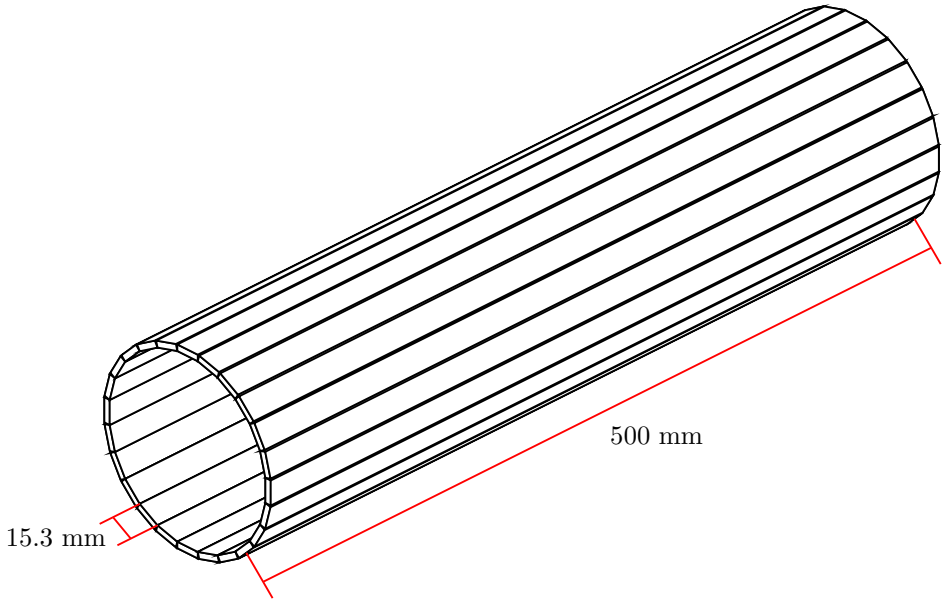

Figure 2.17: PID

covers a slightly larger polar angular range than the NaI (15° to 159°). The small thickness of the PID causes a charged particle to deposit a small amount of energy, ΔE, in it before depositing its remaining energy, E, in the NaI. Since electrons and, for the most part, charged pions are minimally ionizing in the PID, they deposit a rather consistent amount of energy. A proton, however, tends to lose more energy in the PID, especially at lower kinetic energies. Using these two values a ΔE/E plot, like that shown in Figure 2.18, allows for separation of electrons, protons, and charged pions.[57]

2.2.3.3 MWPC

The MWPCs are examples of gas-ionization detectors. They each have a layer of anode wires (parallel to the beam) suspended between two layers of cathode strips (where the strips in each layer are spiraled around, in opposite directions, at a 44.23° angle with respect to the wires, or 88.46° with respect to each other). Figure 2.19 and

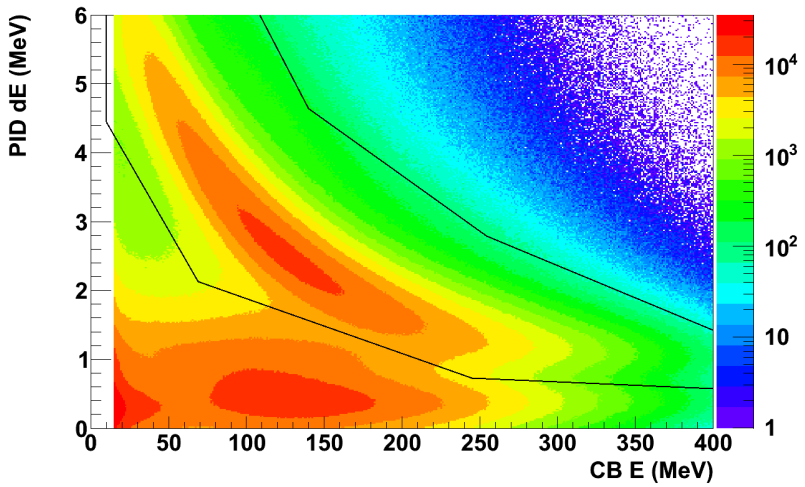

Figure 2.18: PID ΔE vs CB (NaI) E. The proton events result in a 'banana' shape upon which the black line defines the proton cut. The red section below this shows the charged pion events, and the smaller clump near the origin shows the electron events.

Figure 2.20 depict this design. A voltage is applied between the anodes and cathodes, and a gas mixture which ionizes during the passage of a charged particle is pumped into the system. The ionization electrons/holes then drift to the anodes/cathodes, changing the voltage between them and providing the signal that is read out. The inner wire chamber has 232 wires, 69 inner strips, and 77 outer strips. The outer wire chamber has 296 wires, 89 inner strips, and 97 outer strips.[66]

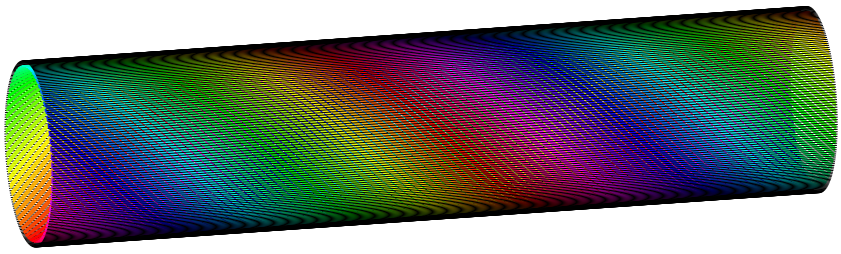

Figure 2.19: Model of an MWPC, showing the inner cathode layer and the layer of anode wires surrounding it.

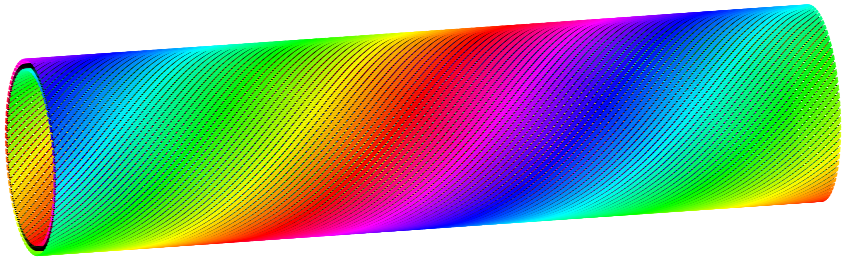

Figure 2.20: Model of an MWPC, showing the two cathode layers sandwiching the layer of anode wires.

2.2.3.4 TAPS

While the loss of detection at backward angles is unavoidable due to the requirements of the frozen spin target, the 'hole' in the CB at forward angles is partially dealt with. A version of the Two Arms Photon Spectrometer (TAPS) is placed downstream of the CB (approximately 1.8 m from target center to detector center), providing angular coverage forward of 20°, with only a small hole for the photon beam. The detector consists of 366 BaF_2 crystals, each of which is a 22.5cm long hexagonal polyhedron with an inner diameter of 5.9cm, as shown in Figure 2.21. An additional 18 BaF_2 crystals in the two innermost rings of TAPS were previously replaced with 72 $PbWO_4$ crystals. This served several purposes, one of which was to improve the angular resolution for very forward-going events. The other purpose was to improve their capabilities in a high rate environment dominated by atomic Compton scattering. This was achieved both by reducing the rate in each detector, and improving the relaxation time by a factor of 100 (from 620 to 6 ns). For this experiment, however, since the $PbWO_4$ crystals are outside of the useful kinematic range for Compton scattering, and due to the high counting still experienced, they are not utilized in the analysis. In general, TAPS has an angular resolution of approximately 0.7° and a similar energy resolution to that of the NaI.[67]

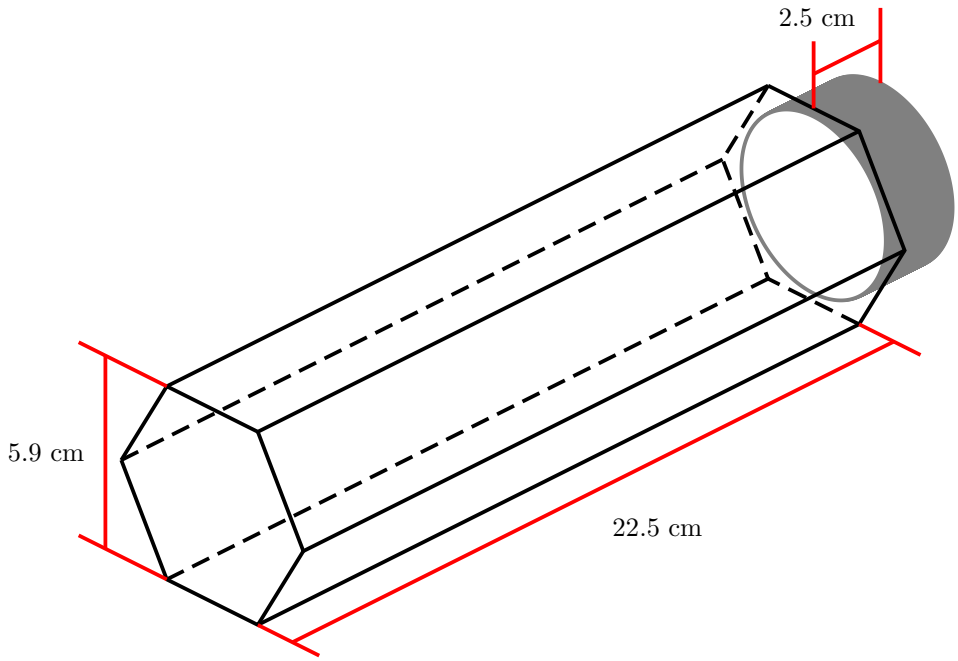

Figure 2.21: BaF2 crystal

Each crystal of TAPS has a 5mm thick plastic scintillator paddle in front of it that provides both veto and particle identification abilities. Similar to the PID, a charged particle will deposit some portion of its energy, ΔE, in the paddle before depositing its remaining energy, E, in the BaF_2 crystals. Each plastic scintillator is individually read out by a wavelength shifting fiber coupled to a PMT, which allows for a direct correlation between a hit in a paddle and a hit in a BaF_2 crystal. Besides tagging the event as charged, and possibly vetoing it, plotting ΔE/E allows for proton selection as done for the NaI and PID. Such a plot is shown in Figure 2.23. Similar to the CB, for the future 'TAPS' will refer to the collection of BaF_2, $PbWO_4$, and the veto paddles.

Given the greater distance from the target to TAPS, as compared to the CB, the detection of a proton can also be checked by measuring the time-of-flight (TOF). As will be discussed in subsection 2.3.2, the event time is started by a trigger in the CB.

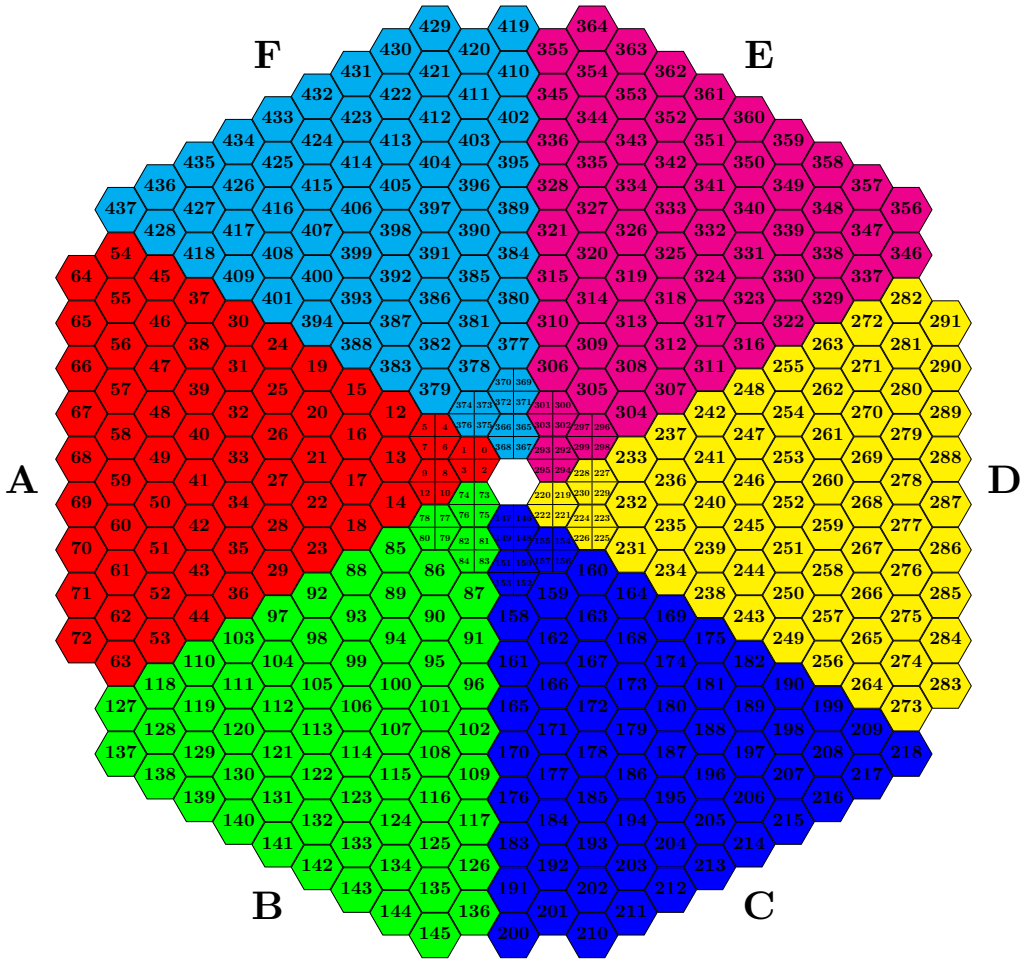

Figure 2.22: TAPS segmentation. This is shown as viewed from behind TAPS (looking towards the target).[63]

With π^0 photoproduction for example, one of the π^0 decay photons could be detected in the CB, starting the time. If the other decay photon is detected in TAPS, the difference between these two times will be unresolvable. If instead the recoil proton is detected in TAPS, this difference will be noticeably longer due to the proton's mass. This TOF, which also becomes larger for protons (or neutrons) of lower kinetic energy, is plotted as a function of the detected energy as shown in Figure 2.24. If desired, a cut is applied to this distribution to select those particles that are more characteristic of nucleons. This is especially useful (albeit not for this experiment) for distinguishing neutrons from photons.

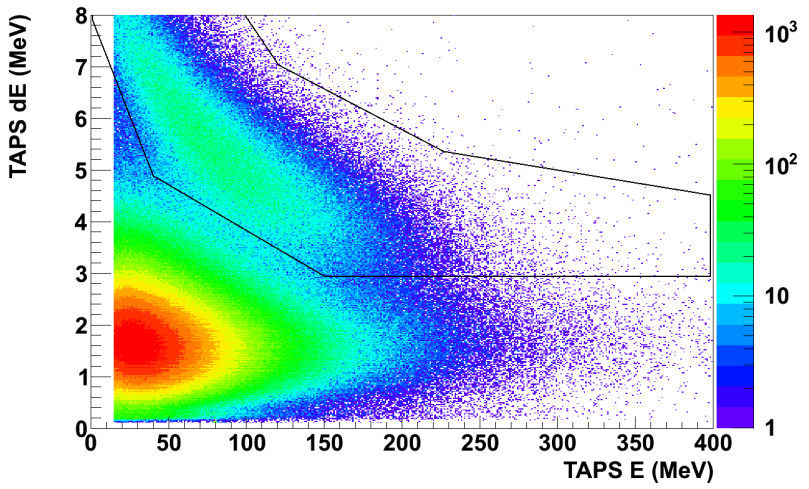

Figure 2.23: TAPS ΔE vs E. The proton events again result in a 'banana' shape upon which the black line defines the proton cut.

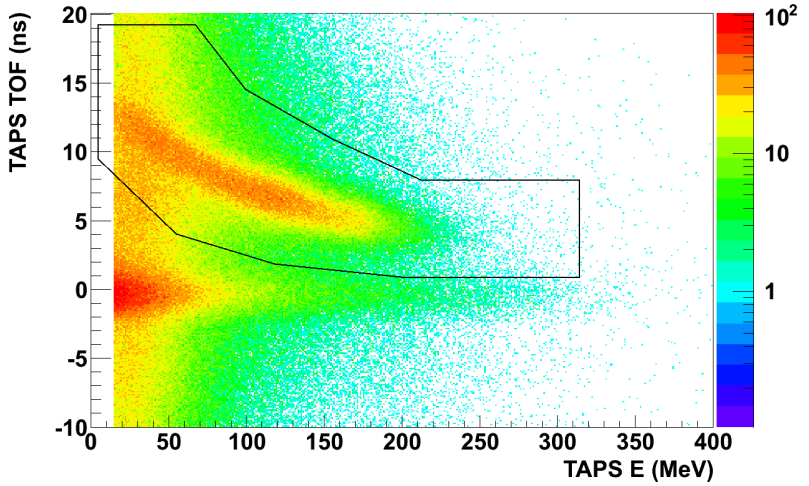

Figure 2.24: TAPS Time-of-Flight. The proton events are the secondary peak just above the electron events, where the black line again defines the proton cut.

2.2.3.5 Cherenkov

Additionally, a gas Cherenkov detector is installed between the CB and TAPS. This simple detector contains a gas mixture that emits Cherenkov radiation with the passage of a highly energetic charged particle, here almost exclusively electrons. This can then serve as a veto for TAPS, allowing for the elimination of electrons originating from pair production.

2.3 Data Acquisition

The signals from the PMTs attached to each detector scintillator must be converted into useful information for the experiment. This process is performed by a complex Data Acquisition (DAQ) system outlined here.

2.3.1 General Concepts

In general a DAQ system in nuclear physics will split the analog signal output from a detector into two branches, the first of which is used to both create a trigger for the event and be analyzed for timing information, and the second of which is analyzed for energy information. The first branch usually runs the analog signal through a discriminator which outputs a square pulse (of adjustable width) if the input is of sufficient height. This removes both electronic noise and events below the energy of interest. The output from the discriminator is then split again, with one line being combined with other detectors in the desired trigger design. The second line from the discriminator typically leads into a Time-to-Digital Converter (TDC), which compares the arrival time of the pulse to a reference pulse provided by the trigger, and assigns a digital number corresponding to this time difference. Typically the energy information is obtained by sending the second branch of the analog output from a PMT into an Analog-to-Digital Converter (ADC), which assigns a digital number corresponding to the size (either amplitude or integral) of the analog signal. The trigger must also be fed into the ADC in some way to instruct it when to analyze the analog signal.

2.3.2 Esum Trigger

The MAMI A2 system, while more complicated as shown in Figure 2.25, still derives from these basic concepts. The analog outputs from the Crystal Ball NaI PMTs are sent into Uppsala modules, which provide active fan-in/fan-out splitting, in batches of 16. In addition to splitting the signal for the energy and timing/trigger

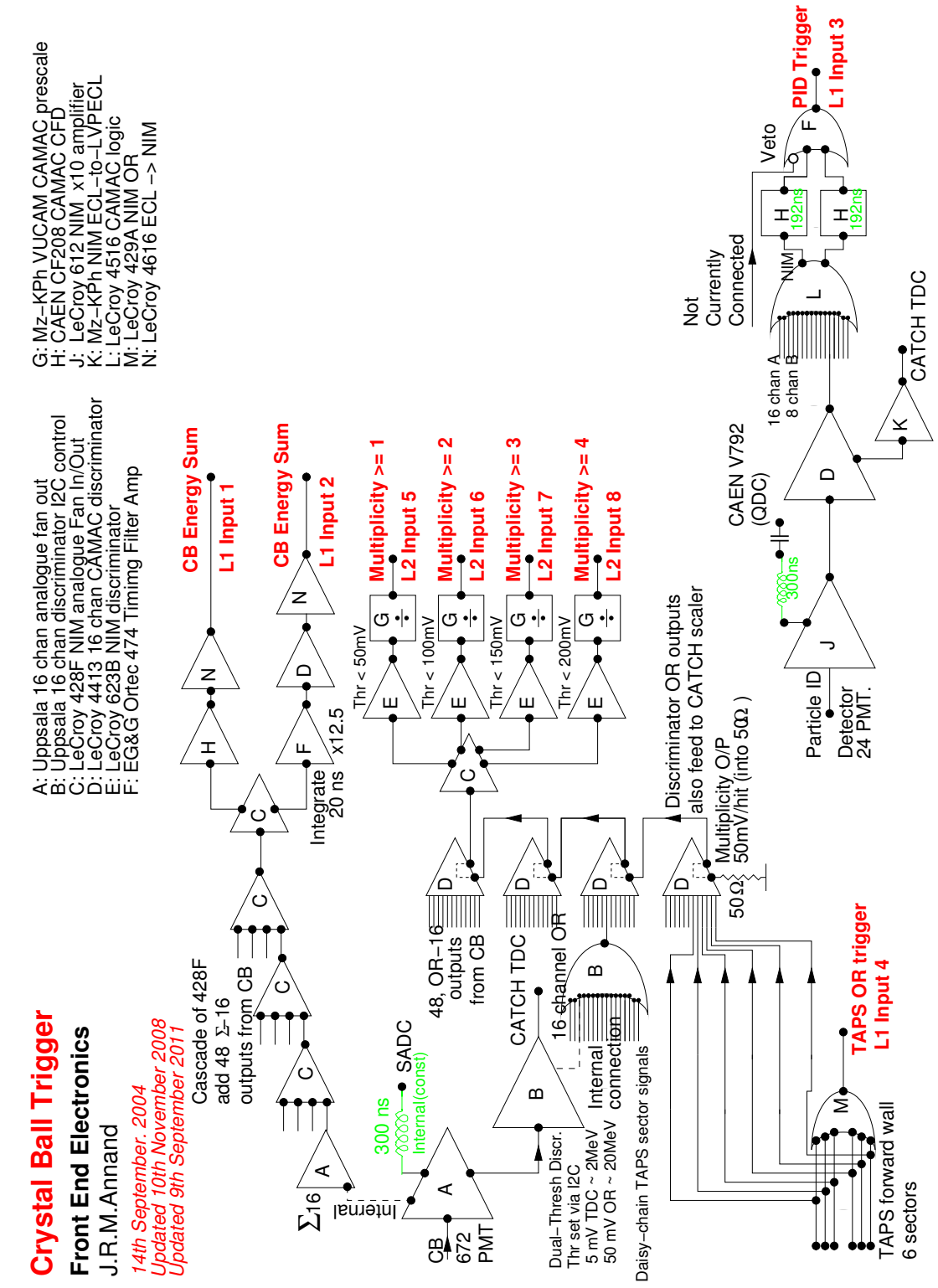

Figure 2.25: Front end of trigger[63]

branches, the module also sums the 16 analog signals into one. The summed signals are daisy-chained together for all 42 modules, providing one analog signal representing the total energy deposition in the NaI, and is therefore called the CB Energy Sum (E_{sum}). This signal, in addition to being analyzed in its own ADC channel, is split and run into two discriminators. The first has a high threshold programmed into it which defines a first level trigger. For this experiment the trigger was set for $E_{\text{sum}} > 100$ MeV, thereby rejecting any event that did not deposit at least 100 MeV into the NaI. The second discriminator has a low threshold of a few MeV, to improve the timing of the E_{sum} trigger. The outputs of both discriminators are put into a logical AND, the output of which is then used as the first level trigger signal. For this experiment this is the only trigger requirement.

2.3.3 Multiplicity Trigger

The A2 system also has the ability for more complicated second level triggers. The timing/trigger branch outputs of the Uppsala module, as described in subsection 2.3.1, are fed into another dual threshold discriminator. The low threshold lines are sent into individual TDC channels for each detector to be analyzed. The high threshold lines are fanned-in together for all 42 Uppsala modules, along with similar signals from the six sectors of TAPS. The number of these 48 'clusters' above threshold then forms a 'multiplicity' number, and the second level trigger can require this multiplicity to be above a specified amount. For this experiment it was desired to run with the simple E_{sum} trigger, accepting events with any multiplicity. The overall master trigger is shown in Figure 2.26, with details provided in [57] and [68].

2.3.4 Detector Readout

When an event satisfies the required trigger conditions all of the various ADC and TDCs must be read out. Different components of the A2 system perform this function in varying ways.

The timing signals for the Tagger, NaI, PID, and MWPC wires are all read into CATCH (Compass, Accumulation, Transfer and Control Hardware) TDCs, which were originally designed for use in COMPASS. These TDCs do not use a start or stop signal, but instead have a constantly running internal ≈ 8.55 GHz oscillator. All of the CATCH TDCs have their oscillators synchronized through a Trigger Control System (TCS), designed at CERN. This allows an entire batch of these modules to have one reference TDC that the trigger is read into, providing a reference count of the oscillator. When a timing signal from a PMT is read into its own TDC channel, the oscillator count is stored in the buffer. The time of that hit is then simply the difference between the count in that TDC and the count in the reference TDC, divided by the oscillator frequency (which gives ≈ 117 ps/count). Both the Tagger and the entire CB system have their own reference TDC channels, allowing a check between them to verify that they are still synchronized. Additionally, the Cherenkov detector timing is analyzed by a CATCH TDC, while its energy is analyzed with a standard ADC.

The analog output from the Tagger is not used for an energy measurement, since the electron energy is determined by which detector it hit along the focal plane. The PID is read out into traditional ADCs. The NaI and MWPC strips detectors, however, are read into Sampling ADCs (SADCs). These SADCs sample the inputs at a rate of 40 MHz and maintain a buffer of these samples for 2 μs. They were set to automatically integrate three different regions of each sample: a section before a pulse, the majority of the pulse itself, and a section of the pulse tail. The combination of the first two provides automatic pedestal suppression, by removing the baseline from the peak and requiring the remaining signal to be above threshold. The combination of the second two checks for potential pile-up, where two separate events end up in the same sample.

The timing and energy information for TAPS is analyzed through standard TDCs and ADCs. However, a benefit to BaF_2 is the ability to perform Pulse Shape Analysis (PSA). This process makes use of the response of a BaF_2 crystal to different radiation. The scintillation light from BaF_2 has both a fast and a slow component to the response, with decay times of 0.6 ns and 630 ns, respectively. By integrating the signal over two different lengths of time, defined by the gate to the ADC, both components can be measured. The ratio between them is indicative of the particle detected.[69] This will be discussed in more detail in subsubsection 3.2.3.2.

2.3.5 Scalers

When an event passes the specified trigger requirements the system is set to 'busy', refusing any further information from the ADCs and TDCs, so that it can digitize and export the information to the main DAQ computer, and from there to a hard disk for storage. This leads to an amount of 'dead time' where the system is unable to recognize relevant events. To account for this, additional logic outputs from various discriminators are sent into 'scaler' modules, which simply count the number of pulses. With only a few exceptions, these modules are not inhibited while the system is digitizing, providing a complete number of hits in a detector element or total possible triggers to the system. One of the exceptions to this rule is to have a trigger signal that is inhibited by the system busy run into its own scaler. A comparison between the inhibited and uninhibited trigger scalers provides a measurement of the 'live time' (or dead time subtracted from unity) of the system.

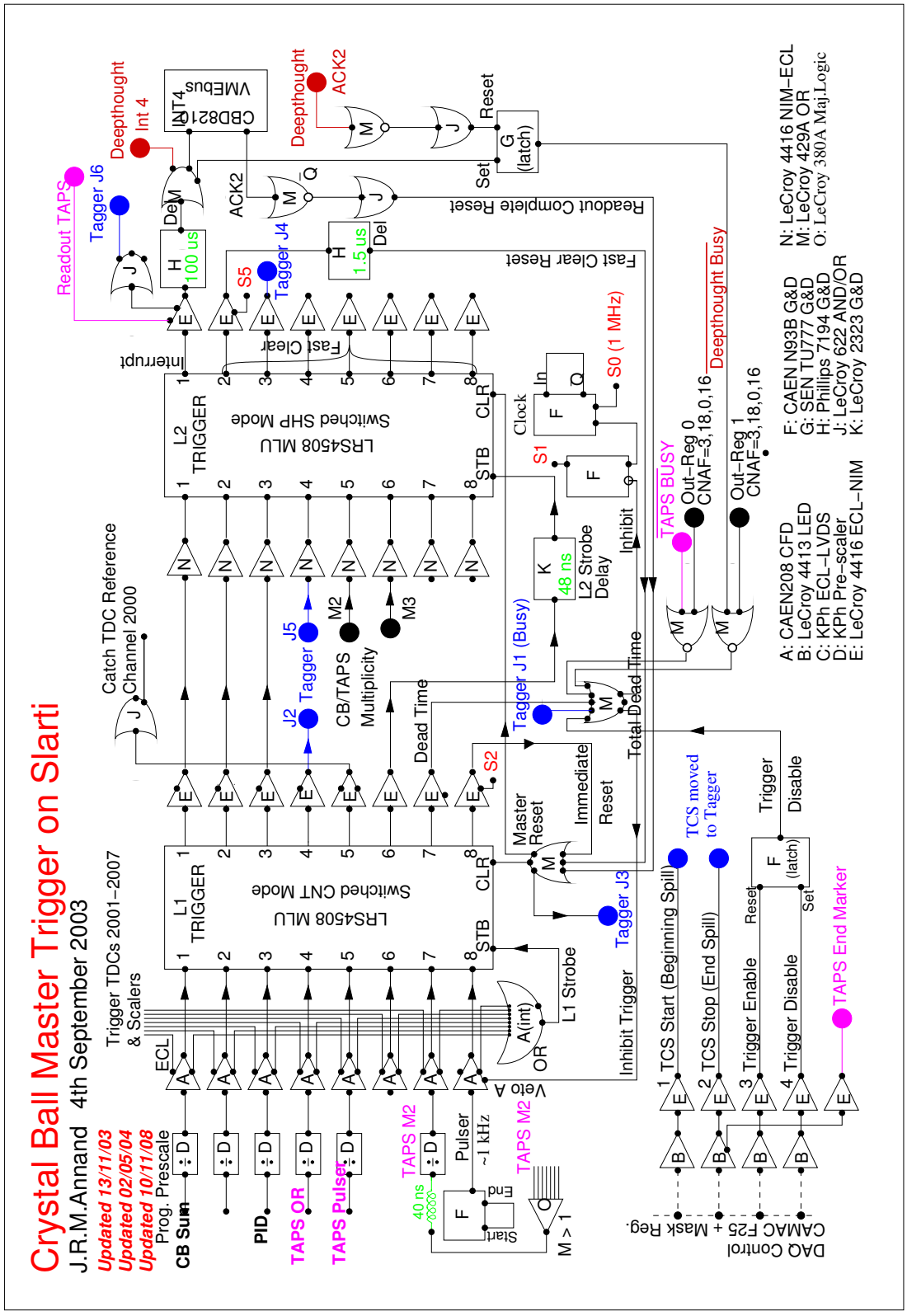

Figure 2.26: Trigger[63]

CHAPTER 3

DATA RECONSTRUCTION

The various detector systems and their corresponding electronics produce event information that is recorded, and later analyzed, by a program named AcquRoot. This program is a set of C++ classes built on top of the ROOT system developed by CERN. For each event, AcquRoot returns a set of 'particles' with pertinent information such as particle type, kinetic energy, momentum, invariant mass, timing, and detector(s) and crystal(s) hit. From this set the specific type of desired event can be chosen with the appropriate selection criteria.

3.1 Software

3.1.1 ROOT

ROOT is an object-oriented data analysis framework developed at CERN in the mid 1990's. Led by Ren Brun and Fons Rademakers, who felt that the increasing processing requirements for the large quantity of data being taken was exceeding the old method of PAW and HBOOK, they sought to upgrade from FORTRAN libraries and procedure-oriented programming to C++ libraries and object-oriented programming. Since 1995 ROOT has grown to now be used by practically every nuclear and particle physics group, as well as countless others.

3.1.2 AcquRoot

AcquRoot is a framework built upon ROOT, providing many additional classes that interface with detectors to take and analyze data. It replaces the older ACQU

which, first written in 1988 by John Annand of the University of Glasgow, interfaced with HBOOK. With the success and widespread adoption of ROOT, AcquRoot was initially conceived as an upgrade to ACQU, but has since become a powerful stand-alone acquisition and analysis framework.

Before proceeding, an important note on the nomenclature used here, which carries over from the previous chapter. An *apparatus* (the CB for instance) is a collection of *detectors* (the NaI, PID, and MWPC in the case of the CB) that work together to produce particle tracks. Each *detector* is a collection of similar *elements* (NaI crystals, scintillator paddles, etc). Each *element* is individually read out with its own ADC and TDC.

3.1.2.1 Analyze Hits

During the decoding of an event an analysis class (TA2UserAnalysis), which inherits from the TA2Analysis class, handles the collection of information from all of the apparati and passes it into a physics class (TA2SpinPolPhysics), which inherits from the TA2Physics class. Each apparatus has an individual class that inherits from the TA2Apparatus class, and each of its constituent detectors also has an individual class that inherits from the TA2Detector class. This is detailed in Table 3.1. The physics class also inherits from the TA2Apparatus class, and can be considered a super-apparatus. Each of the classes along this chain read in configuration files that specify settings for the decoding and histogramming of data within that piece. For instance, the TA2CalArray class has a configuration file that tells AcquRoot what histograms to create for displaying NaI specific results, how many elements the NaI detector has, where each is located, and what their parameters are.

As AcquRoot runs, the analysis class is passed an event from a data file; looks at each element, in each detector, in each apparatus; and converts the digital output of an ADC or TDC back into values for energy or time through Equation 3.1 and

Analysis (TA2Analysis)	Apparatus (TA2Apparatus)	Detector (TA2Detector)
Analysis (TA2UserAnalysis)	CB (TA2CentralApparatus)	NaI (TA2CalArray)
		PID (TA2PlasticPID)
		MWPC (TA2CylMwpc)
	TAPS (TA2Taps)	BaF_2 (TA2TAPS_BaF2)
		Veto (TA2TAPS_Veto)
	Tagger (TA2Tagger)	Ladder (TA2Ladder)

Table 3.1: AcquRoot analysis classes

Equation 3.2 respectively.

$$E = S\left[G(C-P) + Q(C-P)^2\right] \tag{3.1}$$

where S is a global scale factor, G is the gain, C is the ADC channel, P is the pedestal, and Q is a quadratic factor.

$$T = G(C-O) + Q(C-O)^2 \tag{3.2}$$

where G is again the gain, C is the TDC channel, O is the offset, and Q is again a quadratic factor. AcquRoot uses specific lines (usually denoted as 'Element') in the detectors' configuration file to set these calibration parameters for each element. An example is given in Table 3.2, with a corresponding description.

There are some deviations from this standard however. For the PID the positions are given in spherical coordinates r (mm), θ (deg), and ϕ (deg). The MWPC typically excludes the positions given its complicated geometry. For the tagger there are three additional parameters that set the central energy for the element, the overlap

ADC	Num	3015M1	The physical ADC channel number to look at
	Low	2.0	Low software threshold for the ADC (MeV)
	High	2000.0	High software threshold for the ADC (MeV)
	Ped	0.00	ADC pedestal (channel)
	Gain	0.070606	ADC gain (MeV/channel)
TDC	Num	2032M0	The physical TDC channel number to look at
	Low	-400.0	Low software threshold for the TDC (ns)
	High	850.0	High software threshold for the TDC (ns)
	Off	-2068.65	TDC offset (channel)
	Gain	0.117710	TDC gain (ns/channel)
Pos	X	3.619	The x position of the element center (cm)
	Y	45.214	The y position of the element center (cm)
	Z	2.629	The z position of the element center (cm)

Table 3.2: Sample parameter line from a detector configuration file

in energy between adjacent elements, and the scaler channel number for that element. Regardless, all of these factors are determined both through knowledge of the hardware and through calibration, as will be discussed in section 3.2.

3.1.2.2 Determine Clusters

Due to the segmentation of the NaI and BaF_2 detectors, photons typically deposit energy through an electromagnetic shower that spans multiple elements. For a given event the detector classes, as discussed in subsubsection 3.1.2.1, convert the ADC and TDC channel information for an element into values for the energy and time of the hit. These individual hits then need to be restructured into one correlated cluster resulting from the detection of a single particle. The primary method of achieving this is by iterating through the list of element hits and searching for neighboring ones. Additional lines in the NaI and BaF_2 detector configuration files give lists of neighboring elements for each single element in the detector. An element in the NaI typically has 12 defined neighbors as shown in Figure 3.1a, and an element in the BaF_2 typically has 6 defined neighbors as shown in Figure 3.1b.

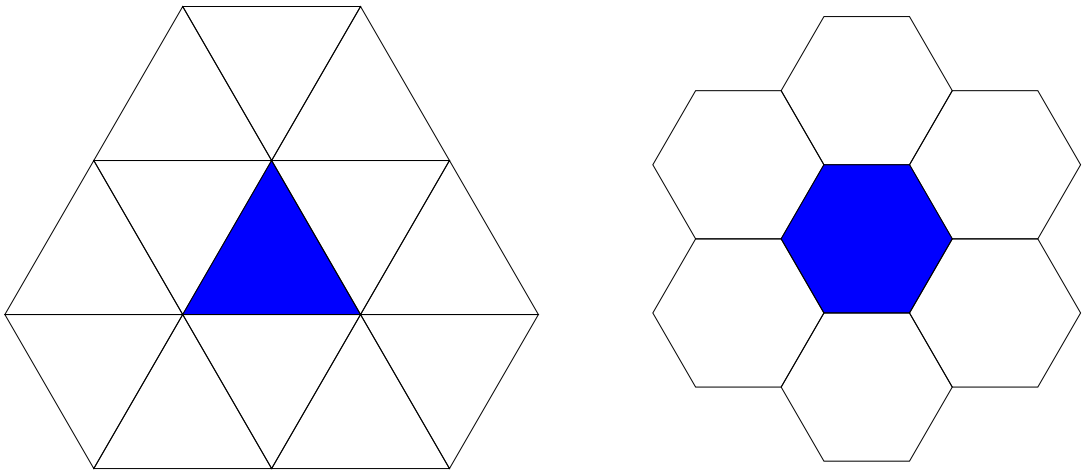

(a) NaI - 12 Neighbors (b) BaF_2 - 6 Neighbors

Figure 3.1: Nearest neighbors of an element for clustering algorithm

The atypical cases for the NaI arise from the joining of the major triangles of the icosahedron, as described in subsubsection 2.2.3.1. While in a flat space the points of six triangles meet to fill the space, in an icosahedron the points of only five major triangles meet to fill the space (imagine folding the major triangles, as shown in Figure 2.15, to meet with each other). So each of the three points of each of the 20 major triangles essentially lose one neighbor, for a total of 11. The atypical cases for the BaF_2 arise when considering the $PbWO_4$ crystals (refer again to Figure 2.22), of which four fit in a space occupied by a single BaF_2 crystal. However, the neighbors are still based on the BaF_2 spacing. So each neighboring group of $PbWO_4$ crystals in a single BaF_2 space contributes three additional neighbors, as shown in Figure 3.2a. The neighbors of a $PbWO_4$ element itself follow the same pattern, but also include the other three $PbWO_4$ elements in its BaF_2 space, as shown in Figure 3.2b.

Both of the TA2CalArray and TA2TAPS_BaF2 classes inherit from another class called TA2ClusterDetector, which performs the clustering algorithm utilizing the read-in lists of neighboring elements. For each event the algorithm first scans through

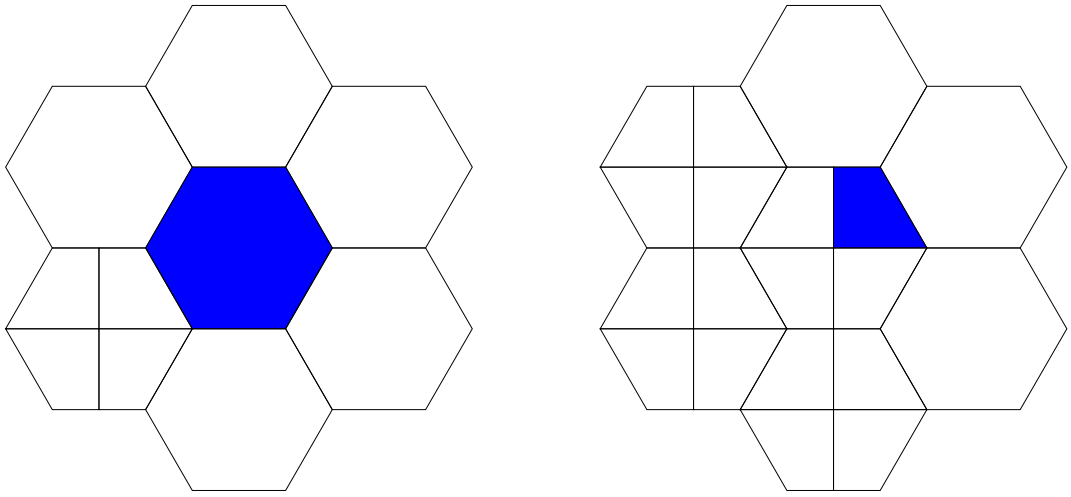

(a) BaF_2 - 9 Neighbors (b) $PbWO_4$ - 18 Neighbors

Figure 3.2: Nearest neighbors for clustering algorithm in TAPS when including the $PbWO_4$

all of the hits and sets the element with the maximum reported energy as the central element of a cluster. The total energy of the cluster is the sum of the energy of the central element and the energy of all neighboring elements, as shown in Equation 3.3. The position of the cluster is set as the $\sqrt{E}$ weighted average of the crystal positions, as shown in Equation 3.4.

$$E_{\text{tot}} = \sum_i E_i \tag{3.3}$$

$$\vec{r}_{\text{tot}} = \frac{\sum_i \vec{r}_i \sqrt{E_i}}{\sum_i \sqrt{E_i}} \tag{3.4}$$

To deal with more energetic photons than this analysis treats (notably above η threshold), where electromagnetic showers can extend beyond the nearest neighbors, an extended search can also be performed. In addition to the nearest neighbors, the algorithm looks for deposition in any other crystals within some specified distance of any of the initial cluster crystals that reported a hit. These hits are then added

to the initial cluster before the $\sqrt{E}$ weighting is performed. This extended search automatically takes place for the BaF_2, but is an option for the NaI.

Once a cluster has been determined through either the initial or extended algorithm, its total energy is compared to a software set threshold energy. If it's above this energy the cluster is accepted, all of the hits that contributed to the cluster are removed from the list, the remaining hits are rescanned for the maximum energy, and the process continues until all of the hits have been converted into clusters. Another optional method can be employed at this point to search for split-offs, situations where a single particle results in what appear to be multiple clusters, and attempt to recombine the clusters into one primary cluster. This method was also not utilized in this analysis.

3.1.2.3 Create Particle Tracks

Once the clustering method is complete the overarching apparatus class then checks for correlations between hits/clusters in the constituent detectors, joining them together into single particle tracks. For the CB there can be a correlation between all three detectors, or any pair of the two. While older versions of the code required a hit in the NaI in order to generate a track, Alexander Mushkarenkov wrote the TA2CentralApparatus class to utilize tracks that never make it to the NaI, partly to help with proton losses, as will be discussed in subsection 5.3.1. A correlation between the NaI and PID requires both to be within some azimuthal range (usually $\pm 15^\circ$) of each other, as shown in Figure 3.3. A correlation between the PID and MWPC requires both to again be within some azimuthal range (usually $\pm 50^\circ$) of each other, as shown in Figure 3.4. A correlation between the MWPC and NaI requires both to be within some total angular range (usually $\pm 20^\circ$) of each other, as shown in Figure 3.5. A correlation of all three requires all three of these cases to be satisfied. The

situation is simpler for TAPS, where a correlation requires that the Veto element hit is directly in front of the cluster center.

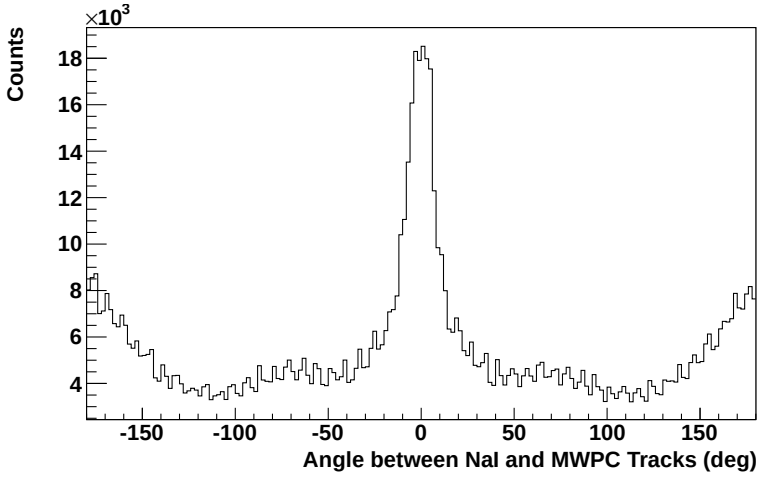

Figure 3.3: Phi correlation between NaI and PID tracks

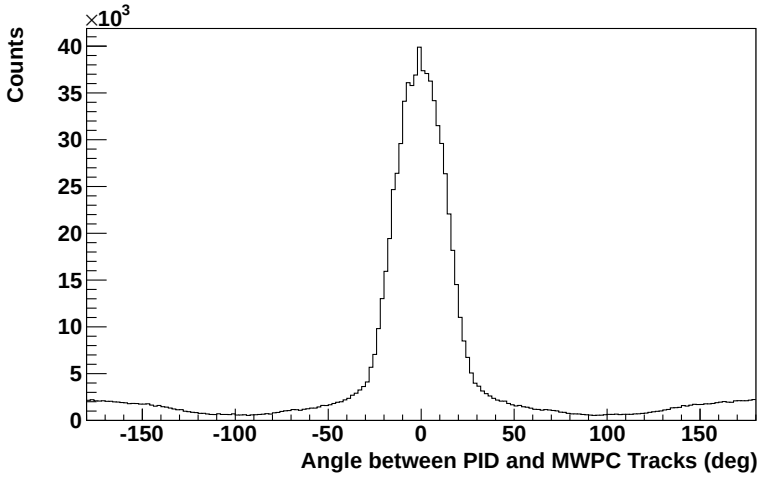

Figure 3.4: Phi correlation between PID and MWPC tracks

Once a track has been determined, all of its information (the detectors and their elements hit, energy, time, direction, vertex, and expected mass) is passed into an instance of the TA2Particle class. This class utilizes ROOT's TLorentzVector class, which allows for various four-momentum calculations, while adding in the ability to store and recall the detector information.

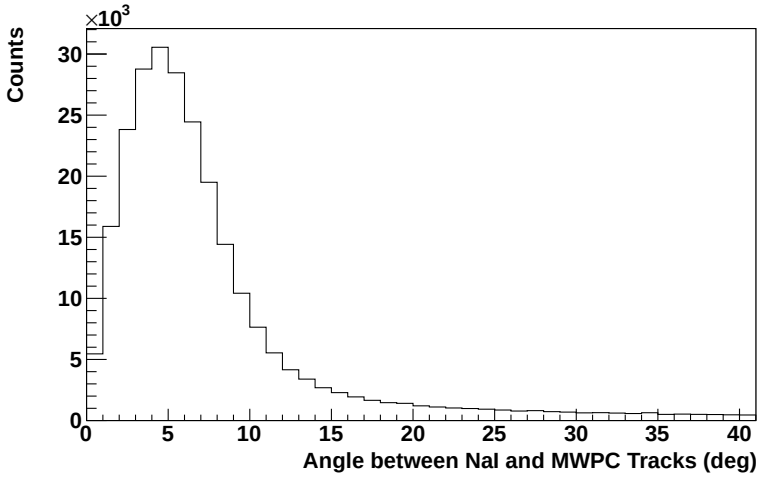

Figure 3.5: Angular correlation between NaI and MWPC tracks

3.1.3 Physics Class

After the creation of the particle tracks, the analysis class then passes this information along to the physics class, which handles actual event selection. Various cuts can be applied at this level depending on the requirements of the user. The main analysis utilized here runs a minimal event selection initially, saving the output into a ROOT TTree format to be further analyzed in another program (as will be discussed in chapter 4). The reasoning behind this is processing time. While the AcquRoot analysis of the full transverse target data takes over a week on the primary machine used, the secondary analysis on the skimmed set of TTrees only takes roughly 14 hours. This helps prevent a full reanalysis of the data for only a minor change in the event selection or histogramming.

One of the primary remaining tasks of the TA2SpinPolPhysics class is to sort through the events and search for possible meson decays (in this case $\pi^0 \rightarrow \gamma\gamma$). This is done by constructing the two-gamma invariant mass, given by Equation 3.5, for each pair of detected photons.

$$m_{\gamma\gamma} = \sqrt{E_{\gamma\gamma}^2 - \vec{p}_{\gamma\gamma}^2} = \sqrt{(E_{\gamma_1} + E_{\gamma_2})^2 - (\vec{p}_{\gamma_1} + \vec{p}_{\gamma_2})^2} \tag{3.5}$$

If the pair of photons are the result of a π^0 decay, then $m_{\gamma\gamma} = m_{\pi^0} = 135$ MeV. If the value for $m_{\gamma\gamma}$ satisfies the specified cut on the spectrum, the photons are tagged as meson decay photons and their summed together four-momenta creates a new π^0 TA2Particle.

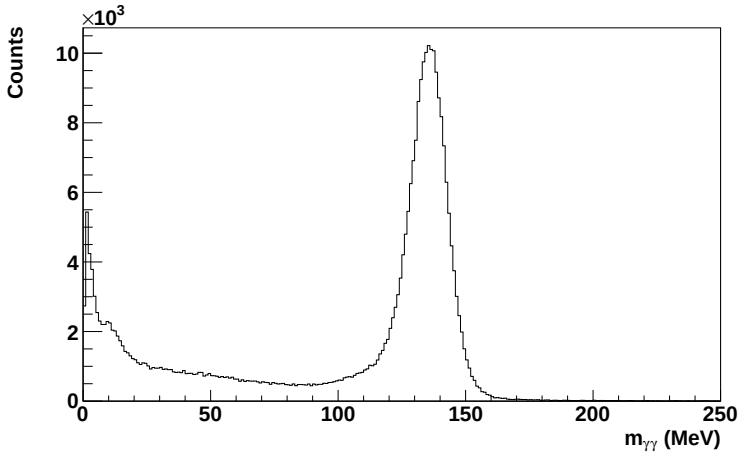

Figure 3.6: Two-gamma invariant mass spectrum. The obvious peak at 135 MeV corresponds to the neutral pion mass.

The rather open-ended event selection performed here only checks to see if either a) there was at least one neutral hit with no π^0 or η meson reconstruction, or b) there was a single π^0 with no η meson reconstruction. In either case the TTree is filled with branches containing information about the neutral, charged, and π^0 particles detected.

3.2 Calibrations

As discussed in subsection 3.1.2, the parameters for each element (see Table 3.2) of each detector must be set in order to properly extract the data. Many of these parameters are basically fixed for an experiment run. The ADC and TDC (and scaler for the tagger) channel numbers do not change unless there is some reordering of the electronics. The position values would only change if the detectors are physically moved with respect to the target, which typically only occurs with a rotation in ϕ

of the PID or a different z position of TAPS (for instance in the inclusion/exclusion of the Cherenkov detector). The software threshold settings for both the ADC and TDC can be adjusted as desired to reject hits that are outside the energy range of interest (for the ADC) or the timing range of correlation (for the TDC).

The remaining parameters (ADC pedestal, ADC gain, TDC offset, and TDC gain), if not fixed themselves, are determined through various calibration methods that are outlined in the following sections. Unless otherwise noted in its section, each calibration method was performed by the author using a system called CaLib. Designed by the University of Basel group (notably Irakli Keshelashvili and Dominik Werthmueller), CaLib uses an AcquRoot physics class called TA2MyCaLib to analyze actual data files with a rough set of calibration parameters. Histograms produced by this physics class are examined in CaLib with a Graphical User Interface (GUI) macro, resulting in new calibration parameters. In some cases only a single pass is needed, but in others the process is iterated multiple times, using the new calibration parameters to re-analyze the data each time.

3.2.1 Tagger

The tagger apparatus (in this experiment) only includes one detector, often called the ladder, so the term tagger will be used synonymously for both the apparatus and the detector.

3.2.1.1 Tagger Time

The tagger TDCs all have a fixed TDC gain of 0.117 ns/channel. The TDC offsets are adjusted on an element by element basis to eliminate differences in cable length and other hardware timing. This results in uniformity in the reporting of an event time regardless of which tagger element is hit. To determine this offset the tagger element hit is plotted as a function of the difference between tagger time and TAPS time, as shown in Figure 3.7a. Since the tagger is run at a high rate, there are many

accidentals recorded for each event, leading to a large background beneath the tagger time. By subtracting the TAPS time from this for a given event the timing peak can be sharpened. The reason for using TAPS instead of the CB is the better timing resolution of the former. This histogram is projected onto the x axis for each bin on the y axis (individual tagger elements), and then fit with a Gaussian peak, as shown in Figure 3.7b. The offset is found by taking the difference between the centroid of the Gaussian fit and zero, and dividing by the gain. Note that since these histograms

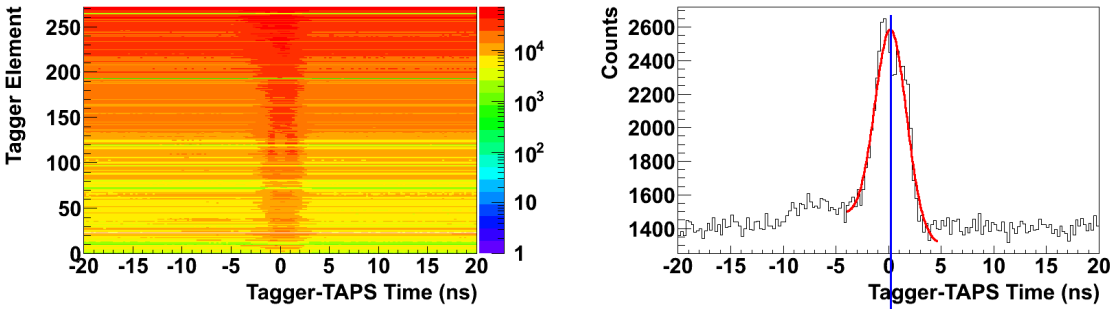

(a) All elements (b) One element

Figure 3.7: Tagger TDC offset calibration

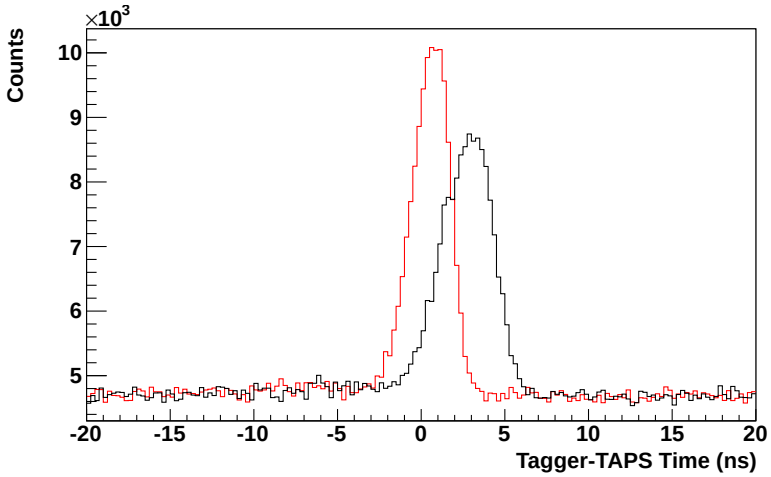

Figure 3.8: Tagger timing peak calibration. The black and red lines show the results before and after calibration, respectively.

look at the tagger time minus TAPS time, the latter actually needs to be calibrated first, as described later in subsubsection 3.2.3.1.

3.2.1.2 Tagger Energy

While the tagger ADCs are not calibrated, since they would not provide very useful information, the additional parameter for the tagger of a central energy does need calibration for a specific MAMI electron beam energy and tagging spectrometer magnetic field. This energy calibration was performed by Duncan Middleton, first by setting the magnetic field of the spectrometer to a standard setting for 450 MeV running. Electron beams of various energies below this, all with very low current, were then sent through the tagger without passing through a radiator first. The precision of the MAMI electron beam energy allows the tagger elements to be calibrated through this scanning method. Due to time requirements this was only performed on a small range of energies, with the overall calibration using an extrapolation of this scan and a program called ugcal.

3.2.2 Crystal Ball

The crystal ball apparatus is composed of three detectors: the NaI, PID, and MWPC.

3.2.2.1 NaI Time

As with the tagger, the TDC gains for the NaI are all fixed at 0.117 ns/channel. The TDC offsets are determined in a similar way, and for similar reasoning, as for the tagger. The NaI element is plotted versus the difference in cluster time between two hits in the CB, as shown in Figure 3.9a. This results in the histogram being filled twice for each pair of hits, with the first element filled at its time minus the second element's time, and the second element filled at its time minus the first element's time. This method assumes that for correlated hits; be they a photon and proton from

Compton scattering, two decay photons from π^0 photoproduction, etc; the difference in time between them should be zero. Since a proton's time-of-flight to the NaI is mostly indistinguishable from a photon this is a good approximation. However, a requirement that the hits appear to be neutral (no correlated hit in the PID or MWPC), helps to insure this assumption.

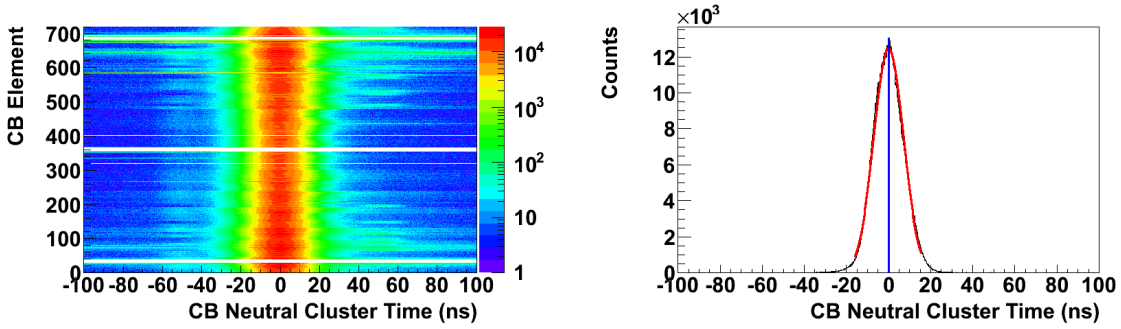

(a) All elements (b) One element

Figure 3.9: NaI TDC offset calibration

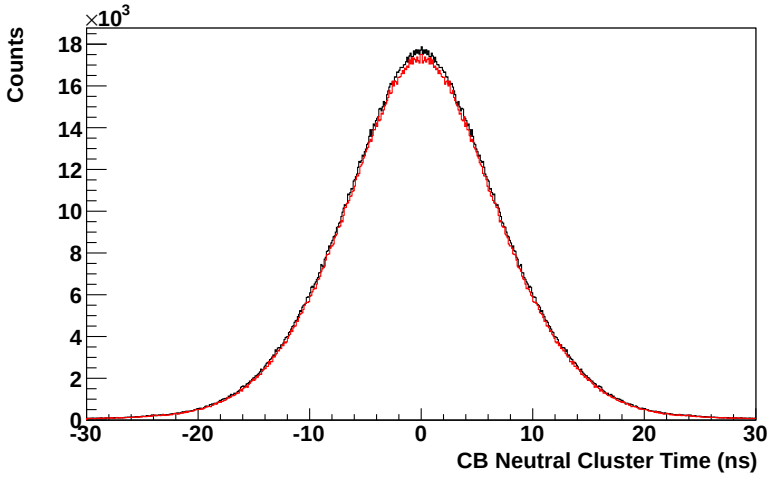

Figure 3.10: NaI timing peak calibration. The black and red lines show the results before and after calibration, respectively.

3.2.2.2 NaI Energy

The NaI energy response is calibrated in two ways. Initially an ^{241}Am^{9}Be source, which produces 4.438 MeV photons, was placed in the center of the CB. While the high voltage for all of the NaI PMTs is provided by only four sources, each PMT base has a small potentiometer to adjust the voltage supplied to the tube. These potentiometers were adjusted until the responses from each crystal all resulted in approximately the same reported ADC channel. The ADC pedestals for each element were recorded, and hardware thresholds were set above this. Unfortunately, using the NaI response to a 4.438 MeV photon to extrapolate out to several hundred MeV is not practical. The ADC gains are therefore determined by using pion photoproduction, $\gamma p \to \pi^0 p \to \gamma\gamma p$, a kinematically overdetermined reaction. Looking at $m_{\gamma\gamma}$, as given by Equation 3.5, a peak is expected at $m_{\gamma\gamma} = m_{\pi^0} = 135$ MeV.

For each pair of hits in the CB, the NaI element is plotted as a function of $\mathrm{m}_{\gamma\gamma}$, as shown in Figure 3.11a. As with the timing, each event fills the histogram twice, once for each element. However, unlike with the timing, the value for $\mathrm{m}_{\gamma\gamma}$ is the same for both. This can also be restricted to only neutral events where neither photon is associated with a PID or MWPC hit. Since the value being plotted is dependent on resulting from the two π^0 decay photons, this restriction is even more important for the energy calibration than the timing calibration. As noted in Equation 3.1, there are two additional factors in the energy conversion, a quadratic factor and a global scale factor. The quadratic factor can be utilized for very high beam energies, where the expected linearity of the NaI no longer holds true. Once the linear gain has been determined as described above, the quadratic gain can be calibrated with the CaLib software by looking at $\gamma p \to \eta p \to \gamma\gamma p$. Since $\mathrm{m}_{\gamma\gamma} = \mathrm{m}_{\eta} = 548$ MeV, this provides a lever arm at higher energy than the π^0. With this experiment being performed at an end-point energy of 450 MeV, η production is unavailable and the quadratic term is unnecessary. The global scale factor can be useful for adjusting an entire detector

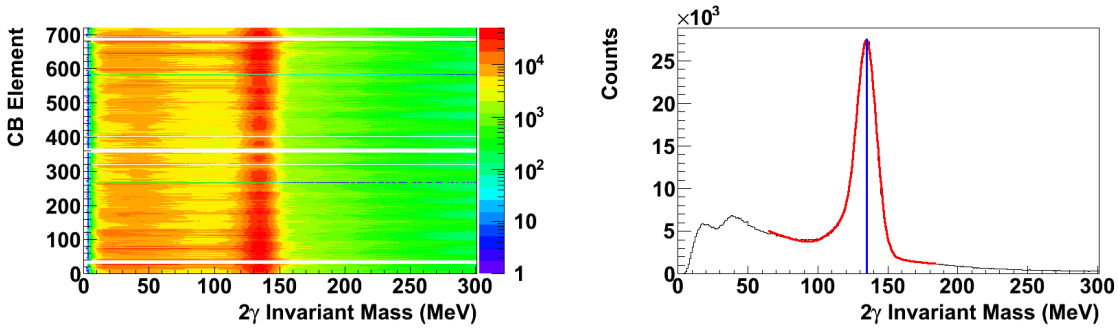

(a) All elements (b) One element

Figure 3.11: NaI ADC gain calibration

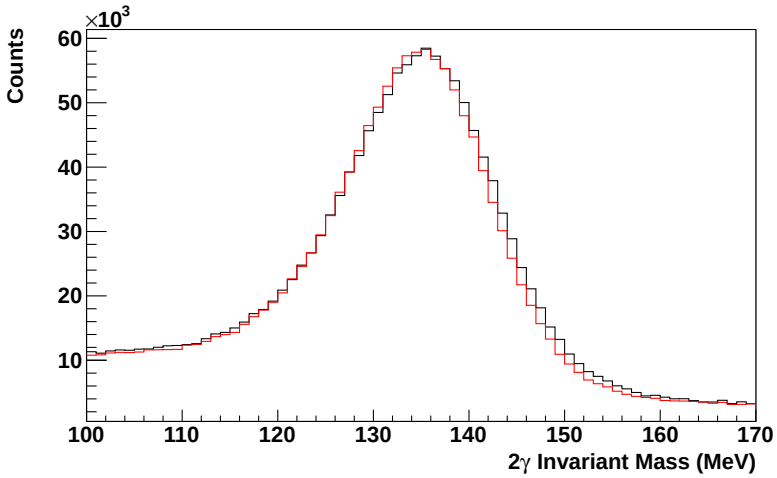

Figure 3.12: NaI $m_{\gamma\gamma}$ peak calibration. The black and red lines show the results before and after calibration, respectively.

if an overall gain shift is observed between runs. It was preferred, however, to leave this factor set to unity and simply recalibrate the detector after a gain shift.

As shown in Figure 3.13 the gains, and therefore the $m_{\gamma\gamma}$ peak, can shift considerably during a single beam-time. A blown fuse in the high voltage breakout for the NaI occurred during the September 2010 beam-time. After repairing the problem the high voltage was brought back to its original setting but the gains of those tubes affected obviously did not return to their original values. To address shifts such as this, the beam-times were divided into segments shown in Table 3.3.

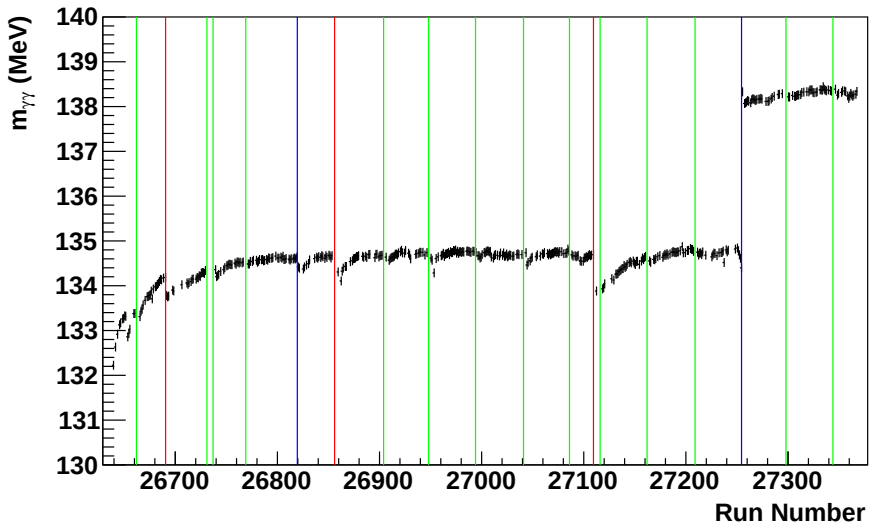

Figure 3.13: September 2010 NaI gain drifts. The various lines show when tagging efficiency runs (green) and target re-polarizations (red) occurred, each of which corresponds to a dip in the gain. The blue line on the left depicts a downtime from MAMI, and the one on the right depicts when the high voltage for a quarter of the NaI briefly tripped.

	Segment 1	Segment 2	Segment 3
Sep 2010	26639-27254	27255-27367	
Jan 2011	35253-35295	35299-35335	35339-35472
Feb 2011	35532-35695	35698-35885	35887-36303

Table 3.3: NaI energy calibration segmentation of runs

3.2.2.3 PID Phi

As mentioned before, the position parameters for each element of each detector should rarely change. The only position parameter that does occasionally change is the orientation of the PID, which occurs if it is removed from the bore of the NaI and later reinserted. For the PID to properly identify charged particles its alignment with respect to the NaI needs to be determined. The PID ϕ parameters are obtained by plotting the PID element hit versus the ϕ of a NaI cluster hit (as shown in Figure 3.15a) fitting a Gaussian to the projection for each element (as shown in

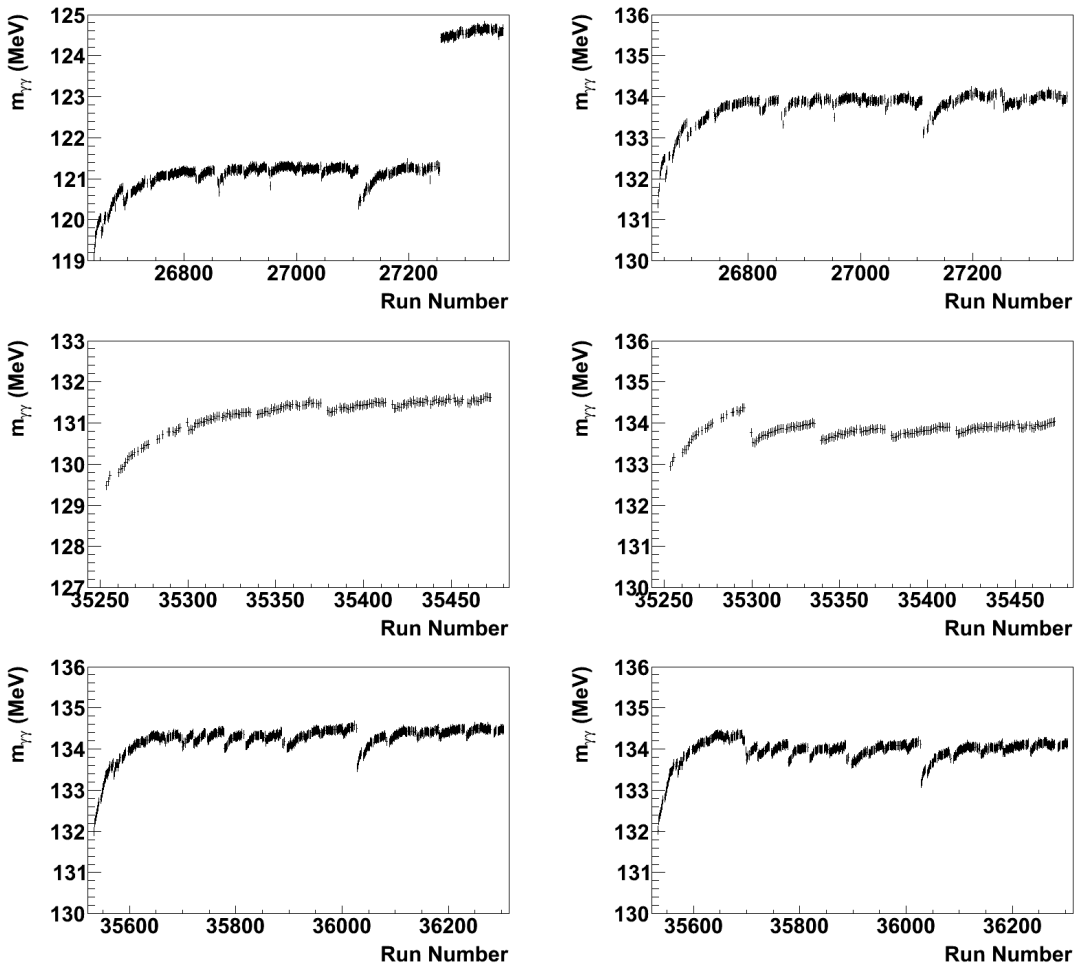

Figure 3.14: NaI $m_{\gamma\gamma}$ drift with respect to run number. Top is from September 2010, middle from January 2011, and bottom from February 2011. Left is before calibrations and right is after calibrations.

Figure 3.15b), and then fitting a line to the centroids of each Gaussian as a function of PID element.

3.2.2.4 PID Time

As with the tagger and NaI, the TDC gains for the PID are all fixed at 0.117 ns/channel. The TDC offsets are also determined in the same way as for the NaI, although now clearly without the option for neutral events, by plotting PID element versus the difference in time between two hits in the PID, as shown in Figure 3.16a.

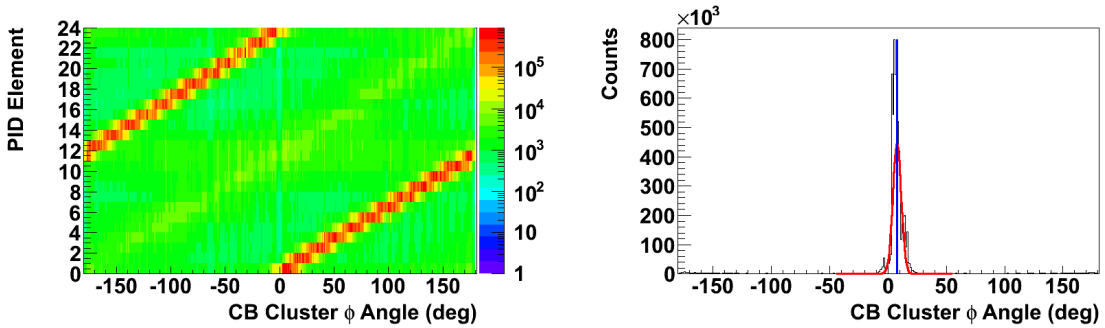

(a) All elements (b) One element

Figure 3.15: PID phi calibration

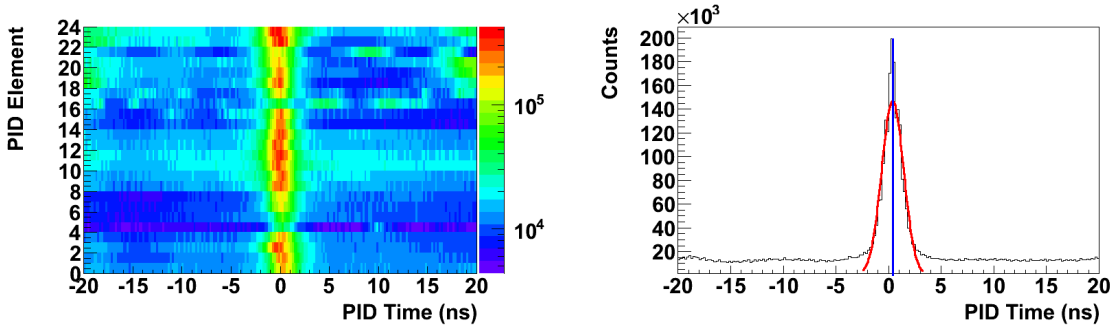

(a) All elements (b) One element

Figure 3.16: PID TDC offset calibration

3.2.2.5 PID Energy

Since the PID elements are only 4 mm thick, charged particles will typically not deposit all of their energy in the PID. This makes a direct calibration difficult. Simulation of energy deposition in both the PID and NaI for a range of proton energies allows for a comparison between it and real data. With real data, the PID ADC channel is plotted as a function of NaI cluster energy, for each PID element, as shown in Figure 3.17a. As discussed previously, the top 'banana' shape is indicative of proton detection. Projections of this histogram onto the y axis for various slices of NaI cluster energy will therefore yield a double peak structure, where the higher ADC channel results from protons in the 'banana', as shown in Figure 3.17b.

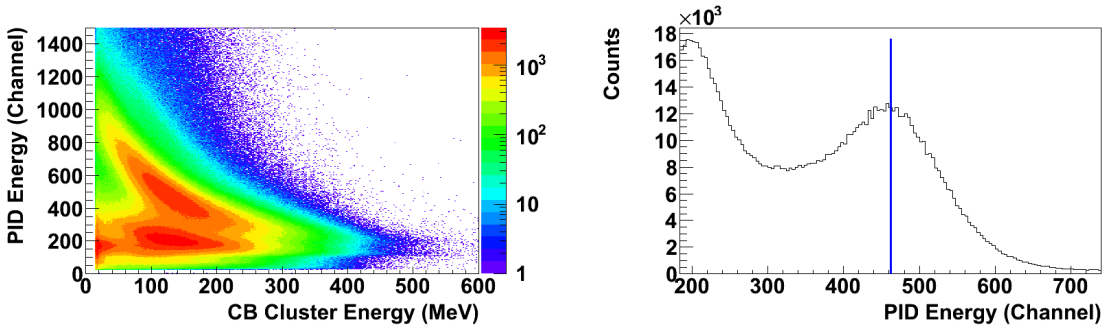

(a) PID energy vs NaI energy

(b) Projection

Figure 3.17: PID energy calibration

By plotting the centroid values of Gaussian fits to the proton peaks as a function of the expected energy deposition in the PID from simulation, a linear relationship is extracted for each PID element (as shown in Figure 3.18), returning both the pedestal and the gain.

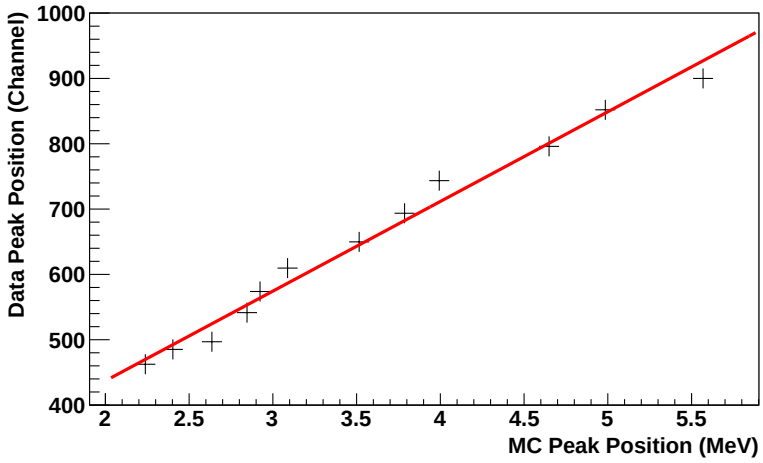

Figure 3.18: PID energy calibration fit

3.2.3 TAPS

The TAPS apparatus is composed of two detectors: the $BaF_2/PbWO_4$ and Veto. As noted before, the $PbWO_4$ is not used in this analysis, but its calibration is identical to the BaF_2 and happens simultaneously.

3.2.3.1 BaF_2 Time

TDC gains for each beam-time were calibrated by Tigran Rostoyman. This is done by incrementally inserting various cables of known length to increase the time of the TDC stop signal. A small run is taken with each cable length, and then a program called TAPSMaintain looks at the various runs to determine what the TDC gain must be for each BaF_2 element.

The TDC offsets are determined in an identical way to the NaI, where the BaF_2 element hit versus the difference in cluster time between two hits in TAPS is plotted. This can also be done requiring only neutral hits (no corresponding hit in the Veto).

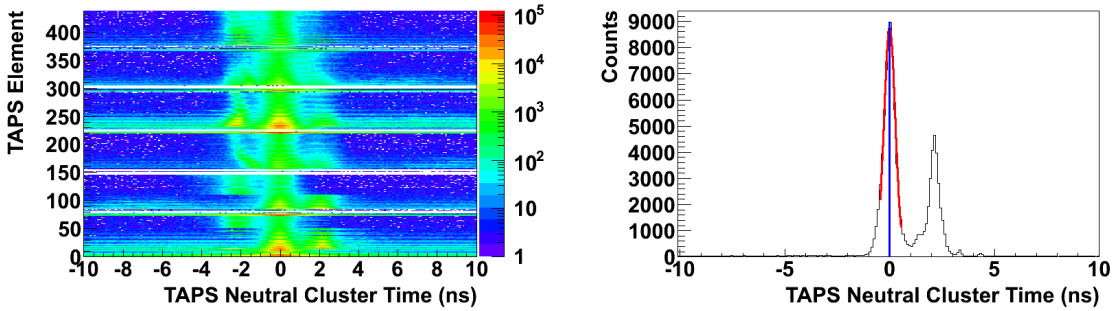

(a) All elements (b) One element

Figure 3.19: BaF_2 TDC offset calibration

The strange double peaking in each individual element, leading to a triple peak when summing all the elements together, is likely due to some fraction of the elements having an offset of about 2 ns, either positive or negative, from the norm. After multiple iterations this effect is considerably reduced, but never removed, as seen in Figure 3.20. For the purposes of this experiment the timing of TAPS is not very important however. Given the Compton kinematics at a beam energy of 450 MeV, the Compton scattered photon can only be detected in the CB, and it's the timing of this particle that's of concern.

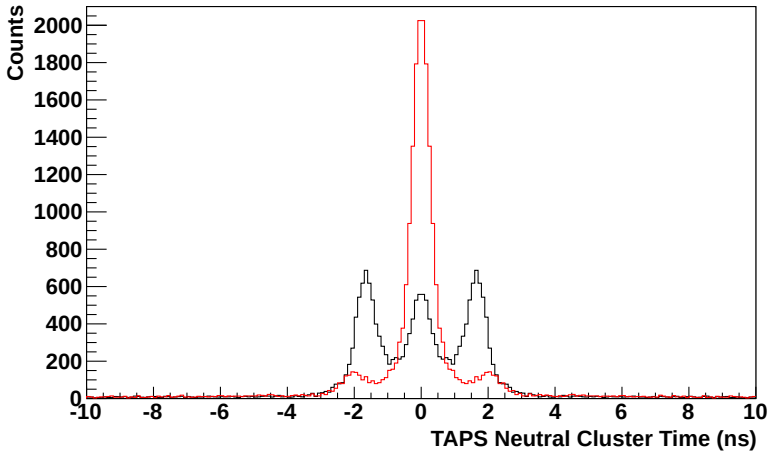

Figure 3.20: BaF_2 timing peak calibration. The black and red lines show the results before and after calibration, respectively.

3.2.3.2 BaF_2 Energy

Each BaF_2 analog signal is fed into two different ADCs, one with a long and one with a short integration gate (called Long Gate, or LG, and Short Gate, or SG, respectively). The LG ADCs function the same as the NaI ADCs, in that they integrate the entire analog signal. The SG ADCs make use of the Pulse Shape Analysis (PSA) abilities of BaF_2 where, as mentioned in subsection 2.3.4, the timing response of the crystal is significantly different for photons and nucleons. With a shortened integration gate, most of a photon response will be integrated, whereas only part of a nucleon response will be. With two sets of ADCs come two separate calibration methods for the gains. The pedestal calibrations are identical however, where the raw ADC spectra are simply scanned through to find the pedestal.

LG ADC gains are calibrated similar to the NaI. The BaF_2 element hit versus $m_{\gamma\gamma}$ is plotted for instances where either both photons are detected in TAPS or one is detected in TAPS and one in the CB. Note that since the former involves two hits in TAPS, each event fills the histogram twice, once for each element. Additionally this can be restricted to only neutral events where neither photon is associated with

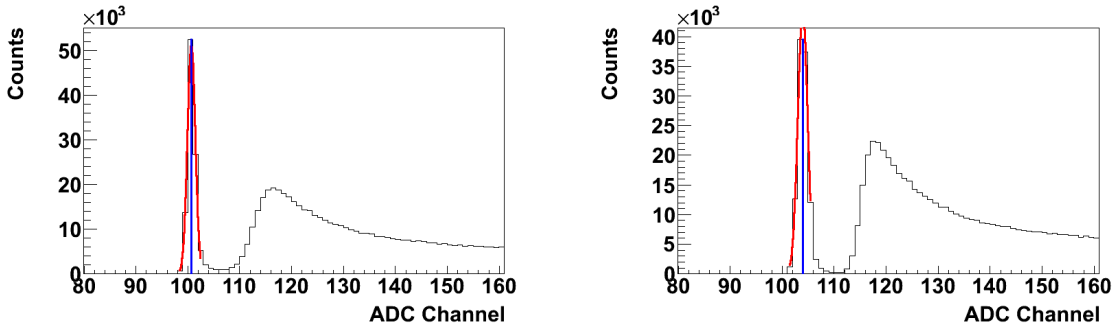

(a) Long Gate (b) Short Gate

Figure 3.21: BaF_2 ADC pedestal calibration

a Veto hit. The quadratic factor can also be determined similar to the NaI, but as with that case it can not be, and was not, determined for these beam-times.

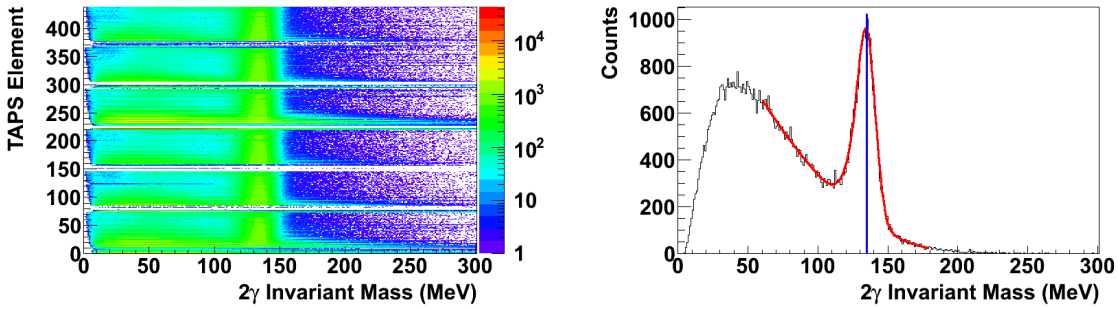

(a) All elements (b) One element

Figure 3.22: BaF_2 LG ADC gain calibration

The BaF_2 ADC gains were also segmented, as given in Table 3.4, to account for gain shifts in this detector. Note that the September 2010 beam-time is segmented

	Segment 1	Segment 2	Segment 3
Sep 2010	26639-26945	26946-27367	
Jan 2011	35253-35472		
Feb 2011	35532-35695	35698-35885	35887-36303

Table 3.4: BaF_2 energy calibration segmentation of runs

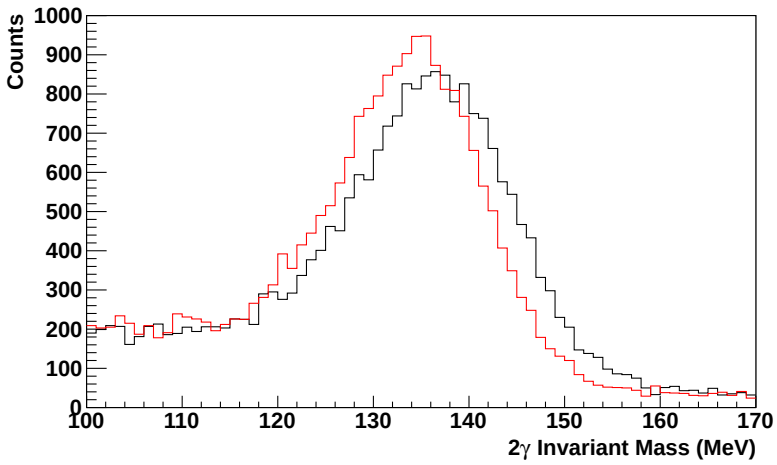

Figure 3.23: BaF_2 $m_{\gamma\gamma}$ peak calibration. The black and red lines show the results before and after calibration, respectively.

differently than for the NaI, the January 2011 beam-time isn't segmented at all, and the February 2011 beam-time is segmented the same as for the NaI.

Given that the SG ADC is by definition leaving out some portion of the analog spectrum, a direct calibration of it is not appropriate. Rather, its usefulness comes about by comparing its response to that of the LG ADC. To this end, the SG ADC gain is calibrated by comparing its output to that of the already calibrated LG ADC. This is done by computing the PSA radius and PSA angle, given by Equation 3.6 and Equation 3.7.

$$r_{\mathrm{PSA}} = \sqrt{E_{\mathrm{LG}}^2 + E_{\mathrm{SG}}^2} \tag{3.6}$$

$$\theta_{\mathrm{PSA}} = \tan^{-1}(E_{\mathrm{SG}}/E_{\mathrm{LG}}) \tag{3.7}$$

The PSA radius is then plotted as a function of PSA angle. For a photon, whose response in BaF_2 is relatively fast, the energy from the SG ADC will be very close to the energy from the LG ADC. Therefore the PSA angle should be 45°, especially at higher energies. Protons on the other hand, especially at lower energies, will deviate from this angle since a larger fraction of their analog signal will only be integrated in the LG ADC. This effect is depicted in Figure 3.25a. Projecting this histogram onto

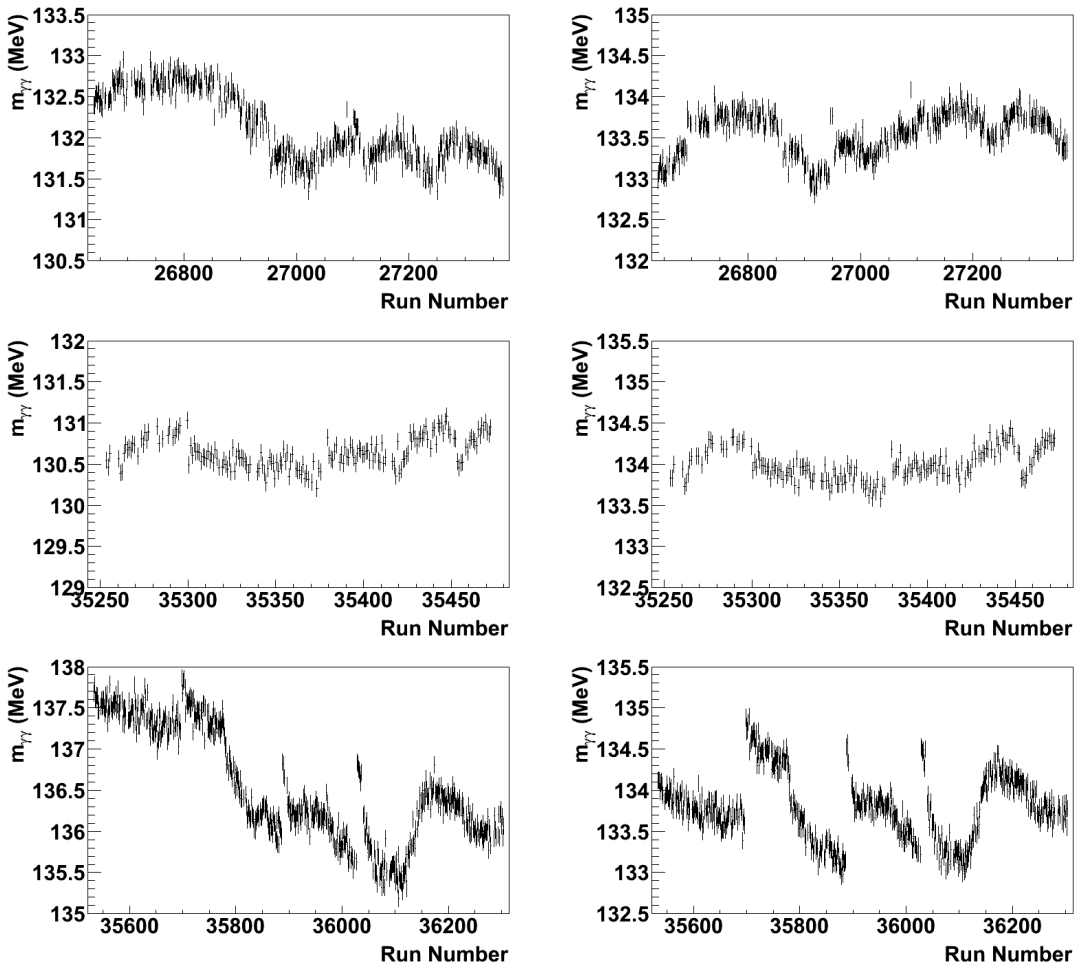

Figure 3.24: BaF_2 $m_{\gamma\gamma}$ drift with respect to run number. Top is from September 2010, middle from January 2011, and bottom from February 2011. Left is before calibrations and right is after calibrations.

the x axis from some minimum PSA radius up (to eliminate the background shown below 100 MeV), the right hand peak can be fitted with a Gaussian and the SG ADC gain adjusted to compensate.

3.2.3.3 Veto Correlation

Similar to the PID, it's important to ensure that the positions of the Veto scintillators are properly set to correlate with a BaF_2 crystal downstream of it. A simple check of this is done by plotting the BaF_2 element hit versus the Veto element hit

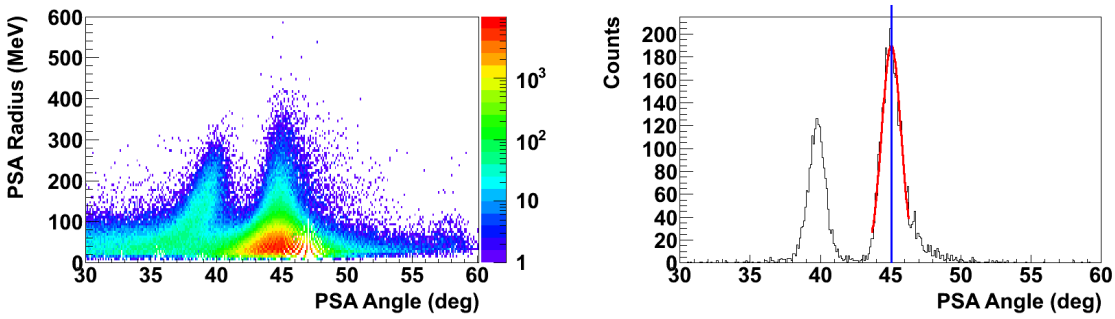

(a) r_{PSA} vs θ_{PSA} (b) Projection

Figure 3.25: BaF_2 SG ADC gain calibration

for any charged particle. If all the elements are both wired (to ADCs) and listed (in the configuration files) in the correct order, there should be a one-to-one correspondence. If a flip has occurred somewhere, the CaLib software will resolve this. For these beam-times all of the veto elements are observed in the proper place.

3.2.3.4 Veto Time

The Veto TDC gains are all fixed at 0.05 ns/channel. The TDC offsets are determined in the exact same method as the PID, by plotting Veto element hit versus the difference in time between two hits in the Veto.

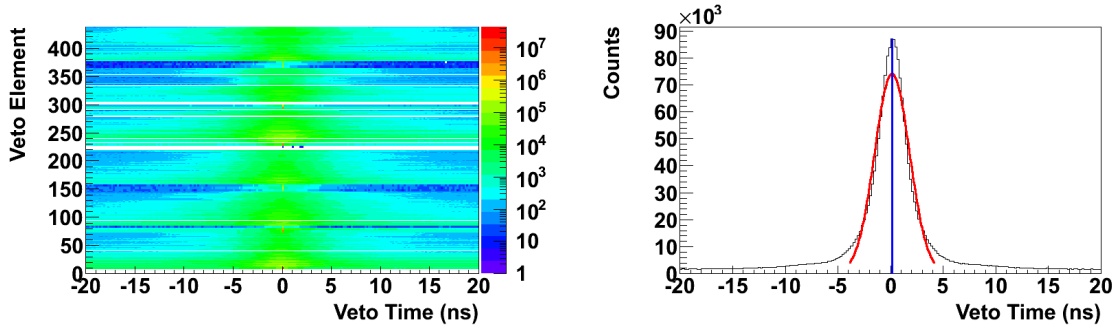

(a) All elements (b) One element

Figure 3.26: Veto TDC offset calibration

3.2.3.5 Veto Energy

Veto ADC pedestals are determined in the same way as for the BaF_2. The ADC gains are calibrated in a similar fashion to the PID, although since the pedestals are determined separately the Veto energy (instead of channel) can be plotted versus BaF_2 cluster energy for each Veto element. This is compared to simulation for TAPS.

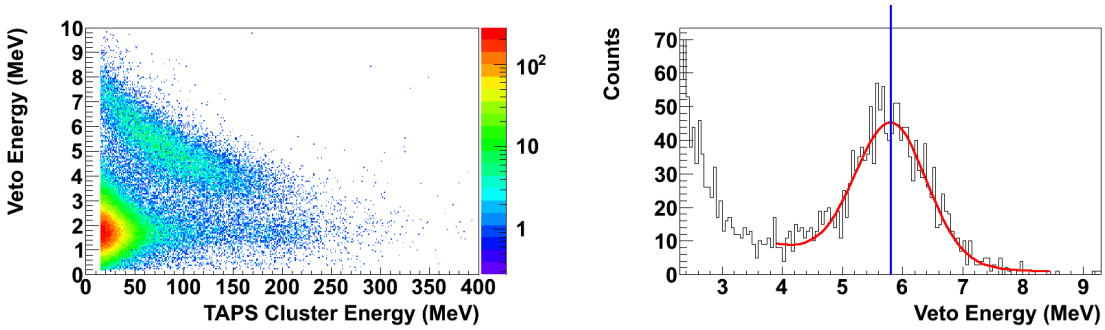

(a) Veto E vs BaF_2 E (b) Projection

Figure 3.27: Veto energy calibration

3.2.4 Target Position

With the NaI properly calibrated it's possible to check the position of the target with respect to the NaI. For each pair of neutral events that hit the NaI, $m_{\gamma\gamma}$ is calculated for various altered positions of the target center. This altered target position is plotted versus its resulting $m_{\gamma\gamma}$, as in Figure 3.29a, and projections of this for each target position bin are fitted with a Gaussian, as in Figure 3.28. The sigma of the Gaussian fit, shown in Figure 3.29b, has its minimum value at the actual target center, and increases on both sides of it. Plotting the sigma as a function of target position, and then fitting this with a simple polynomial extracts a target position value.

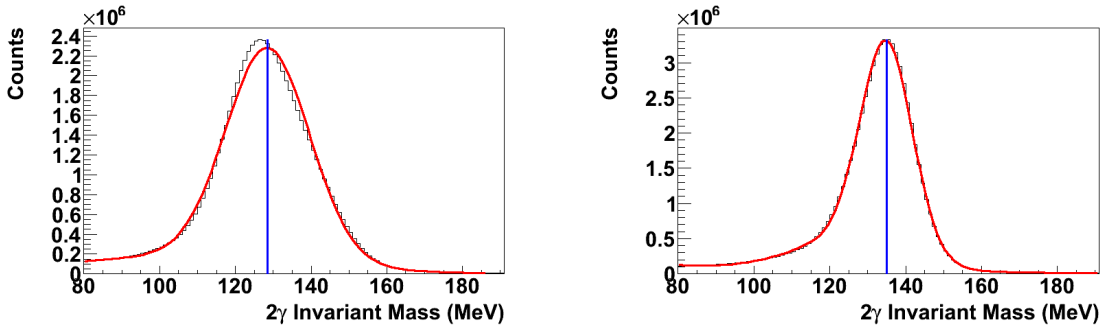

(a) Shifted by 10 cm

(b) Centered at 0 cm

Figure 3.28: Target position effect on $m_{\gamma\gamma}$

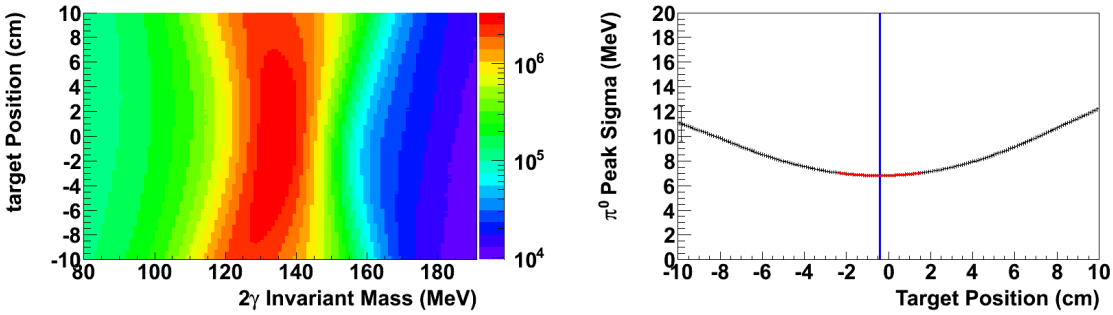

(a) All positions

(b) Fit of widths vs z

Figure 3.29: Target position calibration

3.2.5 Cherenkov

Since the Cherenkov detector is a single element detector, its signal is run into single ADC and TDC channels. It's unnecessary to calibrate the ADC response as the analysis simply looks for any events beyond the pedestal. The TDC calibration, on the other hand, is useful as the vetoing capabilities of the Cherenkov are utilized by determining the time between events in the Cherenkov and events in TAPS. Since the Cherenkov uses one of the CATCH TDCs, its gain is again already known as 0.117 ns/channel. The TDC offset can be determined by simply plotting the time difference between the Cherenkov and TAPS (after TAPS has been calibrated), and working out Equation 3.2 to produce the peak at the desired spot, with zero being the

obvious choice. This results in a TDC offset of 3285 channels. The various Cherenkov distributions are shown in Figure 3.30. As can be seen in Figure 3.30d, there's a clear

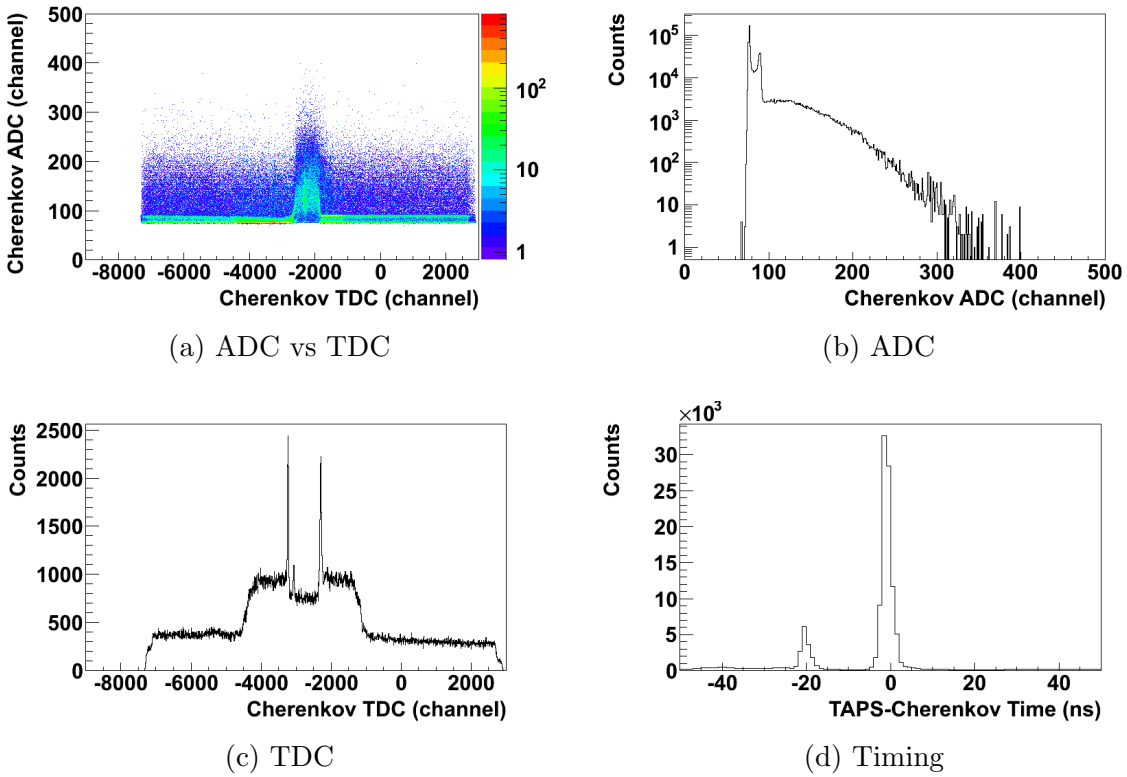

(a) ADC vs TDC

(b) ADC

(c) TDC

(d) Timing

Figure 3.30: Cherenkov distributions

coincidence peak centered at zero. A cut of ±5 ns from zero is applied to this value, and if accepted this can be used to veto either the coincident hit or the entire event, as will be described in subsection 4.1.2.

CHAPTER 4

DATA ANALYSIS

As discussed in subsection 3.1.3, the output from AcquRoot consists of two ROOT files for each data file. The first file contains a TTree which holds particle information (momentum, energy, timing, etc.) on an event by event basis. The second file contains the histograms produced by AcquRoot itself. While most of these are for diagnostic purposes only, two of them are important for correctly combining the data files together. The first histogram is the tagger accumulated scalers, where the scaler counts for each tagger element for the entire run are recorded. By comparing the counts in a tagger element between two different runs the differences in running time, beam current, tagging efficiency, etc., can be accounted for. The second histogram is the system live time, where the live time is periodically read into a scaler channel. As the live time may drift between runs, especially if the beam current is changed, this also needs to be accounted for to compare two different runs together.

These three pieces, the TTree and two histograms, are read in by a secondary analysis code, written by the author. Since the transverse target data was taken with both a positively and a negatively polarized target, as well as a carbon background target, these data files are analyzed in separate passes and then combined together. The code is detailed in the following sections describing the event selection and results formation.

4.1 Event Selection

As noted before, the usefulness of this second pass analysis is in the ability to change settings that do not affect the track reconstruction of the main AcquRoot program and quickly re-analyze the data. Some of these settings, and the reasoning behind them, are:

- Size of tagged photon energy bins - While the tagger gives results for photons between 125.8 and 418.8 MeV, the bins chosen for an analysis will obviously be much smaller, with values dependent upon the physics of interest. For this analysis two sets of bins are analyzed, 272.73-303.32 MeV and 315.25-345.94 MeV (rounded in notation to 273-303 and 315-346 MeV for most of the remainder of this document).

- Size of Compton photon angle bins - Similar to the energy bins, the angular range is broken into sections. Given the small cross section for Compton scattering, 20° bins were chosen to provide enough statistics in each bin.

- Cluster acceptance threshold - As discussed in subsubsection 3.1.2.2, the cluster threshold can be set to different values. For the initial pass, a low threshold of 5 MeV was chosen to accept more clusters. This is then raised in the secondary analysis to 15 MeV to reject low energy noise and/or possible split-offs. A higher threshold than 15 MeV would begin to noticeably decrease the statistics.

- Fiducial cuts in angular acceptance - Although in principle the CB and TAPS combined covers the angular range of $2° - 159°$, there are some regions that are not as efficient, as shown in Figure 4.1. To clean up these edge effects three fiducial cuts are made, $0 - 6°$, $18 - 25°$, and $150 - 180°$. The cuts are shown in Figure 4.2b.

- Prompt and random timing windows - The high beam current run during this experiment results in many accidental events in the tagger. Timing cuts are used to subtract out these accidentals. This is discussed in more detail in section 4.2

- Particle number cuts - The inclusivity (or exclusivity) of the analysis can be adjusted by allowing for events that contain more than the desired number of particles. This is also discussed in more detail in section 4.2.

- Proton opening angle cut size - This is an actual kinematic cut to reject non-Compton events. This is also discussed in more detail in section 4.2

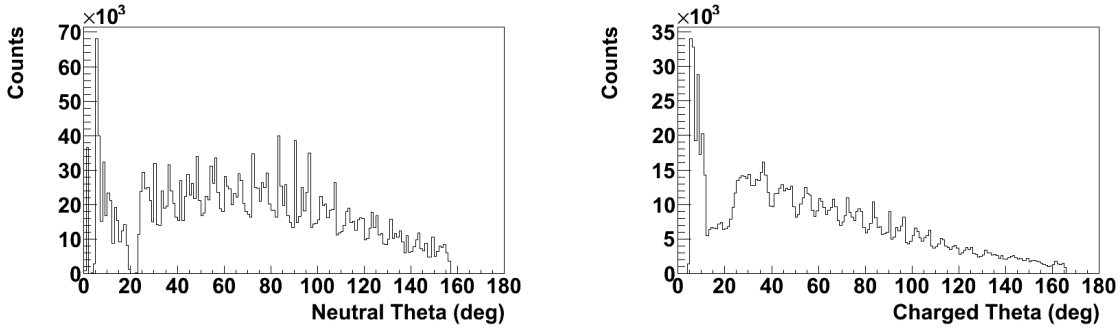

(a) Neutral particle theta

(b) Charged particle theta

Figure 4.1: Theta distribution for detected particles. In addition to the obvious hole in the upstream end of the CB at 160°, there's a clear loss of efficiency between the CB and TAPS at around 20°.

4.1.1 File Comparison

The first part of the analysis reads in the scalers histogram, live time histogram, and the target polarization for each run. The integral of the live time histogram is divided by the number of entries to determine the average live time for that run. The scalers histogram for that run is added to a total tagger scalers histogram for the entire data-set (one each for the three positive and four negative target polarizations, and one for the carbon background target). The scalers histogram is also multiplied

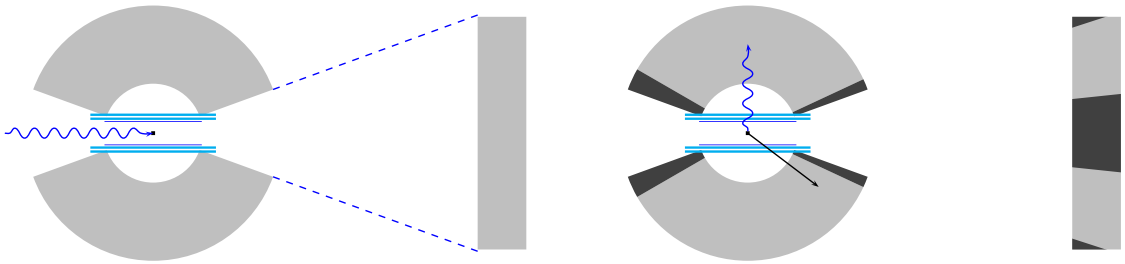

(a) Without fiducial cuts (b) With fiducial cuts

Figure 4.2: Cross section of detectors, showing the establishment of fiducial cuts

by the target polarization for that run and added to a total polarization-weighted scalers file. If the option to account for the live time is selected, the individual scalers histogram from each run is multiplied by the average live time prior to being summed to either the total scalers or the polarization weighted scalers histograms. Samples of these two scaler histograms are shown in Figure 4.3. The importance of comparing

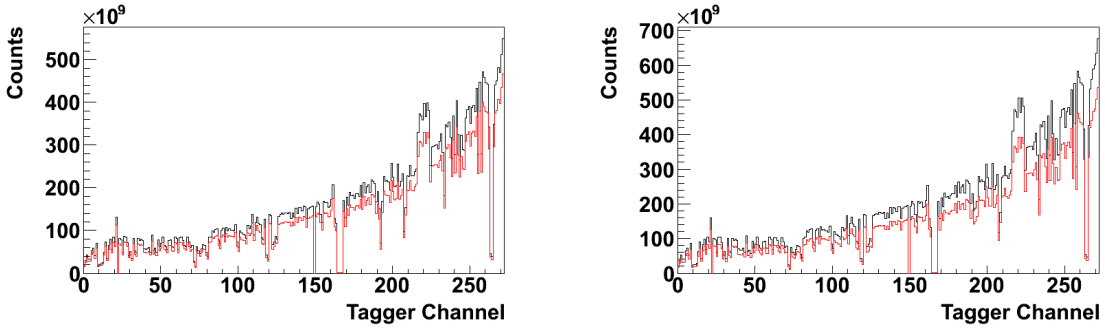

(a) Positive target (b) Negative target

Figure 4.3: Polarization weighted tagger scalers. These are shown in red along with regular tagger scalers shown in black.

these histograms on a run by run basis is clear when plotting the integral of each as a function of the run number. These plots are shown in Figure 4.4.

Once all of the files in a particular polarization data-set have been included, the 'flux' for a specific energy bin is determined by integrating the total scalers histogram

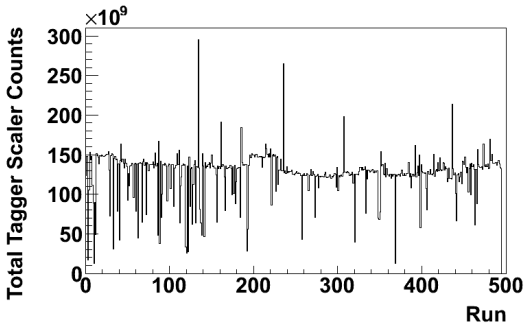

(a) Positive target

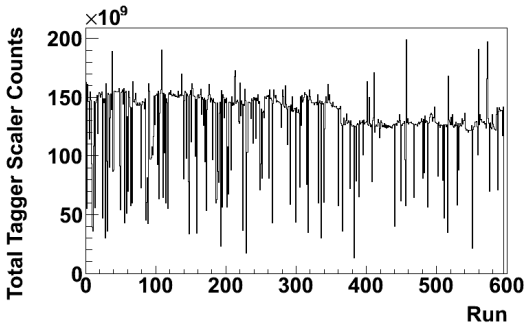

(b) Negative target

Figure 4.4: Total tagger scalers for each run

over that energy bin. A ratio of the positive target polarization flux over the negative target polarization flux can then be used, if necessary, to scale the negative target data-set to the positive target data-set. The positive and negative total histograms are shown in Figure 4.5a. The ratio between them (for each tagger channel) is shown in Figure 4.5b, along with lines denoting the two energy regions of interest (blue for 273-303 MeV, and red for 315-346 MeV). Zooming in on the ratio histogram

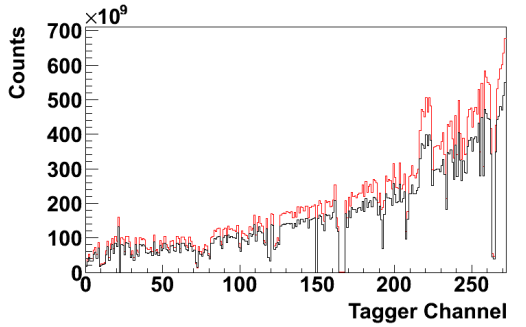

(a) Positive (black) and negative (red)

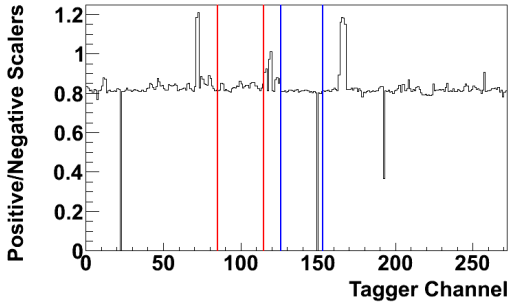

(b) Ratio of positive to negative scalers

Figure 4.5: Comparison between positive and negative data-sets

for the two energy bins gives a rough idea of the overall ratio for those bins, as shown in Figure 4.6. The average target polarization is determined by integrating

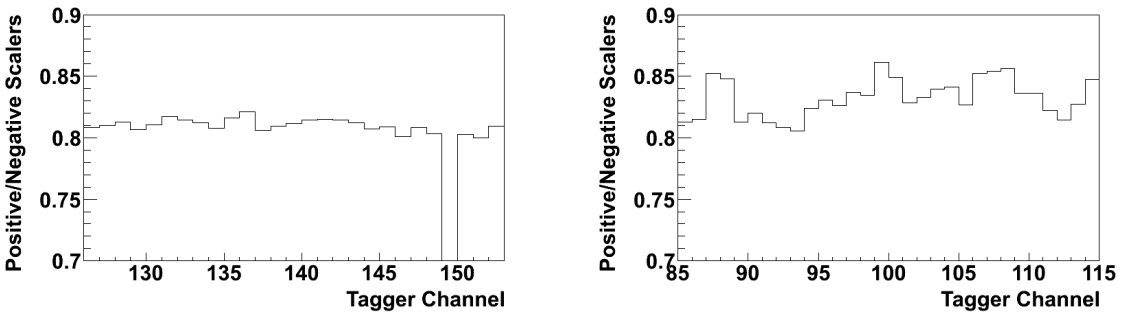

(a) Ratio 273-303 MeV (b) Ratio 315-346 MeV

Figure 4.6: Comparison between positive and negative data-sets, zoomed in

the polarization weighted total scalers histogram over that energy bin, and dividing by the 'flux' for the same energy bin. This is shown in Figure 4.7.

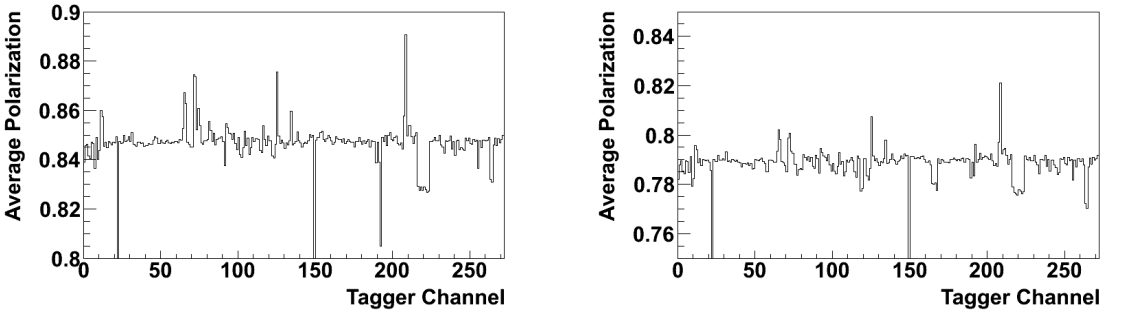

(a) Positive (b) Negative

Figure 4.7: Average polarizations for data-sets

4.1.2 TTree Analysis

While the histograms are being summed together, the individual TTrees are included into a larger collection called a TChain. This is the piece that undergoes the event-selection component of the analysis.

The first task in examining the TTree is to check the integrity of the file. Occasionally the DAQ system essentially freezes, with the TCS loosing synchronization between the various detector systems. While it's expected that analysis of 'out of

sync' data would result in a very small number of background events, it's an easy enough problem to compensate for. The CB reference TDC can be subtracted from the tagger reference TDC, and checked on an event-by-event basis. Examples of this distribution for a file that remained in sync and a file that went out of sync are shown in Figure 4.8. While these figures look the same, zooming in on the y-axis depicts

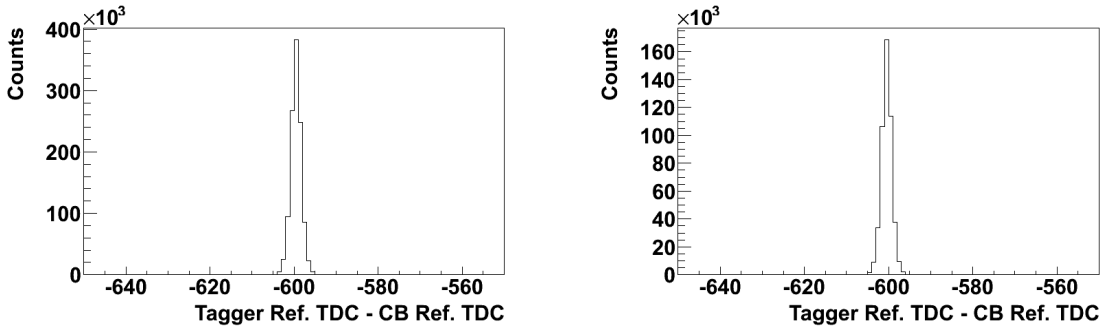

(a) In sync (b) Out of sync

Figure 4.8: Synchronization check

the difference, as shown in Figure 4.9. While the structure of the peak in the out of sync file remains the same for the majority of the file, once it loses sync the timing structure is completely lost, resulting in the events outside of the peak. A timing cut on the peak in this timing difference can eliminate data taken after synchronization is lost.

For each event the analysis loops through each of the neutral particles and rejects it if its energy is below the cluster threshold chosen, or if it's detected within one of the fiducial cuts, or if it's detected in TAPS in time with a hit in the Cherenkov detector (if the Cherenkov detection is selected as a cut). If the neutral particle is rejected for any of the above reasons it's removed from the list and the number of neutral particles is reduced by one. If the neutral was also part of a π^0, as determined by the reconstruction in AcquRoot, that π^0 is also rejected and the number of accepted pions is reduced by one. This process is illustrated in Figure 4.10.

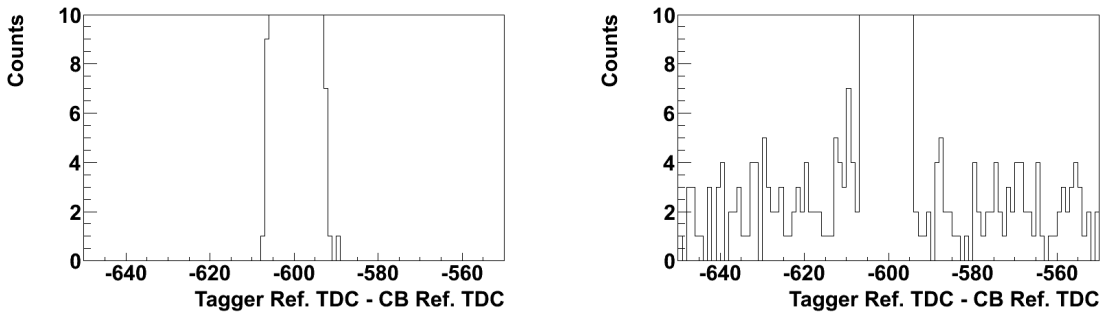

(a) In sync

(b) Out of sync

Figure 4.9: Synchronization check, zoomed in

The analysis then also loops through each of the charged particles and rejects it if its energy is below the cluster threshold chosen (unless it was detected in both the PID and the MWPC), or if it's detected within one of the fiducial cuts, or if it's detected in TAPS in time with a hit in the Cherenkov detector (if the Cherenkov detection is selected as a cut). If the charged particle is rejected for any of the above reasons it's removed from the list and the number of charged particles is reduced by one. If the decision is made to require proton identification specifically, it is also rejected if none of the proton cuts established in AcquRoot were satisfied. This does not, however, reduce the number of charged particles, which is important for selection of Compton events as outlined below. This process is illustrated in Figure 4.11.

4.2 Compton Scattering

Once the various particle cuts as outlined previously have been performed, it must be determined whether the event is to be considered a Compton scattering event. This requires that:

- The number of accepted π^0 is equal to zero
- The number of accepted neutral particles is one or more (or exactly one if an exclusive cut on the number of neutral particles has been selected)

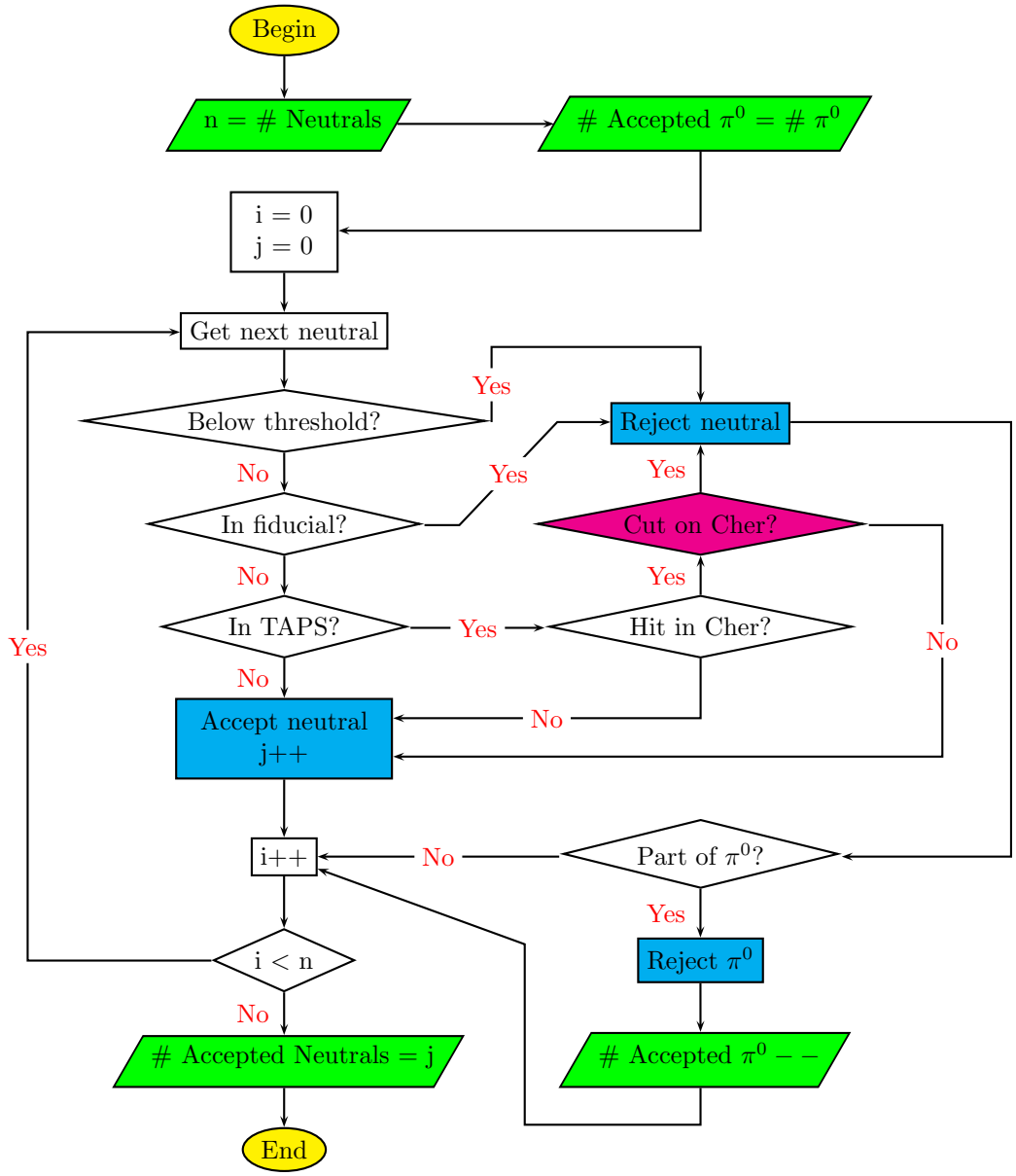

Figure 4.10: Neutral particle selection

- The number of accepted charged particles is one or more (or exactly one if an exclusive cut on the number of charged particles has been selected)
- If desired, the event can be rejected if there was any correlated detection in the Cherenkov.

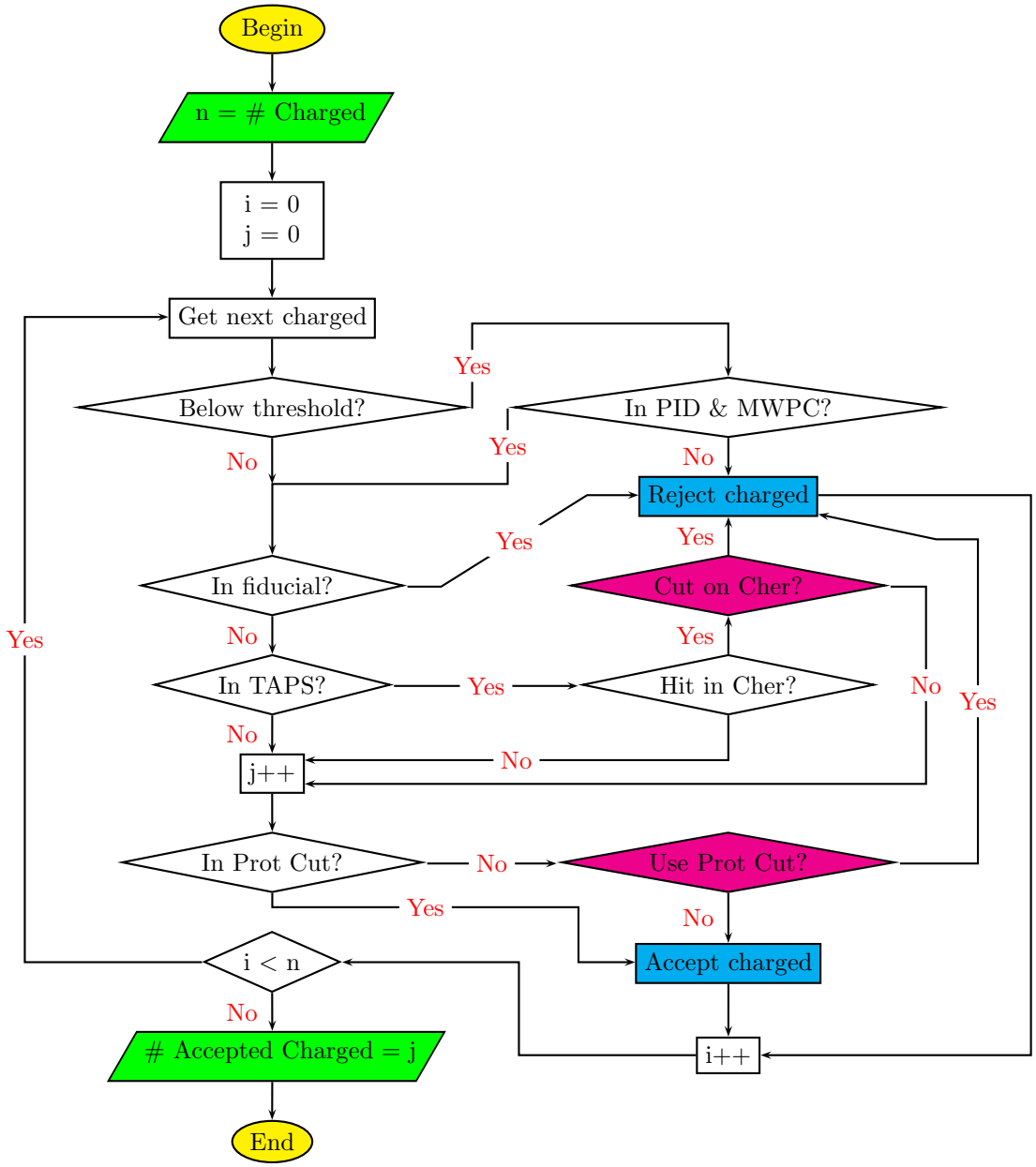

Figure 4.11: Charged particle selection

If the event passes these tests, it loops through all available neutral particles (which will only be one if the exclusive cut on the number of neutral particles has been selected). For each of these it loops through all available tagged photons, selecting only those that lie within the energy regions desired. The time difference between the tagged photon and the neutral particle is calculated, and depending on

the timing windows specified this event is denoted as a prompt or random event. The prompt/random structure in the tagged photon time spectrum is shown in Figure 4.12a and Figure 4.13a. As noted in subsubsection 3.2.1.1, this distribution is sharpened by subtracting the time of a detected neutral particle in either the CB or TAPS. This is shown in Figure 4.12b and Figure 4.13b.

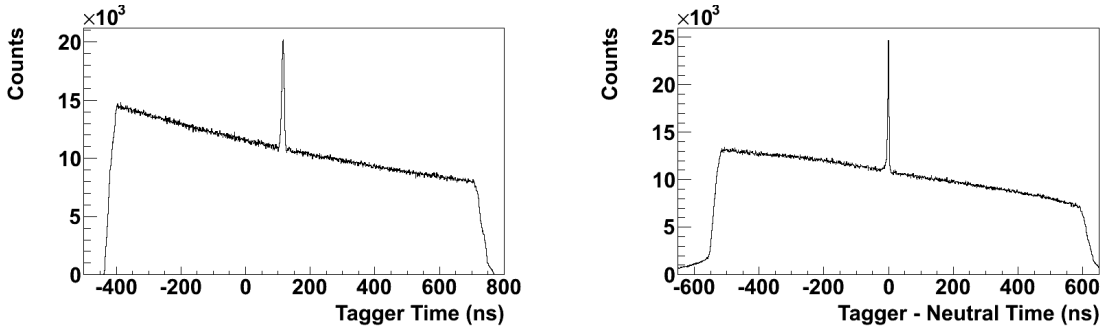

(a) Tagger time (b) Tagger minus neutral time

Figure 4.12: Compton scattering timing spectra showing the prompt peak

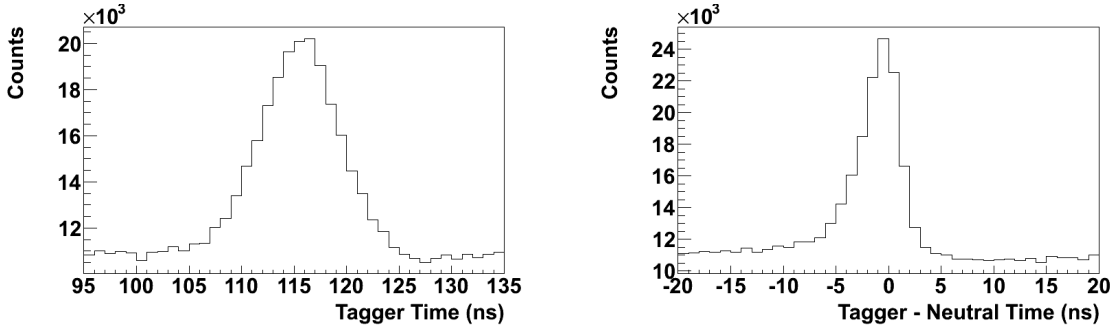

(a) Tagger time (b) Tagger minus neutral time

Figure 4.13: Compton scattering timing spectra zoomed in on the prompt peak

The next step is to construct what's called a 'missing' mass. This method is often employed to account for an undetected final state particle. By knowing the initial state (tagged photon and at rest proton) and detecting part of the final state (scattered photon in the case of Compton scattering) the conservation rules can again

be invoked to determine what the 'missing' particle must be. The missing mass is therefore the invariant mass of this particle, and in this case should equal the mass of a proton.

$$m_{miss} = \sqrt{E_{miss}^2 - \vec{p}_{miss}^2} = \sqrt{(E_i - E_f)^2 - (\vec{p}_i - \vec{p}_f)^2}$$
$$= \sqrt{(E_{\gamma_i} + m_p - E_{\gamma_f})^2 - (\vec{p}_{\gamma_i} - \vec{p}_{\gamma_f})^2} \tag{4.1}$$
$$\xrightarrow[\text{Compton}]{} m_p = 938.27\,\text{MeV} \tag{4.2}$$

This method proves to be useful even when the recoil proton is detected. Both the CB and TAPS perform photon detection very well, with good energy and angular resolution. Proton detection is more difficult, due to energy loss from the travel of the massive particle to the detector, and to the different response of a detector to a proton as opposed to a photon.

The values for the missing mass, Compton photon theta, and Compton photon phi are then filled into one of eight histograms. The number 'eight' derives from there being two sets of target polarization, each with two sets of beam helicity, each with both a prompt and random histogram. Combined versions of these (the method of which is described in chapter 6), for Compton theta of 100-120°, are shown in Figure 4.14 and Figure 4.15. As shown (or rather not shown) in the figures there's a lack of a discernible peak at the proton mass of 938.27 MeV. It exists as little more than a bump on a large increasing background, both from non-hydrogen nucleons in the butanol target (as discussed in subsubsection 2.2.2.2), as well as from π^0 photoproduction masquerading as Compton scattering. This will be discussed in detail in section 4.5. This background prompts the requirement of detecting the recoil proton. Even suffering from energy losses, the direction of the proton is expected to mostly maintain its integrity. Within the tagged photon loop, the program then loops through all available charged particles (which will only be one if the exclusive cut on

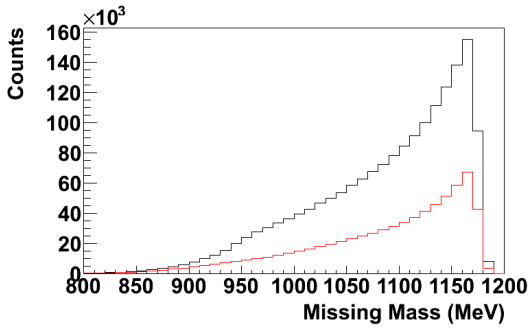

(a) Prompt (black) and random (red)

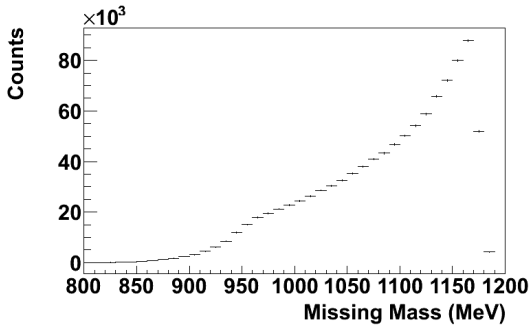

(b) Subtracted

Figure 4.14: Compton scattering with the positive transversely polarized butanol target. Shown are the prompt and random missing mass distributions, as well as the subtracted result.

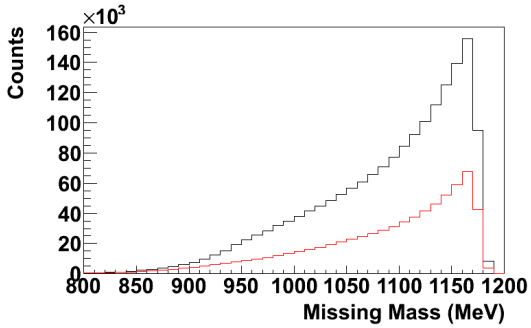

(a) Prompt (black) and random (red)

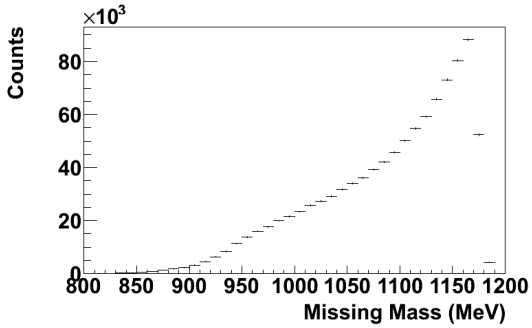

(b) Subtracted

Figure 4.15: Compton scattering with the negative transversely polarized butanol target. Shown are the prompt and random missing mass distributions, as well as the subtracted result.

the number of charged particles has been selected). If the requirement for satisfying a proton identification cut previously rejected a given charged particle, it will not be analyzed.

For each accepted proton a check requiring that it traveled in a direction similar to the expected one (the direction of the 'missing' particle) is made. This is done by determining the angle between the detected and missing particles, referred to as the proton opening angle, as given by Equation 4.3.

$$\theta_{\mathrm{OA}} = \cos^{-1}\left[\frac{\vec{p_{p_f}} \cdot (\vec{p_{\gamma_i}} - \vec{p_{\gamma_f}})}{\sqrt{p_{p_f}^2 (\vec{p_{\gamma_i}} - \vec{p_{\gamma_f}})^2}}\right] \tag{4.3}$$

Setting this opening angle cut to 10° significantly reduces the background in the missing mass spectra, as shown in Figure 4.16 and Figure 4.17. It's clear that the opening

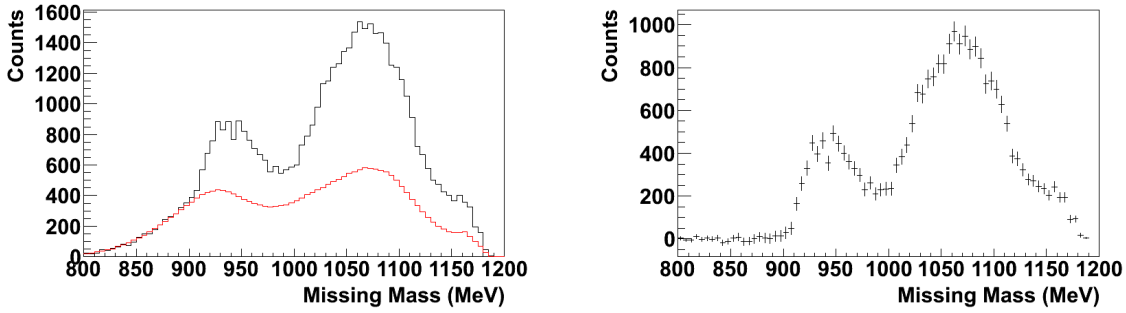

(a) Prompt (black) and random (red) (b) Subtracted

Figure 4.16: Compton scattering with the positive transversely polarized butanol target, utilizing a 10° proton opening angle cut. Shown are the the prompt and random missing mass distributions, as well as the subtracted result.

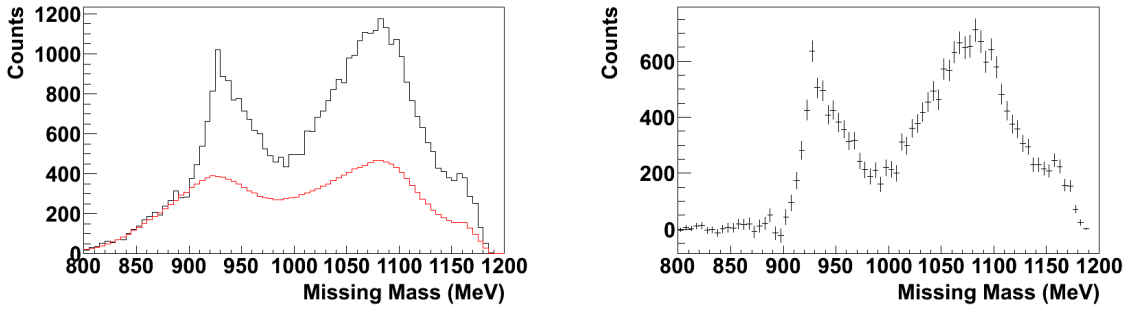

(a) Prompt (black) and random (red) (b) Subtracted

Figure 4.17: Compton scattering with the negative transversely polarized butanol target, utilizing a 10° proton opening angle cut. Shown are the prompt and random missing mass distributions, as well as the subtracted result.

angle cut significantly improves the spectra, pulling out a peak at the appropriate position of 938.27 MeV. The validity of this particular value of the opening angle cut is discussed in section 4.4 and in subsection 5.3.1.

4.3 Carbon Background

Although the application of an opening angle cut on the proton improved the results, there is clearly background remaining in the missing mass spectra. The next obvious task is to remove any contribution from the non-hydrogen elements in the butanol target. As described before, this is done by taking data on a similar setup with the only difference being the use of a carbon target in place of the butanol beads. With the specific selection of the carbon target, as detailed in subsubsection 2.2.2.2, the expectation was that the analysis would be identical to that of the butanol target. The analysis code passes the data through the same loops, using the same event selection, and undergoing the same cuts. This results in missing mass spectra for Compton-like events from the carbon target, as shown in Figure 4.18. To compare

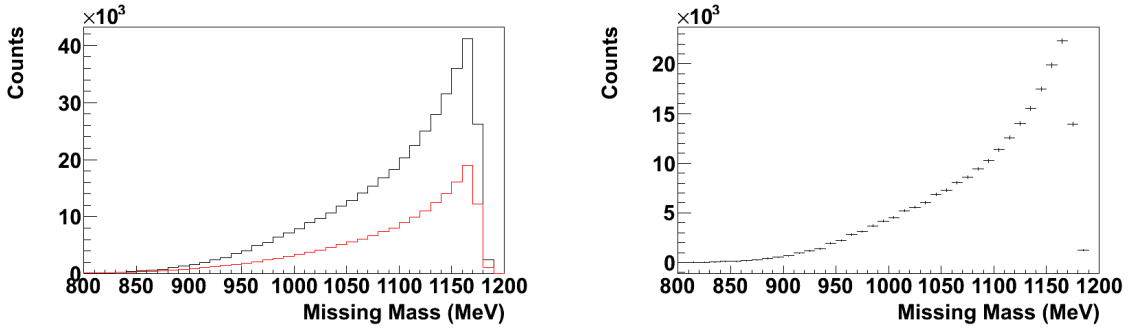

(a) Prompt (black) and random (red)

(b) Subtracted

Figure 4.18: Compton scattering with the carbon target. Shown are the prompt and random missing mass distributions, as well as the subtracted result.

the butanol and carbon spectra, the carbon results have to be scaled by the ratio of the overall butanol target running time to the overall carbon target running time. This ratio can be constructed with the live time corrected tagger scalers as discussed in subsection 4.1.1. Through analysis of π^0 photoproduction, however, it was determined that this scaling factor is actually insufficient to properly account for the carbon background. As will be shown in section 4.4 and further discussed in subsection 5.2.1, an additional scaling factor of 1.306 has been applied to all of the following carbon

subtraction spectra. Once they've been properly scaled, the carbon target spectra can be subtracted directly from the butanol target spectra to give 'proton' target spectra, as shown in Figure 4.19 and Figure 4.20.

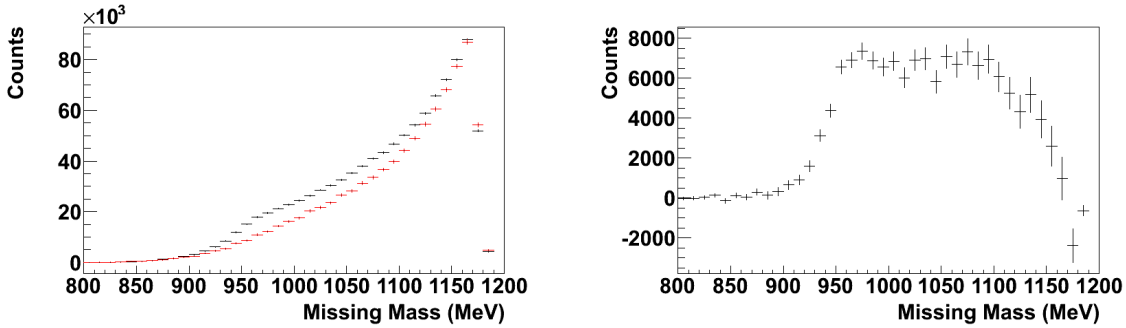

(a) Positive (black) and carbon (red)

(b) Subtracted

Figure 4.19: Compton scattering with both the positive transversely polarized butanol target and the carbon target. Shown are the two together (after scaling the carbon) and their subtraction.

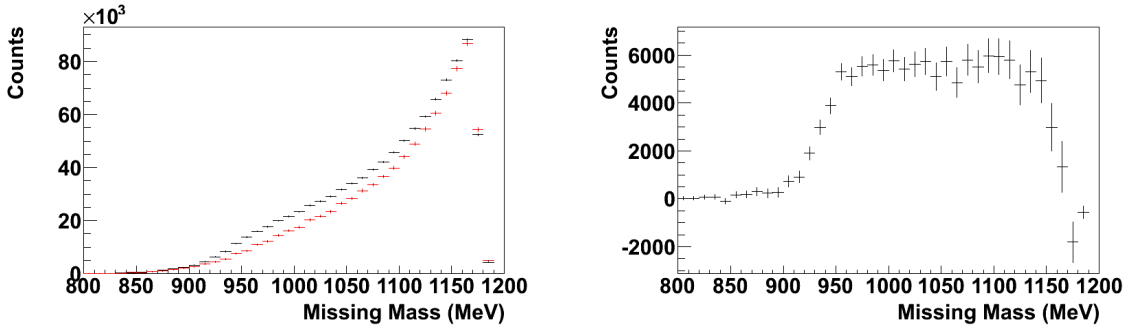

(a) Negative (black) and carbon (red)

(b) Subtracted

Figure 4.20: Compton scattering with both the negative transversely polarized butanol target and the carbon target. Shown are the two together (after scaling the carbon) and their subtraction.

To mimic the butanol data analysis, the same proton opening angle cut is applied to the carbon data analysis. So to compare to the butanol data where a 10° opening angle cut was applied, the carbon data needs to be run with the same cut, reducing the spectra to those shown in Figure 4.21. Comparing the carbon with the butanol

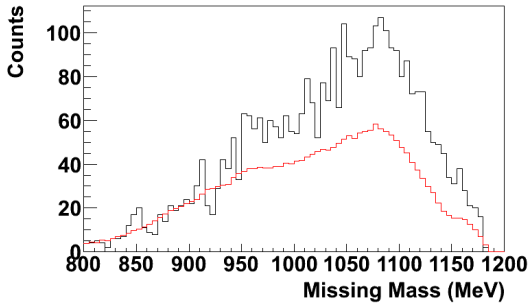

(a) Prompt (black) and random (red)

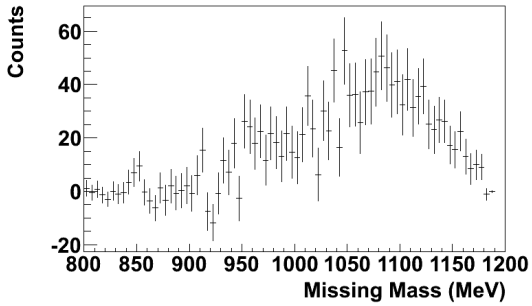

(b) Subtracted

Figure 4.21: Compton scattering with the carbon target, utilizing a 10° proton opening angle cut. Shown are both the prompt and random missing mass distributions, as well as the subtracted result.

then gives Figure 4.22 and Figure 4.23.

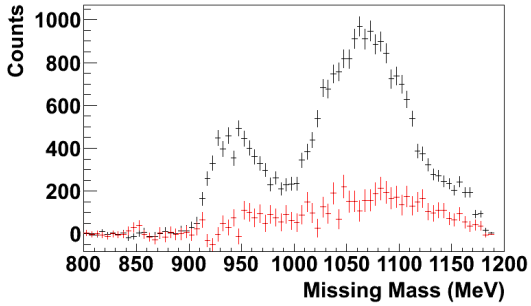

(a) Positive (black) and carbon (red)

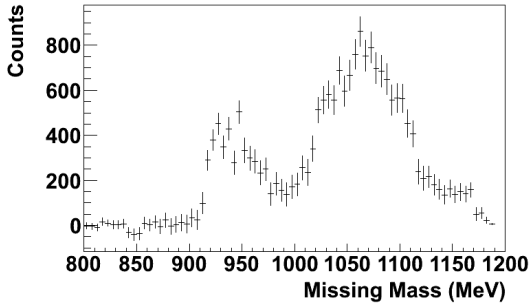

(b) Subtracted

Figure 4.22: Compton scattering with both the positive transversely polarized butanol target and the carbon target, utilizing a 10° proton opening angle cut. Shown are the two together (after scaling the carbon) and their subtraction.

From these spectra it's clear to see that without the opening angle cut a very large portion of the background is due to scattering off of the carbon and oxygen in the butanol target. Even with the subtraction though, an analysis without an opening angle cut results in only a 'shoulder' where the Compton signal is expected. After applying an opening angle cut, the contribution from the carbon background is almost entirely removed.

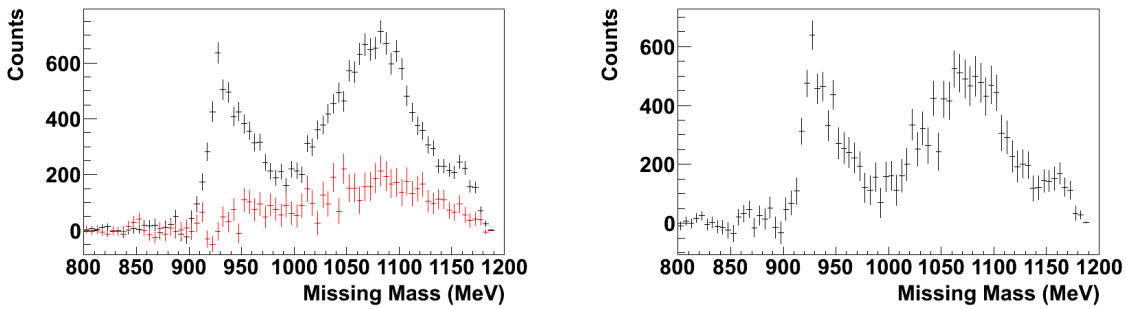

(a) Negative (black) and carbon (red)

(b) Subtracted

Figure 4.23: Compton scattering with both the negative transversely polarized butanol target and the carbon target, utilizing a 10° proton opening angle cut. Shown are the two together (after scaling the carbon) and their subtraction.

4.4 Pion Photoproduction

Even outside of calibrations, studying pion photoproduction in this Compton analysis provides useful information. Given its much larger cross section, which is about 100 times that of Compton in this energy range, it allows for quick checks in the methodology of the analysis. For instance, pion photoproduction also exhibits double polarization asymmetries. From investigation of these, it was determined that the helicity bit in the data stream was reversed between September 2010 and February 2011. This flip was due to a simple reversal of cables on the accelerator control side, since the 'trigger' for flipping the polarization of the electron beam actually comes from a pulser on the A2 hall side.

Studying pion photoproduction is also helpful in determining the proton energy losses and detection efficiencies (discussed in subsection 5.3.1) as well as attempting to compensate for the remaining background in the Compton missing mass peaks even after opening angle cuts and carbon subtraction has been utilized (discussed in section 4.5)

The pion analysis runs similar to the Compton analysis. After performing the same particle cuts as described in subsection 4.1.2, a check is made that the number

of accepted reconstructed neutral pions is one or more (or exactly one if an exclusive cut on the number of neutral pions has been selected). Then for the one pion, or for each pion if the exclusive cut has not been selected, the analysis loops through all available tagged photons, selecting only those that lie within the energy regions desired. The time difference between the tagged photon and the pion is calculated, as shown in Figure 4.24 and Figure 4.25, and depending on the timing windows specified this event is denoted as a prompt or random event.

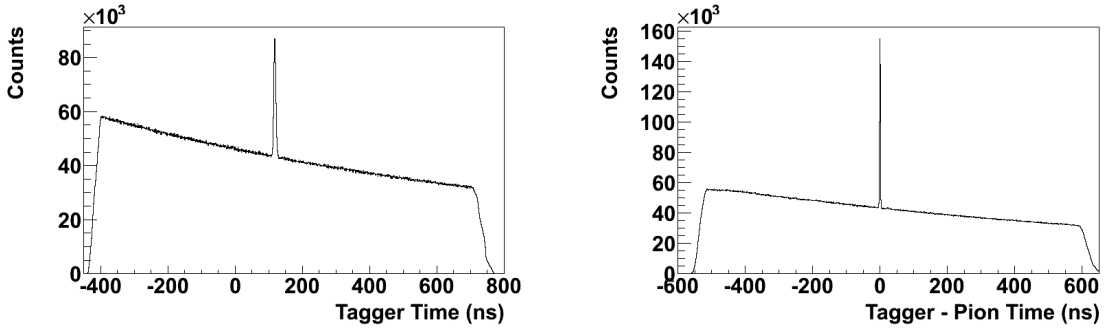

(a) Tagger time (b) Tagger minus pion time

Figure 4.24: Pion photoproduction timing spectra showing the prompt peak

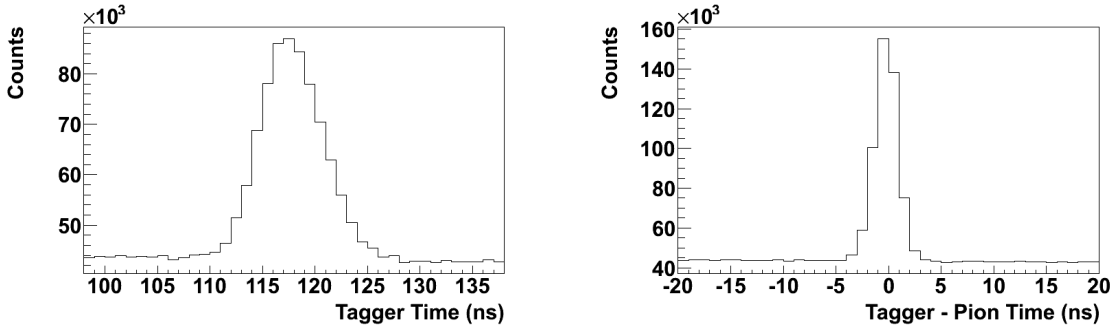

(a) Tagger time (b) Tagger minus pion time

Figure 4.25: Pion photoproduction timing spectra zoomed in on the prompt peak

The missing mass, given in Equation 4.4, is then constructed similar to that for Compton scattering. Note that this is a more inclusive selection than for Compton,

since any number of neutral and charged particles could have been detected, as long as there were two neutrals that combined to form a π^0.

$$m_{miss} = \sqrt{E_{miss}^2 - \vec{p}_{miss}^2} = \sqrt{(E_i - E_f)^2 - (\vec{p}_i - \vec{p}_f)^2}$$
$$= \sqrt{(E_\gamma + m_p - E_{\gamma_1} - E_{\gamma_2})^2 - (\vec{p}_\gamma - \vec{p}_{\gamma_1} - \vec{p}_{\gamma_2})^2} \quad (4.4)$$

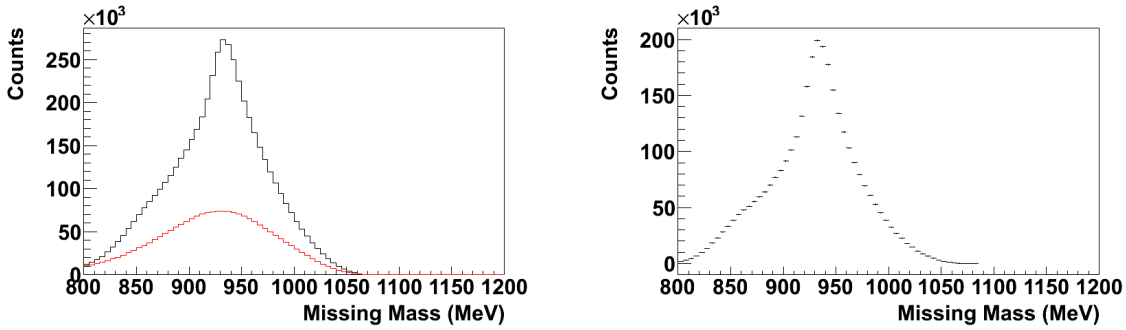

(a) Prompt (black) and random (red) (b) Subtracted

Figure 4.26: Pion photoproduction with the positive transversely polarized butanol target. Shown are the prompt and random missing mass distributions, as well as the subtracted result.

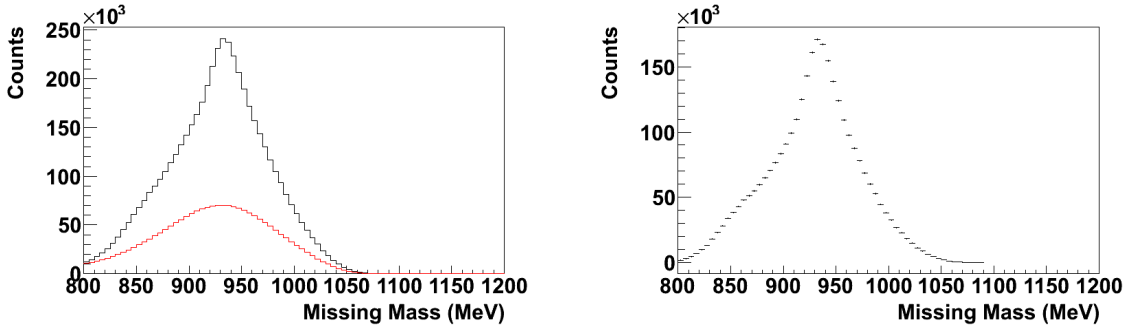

(a) Prompt (black) and random (red) (b) Subtracted

Figure 4.27: Pion photoproduction with the negative transversely polarized butanol target. Shown are the prompt and random missing mass distributions, as well as the subtracted result.

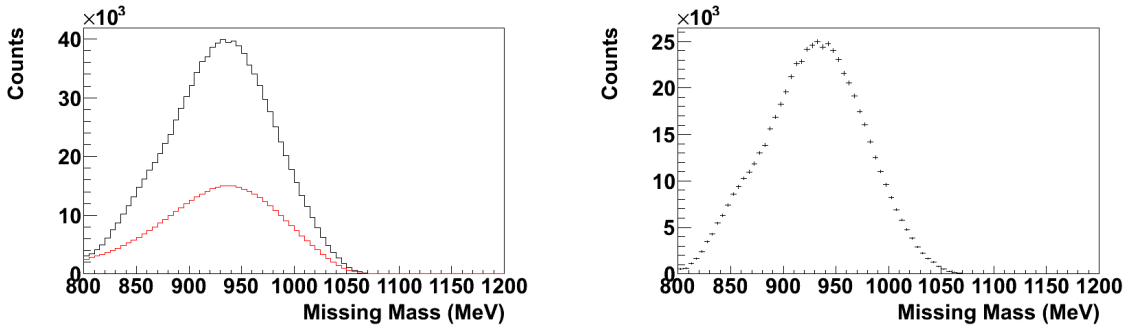

(a) Prompt (black) and random (red)

(b) Subtracted

Figure 4.28: Pion photoproduction with the carbon target. Shown are the prompt and random missing mass distributions, as well as the subtracted result.

As mentioned in section 4.3, the carbon scaling factor determined solely from the running time and live time is clearly insufficient when examining Figure 4.29 and Figure 4.30. Both the lower and higher missing mass sides of the peak clearly have some remaining background in them that appear to have roughly the same shape as the carbon spectra. By scanning through additional scaling factors applied to the carbon spectra, and looking for the best agreement, a more suitable value is determined. This process will be discussed in more detail in subsection 5.2.1. The additional factor (multiplied by the factor determined through flux comparisons), results in greatly improved subtracted spectra shown in Figure 4.31 and Figure 4.32. This factor, determined to be 1.306 (or 1.234 for the 315-346 MeV bin), is used identically for the Compton analysis, where low statistics prevent a similar undertaking.

4.5 Pion Photoproduction Background

Given the energy range being analyzed, the remaining background in the Compton missing mass distributions is expected to be the result of pion photoproduction masquerading as Compton scattering. There are three primary ways that this could occur:

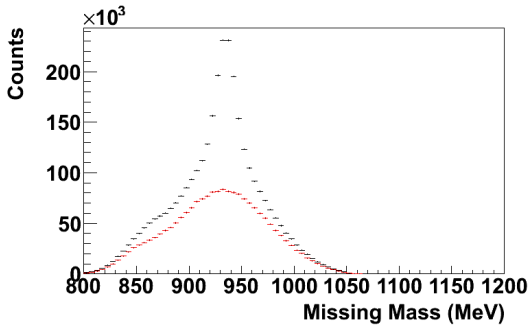

(a) Positive (black) and carbon (red)

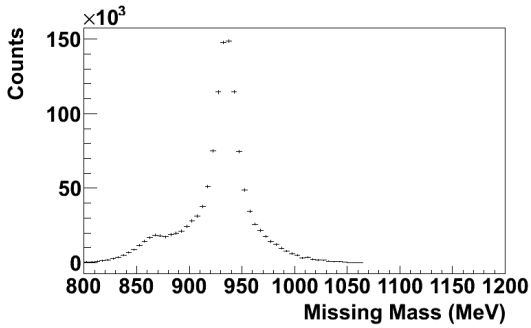

(b) Subtracted

Figure 4.29: Pion photoproduction with both the positive transversely polarized butanol target and the carbon target, utilizing the original carbon scaling factor. Shown are the two together (after scaling the carbon) and their subtraction.

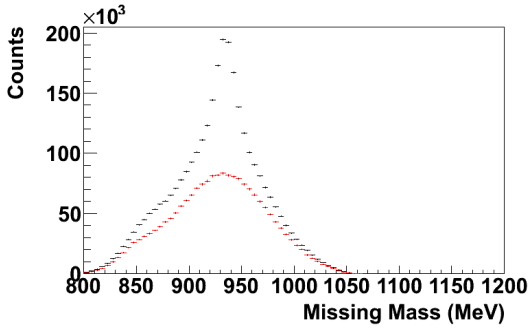

(a) Negative (black) and carbon (red)

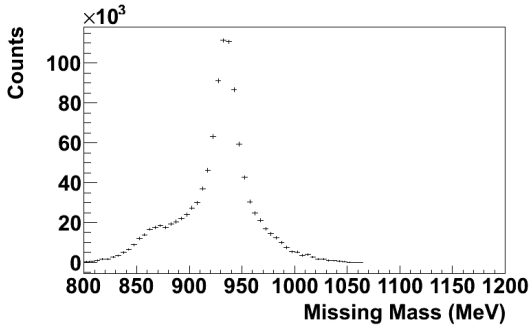

(b) Subtracted

Figure 4.30: Pion photoproduction with both the negative transversely polarized butanol target and the carbon target, utilizing the original carbon scaling factor. Shown are the two together (after scaling the carbon) and their subtraction.

- One of the decay photons is not detected
- The recoil proton is not detected and one of the decay photons is misidentified as a charged particle
- The recoil proton and one of the decay photons is summed together as one charged cluster

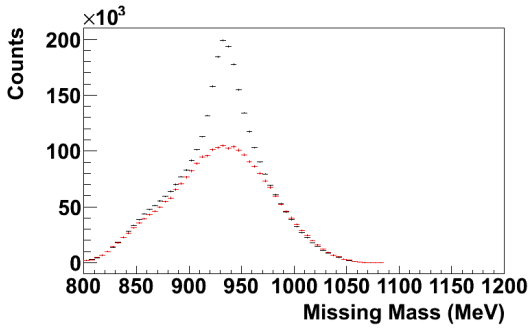

(a) Positive (black) and carbon (red)

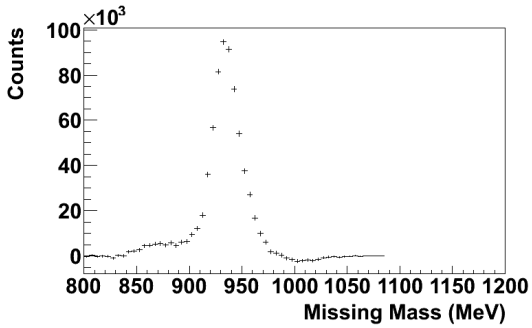

(b) Subtracted

Figure 4.31: Pion photoproduction with both the positive transversely polarized butanol target and the carbon target, utilizing the adjusted carbon scaling factor. Shown are the two together (after scaling the carbon) and their subtraction.

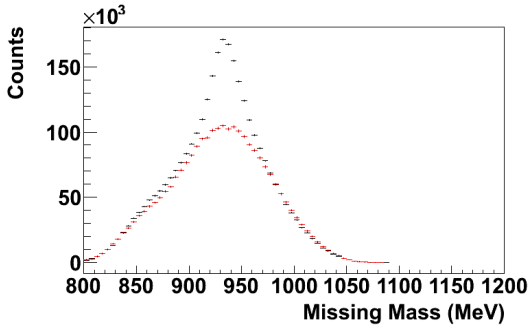

(a) Negative (black) and carbon (red)

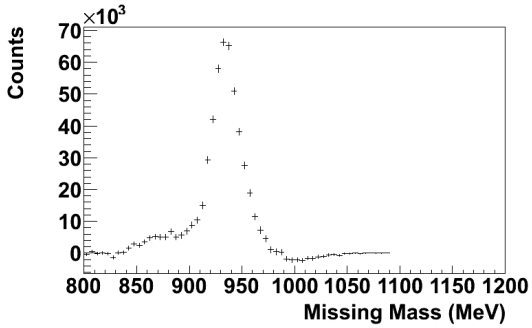

(b) Subtracted

Figure 4.32: Pion photoproduction with both the negative transversely polarized butanol target and the carbon target, utilizing the adjusted carbon scaling factor. Shown are the two together (after scaling the carbon) and their subtraction.

4.5.1 Lost Decay Photon

The first background possibility, of missing one of the decay photons, is due to various losses of detection efficiency in the CB/TAPS system, notably after the establishment of the fiducial cuts shown in Figure 4.2b. These cuts provide (or expand) holes in which one of the decay photons can escape detection. For instance, it's very possible for one of the decay photons to travel straight back upstream and appear as a Compton event, as shown in Figure 4.33.

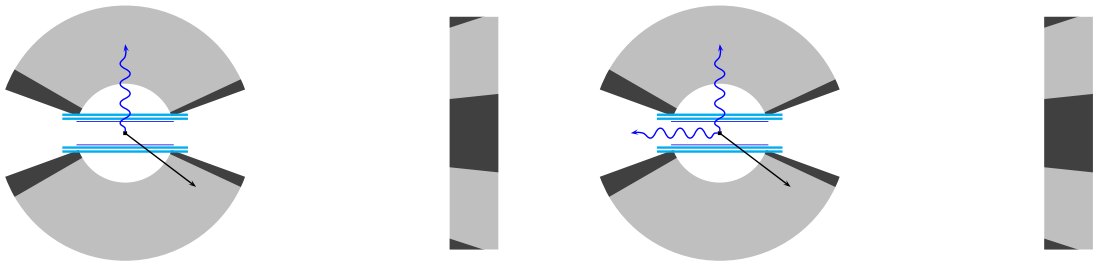

(a) Compton (b) Pion

Figure 4.33: Cross section of detectors, drawn to scale, showing Compton-like pion photoproduction events

The resulting missing mass from these events was computed with a simple Monte Carlo of pion photoproduction events, with results shown in Figure 4.34 to Figure 4.36. In each case the missing mass is first plotted as a function of the angle

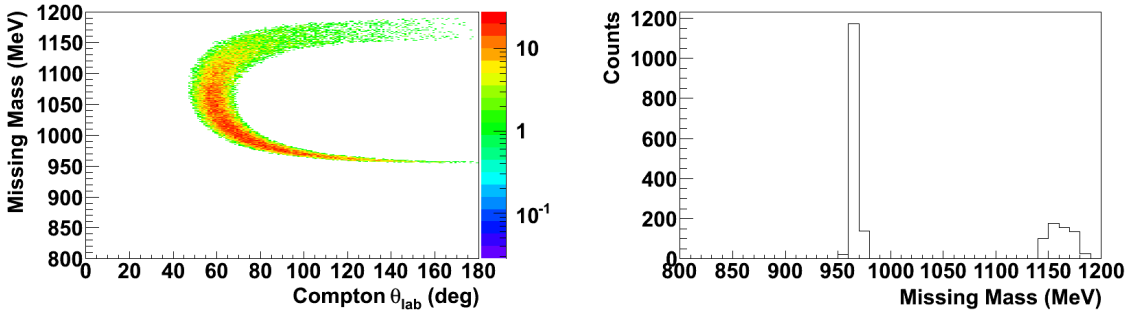

(a) All angles (b) 100-120°

Figure 4.34: Monte Carlo pion photoproduction events where one of the decay photons ends in the forward fiducial cut in TAPS

of the detected photon (which would be the mistaken Compton photon), and then simply plotted for the same $100 - 120°$ range as shown previously. The arc like shape of these distributions arises from the kinematics of π^0 photoproduction. Given its three body nature, the decay photon traveling into each fiducial can have two ranges of energy for a given angle of the detected decay photon. The more forward (or backward) going the detected photon is, the more distinct the separation between these

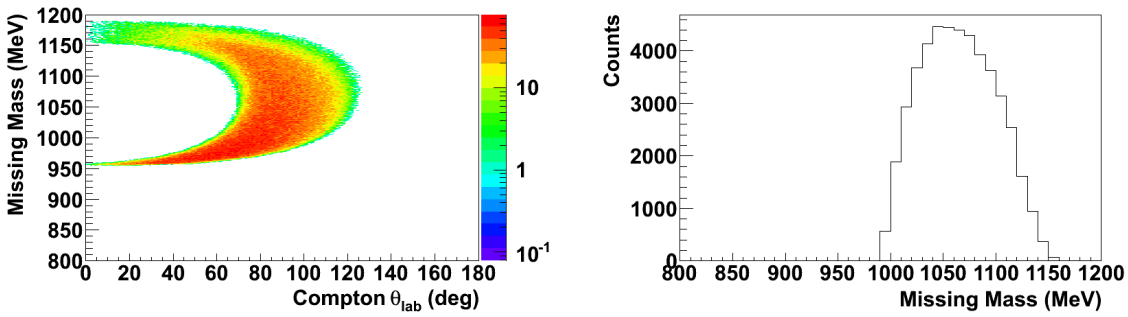

(a) All angles (b) 100-120°

Figure 4.35: Monte Carlo pion photoproduction events where one of the decay photons ends in the backward fiducial cut in the CB

two energy ranges is. The end of the arc that approaches 950 MeV indicates that

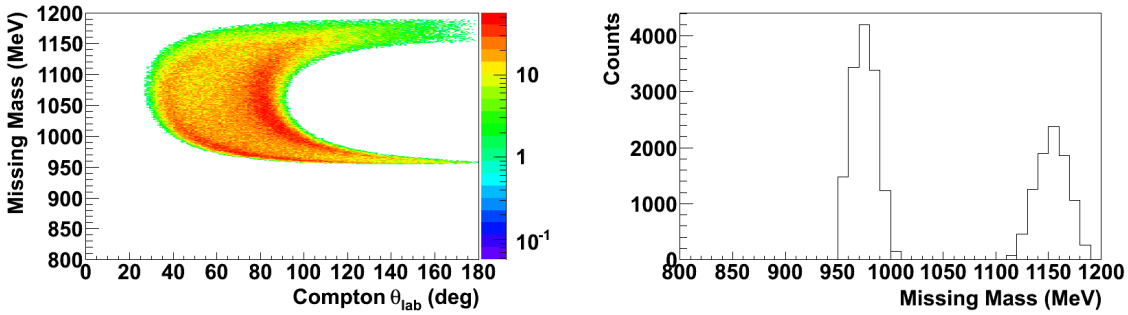

(a) All angles (b) 100-120°

Figure 4.36: Monte Carlo pion photoproduction events where one of the decay photons ends in the middle fiducial cut between the CB and TAPS

the lost decay photon was 'soft', taking away only a small amount of energy, leaving the detected decay photon looking very similar to a Compton scattered photon. The other end of the arc indicates that the lost decay photon was 'hard', taking much of the final state energy with it.

To reduce some of these events, the same opening angle cut (10°) can be applied to the remaining photon and the recoil proton, resulting in Figure 4.37 to Figure 4.39. While the opening angle cut does remove much of the higher missing mass component

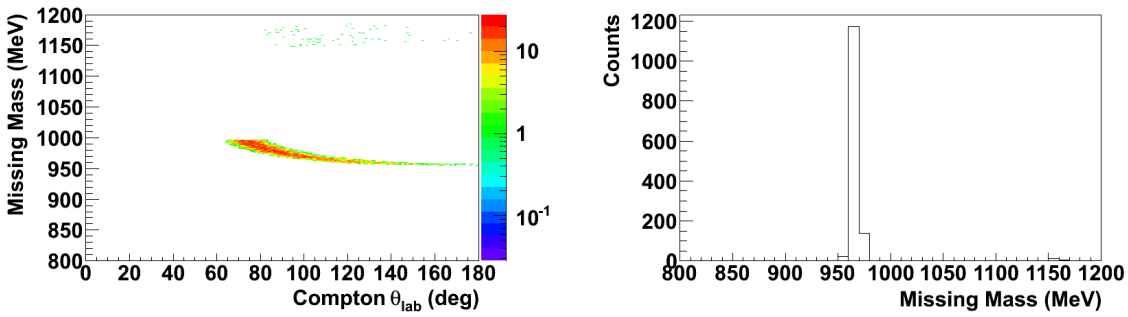

(a) All angles (b) 100-120°

Figure 4.37: Monte Carlo pion photoproduction events where one of the decay photons ends in the forward fiducial cut in TAPS, and the remaining photon and the recoil proton satisfy the 10° opening angle cut

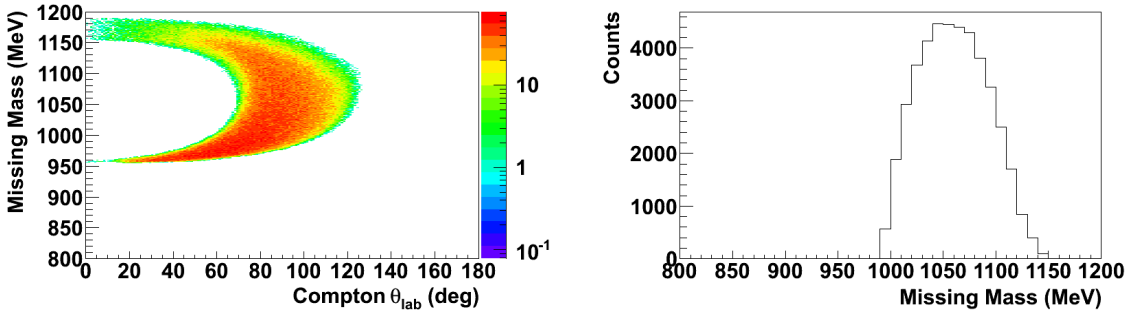

(a) All angles (b) 100-120°

Figure 4.38: Monte Carlo pion photoproduction events where one of the decay photons ends in the backward fiducial cut in the CB, and the remaining photon and the recoil proton satisfy the 10° opening angle cut

for both the TAPS and CB/TAPS fiducial cases, it unfortunately leaves behind a large amount of the CB fiducial case and the lower missing mass component for both the TAPS and CB/TAPS fiducial cases. Given their proximity to the proton mass, and therefore to a Compton signal, this is an important background to account for.

4.5.2 Lost Recoil Proton

The second background possibility, of missing the recoil proton and misidentifying a decay photon as a charged particle, can come about in two different ways. Either

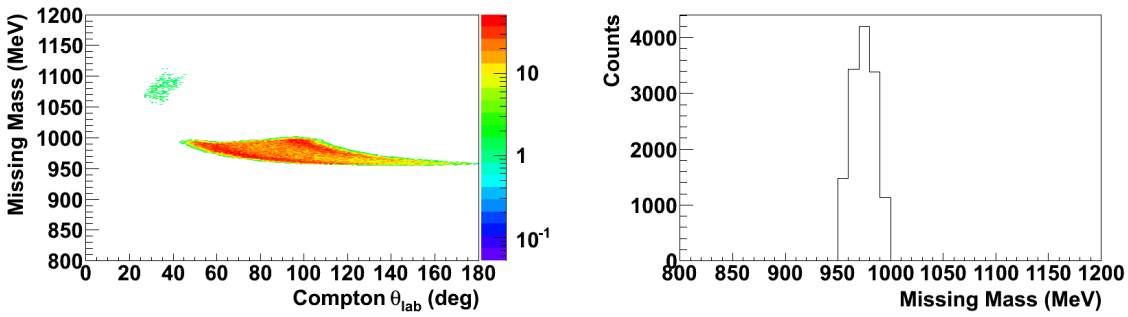

(a) All angles (b) 100-120°

Figure 4.39: Monte Carlo pion photoproduction events where one of the decay photons ends in the middle fiducial cut between the CB and TAPS, and the remaining photon and the recoil proton satisfy the 10° opening angle cut

the proton can be lost in the same way as for a decay photon, where it ends up in a fiducial cut, or by suffering from enough energy loss that it never makes it to the detector. This background also assumes that one of the decay photons is accidentally tagged as a charged particle, the likelihood of which is an important question. For simplicity this first pass assumes it does. The results are shown in Figure 4.40 to Figure 4.42. In this situation there are no results for the proton ending up in the CB

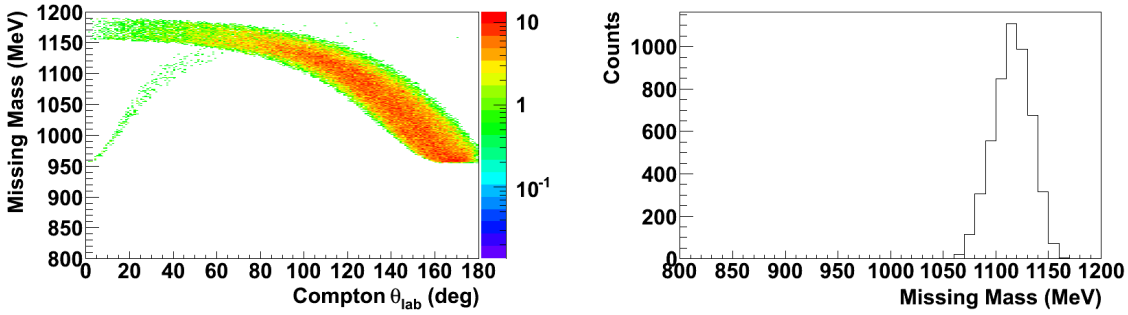

(a) All angles (b) 100-120°

Figure 4.40: Monte Carlo pion photoproduction events where the recoil proton ends in the forward fiducial cut in TAPS

fiducial, since kinematically the proton must travel forward.

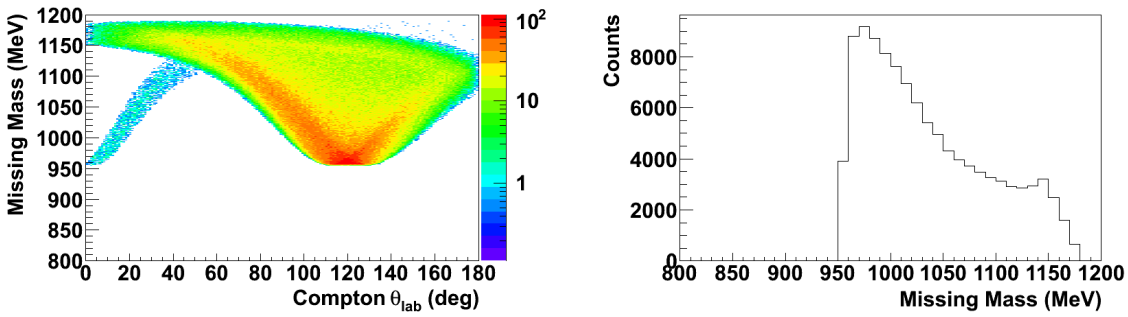

(a) All angles (b) 100-120°

Figure 4.41: Monte Carlo pion photoproduction events where the recoil proton ends in the middle fiducial cut between the CB and TAPS

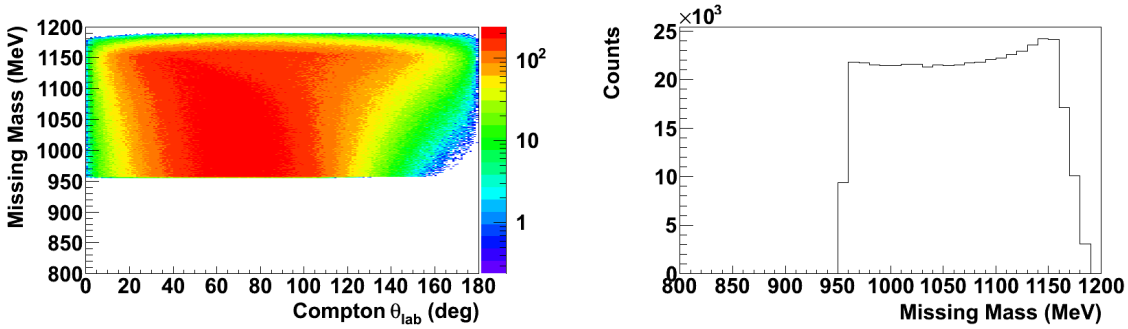

(a) All angles (b) 100-120°

Figure 4.42: Monte Carlo pion photoproduction events where the proton is stopped

For these possibilities, applying the 10° opening angle cut between the two decay photons significantly changes the results, as shown in Figure 4.43 to Figure 4.45. As evidenced by this rough check, even if all instances of a proton being lost result in a misidentified Compton event (despite the oddness of one of the decay photons being tagged as a charged particle), the net effect is only about 7% of that from a lost decay photon in the immediate region of interest around the Compton peak. This number becomes even smaller at more forward Compton angles, or if integrating higher than 980 MeV (at which point the hole in the CB becomes important). An important point to note here is that these quick analyses have no energy or angular smearing

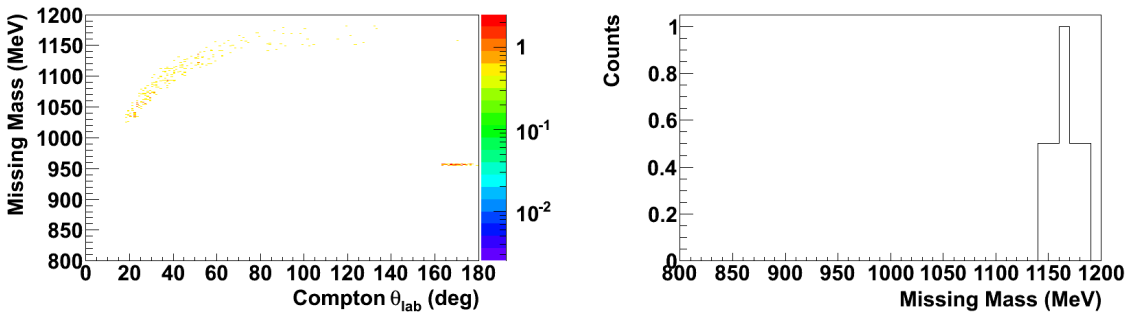

(a) All angles (b) 100-120°

Figure 4.43: Monte Carlo pion photoproduction events where the recoil proton ends in the forward fiducial cut in TAPS, and the decay photons satisfy the 10° opening angle cut

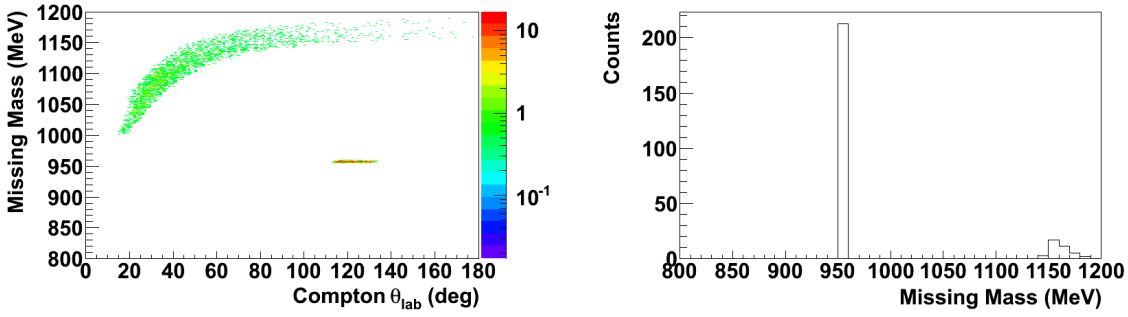

(a) All angles (b) 100-120°

Figure 4.44: Monte Carlo pion photoproduction events where the recoil proton ends in the middle fiducial cut between the CB and TAPS, and the decay photons satisfy the 10° opening angle cut

applied to them. A more detailed check will be done in the following chapter, but this serves as a simple guide for the analysis.

4.5.3 Combined Decay Photon and Recoil Proton

The third background possibility, of a decay photon and the recoil proton being detected in the same cluster, is also an unlikely process. A single cluster in the CB subtends a cone with a half-angle of approximately 15°. This requires that the angle between a decay photon and the recoil proton be less than this value. Using the

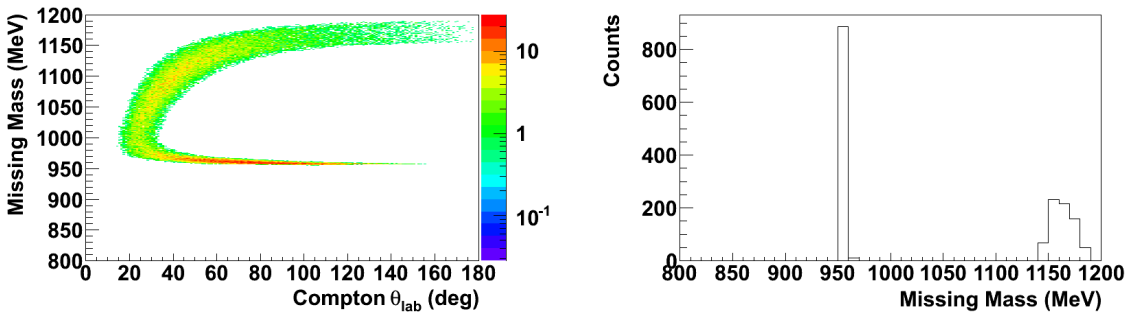

(a) All angles (b) 100-120°

Figure 4.45: Monte Carlo pion photoproduction events where the proton is stopped, and the decay photons satisfy the 10° opening angle cut

same rough checks as above, this angle is shown in Figure 4.46. Looking only at

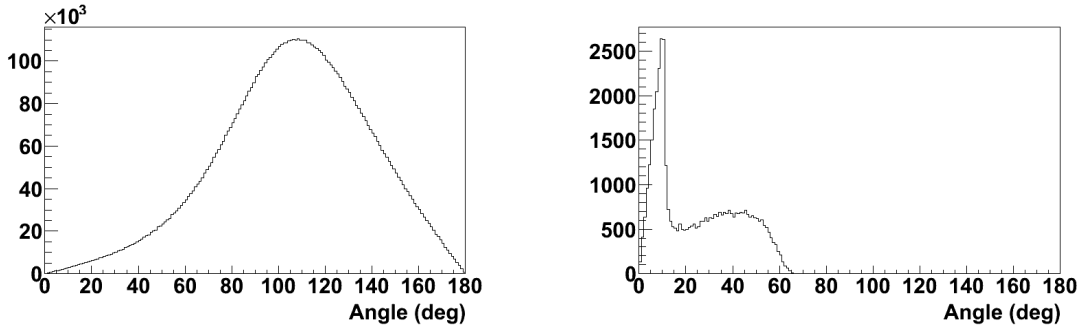

(a) No opening angle cut (b) 10° opening angle cut

Figure 4.46: Monte Carlo pion photoproduction events showing the angle between one of the decay photons and the recoil proton

events that are within this 15° cone, the missing mass distributions are shown in Figure 4.47. Additionally requiring the 10° opening angle cut, the edited missing mass distributions are shown in Figure 4.48. These events obviously pose something of a problem since the signal, even after applying an opening angle cut, is in the proper region with a strength approaching that of the first possibility investigated. However a more detailed simulation will be necessary to examine this.

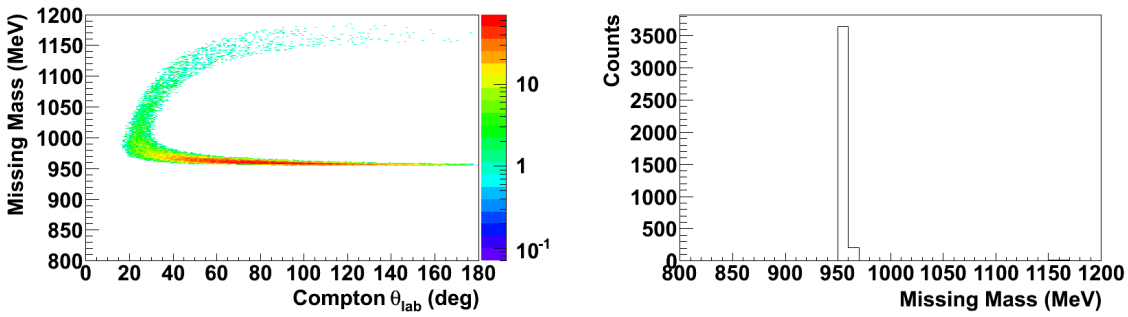

(a) All angles (b) 100-120°

Figure 4.47: Monte Carlo pion photoproduction events where one of the decay photons and the recoil proton are within 15° of each other

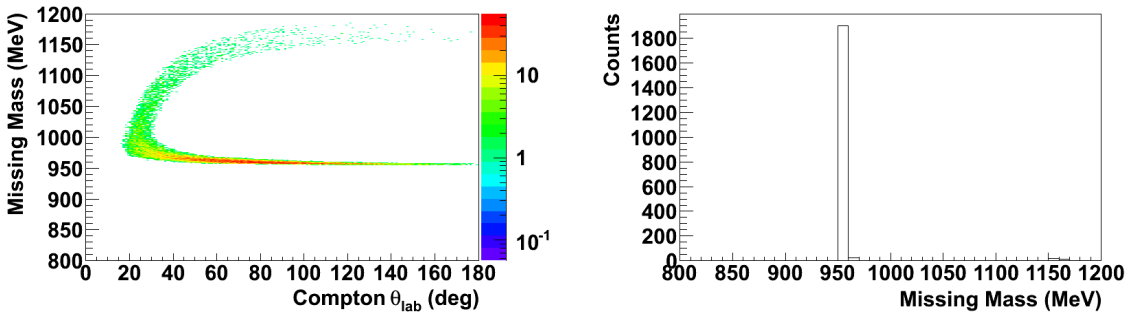

(a) All angles (b) 100-120°

Figure 4.48: Monte Carlo pion photoproduction events where one of the decay photons and the recoil proton are within 15° of each other, and the other decay photon and this cluster satisfy the 10° opening angle cut

4.5.4 Ring Analysis

There are two ways to handle the first problem noted, where one of the decay photons is lost into a fiducial cut. It can either be studied in more detailed Monte Carlo simulation (also discussed in chapter 5), or through an altered analysis of the actual data. The benefit to using the real data is by minimizing the scaling of the background needed before subtracting it out. This analysis, which will be referred to as the ring analysis (for reasons that will be made clear momentarily) is run simultaneously with the Compton analysis. The first step is to define angular

regions close to each fiducial cut. These regions are then azimuthal rings in the detectors (hence the name 'ring analysis'), as depicted in Figure 4.49. The analysis

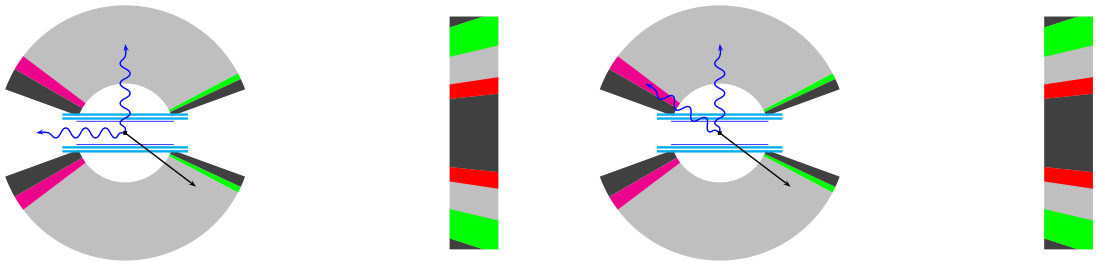

(a) Photon in fiducial cut

(b) Photon in ring

Figure 4.49: Cross section of detectors, drawn to scale, showing construction of rings

looks for pion photoproduction events where one of the decay photons is detected in one of the rings, as shown in Figure 4.49a. Kinematically these situations are close to those where the decay photon is lost in the adjacent fiducial cut, as shown in Figure 4.49b. By ignoring the photon detected in the ring, the remaining photon and proton are analyzed as if they were a Compton event. The resulting missing mass distributions can then be subtracted directly from the Compton distributions to remove this background. To test this, the same basic Monte Carlo check can look at these ring events and compare them to the lost fiducial events, as shown in Figure 4.50 to Figure 4.52.

The ring analysis for the TAPS fiducial cut and for the CB/TAPS fiducial cut both work quite well. The discrepancy in the ring analysis for the CB fiducial cut can be explained by the large angular region of this fiducial (150-180°). The kinematics of the ring region are clearly different from those of the fiducial region. To account for this, a scaling function is applied to the 'Compton' angle (the angle of the photon NOT detected in the ring) to shift it into a more kinematically appropriate region. This function is computed by first looking at the kinematics assuming the ring photon

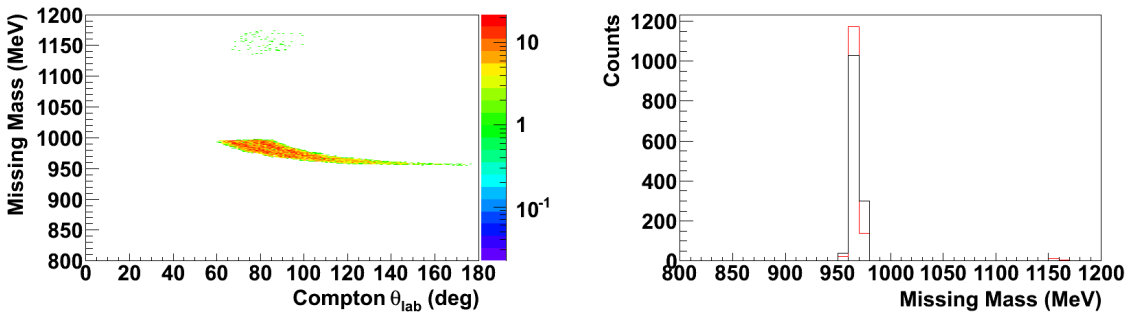

(a) All angles (b) 100-120°, ring (black) and fiducial (red)

Figure 4.50: Monte Carlo pion photoproduction events where one of the decay photons ends in the forward ring in TAPS, and the remaining photon and the recoil proton satisfy the 10° opening angle cut

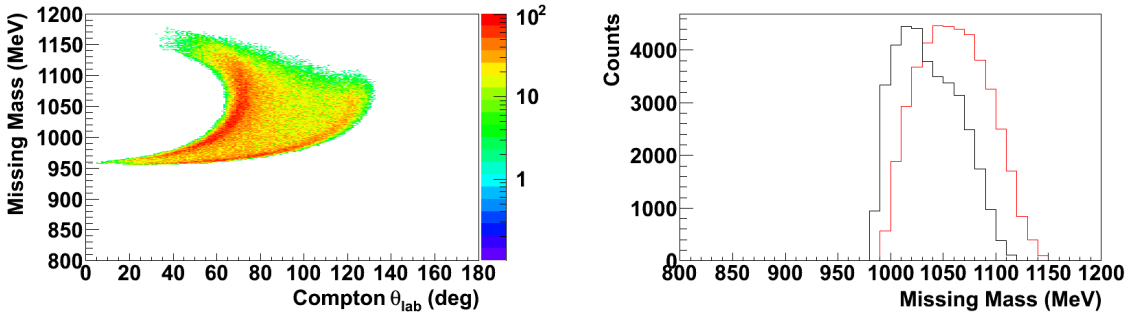

(a) All angles (b) 100-120°, ring (black) and fiducial (red)

Figure 4.51: Monte Carlo pion photoproduction events where one of the decay photons ends in the backward ring in the CB, and the remaining photon and the recoil proton satisfy the 10° opening angle cut

instead went directly upstream at 180° (keeping the energy of the 'Compton' photon fixed), and solving the quadratic equation

$$AE_{\gamma_2}^2 + BE_{\gamma_2} + C = 0 \tag{4.5}$$

for the energy of this upstream photon

$$E_{\gamma_2} = \frac{-B + \sqrt{B^2 - 4AC}}{2A} \tag{4.6}$$

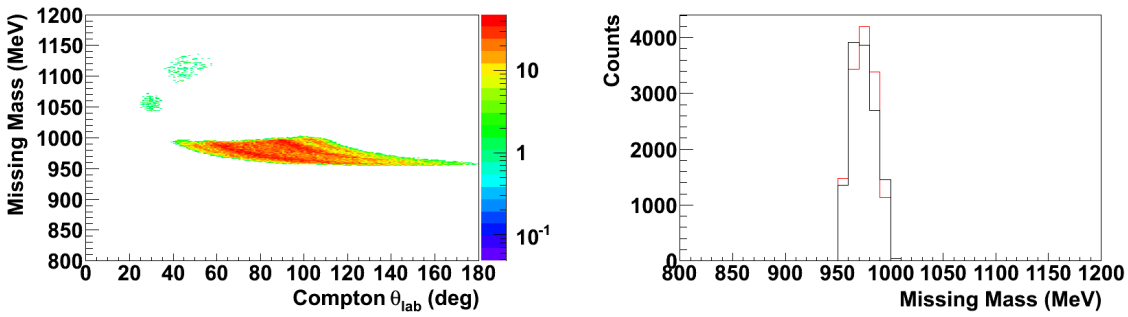

(a) All angles (b) 100-120°, ring (black) and fiducial (red)

Figure 4.52: Monte Carlo pion photoproduction events where one of the decay photons ends in the middle rings between the CB and TAPS, and the remaining photon and the recoil proton satisfy the 10° opening angle cut

where the three coefficients are giving by:

$$A = 2E_\gamma + m_p \tag{4.7}$$

$$B = m_p E_{\gamma_1} + 2E_{\gamma_1} E_\gamma - m_p E_\gamma - \frac{m_{\pi_0}^2}{2} \tag{4.8}$$

$$C = -\frac{E_\gamma m_{\pi_0}^2}{2} \tag{4.9}$$

Having determined the energy of the ring-photon, the angle of the 'Compton' photon can be calculated by

$$\theta_0 = \cos^{-1}\left(\frac{m_{\pi_0}^2}{2E_{\gamma_1}E_{\gamma_2}} - 1\right) \tag{4.10}$$

Using this, the actual detected angle of the 'Compton' photon is scaled with the following function

$$\theta_{\text{new}} = \theta_0\left[1 + \left(\frac{s_1}{s_2}\right)\left[e^{s_2\left(\frac{\theta-\theta_0}{\theta_0}\right)} - e^{-s_3\left(\frac{\theta-\theta_0}{\theta_0}\right)}\right]\right] \tag{4.11}$$

where s_1, s_2, and s_3, are energy (of the 'Compton' photon) dependent parameters chosen to best match the ring with the fiducial results (from Monte Carlo). They are given by the following equations:

$$s_1(E_{\gamma_1}) = s_{1a} + s_{1b}E_{\gamma_1} + s_{1c}E_{\gamma_1}^2 + s_{1d}E_{\gamma_1}^3 \tag{4.12}$$

$$s_2(E_{\gamma_1}) = \frac{s_{2a}}{1 + e^{-\frac{E_{\gamma_1} - s_{2b}}{s_{2c}}}} + s_{2d} \tag{4.13}$$

$$s_3(E_{\gamma_1}) = \frac{s_{3a}}{1 + e^{-\frac{E_{\gamma_1} - s_{3b}}{s_{3c}}}} + s_{3d} \tag{4.14}$$

where the parameters of these are constants given in Table 4.1. Applying this angular

	a	b	c	d
s_1	0.1059	4.587×10^{-3}	-2.29×10^{-5}	4.067×10^{-8}
s_2	7.314	195.2	19.23	6.846
s_3	2.598	175.0	18.98	6.951

Table 4.1: Parameters for angle shifting in ring analysis

shift to the Monte Carlo results in Figure 4.53.

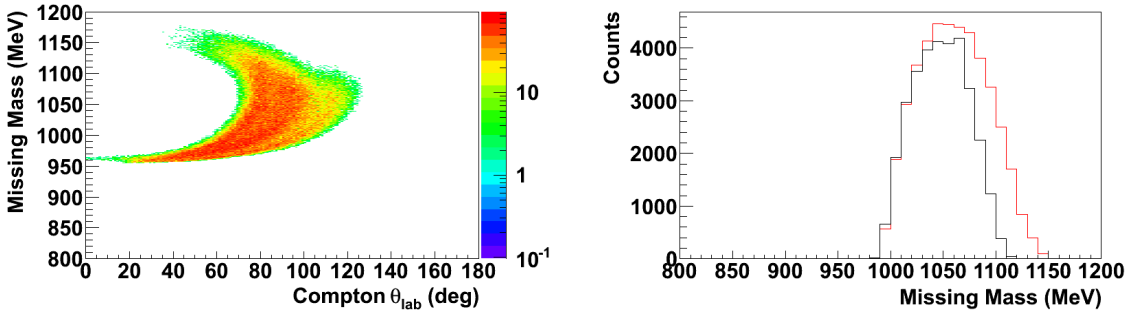

(a) All angles

(b) 100-120°, ring (black) and fiducial (red)

Figure 4.53: Monte Carlo pion photoproduction events where one of the decay photons ends in the backward ring in the CB, after applying an angular shift, and the remaining photon and the recoil proton satisfy the 10° opening angle cut

To apply this methodology in the real analysis, a similar track to the Compton analysis is followed. For each event the analysis checks if the number of accepted π^0 is one, and if so it loops through each fiducial cut and takes the following steps.

- First an initial value for the CB energy sum is set to the experimental value.

- The analysis then loops through each accepted neutral particle, and makes several checks.
  - If the neutral particle is part of the π^0 and a neutral hasn't already been found for the ring associated with the current fiducial cut, it checks if the neutral is in the ring.
  - If the neutral is in the ring, and was detected in the CB, the energy sum is reduced by its energy to reflect the trigger condition if the neutral had instead entered the associated fiducial cut.
  - If the energy sum is still above 100 MeV then the ring event is accepted, and the neutral is tagged as such.

Once all fiducial cuts/rings have been checked over, the ring analysis (to again mimic the Compton analysis) requires that:

- The number of accepted neutral particles is two or more (or exactly two if an exclusive cut on the number of neutral particles has been selected)
- The number of accepted charged particles is one or more (or exactly one if an exclusive cut on the number of charged particles has been selected)
- If desired, the event can be rejected if there was any correlated detection in the Cherenkov.

For each accepted ring event the analysis first checks the accepted π^0, and if desired forces the two photon invariant mass to the π^0 mass. It then loops over all available neutral particles (which will only be two if the exclusive cut on the number of neutral particles has been selected), skipping the one that resulted in a ring. For each neutral it then loops over all available tagged photons, checking if it's within a desired energy bin. If so the difference in time between the tagged photon and the neutral is calculated, determining if it's a prompt or random event. The missing mass

is first calculated looking at the full π^0, which is important to first check that it is a legitimate pion photoproduction event. The analysis then loops over all available charged particles (which will only be one if the exclusive cut on the number of neutral particles has been selected). The proton opening angle is also first calculated looking at the full π^0. Assuming it passes this check, the analysis then recalculates the proton opening angle assuming the ring photon is lost (thereby appearing as a Compton event), and checks that it satisfies the opening angle cut for Compton scattering. If the current neutral particle being analyzed is the other decay photon, as opposed to the one that was detected in a ring (which is the only case if the exclusive cut on the number of neutral particles has been selected), the polar angle can be scaled to adjust the kinematics. Finally the missing mass is recalculated, again assuming the ring photon is lost, taking into account the possibly shifted photon angle.

The ring analysis produces the missing mass spectra shown in Figure 4.54 to Figure 4.68. Subtracting the three ring spectra, after completing the prompt/random and carbon subtraction, gives the Compton missing mass spectra shown in Figure 4.69 and Figure 4.70, where this ring analysis method clearly produces reasonable results similar to the rough Monte Carlo checks shown before. It eliminates a large portion of the higher missing mass background in these spectra, while providing some background subtraction in the region of interest (around 950 MeV). To determine the number of counts for each polarization to be used in calculating asymmetries, these subtracted spectra are integrated up to a conservative upper limit of 940 MeV (just above the proton mass). This reduces the likelihood of including similar π^0 photoproduction events that have not been eliminated with the ring analysis. To improve this limit there is a need to study these backgrounds in more depth with a detailed simulation method. This will help to show if this ring method properly accounts for the background and/or whether a more complete subtraction method can be found.

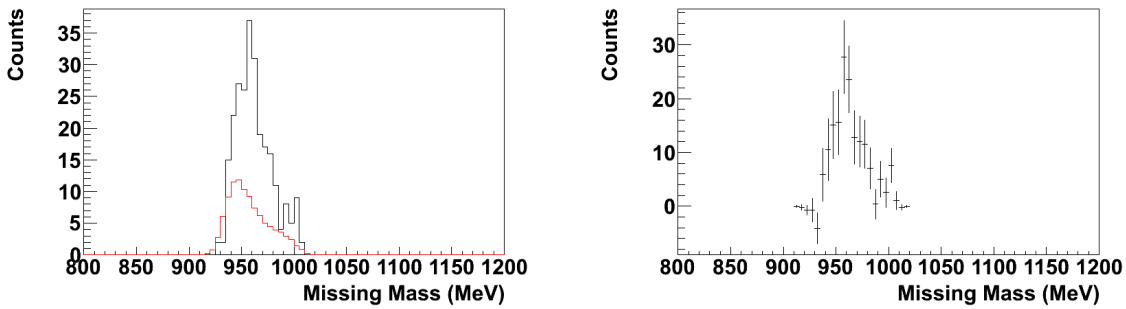

(a) Prompt (black) and random (red) (b) Subtracted

Figure 4.54: TAPS ring analysis with the positive transversely polarized butanol target. Shown are the prompt, random, and subtracted missing mass distributions.

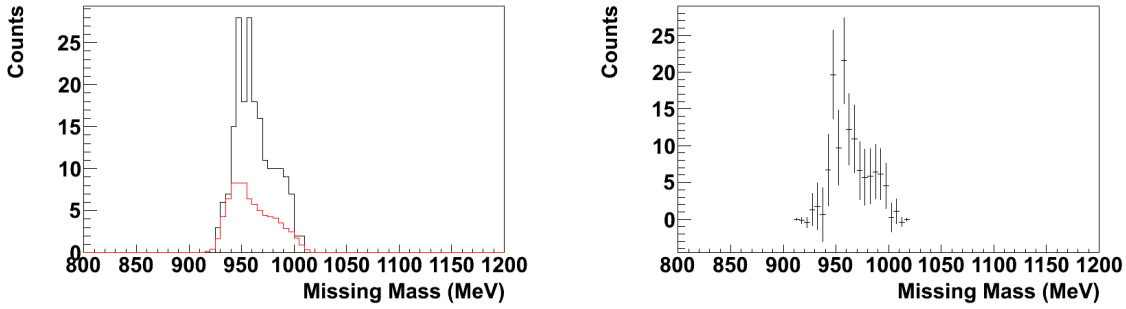

(a) Prompt (black) and random (red) (b) Subtracted

Figure 4.55: TAPS ring analysis with the negative transversely polarized butanol target. Shown are the prompt, random, and subtracted missing mass distributions.

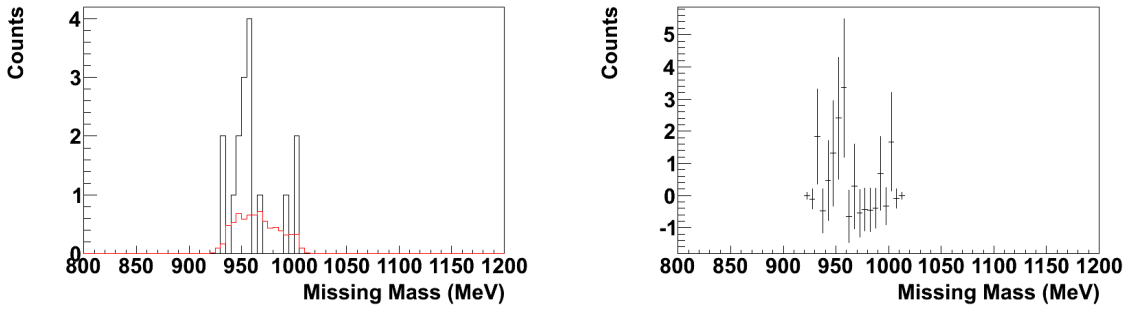

(a) Prompt (black) and random (red) (b) Subtracted

Figure 4.56: TAPS ring analysis with the carbon target. Shown are the prompt, random, and subtracted missing mass distributions.

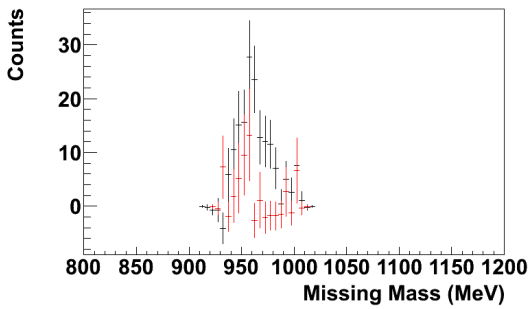

(a) Positive (black) and carbon (red)

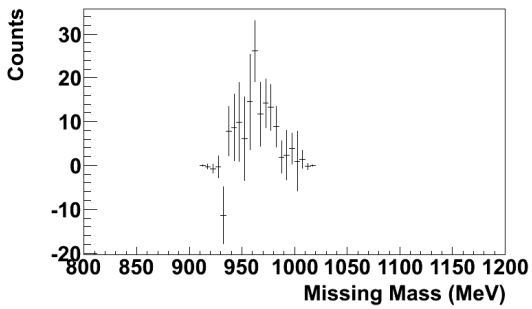

(b) Subtracted

Figure 4.57: TAPS ring analysis with both the positive transversely polarized butanol target and the carbon target. Shown are the two together (after scaling the carbon) and their subtraction.

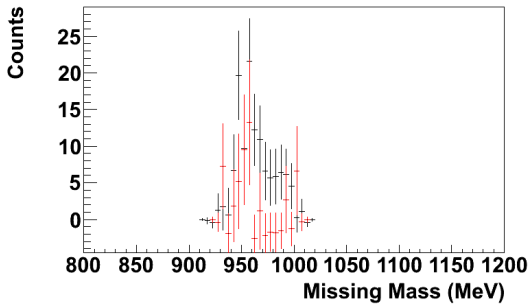

(a) Negative (black) and carbon (red)

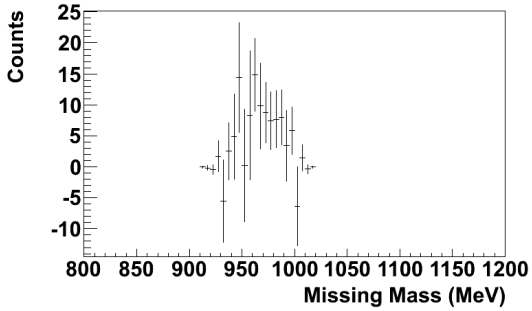

(b) Subtracted

Figure 4.58: TAPS ring analysis with both the negative transversely polarized butanol target and the carbon target. Shown are the two together (after scaling the carbon) and their subtraction.

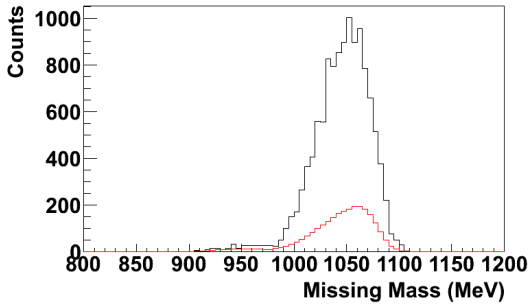

(a) Prompt (black) and random (red)

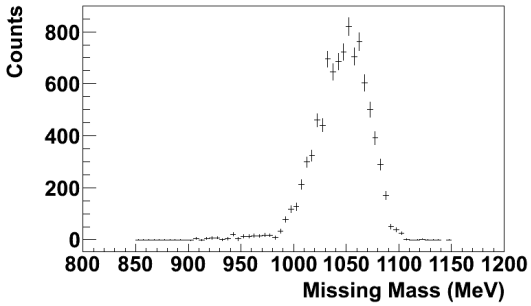

(b) Subtracted

Figure 4.59: CB ring analysis with the positive transversely polarized butanol target. Shown are the prompt, random, and subtracted missing mass distributions.

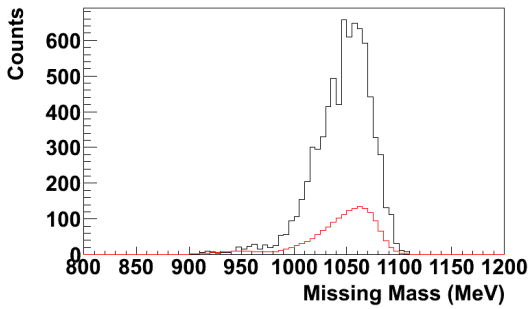

(a) Prompt (black) and random (red)

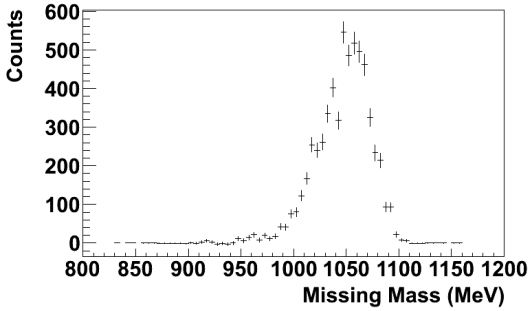

(b) Subtracted

Figure 4.60: CB ring analysis with the negative transversely polarized butanol target. Shown are the prompt, random, and subtracted missing mass distributions.

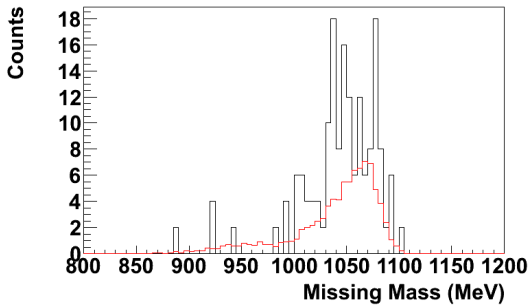

(a) Prompt (black) and random (red)

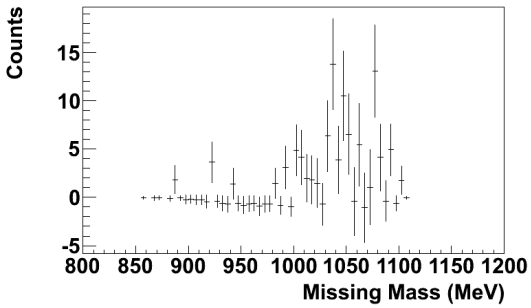

(b) Subtracted

Figure 4.61: CB ring analysis with the carbon target. Shown are the prompt, random, and subtracted missing mass distributions.

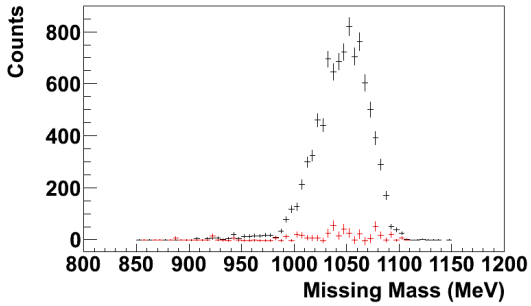

(a) Positive (black) and carbon (red)

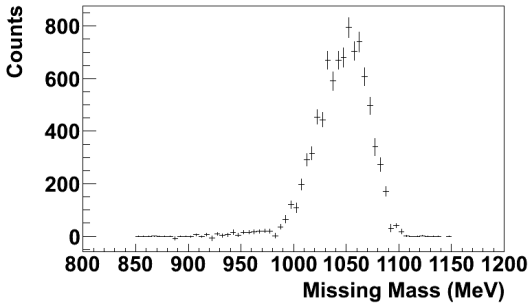

(b) Subtracted

Figure 4.62: CB ring analysis with both the positive transversely polarized butanol target and the carbon target. Shown are the two together (after scaling the carbon) and their subtraction.

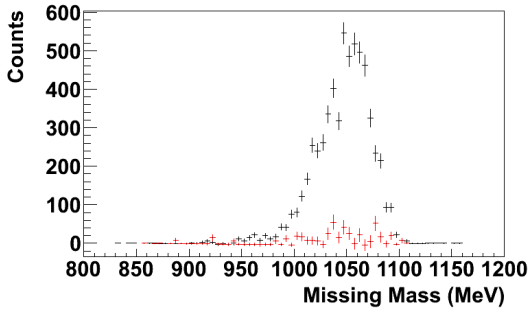

(a) Negative (black) and carbon (red)

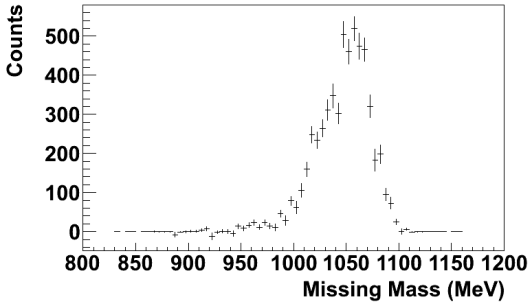

(b) Subtracted

Figure 4.63: CB ring analysis with both the negative transversely polarized butanol target and the carbon target. Shown are the two together (after scaling the carbon) and their subtraction.

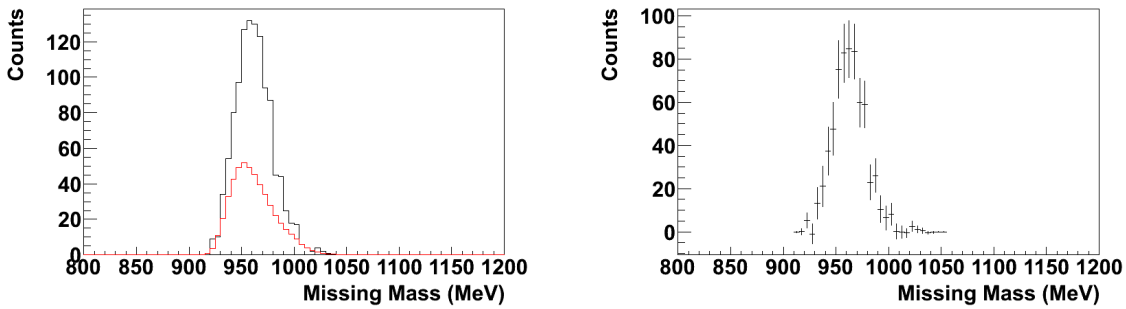

(a) Prompt (black) and random (red) (b) Subtracted

Figure 4.64: CB/TAPS ring analysis with the positive transversely polarized butanol target. Shown are the prompt, random, and subtracted missing mass distributions.

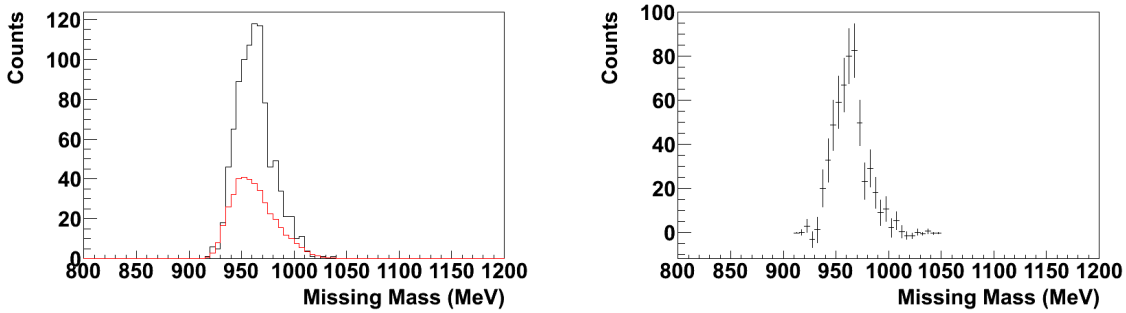

(a) Prompt (black) and random (red) (b) Subtracted

Figure 4.65: CB/TAPS ring analysis with the negative transversely polarized butanol target. Shown are the prompt, random, and subtracted missing mass distributions.

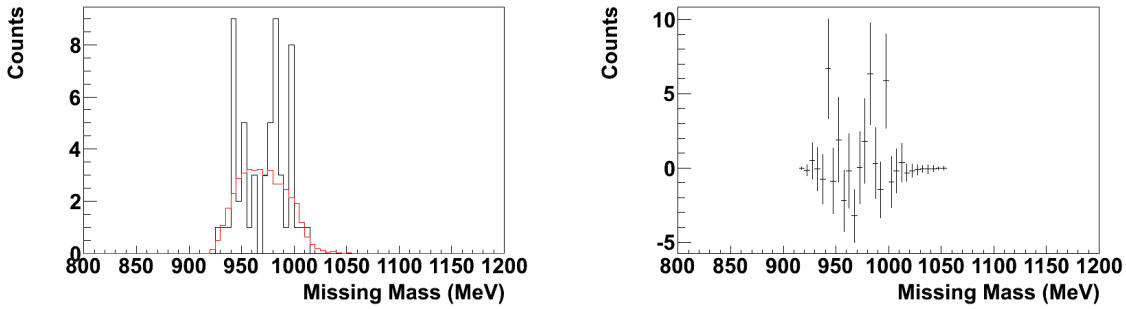

(a) Prompt (black) and random (red) (b) Subtracted

Figure 4.66: CB/TAPS ring analysis with the carbon target. Shown are the prompt, random, and subtracted missing mass distributions.

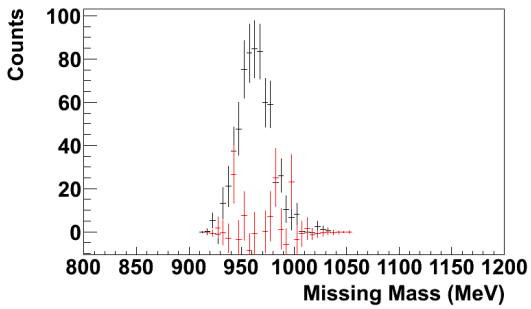

(a) Positive (black) and carbon (red)

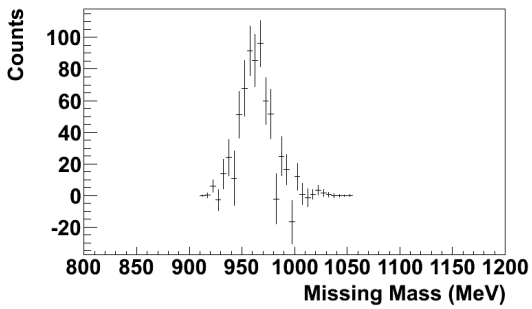

(b) Subtracted

Figure 4.67: CB/TAPS ring analysis with both the positive transversely polarized butanol target and the carbon target. Shown are the two together (after scaling the carbon) and their subtraction.

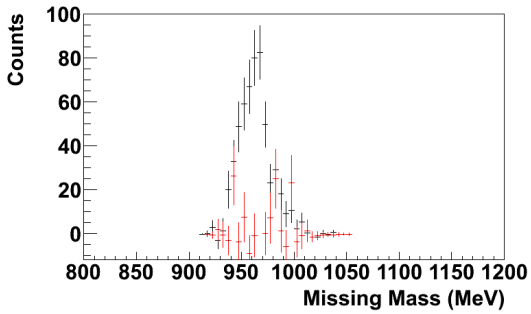

(a) Negative (black) and carbon (red)

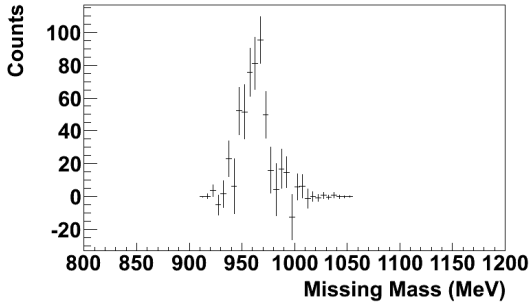

(b) Subtracted

Figure 4.68: CB/TAPS ring analysis with both the negative transversely polarized butanol target and the carbon target. Shown are the two together (after scaling the carbon) and their subtraction.

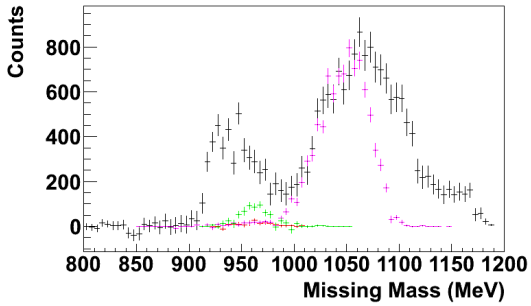

(a) Compton (black), TAPS ring (red), CB ring (magenta), and CB/TAPS ring (green)

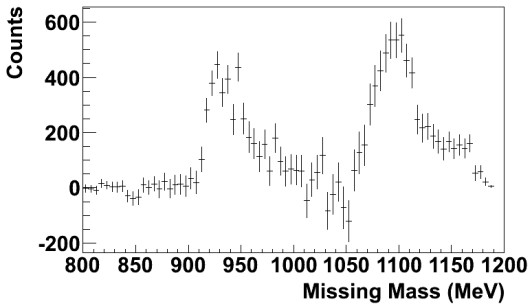

(b) Subtracted

Figure 4.69: Compton scattering minus ring analysis for the positive transversely polarized butanol target

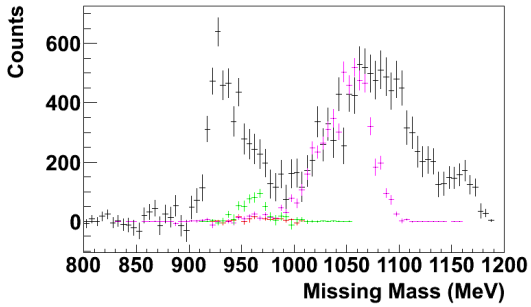

(a) Compton (black), TAPS ring (red), CB ring (magenta), and CB/TAPS ring (green)

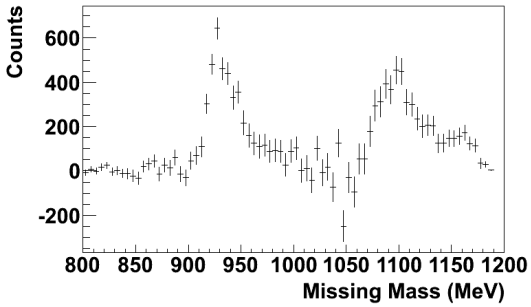

(b) Subtracted

Figure 4.70: Compton scattering minus ring analysis for the negative transversely polarized butanol target

CHAPTER 5

SIMULATION

In order to understand, and possibly account for, the additional background in the missing mass spectra a more detailed simulation study is necessary. The previous Monte Carlo studies simply utilized an event generator EventGen, written by the author, that uses theoretical cross sections to weight the throwing of events, and for Compton scattering cross sections it utilizes the dispersion code of Barbara Pasquini. For π^0 photoproduction cross sections it utilizes either the MAID[70][71][72] or SAID[73] database. While useful for a first pass analysis, EventGen does not take into account interactions between the particles and the experimental setup resulting in energy loss and/or multiple scattering in the Frozen Spin Target cryostat, as well as the electromagnetic showers and energy smearing in the detectors themselves.

To study these effects the output from EventGen is passed into a Geant4[74][75][76] simulation of the entire A2 system[77]. The A2 simulation outputs a TTree that is read into AcquRoot which decodes and interprets it as real data. While Geant4 handles energy loss, multiple scattering, and electromagnetic showers, the energy smearing needs to be applied on the AcquRoot side as this is a by product of both the response of the detector material and the conversion of the signal in the electronics. For the NaI and BaF_2 the energy resolution is provided by the energy (in GeV) dependent functions in Equation 5.1 and Equation 5.2 respectively.

$$\Delta E_{\mathrm{CB}} = 0.0204\,\mathrm{GeV} \times (E/\mathrm{GeV})^{3/5} \tag{5.1}$$

$$\Delta E_{\mathrm{TAPS}} = 0.015\,\mathrm{GeV} \times (E/\mathrm{GeV})^{1/2} \tag{5.2}$$

5.1 Compton Scattering

The first simulation of interest is simple Compton scattering itself. By running the full simulation on Compton scattering the expected missing mass spectra can be generated and compared with the experimental version. It's vital to know whether the peak structure seen in the data is of a reasonable shape and width, to help justify the integration limits used in determining the total number of events. This also helps determine to what degree the tail of the peak is composed of background events. The missing mass distribution from the simulation, for the 273-303 MeV tagged photon energy bin, is shown in Figure 5.1, along with two different line shapes. A simple

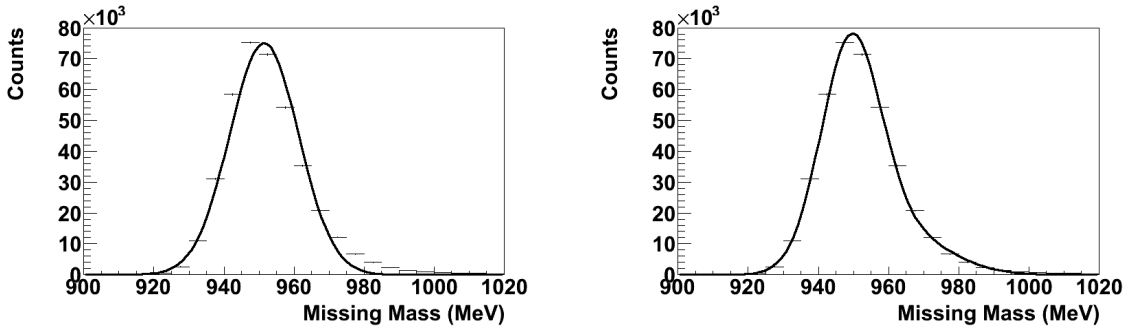

(a) Gaussian (b) Double Gaussian

Figure 5.1: A2 simulation of Compton scattering, showing accompanying Gaussian and double Gaussian fits

Gaussian shape, as given in Equation 5.3 (where h is the height, c is the centroid, and w is the width of the peak), clearly doesn't fit the Compton peak in Figure 5.1a due to the tail on the higher missing mass side.

$$y = he^{-\frac{1}{2}\left(\frac{x-c}{w}\right)^2} \tag{5.3}$$

This can be better fit with a combination of two Gaussians, as shown in Figure 5.1b. Rather than having two floating Gaussians however, it's beneficial to connect the two together with

$$y = h\left[e^{-\frac{1}{2}\left(\frac{x-c}{wb}\right)^2} + h'e^{-\frac{1}{2}\left(\frac{x-c-c'b}{ww'b}\right)^2}\right] \tag{5.4}$$

where h' is the relative height, c' is the relative centroid offset, and w' is the relative width of the second Gaussian with respect to the first. The b represents a broadening factor, set to unity for this fitting, for adjustment of the width of the entire function to match real data. This allows h', c', w, and w' to be fixed by the simulation. Additionally, if the simulation width is to be trusted as accurate, b can also be fixed at unity. The parameter values are given in Table 5.1, and with a similar analysis for the 315-346 MeV tagged photon energy bin in Table 5.2.

5.2 Pion Photoproduction

Before using the Compton line shape on the real data, it's helpful to have some knowledge about the broadening factor b. This is done by performing a similar analysis on simulated π^0 photoproduction. Using the MAID database for cross section weighting, a set of π^0 events is produced with EventGen, run through the A2 simulation, and then analyzed with AcquRoot. Constructing, and then fitting, the simulated π^0 missing mass, for the 273-303 MeV tagged photon energy bin, gives the results in Figure 5.2. For a better comparison to Compton kinematics, it's useful to constrain this with the actual mass of the π^0. While the cut on the calculated value for $m_{\gamma\gamma}$ ensures that this value is within the proper range, it can be further constrained by following through the process

$$q + m_p = k_1 + k_2 + p \tag{5.5}$$

$$(q + m_p) - (k_1 + k_2) = p \tag{5.6}$$

$$(q + m_p)^2 - (k_1 + k_2)^2 = p^2 \tag{5.7}$$

$$(q + m_p)^2 - 2(q + m_p) \cdot (k_1 + k_2) + m_{\pi^0}^2 = m_{\text{miss}}^2 \tag{5.8}$$

where q, k_1, k_2, and p, are the four momenta of the incident photon, the two π^0 decay photons, and the recoil proton, respectively. As with the Compton shape,

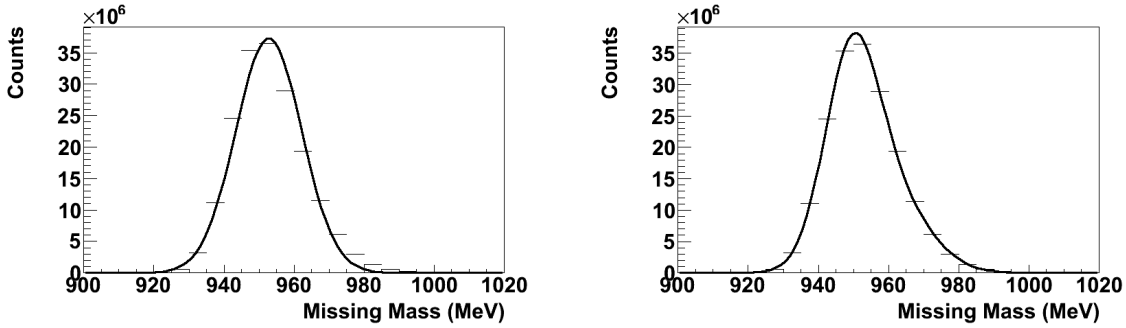

(a) Gaussian (b) Double Gaussian

Figure 5.2: A2 simulation of pion photoproduction, showing accompanying Gaussian and double Gaussian fits

the missing mass is best fit by the double Gaussian function of Equation 5.4. The parameter values are also given in Table 5.1, and with a similar analysis for the 315-346 MeV tagged photon energy bin in Table 5.2.

	h	c	w	h'	c'	w'
Compton	71550	949.2	8.542	0.1706	14.95	1.538
Pion	3.13e7	949.4	7.736	0.3609	11.24	1.384

Table 5.1: Average parameters for Monte Carlo line shape (273-303 MeV)

	h	c	w	h'	c'	w'
Compton	87090	951.3	9.546	0.1513	16.64	1.540
Pion	2.26e7	951.9	8.754	0.3048	12.70	1.377

Table 5.2: Average parameters for Monte Carlo line shape (315-346 MeV)

While the parameters between the Compton and pion line shapes are noticeably different, an interesting test is to see if one can be used to fit the other, adjusting only h and b. This is shown in Figure 5.3. Fitting the Compton result using the pion parameters requires a broadening parameter of $b = 1.079$, and fitting the pion result

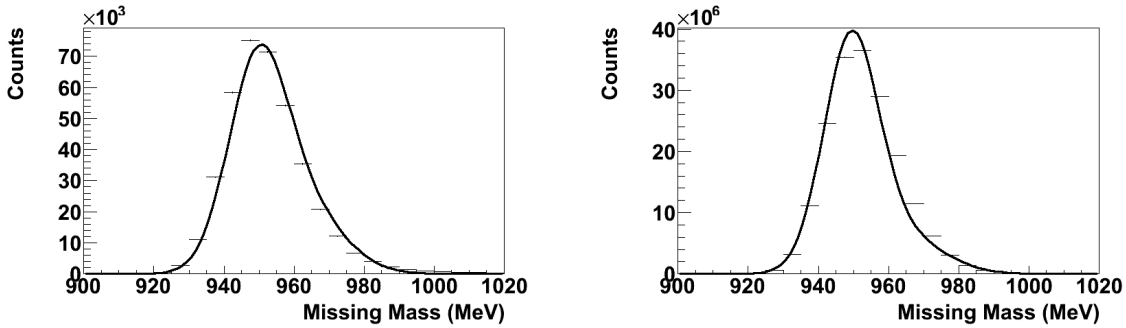

(a) Compton fit with pion parameters

(b) Pion fit with Compton parameters

Figure 5.3: A2 simulation of Compton scattering and pion photoproduction, fitting each with the parameters from the opposite case. This is done by fixing the fit parameters, except for the height, from the opposite case and allowing the broadening parameter to float.

with the Compton parameters requires a broadening parameter of $b = 0.9085$. Very close inspection reveals that these constrained fits are not as good as the individually determined ones, but the broadening parameter does perform a decent job in matching them.

5.2.1 Fitting to Data

Another check is to take the pion function and fit it to the π^0 missing mass spectra from actual data, again utilizing the m_{π^0} constraint given in Equation 5.8, fitting with either a fixed (at unity) or floating broadening factor. The results of these fits are shown in Figure 5.4. The clear need for a non-unity broadening factor indicates that the simulation is somehow not fully describing the experimental energy resolutions. For the best fit, the broadening factor arrived at is $b = 1.392$ (or for the 315-346 MeV bin it is $b = 1.377$). It's important to note that a step has been skipped here, as the data these curves are fit to are after the carbon subtraction. As mentioned in section 4.4, an additional scaling factor had to be applied to the carbon data (in addition to the scaling factor determined from ratios of live time corrected tagger scalers). This scaling factor is also derived from the use of the Monte Carlo line

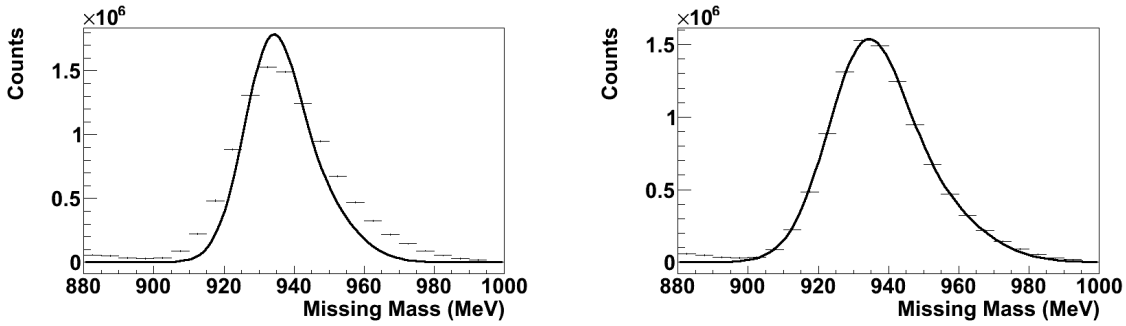

(a) Height and centroid

(b) Height, centroid, and broadening

Figure 5.4: Pion photoproduction data with fit from simulation, adjusting either height and centroid or height, centroid, and line shape broadening factor b

shape, by fitting it to spectra (after a carbon subtraction scaled by various values) and observing where the value of χ^2 is minimized for the fit.

Assuming that perhaps the discrepancy between the Monte Carlo line shape and the data in Figure 5.4 is due to a poor choice of carbon scaling, this process of iterating over various carbon scaling factors can be performed with the line shape broadening factor $b = 1$. Results of this are shown in Figure 5.5. While it's possible to choose a carbon scaling factor such that the resulting missing mass matches the simulated line shape, it leads to an overshoot in the subtraction, resulting in negative counts. For this reason the line shape was deemed to be lacking the proper energy resolution. To account for this the process is repeated allowing the line shape broadening factor, b, to vary as well, producing Figure 5.6. While the fit at a carbon scaling factor of 1 is still deficient, the fit at a carbon scaling factor of 1.306 (where the value of χ^2 is minimized) is sufficient and doesn't lead to an undershoot in the subtraction. Repeating the process for the 315-346 MeV data has a similar result, with a carbon scaling factor of 1.234. The simulated line shape broadening factors, as noted in the beginning of this section, are also determined from the fits when χ^2 is minimized. For reference these broadening factors are provided in Table 5.3.

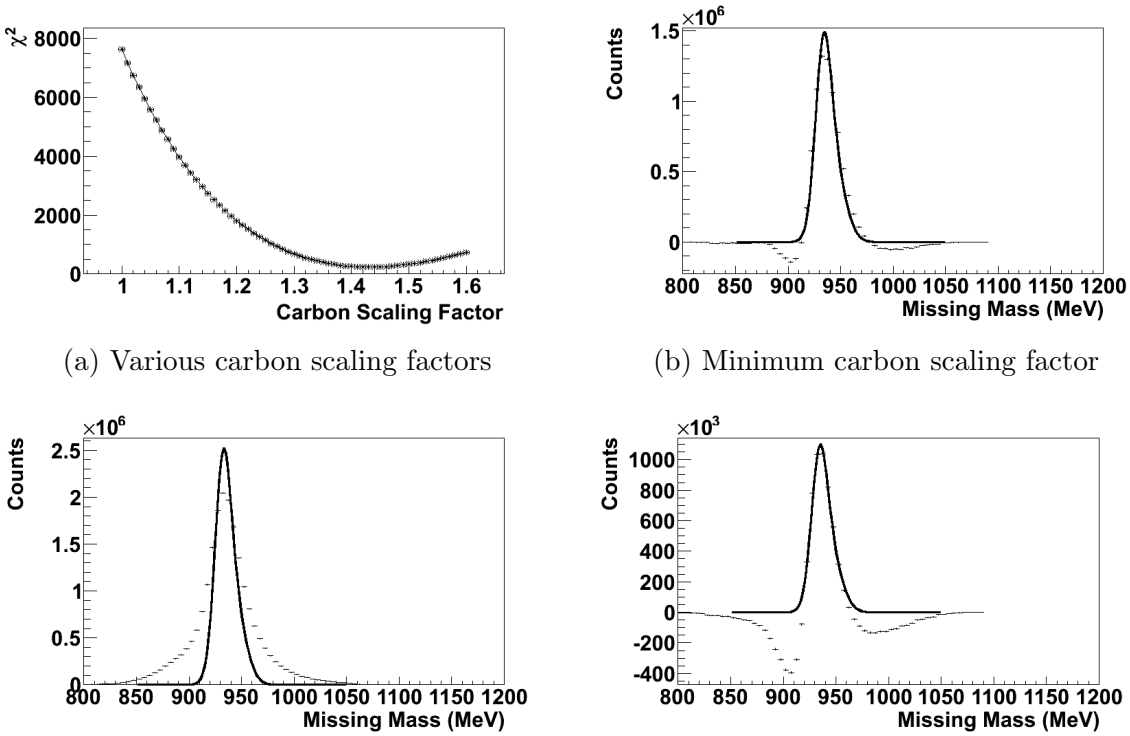

(a) Various carbon scaling factors

(b) Minimum carbon scaling factor

(c) Carbon scaling factor of 1.0

(d) Carbon scaling factor of 1.6

Figure 5.5: Pion photoproduction data with fit from simulation, adjusting only height and centroid, for various carbon scaling factors

Energy	Carbon	Line Shape
273-303	1.306	1.392
315-346	1.234	1.377

Table 5.3: Carbon scaling and line shape broadening factors

5.2.2 Background Subtraction

As discussed in subsection 4.5.4, the full simulation of π^0 photoproduction also allows the ring analysis method to be checked. Firstly, those events that appear to be Compton events, for any of the various reasons stated before, are analyzed as such and produce missing mass spectra as given in Figure 5.7a. Running these simulated events through the same ring analysis as for real data gives an indication of the efficiency with which the ring analysis removes the background in the Compton

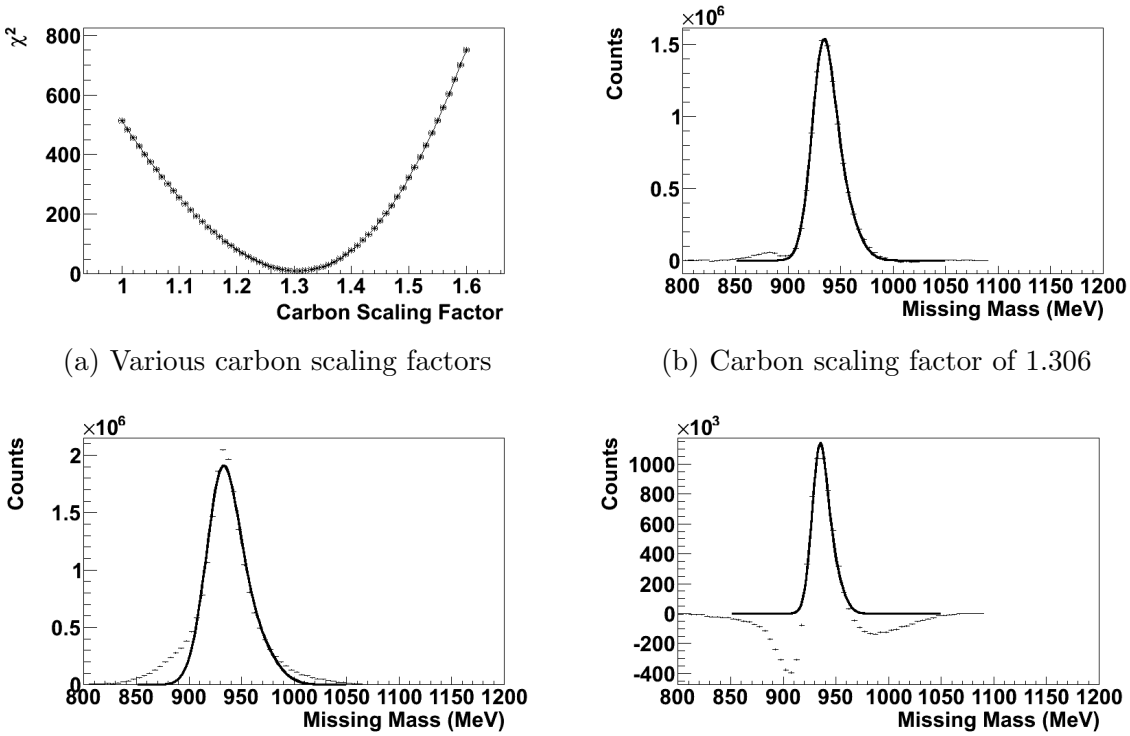

(a) Various carbon scaling factors

(b) Carbon scaling factor of 1.306

(c) Carbon scaling factor of 1.0

(d) Carbon scaling factor of 1.6

Figure 5.6: Pion photoproduction data with fit from simulation, adjusting height, centroid and line shape broadening factor b, for various carbon scaling factors

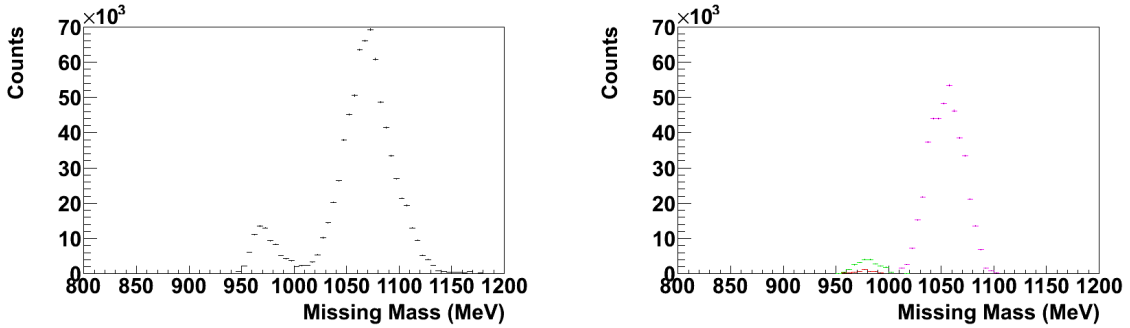

(a) Compton

(b) Ring

Figure 5.7: A2 simulation of pion photoproduction, analyzed as Compton or through the ring analysis

spectra, as shown in Figure 5.7b. While the ring analysis does account for some of this background, it's also clearly missing some of it, especially at higher missing mass.

Another possible method of background subtraction is to instead take the distribution predicted by the simulation for π^0 photoproduction that appears as Compton scattering (as shown in Figure 5.7a), and apply it to the actual data instead of using the ring analysis. The series of steps is shown in Figure 5.8.

- Figure 5.8a - The result from the simulation is roughly scaled to match its height with the Compton background at around 1070 MeV. Here the assumption is that this background is completely due to misidentified π^0 events, but that it suffers from the same broadening as that shown for observed π^0 events in Figure 5.4.

- Figure 5.8b - The simulation shapes are fit by a combination of the same double Gaussian given by Equation 5.4 for the lower missing mass peak, and a simple Gaussian for the higher missing mass peak.

- Figure 5.8c - Holding the centroid of the higher missing mass Gaussian fit fixed, it's refit to the primary background peak from the actual data. The ratio of the final to initial height of this Gaussian is then multiplied to the height of the initial lower missing mass double Gaussian fit. Likewise, the ratio of the final to initial width of the higher missing mass Gaussian is used as the broadening factor of the initial lower missing mass double Gaussian fit.

- Figure 5.8d - The two functions are then summed together to provide a background shape that can be used to subtract off the background.

While this method appears successful in this instance, there are various assumptions that would be of concern if using it in general, namely that:

- The background is entirely from π^0 background that's taken into account with the simulation.

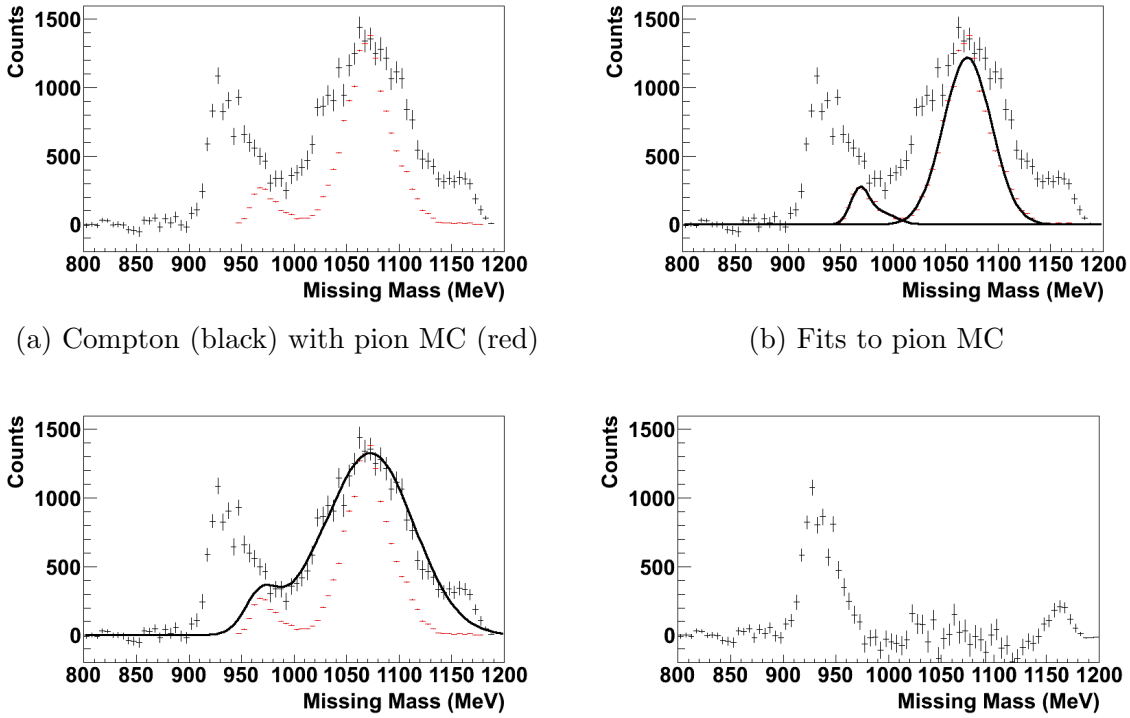

(a) Compton (black) with pion MC (red)

(b) Fits to pion MC

(c) Fit scaled to Compton

(d) Compton with fit subtracted

Figure 5.8: A2 simulation of pion photoproduction, fitted to background in Compton scattering spectra

- The shapes of the simulated background are properly described by these Gaussian and double Gaussian functions.
- The actual background will only differ from the simulation by its width, and therefore holding the centroids of the fits to the simulation and broadening their width and heights as described is an appropriate response.

Because of these concerns, the justification for this method of background subtraction becomes tenuous, and is therefore not used at the present time.

5.3 Proton Energy Corrections

5.3.1 Proton Energy Loss

The A2 simulation also provides a way to investigate the energy loss of the recoil proton. Traveling from the event center to a detector requires passing through target material, the ^{3}He/^{4}He bath, the cryostat shells, the transverse holding coil, air, and then various detectors as well as their structural shells. This causes a massive particle, such as a proton, to undergo interactions with various types of material, losing energy along the way. With a detailed Geant4 simulation, such as exists for the A2 setup, these interactions can be reproduced for protons of various energies.

To study these effects the method employed by J. Robinson[64] was repeated, by the author, with the Frozen Spin Target. The simulation was run with a beam of protons of various energies sent isotropically over all angles. This must be done at all angles since the material traversed by the proton is not uniform over theta, or over phi. The simulation follows the path of the proton, allowing it to interact with the traversed material at accepted probabilities. For each proton the detected energy, E_k^d (determined through analysis in AcquRoot), is compared to the actual energy, E_k^a, demonstrating a sample energy loss for protons of that energy traveling in that direction.

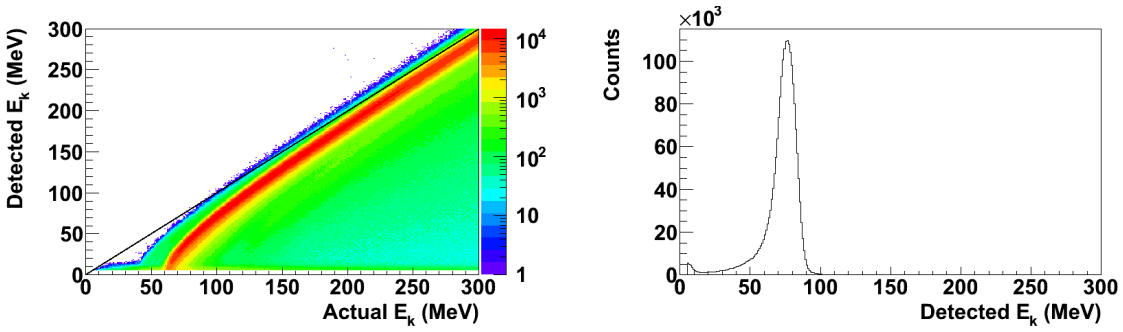

(a) Detected vs Actual

(b) Detected for 100-110 MeV

Figure 5.9: A2 simulation of protons, looking at the detected energy as a function of the actual energy

As evidenced in Figure 5.9, the simulation projects that a 300 MeV proton will on average lose about 20 MeV, while a 65 MeV proton will on average be completely stopped. Plotting the difference between the actual and detected energies further illustrates this effect, as shown in Figure 5.10.

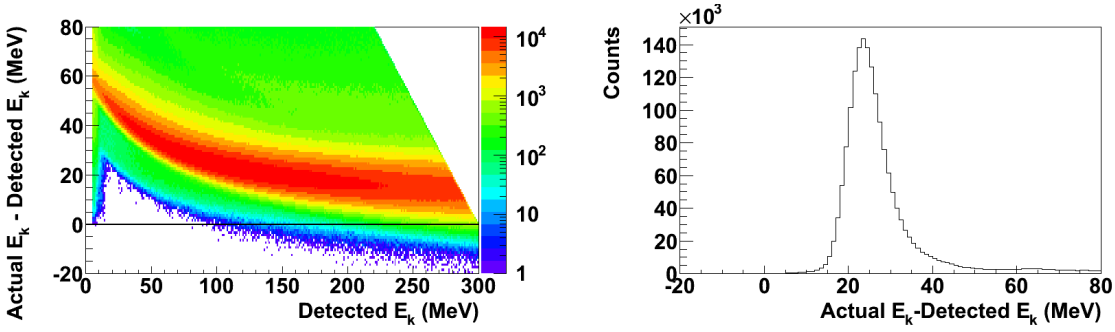

(a) Difference vs Detected

(b) Difference for 100-110 MeV

Figure 5.10: A2 simulation of protons, looking at the difference in energy as a function of the detected energy

This difference is used to determine the actual energy from the detected energy using Equation 5.9,

$$E_k^a = E_k^d + L(E_k^d, C) \tag{5.9}$$

where $L(E_k^d, C)$ is the average energy loss experienced for a proton detected in crystal C with energy E_k^d. To determine the functional form of L, projections onto the difference (y) axis for various slices of the detected kinetic energy, as shown in Figure 5.10b, are fitted with Gaussians. The mean values of each Gaussian fit are then plotted as a function of the detected kinetic energy, and then fit with the form given in Equation 5.10.

$$L(E_k^d, C) = l_1(C) + \frac{l_2(C)}{E_k^d - l_3(C)} \tag{5.10}$$

It is also useful, as will be discussed in subsection 5.3.2, to have the inverse relation determining the detected energy from the actual energy. This is done in the same

manner, by plotting the difference as a function of the actual energy, as shown in Figure 5.11.

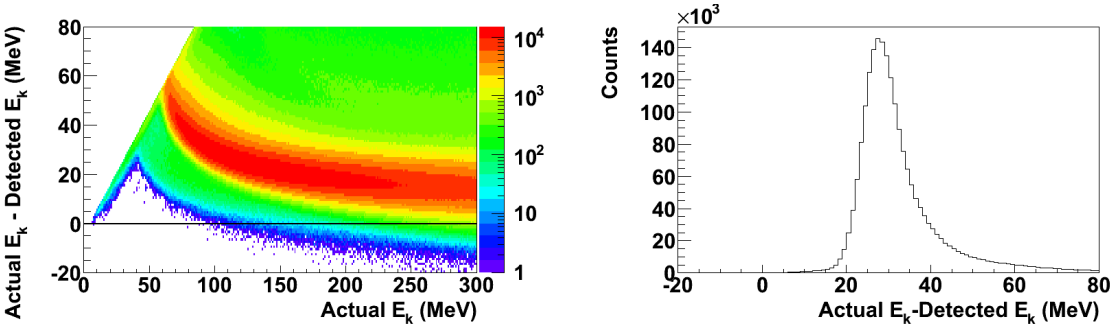

(a) Difference vs Actual

(b) Difference for 100-110 MeV

Figure 5.11: A2 simulation of protons, looking at the difference in energy as a function of the actual energy

The equation for going from actual to detected energy is given by Equation 5.11

$$E_k^d = E_k^a - L'(E_k^a, C) \tag{5.11}$$

where $L'(E_k^a, C)$ is the average energy loss experienced for a proton detected in crystal C with actual energy E_k^a, whose functional form (given in Equation 5.12) is the same as L.

$$L'(E_k^a, C) = l_1'(C) + \frac{l_2'(C)}{E_k^a - l_3'(C)} \tag{5.12}$$

	l_1	l_2	l_3	l_1'	l_2'	l_3'
CB	4.58	3240	-46.9	7.93	1820	26.6
TAPS	5.39	3500	-52.9	10.3	1830	26.8

Table 5.4: Average parameters for proton energy loss calculation

Plotting L and L', on Figure 5.10a and Figure 5.11a, gives Figure 5.12a and Figure 5.12b, respectively. Applying this correction factor to the detected proton

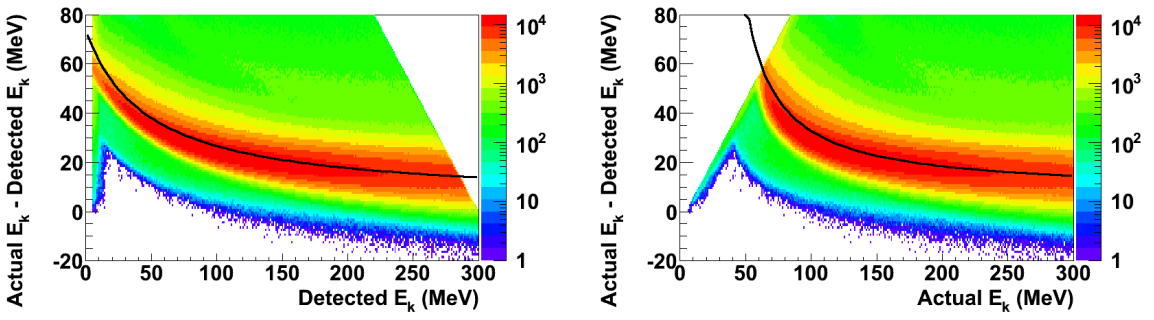

(a) Detected (b) Actual

Figure 5.12: A2 simulation of protons, looking at the fits to the difference in energy as a function of the detected or actual energy

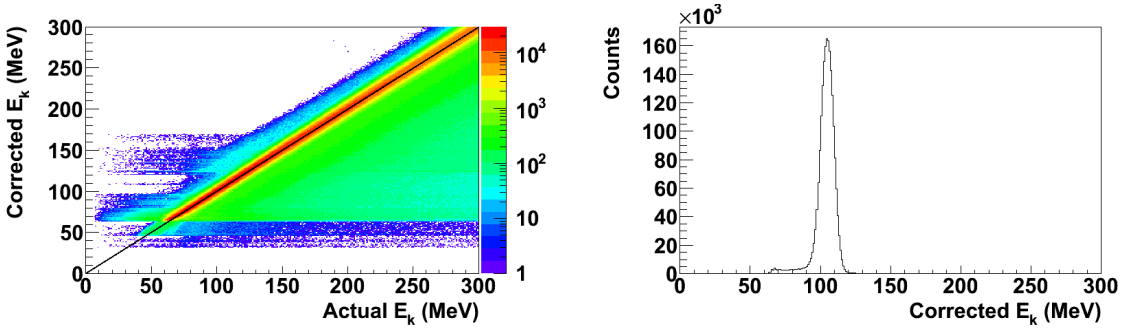

(a) Detected vs Actual (b) Detected for 100-110 MeV

Figure 5.13: A2 simulation of protons, looking at the corrected energy as a function of the actual energy

energy in AcquRoot and producing the same plots as Figure 5.9a and Figure 5.11a, with the corrected energy, results in Figure 5.13a and Figure 5.14a, respectively.

It should be noted that the plots shown previously are the combined results from all crystals. By throwing 75 million protons with energies of 0-300 MeV each NaI element has about 350 events/MeV. However, the analysis is performed in 5 MeV wide bins so that each element has about 1750 events/5 MeV. Since TAPS subtends a smaller solid angle, each element only has about 20 events/MeV, or 100 events/5 MeV. Given its symmetry about phi, however, elements can be grouped together into similar theta 'rings', providing between 3600 events/5 MeV and 6000 events/5 MeV.

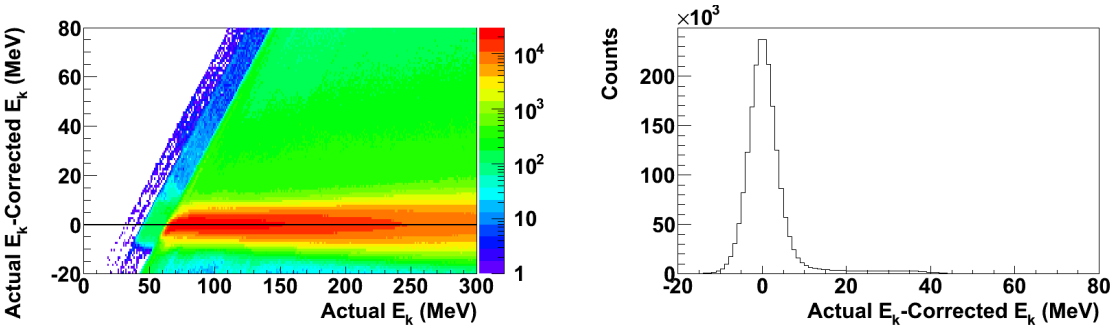

(a) Difference vs Actual (b) Difference for 100-110 MeV

Figure 5.14: A2 simulation of protons, looking at the corrected difference in energy as a function of the actual energy

To check the validity of this process on an individual basis, the results are looked at for a relevant region in both the CB and TAPS. For the CB crystal 674 is chosen, as this subtends approximately 30-40° in theta, and 85-95° in phi. For the 273-303 MeV tagged photon energy bin this theta range corresponds to 58-88 MeV in proton energy. These results are shown in Figure 5.15 and Figure 5.16.

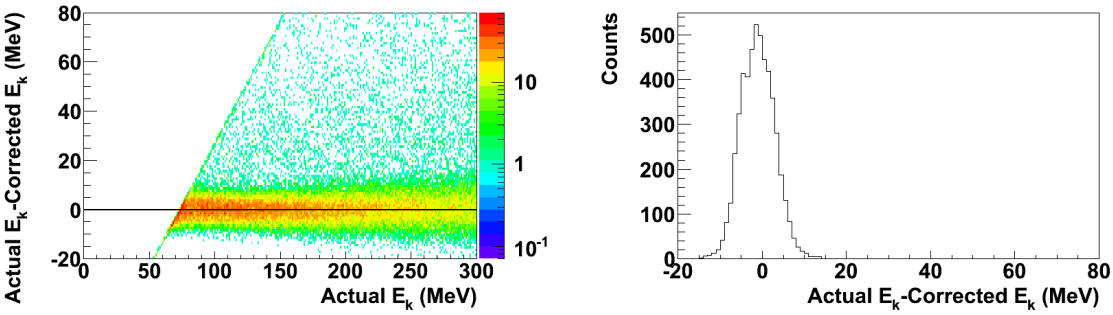

(a) Difference vs Actual (b) Difference for 58-88 MeV

Figure 5.15: A2 simulation of protons detected in the CB (crystal 674), looking at the corrected difference in energy as a function of the actual energy

For TAPS, the 9th ring from the center (which as shown in Figure 2.22 corresponds to crystals 45-53, 118-126, 191-199, 264-272, 337-345, and 410-418) subtends 15-

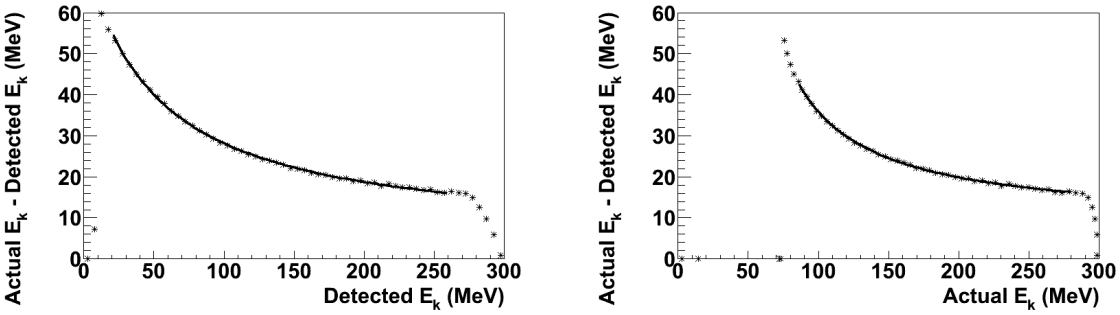

(a) Detected (b) Actual

Figure 5.16: A2 simulation of protons detected in the CB (crystal 674), looking at the fits to the difference in energy as a function of the detected or actual energy

16.7° in theta, covering proton energies of 92-110 MeV. These results are shown in Figure 5.17 and Figure 5.18.

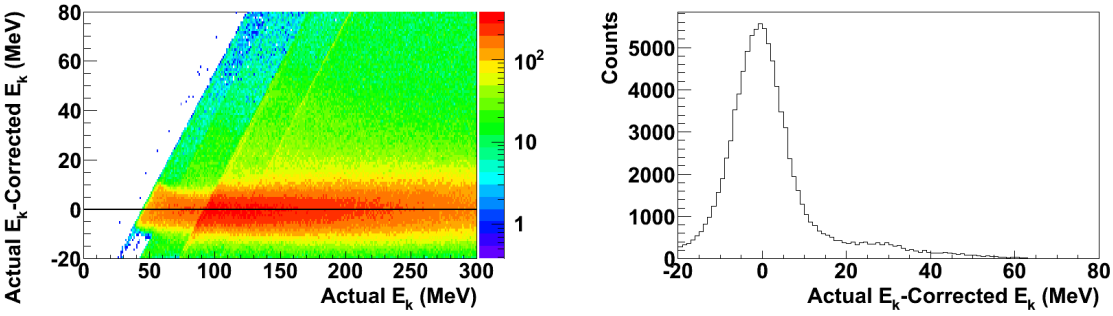

(a) Difference vs Actual (b) Difference for 92-110 MeV

Figure 5.17: A2 simulation of protons detected in TAPS (ring nine), looking at the corrected difference in energy as a function of the actual energy

For these individual choices (CB crystal 674, and TAPS ring 9), the parameters are given in Table 5.5.

	l_1	l_2	l_3	l'_1	l'_2	l'_3
CB	4.66	3510	-49.5	8.65	1900	30.2
TAPS	11.98	4900	-57.2	18.2	2330	49.1

Table 5.5: Selected crystal/ring parameters for proton energy loss calculation

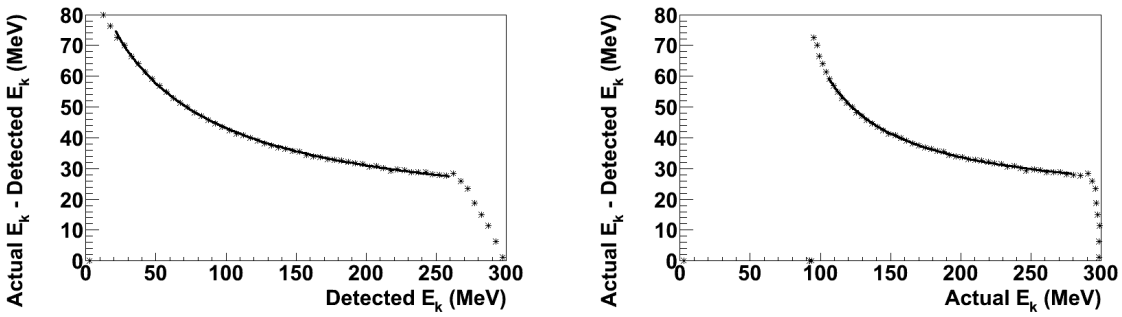

(a) Detected (b) Actual

Figure 5.18: A2 simulation of protons detected in TAPS (ring nine), looking at the fits to the difference in energy as a function of the detected or actual energy

This simulation also permits a check of the proton deflection, and the validity of the opening angle cut used in the primary analysis. Plotting the angle between the 'detected' and initial proton vectors gives Figure 5.19a. From this it's clear that a 10° opening angle cut on the proton direction is reasonable.

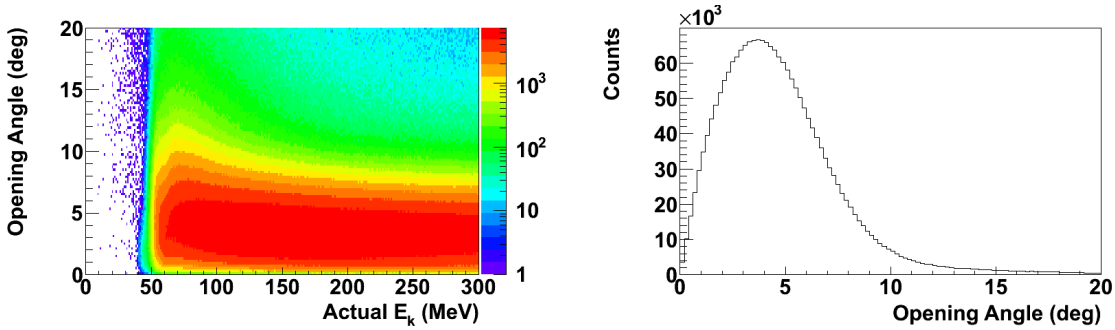

(a) Opening angle vs Actual (b) Opening angle for 100-110 MeV

Figure 5.19: A2 simulation of protons, looking at the proton opening angle as a function of the actual energy

5.3.2 Proton Response

In addition to the energy losses suffered by the proton in getting to a detector, another effect causes a discrepancy in the measurement of its energy. The NaI and BaF_2 crystals are both calibrated for photon detection, and proton deposition results

in a response different to that of photons. This can be observed by looking at actual π^0 photoproduction data, as described in the previous chapter. If the analysis is adjusted to also require the detection of the recoil proton, the kinetic energy from the missing mass four-vector can be compared to the measured energy of the recoil proton. This proton will, of course, suffer the same energy loss as just described. To properly compare them the actual energy of the missing particle is converted to what should be the detected energy using Equation 5.11 (hence why it was important to construct it). This 'detected' energy E_k^d, the energy of the proton when it hits a detector crystal, can be related to the 'measured' energy E_k^m that the analysis returns via the crystal, photomultiplier tube, electronics, and software calibration.

$$E_k^d = E_k^m + A(E_k^m) \tag{5.13}$$

where $A(E_k^m)$ is the attenuation effect in the crystals. Since this effect should be identical for each crystal of the same type, it's only necessary to calculate it globally for the entire detector. However, since NaI and BaF_2 have intrinsically different characteristics, this function, as given in Equation 5.14, must be determined for each one separately.

$$A(E_k^m) = a_1 + \frac{a_2}{E_k^m - a_3} \tag{5.14}$$

This factor is determined in a similar way as the energy loss, by plotting the difference between the 'detected' and 'measured' energy as a function of the 'measured' energy, as shown in Figure 5.20a and Figure 5.21a for the CB and TAPS, respectively. Projections onto the difference (y) axis, for each bin of the 'measured' energy (x) axis, are fit with a Gaussian function, as shown in Figure 5.20b and Figure 5.21b for the CB and TAPS, respectively. The centroids of these Gaussian fits are plotted as a function of the 'measured' energy, as shown in Figure 5.22a and Figure 5.22b for the CB and TAPS, respectively, and then fit with the functional form of Equation 5.14. Results of these fits give the parameters listed in Table 5.6.

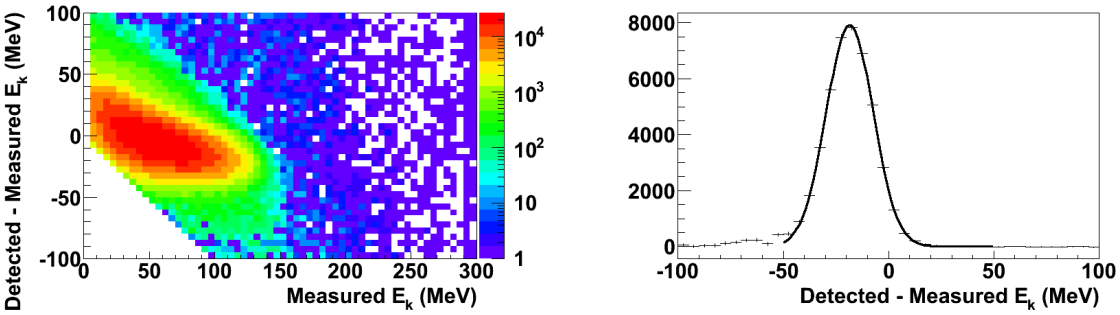

(a) Difference vs Measured (b) Difference for 105-110 MeV

Figure 5.20: Protons detected in the CB from pion photoproduction, looking at the difference in energy as a function of the measured energy

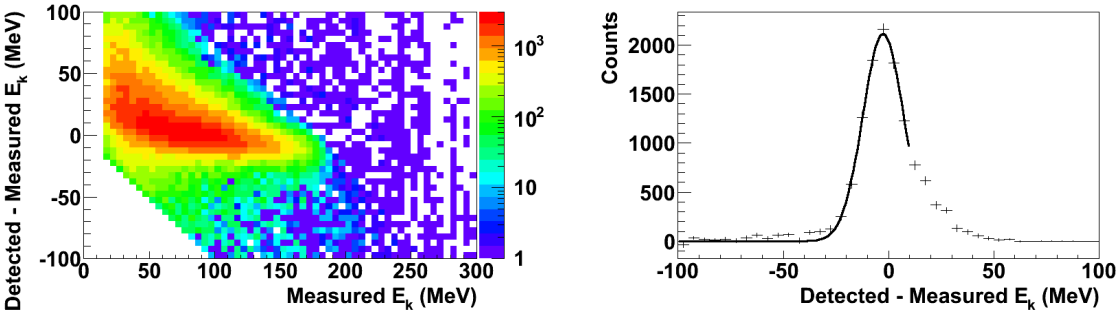

(a) Difference vs Measured (b) Difference for 105-110 MeV

Figure 5.21: Protons detected in TAPS from pion photoproduction, looking at the difference in energy as a function of the measured energy

	a_1	a_2	a_3
CB	-49.0	5400	-69.7
TAPS	-25.5	3270	-37.1

Table 5.6: Parameters for proton energy attenuation calculation

Both corrections can be applied in sequence to convert a measured energy from AcquRoot into an actual proton energy, using Equation 5.15.

$$E_k^a = E_k^m + A(E_k^m) + L(E_k^m + A(E_k^m), C) \tag{5.15}$$

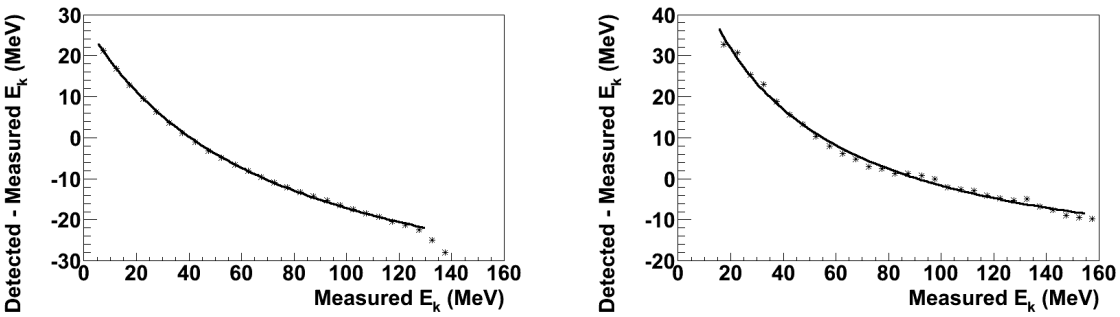

(a) CB (b) TAPS

Figure 5.22: Protons detected from pion photoproduction, looking at fits to the difference in energy as a function of the measured energy

5.3.3 Missing Energy

The real test of this energy correction is to fully apply it to actual data. The missing energy, given in Equation 5.16, can be calculated for the same π^0 photoproduction reactions as analyzed in the previous section.

$$E_{miss} = E_{\gamma_i} + m_p - E_{\pi^0} - E_p \tag{5.16}$$

Plotting the missing mass for this reaction as a function of the missing energy, calculated before applying the energy correction, produces the image in Figure 5.23. As shown the missing energy, which should be zero, is centered around 20 MeV. With the application of the energy correction, this is shifted into Figure 5.24. The peak is now clearly centered around zero, with a much smaller width.

For π^0 photoproduction in this energy range, such an analysis isn't exceptionally helpful however. While the missing energy peak is narrower, as expected there is clearly very little background to this reaction. In principle this could be very helpful for Compton scattering, where the missing energy would perhaps further distinguish the events of interest from background (π^0 photoproduction) events. For Compton

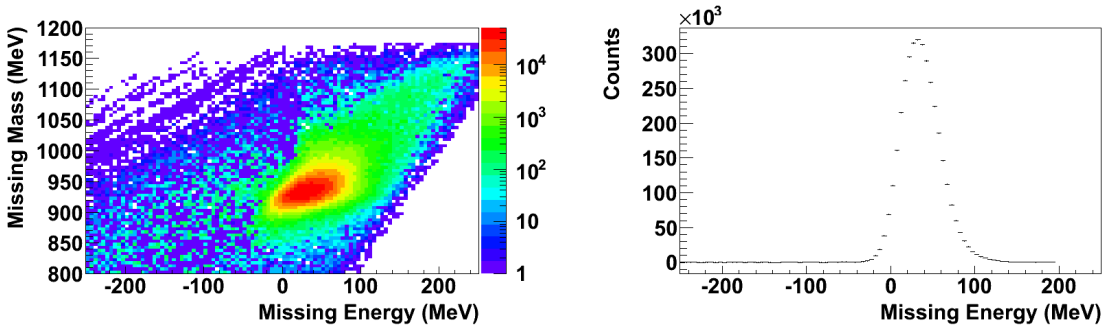

(a) Missing mass vs energy (b) Missing mass of 900-980 MeV

Figure 5.23: Pion photoproduction missing energy before applying the proton energy corrections. Shown are missing mass plotted against missing energy (left) and projection onto the missing energy axis for missing mass of 900-980 MeV (right).

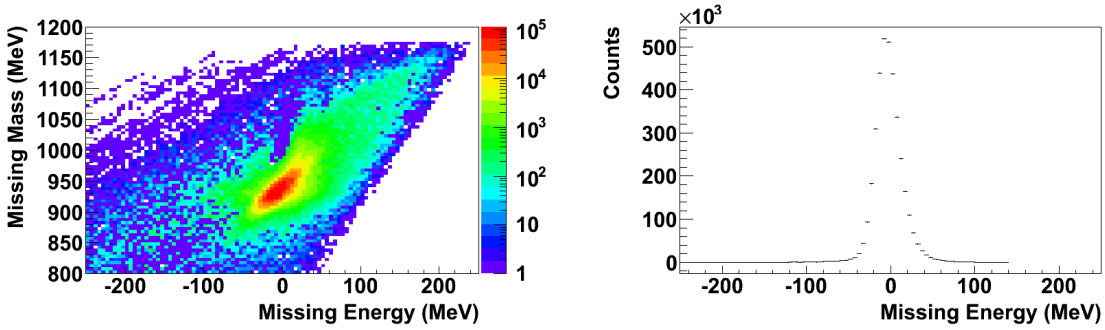

(a) Missing mass vs energy (b) Missing mass of 900-980 MeV

Figure 5.24: Pion photoproduction missing energy after applying the proton energy corrections. Shown are missing mass plotted against missing energy (left) and projection onto the missing energy axis for missing mass of 900-980 MeV (right).

scattering the missing energy, as given by Equation 5.17, can be similarly calculated and plotted.

$$E_{miss} = E_{\gamma_i} + m_p - E_{\gamma_f} - E_p \tag{5.17}$$

The uncorrected proton case results in missing energies shown in Figure 5.25. The situation is obviously similar, where the missing energy peak is shifted, now by about 50 MeV on average. The 'comet' like structure in the upper right is the same high missing mass structure shown earlier. Applying the proton energy corrections results

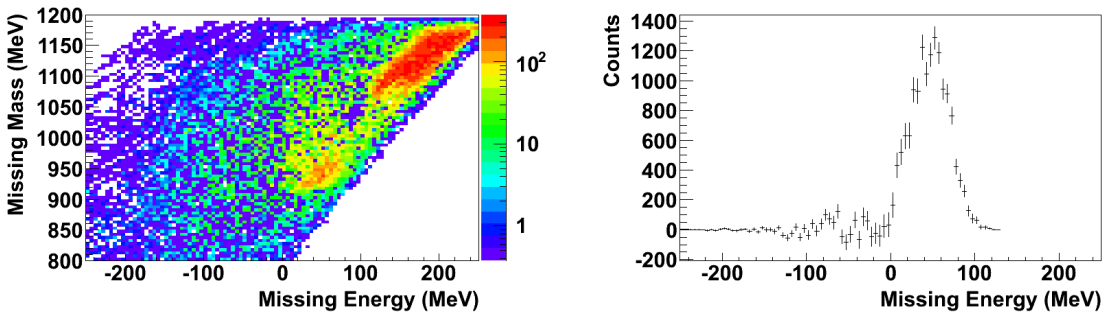

(a) Missing mass vs energy

(b) Missing mass of 900-980 MeV

Figure 5.25: Compton scattering missing energy before applying the proton energy corrections. Shown are missing mass plotted against missing energy (left) and projection onto the missing energy axis for missing mass of 900-980 MeV (right).

in Figure 5.26. The correction clearly tightens up these distributions, both for the

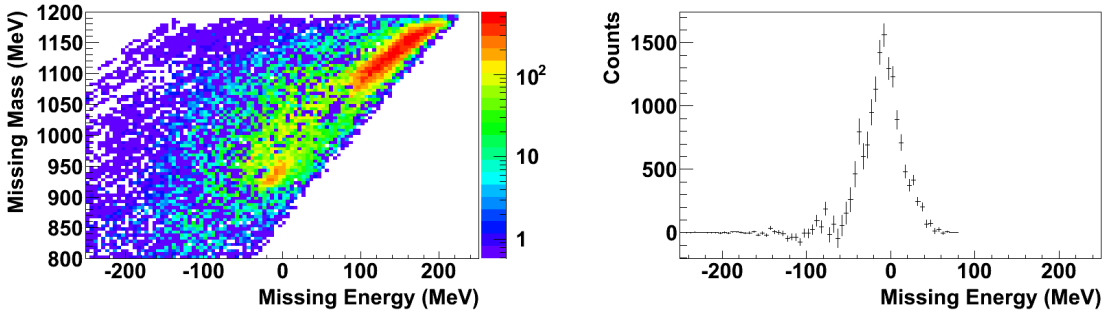

(a) Missing mass vs energy

(b) Missing mass of 900-980 MeV

Figure 5.26: Compton scattering missing energy after applying the proton energy corrections. Shown are missing mass plotted against missing energy (left) and projection onto the missing energy axis for missing mass of 900-980 MeV (right).

Compton 'island' located at 938 MeV in missing mass and 0 MeV in missing energy and the π^0 photoproduction background 'comet'. Unfortunately, since it doesn't improve the separation between these two structures, utilizing the missing energy in the event selection was dropped.

5.4 Proton Detection

The end result of the previous section is an energy correction for proton detection. However, an obvious problem with this concept is that such a correction can only be applied to a proton that is actually detected. It was noted that the likelihood of a proton making it to a crystal rapidly diminished below 65 MeV. To study the detection likelihood in quantitative detail, a similar combination of simulation and analysis of π^0 photoproduction data is used. Firstly, the simulation provides some direct insight into this. The same isotropic proton data used for the energy loss study is examined for a given initial proton energy, observing how often it results in energy deposition in the detector system. Comparing the number of these 'accepted' events to the number of initial 'thrown' events gives the plots in Figure 5.27. The black

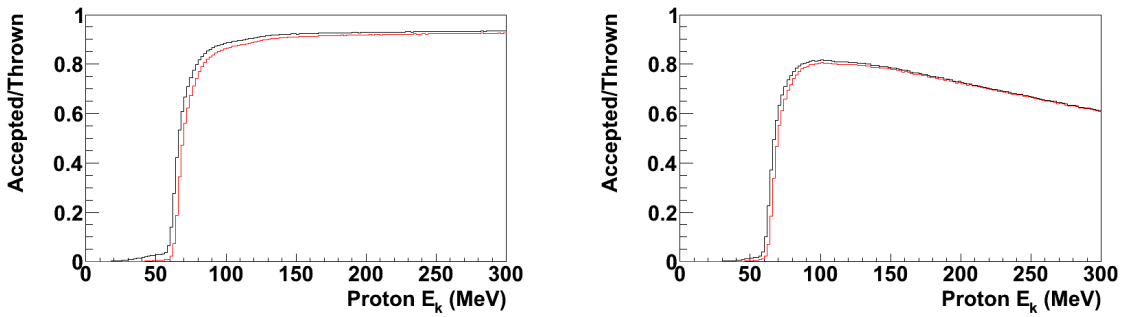

(a) Before AcquRoot (b) After AcquRoot

Figure 5.27: A2 simulation of protons, looking at the number of accepted events

curves represent cases where any amount of energy deposition is required, whereas the red curves represent a requirement of the typical 15 MeV cluster threshold. As shown in the figure, this can be looked at either directly from the output of the Geant4 simulation, or after running it through AcquRoot. The resulting difference between these two situations at higher proton energies is due to the chances of a high energy proton resulting it more than one apparent cluster in the reconstruction. In general

this would be of concern, but for this analysis the most energetic protons expected are only 110 MeV.

The π^0 photoproduction data is used to refine this, knowing that while the simulation is rather advanced, it simply can not account for certain effects. The analysis is performed in a similar manner as for the proton response (see subsection 5.3.2). Cases where a recoil particle is detected are compared to cases where it's not. This becomes more complicated depending on the requirements for deciding the relevance of the detected particle. While the analysis would primarily require that the recoil particle is charged, it is also useful to check for recoil particles that perhaps are mistakenly determined to be neutral. In all cases exclusive particle number cuts are used, requiring that two neutral particles are detected that appear to be the result of a π^0 decay, and that at most only one other particle is detected. The number of events is broken into three situations depending on the latter:

- N_C - Events where a possible recoil particle is detected, and identified as charged
- N_N - Events where a possible recoil particle is detected, and identified as neutral
- N_M - Events where the recoil particle is missing

It's also important to apply the typical opening angle cut to the possible recoil particle, to keep this analysis similar to the primary analysis. For both the charged and neutral recoil cases edited versions of the above numbers are then:

- $N'_C(\theta_{OA})$ - Events where a possible recoil particle is detected within the specified opening angle, and identified as charged
- $N'_N(\theta_{OA})$ - Events where a possible recoil particle is detected within the specified opening angle, and identified as neutral

Note that $N'_C(180°) = N_C$ and that $N'_N(180°) = N_N$. An efficiency that incorporates detection, reconstruction, and identification, of a charged recoil particle can be defined as

$$\epsilon = \frac{N'_C(\theta_{OA})}{N_C + N_M} \tag{5.18}$$

Given the proton energy determination issues detailed previously, and in order to match with the missed recoil events, the proton energy and angle used in binning the following plots are determined from the missing recoil particle.

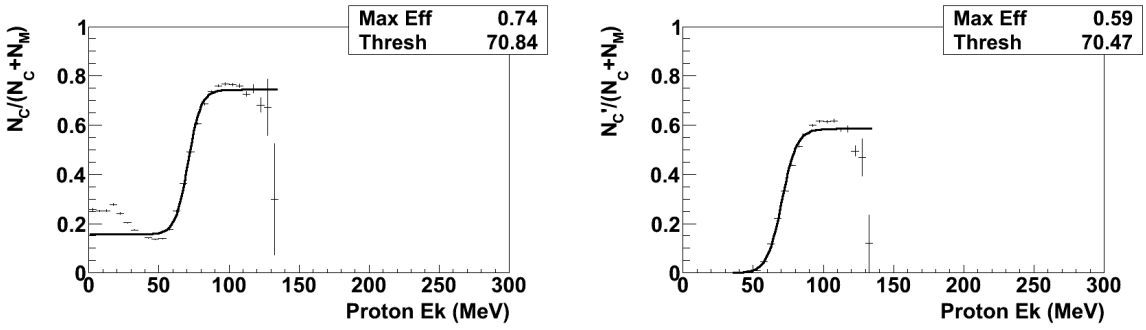

(a) No OA Cut

(b) 10° OA cut

Figure 5.28: Proton efficiencies using π^0 photoproduction data, looking at events that either include a charged particle or miss the recoil particle. The kinematically determined recoil particle has a polar range of 35-40°.

The structure below 50 MeV in the result without an opening angle cut clearly points to the existence of many events that fall outside the typical opening angle cut. Knowing that the chances of detecting a proton below 50 MeV are basically zero, it's obvious that the opening angle cut is important to remove background events. Of note is the fact that the difference between the minimum and maximum efficiency is essentially the same for both of these plots, lending credence to the efficiency calculated with the opening angle cut.

To see how many events are possibly being lost due to misidentification of the charged recoil particle as a neutral particle, the efficiency is constructed as

$$\epsilon = \frac{N'_C(\theta_{OA})}{N_C + N_N + N_M} \tag{5.19}$$

which incorporates these neutral events into the denominator of the efficiency. To see if analysis of the neutral events within an opening angle cut would be beneficial, the efficiency is calculated as

$$\epsilon = \frac{N'_C(\theta_{OA}) + N'_N(\theta_{OA})}{N_C + N_N + N_M} \tag{5.20}$$

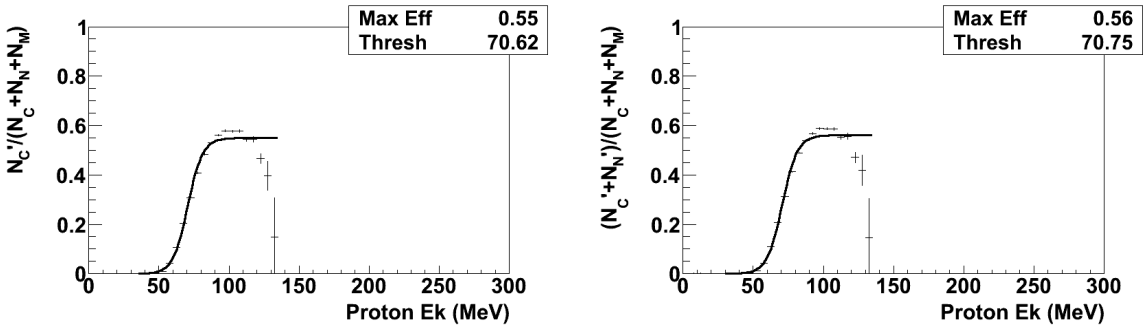

(a) Charged (b) Charged and Neutral

Figure 5.29: Proton efficiencies using π^0 photoproduction data, looking at events that include a charged particle, a neutral particle, or miss the recoil particle. The kinematically determined recoil particle has a polar range of 35-40°.

Figure 5.29 shows that the efficiency when including neutral particles is decreased as compared to Figure 5.28, even when analyzing neutral particles that satisfy the opening angle cut as proper recoil particles. To further investigate how the neutral events play a role, it's useful to plot the number of charged or neutral events as a function of their opening angle.

The odd double peak structure at 25-50° in Figure 5.30 is explained by the high background rates in TAPS. This was determined by noting that these plots are for recoils expected at 35-40°, the centroid of which matches the position of the dip between the two peaks. While the nature of the opening angle implies that these events could be from anywhere on a 25-50° cone, the fact that this cone intersects the center of TAPS was very telling. In addition, the position of these double peaks shifts

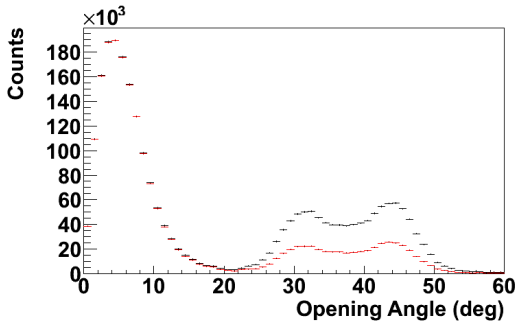

(a) Charged

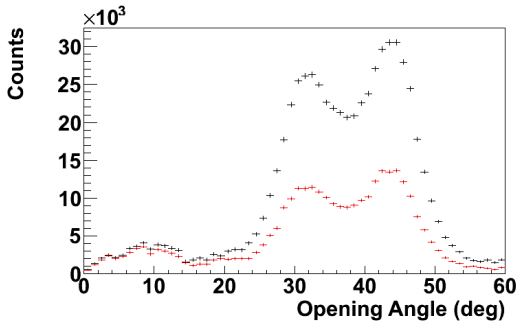

(b) Neutral

Figure 5.30: Opening angle for charged and neutral recoils in π^0 photoproduction. The kinematically determined recoil particle has a polar range of 35-40°, with the black points depicting recoils of all energies, and the red points depicting recoils of at least 50 MeV.

appropriately for other recoil angle ranges. To test this, the downstream fiducial cut on TAPS is expanded from 6° to 12° in Figure 5.31b.

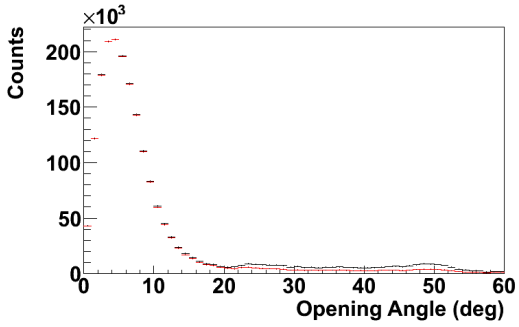

(a) Charged

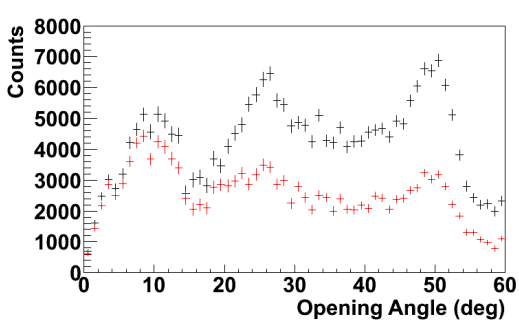

(b) Neutral

Figure 5.31: Opening angle for charged and neutral recoils in π^0 photoproduction with a larger TAPS fiducial cut. The kinematically determined recoil particle has a polar range of 35-40°, with the black points depicting recoils of all energies, and the red points depicting recoils of at least 50 MeV.

The larger fiducial cut clearly eliminates a large portion of the background beyond an opening angle of 10°, and the efficiencies can be recalculated using this data.

While the result looking at only charged recoils without an opening cut is obviously affected by this change, the remaining efficiencies are not. As the other three

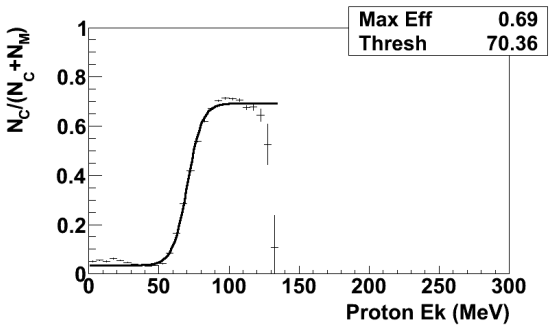

(a) No OA Cut

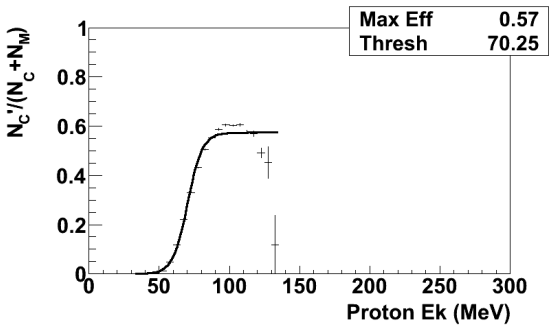

(b) 10° OA cut

Figure 5.32: Proton efficiencies using π^0 photoproduction data with a larger TAPS fiducial cut, looking at events that either include a charged particle or miss the recoil particle. The kinematically determined recoil particle has a polar range of 35-40°.

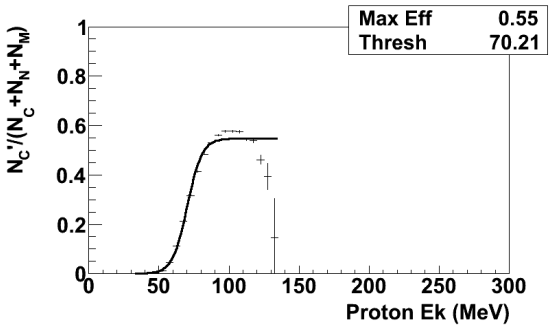

(a) Charged

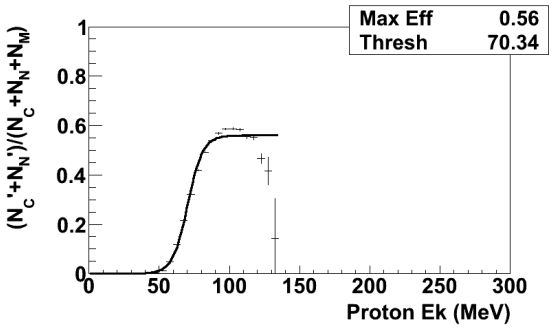

(b) Charged and Neutral

Figure 5.33: Proton efficiencies using π^0 photoproduction data with a larger TAPS fiducial cut, looking at events that include a charged particle, a neutral particle, or miss the recoil particle. The kinematically determined recoil particle has a polar range of 35-40°.

require opening angle cuts in the numerator, the denominator is clearly dominated by the number of events that miss the recoil particle entirely. Since Figure 5.30 and Figure 5.31 depict the contribution of neutral events (especially inside the opening angle cut) to be very small compared to charged recoils, Equation 5.18 is chosen to best represent the proton efficiency. For various other angles this results in the efficiencies in Figure 5.34.

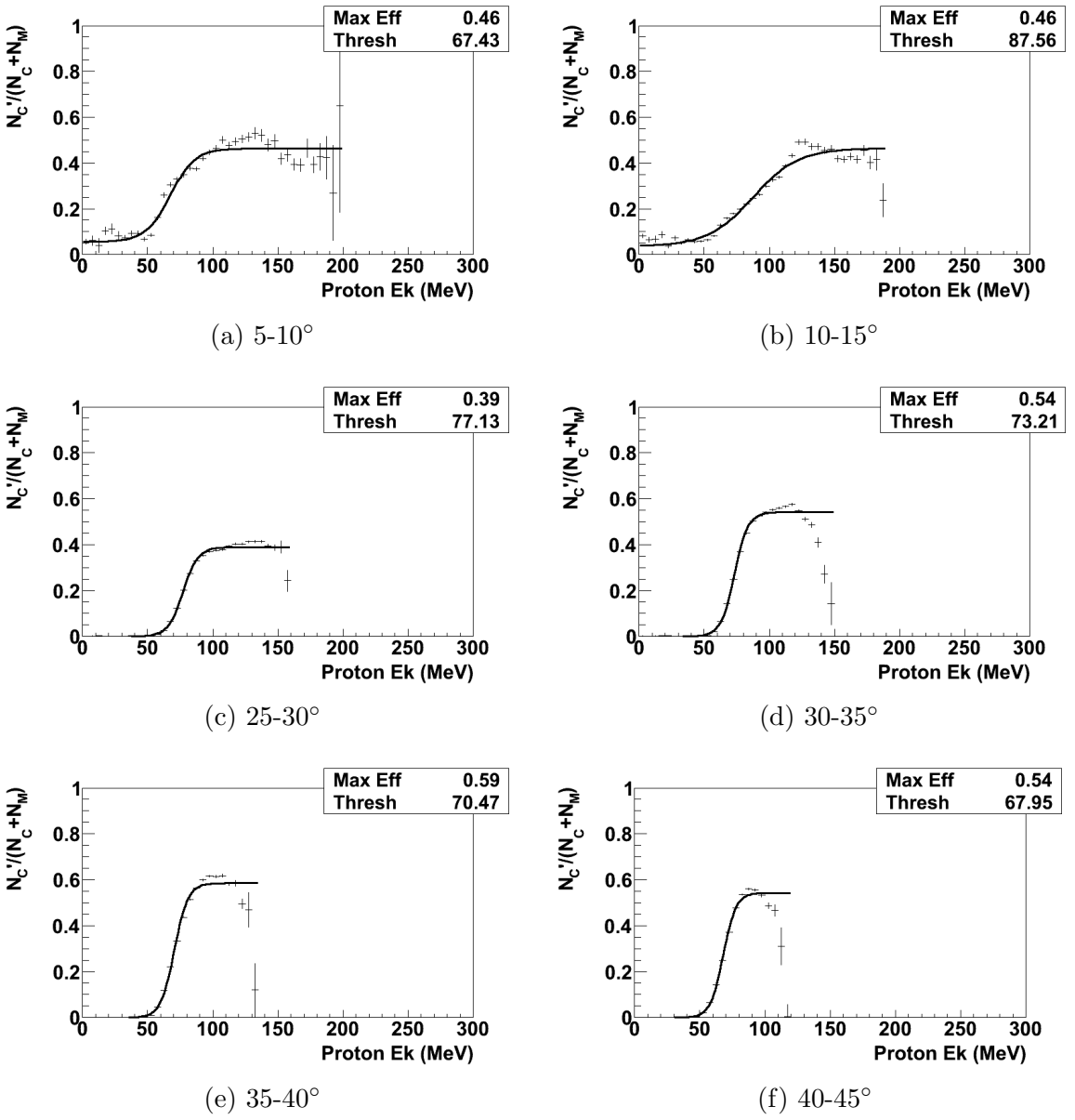

(a) 5-10° (b) 10-15°

(c) 25-30° (d) 30-35°

(e) 35-40° (f) 40-45°

Figure 5.34: Proton efficiencies using π^0 photoproduction data, looking at events that either include a charged particle or miss the recoil particle

Other angular ranges are unfortunately unavailable due to the forward fiducial cut of 0-6° (which slightly cuts into and therefore reduces the first range), the middle fiducial cut of 18-25° (which obviously affects the acceptance of the 25-30° range, hence the 39% maximum efficiency), and the kinematic ranges for π^0 photoproduction with a 450 MeV endpoint energy (which is seen in the reduction of the highest kinetic

energy detectable in a given angular range, 200 MeV at 5-10° versus 120 MeV at 40-45°). It's already clear to see, however, that even once away from the edge of the CB the proton efficiency is only about 60%, with a threshold of about 70 MeV. This demonstrates one of the primary difficulties with this experiment. Besides having large backgrounds from π^0 photoproduction, there's only a small kinematic range that's detectable. This range is also further reduced by the inclusion of the Cherenkov, which places TAPS further downstream creating the gap between it and the CB as depicted in Figure 4.1.

CHAPTER 6

ASYMMETRIES

Regardless of the method used to obtain the number of counts, the analysis separates events into bins in tagged photon energy, theta, and phi. For the transversely polarized target data it also separates events into one of four categories depending on target and beam polarization:

- Positive target polarization, right helicity beam = $N^R_{+x}(E, \theta, \phi)$
- Positive target polarization, left helicity beam = $N^L_{+x}(E, \theta, \phi)$
- Negative target polarization, right helicity beam = $N^R_{-x}(E, \theta, \phi)$
- Negative target polarization, left helicity beam = $N^L_{-x}(E, \theta, \phi)$

6.1 Compton Asymmetry

To produce Σ_{2x}, as described in Equation 1.38, the cross sections for a given energy, theta, and phi, need to be multiplied by various factors to be converted into counts:

$$N(E, \theta, \phi) = \sigma(E, \theta, \phi)\, \Omega(\theta, \phi)\, \Phi(E)\, L\, \rho\, t\, \epsilon(E, \theta, \phi) \tag{6.1}$$

where σ (more appropriately written as $d\sigma/d\Omega$) is the cross section, Ω is the solid angle of the phase space being summed together, Φ is the photon flux, L is the target length, ρ is the target density, and t is the running time. The ϵ represents the efficiency, which is actually made up of three components: tagging, $\epsilon_t(E)$; detection, $\epsilon_d(\theta, \phi)$; and acquisition, ϵ_a; efficiencies.

Due to the relatively quick helicity flipping of the beam (approximately 1 Hz), the various factors are identical for the right and left helicity states. Even if the flux, or one of the efficiencies, drift over the course of the experiment, both helicity sets will observe the same effect. Taking the positive target polarization data, the difference between the right and left counts divided by their sum gives

$$\frac{N^R_{+x}(E,\theta,\phi) - N^L_{+x}(E,\theta,\phi)}{N^R_{+x}(E,\theta,\phi) + N^L_{+x}(E,\theta,\phi)} = \frac{\sigma^R_{+x}(E,\theta,\phi) - \sigma^L_{+x}(E,\theta,\phi)}{\sigma^R_{+x}(E,\theta,\phi) + \sigma^L_{+x}(E,\theta,\phi)} \tag{6.2}$$

While the right hand side looks like Equation 1.38, it's important to note that the theoretical asymmetry Σ_{2x} assumes two things:

- The target and beam polarizations are both 100%.
- The scattered photon is detected at the same azimuthal angle as the direction of polarization (otherwise the effective polarization at that angle is less than the maximum, and therefore a similar concern as the first point).

6.1.1 Generalized Cross Sections and Counts

While the second assumption is false because of the choice to utilize the entire detector (in order to get decent statistics), the first is simply impossible for this experiment. The generalized cross sections for the actual experiment need to be related to the ideal cross sections on the plane of polarization (for either polarization direction) by

$$\sigma^R_{\pm}(E,\theta,\phi) = \left[\frac{1+P(E,\phi)}{2}\right]\sigma^R_{\pm}(E,\theta) + \left[\frac{1-P(E,\phi)}{2}\right]\sigma^L_{\pm}(E,\theta) \tag{6.3}$$

$$\sigma^L_{\pm}(E,\theta,\phi) = \left[\frac{1+P(E,\phi)}{2}\right]\sigma^L_{\pm}(E,\theta) + \left[\frac{1-P(E,\phi)}{2}\right]\sigma^R_{\pm}(E,\theta) \tag{6.4}$$

where $P(E,\phi)$ is the degree of polarization at a particular azimuthal angle. This is given by

$$P(E,\phi) = P_T P_\gamma(E)\cos(\phi_0 - \phi) \tag{6.5}$$

where P_T is the degree of target polarization, $P_\gamma(E)$ is the degree of beam polarization (given by the form in Equation 2.2), and ϕ_0 is the azimuthal direction of the target polarization. Using these relations in Equation 6.2, and following through with the algebra, results in

$$\begin{aligned}\frac{N^R_{+x}(E,\theta,\phi) - N^L_{+x}(E,\theta,\phi)}{N^R_{+x}(E,\theta,\phi) + N^L_{+x}(E,\theta,\phi)} &= P_{+x}P_\gamma(E)\cos(\phi_{+x}-\phi)\frac{\sigma^R_{+x}(E,\theta) - \sigma^L_{+x}(E,\theta)}{\sigma^R_{+x}(E,\theta) + \sigma^L_{+x}(E,\theta)} \\ &= \Sigma_{2x}(E,\theta)P_{+x}P_\gamma(E)\cos(\phi_{+x}-\phi) \qquad (6.6)\end{aligned}$$

where P_{+x} and ϕ_{+x} have replaced P_T and ϕ_0, respectively, to differentiate between positive and negative polarizations. Therefore the actual asymmetry is

$$\Sigma_{2x}(E,\theta) = \frac{1}{P_{+x}P_\gamma(E)\cos(\phi_{+x}-\phi)}\frac{N^R_{+x}(E,\theta,\phi) - N^L_{+x}(E,\theta,\phi)}{N^R_{+x}(E,\theta,\phi) + N^L_{+x}(E,\theta,\phi)} \qquad (6.7)$$

This relation is adjusted for the negative target polarization by simply changing ϕ_0 (replacing ϕ_{+x} with ϕ_{-x}).

$$\Sigma_{2x}(E,\theta) = \frac{1}{P_{-x}P_\gamma(E)\cos(\phi_{-x}-\phi)}\frac{N^R_{-x}(E,\theta,\phi) - N^L_{-x}(E,\theta,\phi)}{N^R_{-x}(E,\theta,\phi) + N^L_{-x}(E,\theta,\phi)} \qquad (6.8)$$

With the target used for this experiment the polarization direction is flipped completely. This means that $\phi_{+x} = \phi_{-x} + \pi$, and since $\cos(\phi+\pi) = -\cos(\phi)$ it's easy to verify the parity argument noted in section 1.2, which says that

$$\sigma^R_{+x}(E,\theta,\phi) = \sigma^L_{-x}(E,\theta,\phi) \qquad (6.9)$$

$$\sigma^R_{-x}(E,\theta,\phi) = \sigma^L_{+x}(E,\theta,\phi) \qquad (6.10)$$

6.1.2 Phi Fitting

There are then two different ways of constructing this asymmetry for a given energy and theta. The first is to take the difference between right and left helicity

counts divided by their sum, for various values of ϕ at a given value of E and θ, and then fit the resulting distribution with $\Sigma_{2x}(E,\theta)P_T P_\gamma(E)\cos(\phi_0 - \phi)$. An example of this for the 100-120° point is shown in Figure 6.1. Knowing the values for P_T, P_γ, and ϕ_0, the value for Σ_{2x} is determined from the amplitude of this fit.

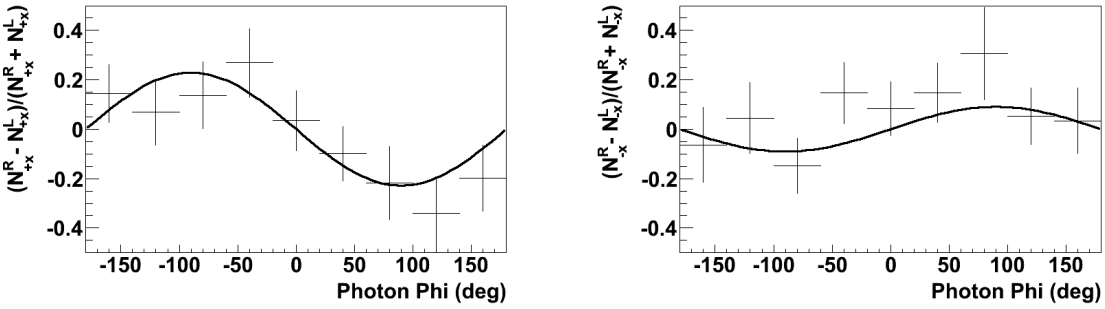

(a) Positive target

(b) Negative target

Figure 6.1: Phi asymmetry distributions for Compton scattering at 100-120°, with both a positive and negative target polarization

6.1.3 Phi Summation

The second method, useful for lower statistics, is to integrate over phi, for a given theta bin, over each hemisphere of the detector. The pole of one hemisphere (to be called the 'adjacent' hemisphere, or $\phi = A$) is intersected by the polarization vector, and the pole of the other hemisphere (the 'opposite' hemisphere, or $\phi = O$) is clearly opposite this. With a polarization azimuth of ϕ_0, the 'adjacent' hemisphere implies an integration from $\phi_0 - \frac{\pi}{2}$ to $\phi_0 + \frac{\pi}{2}$, and the 'opposite' hemisphere implies an integration from $\phi_0 - \frac{3\pi}{2}$ to $\phi_0 - \frac{\pi}{2}$. The counts obtained in this way will reflect an average cross section. For example, the average right helicity cross section for the adjacent hemisphere is

$$\begin{aligned}\bar{\sigma}^R(E,\theta,A) &= \frac{1}{\pi}\int_{\phi_0-\frac{\pi}{2}}^{\phi_0+\frac{\pi}{2}} \left\{\left[\frac{1+P(E,\phi)}{2}\right]\sigma^R(E,\theta) + \left[\frac{1-P(E,\phi)}{2}\right]\sigma^L(E,\theta)\right\} d\phi \\ &= \frac{\sigma^R(E,\theta)+\sigma^L(E,\theta)}{2\pi}\int_{\phi_0-\frac{\pi}{2}}^{\phi_0+\frac{\pi}{2}} d\phi \\ &\quad + \frac{\sigma^R(E,\theta)-\sigma^L(E,\theta)}{2\pi}\int_{\phi_0-\frac{\pi}{2}}^{\phi_0+\frac{\pi}{2}} P(E,\phi)d\phi \\ &= \frac{\sigma^R(E,\theta)+\sigma^L(E,\theta)}{2} + \frac{P_T P_\gamma(E)}{\pi}\left[\sigma^R(E,\theta)-\sigma^L(E,\theta)\right] \end{aligned} \tag{6.11}$$

since

$$\begin{aligned}\int_{\phi_0-\frac{\pi}{2}}^{\phi_0+\frac{\pi}{2}} P(E,\phi)d\phi &= \int_{\phi_0-\frac{\pi}{2}}^{\phi_0+\frac{\pi}{2}} P_T P_\gamma \cos(\phi_0-\phi)d\phi \\ &= -P_T P_\gamma \sin(\phi_0-\phi)\Big|_{\phi_0-\frac{\pi}{2}}^{\phi_0+\frac{\pi}{2}} = 2P_T P_\gamma \end{aligned} \tag{6.12}$$

For the opposite hemisphere the only differences are the limits on the integral. So with the polarization

$$\int_{\phi_0-\frac{3\pi}{2}}^{\phi_0-\frac{\pi}{2}} P(E,\phi)d\phi = -P_T P_\gamma \sin(\phi_0-\phi)\Big|_{\phi_0-\frac{3\pi}{2}}^{\phi_0-\frac{\pi}{2}} = -2P_T P_\gamma \tag{6.13}$$

the average right helicity cross section is

$$\bar{\sigma}^R(E,\theta,O) = \frac{\sigma^R(E,\theta)+\sigma^L(E,\theta)}{2} - \frac{P_T P_\gamma(E)}{\pi}\left[\sigma^R(E,\theta)-\sigma^L(E,\theta)\right] \tag{6.14}$$

Looking at Equation 6.3 and Equation 6.4, it's clear that to construct the average cross sections, for left helicity, the right and left helicity components of Equation 6.11 and Equation 6.14 simply need to be flipped. So the adjacent hemisphere gives

$$\bar{\sigma}^L(E,\theta,A) = \frac{\sigma^L(E,\theta)+\sigma^R(E,\theta)}{2} + \frac{P_T P_\gamma(E)}{\pi}\left[\sigma^L(E,\theta)-\sigma^R(E,\theta)\right] \tag{6.15}$$

and the opposite hemisphere gives

$$\bar{\sigma}^L(E,\theta,O) = \frac{\sigma^L(E,\theta)+\sigma^R(E,\theta)}{2} - \frac{P_T P_\gamma(E)}{\pi}\left[\sigma^L(E,\theta)-\sigma^R(E,\theta)\right] \tag{6.16}$$

It's trivial to see from Equation 6.11 to Equation 6.16 that $\bar{\sigma}^R(E,\theta,A) = \bar{\sigma}^L(E,\theta,O)$ and that $\bar{\sigma}^R(E,\theta,O) = \bar{\sigma}^L(E,\theta,A)$. Applying this summing method for the adjacent hemisphere to Equation 6.2, and following the algebra as done in Equation 6.6 gives

$$\begin{aligned}\frac{N^R(E,\theta,A) - N^L(E,\theta,A)}{N^R(E,\theta,A) + N^L(E,\theta,A)} &= \frac{\bar{\sigma}^R(E,\theta,A) - \bar{\sigma}^L(E,\theta,A)}{\bar{\sigma}^R(E,\theta,A) + \bar{\sigma}^L(E,\theta,A)} \\ &= \frac{2P_T P_\gamma(E)}{\pi}\left[\frac{\sigma^R(E,\theta) - \sigma^L(E,\theta)}{\sigma^R(E,\theta) + \sigma^L(E,\theta)}\right] \\ &= \Sigma_{2x}(E,\theta)\frac{2P_T P_\gamma(E)}{\pi} \end{aligned} \tag{6.17}$$

Solving for the asymmetry results in

$$\Sigma_{2x}(E,\theta) = \frac{\pi}{2P_T P_\gamma(E)}\left[\frac{N^R(E,\theta,A) - N^L(E,\theta,A)}{N^R(E,\theta,A) + N^L(E,\theta,A)}\right] \tag{6.18}$$

or if following through with the opposite hemisphere

$$\Sigma_{2x}(E,\theta) = \frac{\pi}{2P_T P_\gamma(E)}\left[\frac{N^L(E,\theta,O) - N^R(E,\theta,O)}{N^L(E,\theta,O) + N^R(E,\theta,O)}\right] \tag{6.19}$$

The beauty of this method is the ability to then sum these two hemispheres together into one calculation, without having conflicting factors for converting between cross sections and counts. To do this the denominator on the right hand side of each equation is moved to the left hand side.

$$\begin{aligned} 2P_T P_\gamma(E)\left[N^R(E,\theta,A) + N^L(E,\theta,A)\right]\Sigma_{2x}(E,\theta) &= \pi\left[N^R(E,\theta,A) - N^L(E,\theta,A)\right] \\ 2P_T P_\gamma(E)\left[N^L(E,\theta,O) + N^R(E,\theta,O)\right]\Sigma_{2x}(E,\theta) &= \pi\left[N^L(E,\theta,O) - N^R(E,\theta,O)\right] \end{aligned}$$

The left hand sides of each equation are then summed together, as are the right hand sides.

$$2P_T P_\gamma(E)\left[N^R(E,\theta,A)+N^L(E,\theta,A)+N^L(E,\theta,O)+N^R(E,\theta,O)\right]\Sigma_{2x}(E,\theta)$$
$$=\pi\left[N^R(E,\theta,A)-N^L(E,\theta,A)+N^L(E,\theta,O)-N^R(E,\theta,O)\right] \quad (6.20)$$

and solving for Σ_{2x} gives

$$\Sigma_{2x}(E,\theta)=\frac{\pi}{2P_T P_\gamma(E)}\left[\frac{N^R(E,\theta,A)-N^L(E,\theta,A)+N^L(E,\theta,O)-N^R(E,\theta,O)}{N^R(E,\theta,A)+N^L(E,\theta,A)+N^L(E,\theta,O)+N^R(E,\theta,O)}\right] \quad (6.21)$$

6.1.4 Phi Fitting of Combined Polarizations

While either method (fitting over phi, or integrating over the hemispheres) can be done for each polarization separately, and then taking the average of the two asymmetries as the final answer, given the small statistics it's beneficial to further combine the two sets into one. To combine them for the phi fitting method Equation 6.7 and Equation 6.8 are rewritten as

$$P_{+x}P_\gamma(E)\cos(\phi_{+x}-\phi)\left[N^R_{+x}(E,\theta,\phi)+N^L_{+x}(E,\theta,\phi)\right]\Sigma_{2x}(E,\theta)$$
$$=N^R_{+x}(E,\theta,\phi)-N^L_{+x}(E,\theta,\phi) \quad (6.22)$$
$$P_{-x}P_\gamma(E)\cos(\phi_{-x}-\phi)\left[N^R_{-x}(E,\theta,\phi)+N^L_{-x}(E,\theta,\phi)\right]\Sigma_{2x}(E,\theta)$$
$$=N^R_{-x}(E,\theta,\phi)-N^L_{-x}(E,\theta,\phi) \quad (6.23)$$

Subtracting the left side of the positive polarization by the negative (and similarly for the right side) gives

$$\Sigma_{2x}(E,\theta)\Big\{P_{+x}P_\gamma(E)\cos(\phi_{+x}-\phi)\left[N^R_{+x}(E,\theta,\phi)+N^L_{+x}(E,\theta,\phi)\right]$$
$$-P_{-x}P_\gamma(E)\cos(\phi_{-x}-\phi)\left[N^R_{-x}(E,\theta,\phi)+N^L_{-x}(E,\theta,\phi)\right]\Big\}$$
$$=N^R_{+x}(E,\theta,\phi)-N^L_{+x}(E,\theta,\phi)-N^R_{-x}(E,\theta,\phi)+N^L_{-x}(E,\theta,\phi) \quad (6.24)$$

Solving for the asymmetry (note the dropping of the (E, θ, ϕ) dependence from the counts, solely for the sake of brevity) gives

$$\Sigma_{2x}(E,\theta) = \frac{N^R_{+x} - N^L_{+x} - N^R_{-x} + N^L_{-x}}{P_\gamma(E)\cos(\phi_{+x} - \phi)\left[P_{+x}\left(N^R_{+x} + N^L_{+x}\right) + P_{-x}\left(N^R_{-x} + N^L_{-x}\right)\right]} \tag{6.25}$$

where only the cos function for the positive polarization is shown. As noted before, $\cos(\phi_{-x} - \phi) = -\cos(\phi_{+x} - \phi)$, so the two cos functions can be expressed as one, arbitrarily chosen as the positive polarization. The reason for subtracting both sides, as opposed to summing as done in Equation 6.20, is to leave the denominator as a sum total after replacing the cos functions. When applied to the data, again for the 100-120° point, the result is Figure 6.2.

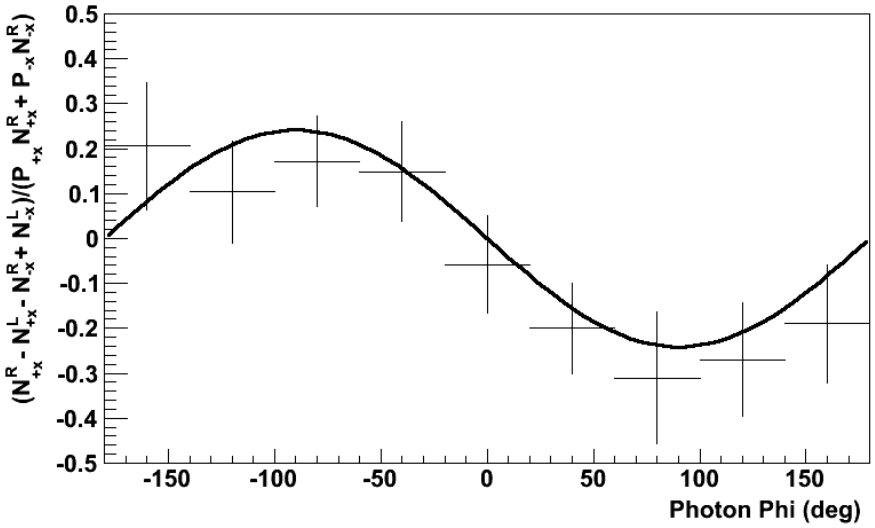

Figure 6.2: Phi asymmetry distributions for Compton scattering at 100-120°, summing together both positive and negative target polarization data sets

If the various factors in Equation 6.1, as well as the actual polarization magnitudes, were identical then the counts, like the cross sections, would satisfy

$$N^R_{+x}(E,\theta,\phi) = N^L_{-x}(E,\theta,\phi) \tag{6.26}$$

$$N^L_{+x}(E,\theta,\phi) = N^R_{-x}(E,\theta,\phi) \tag{6.27}$$

simplifying Equation 6.25.

6.1.5 Phi Summation of Combined Polarizations

To sum together both polarizations in the hemisphere summing method, it again helps to pick one of the polarizations to represent the general direction, in this case to distinguish between the adjacent and opposite hemispheres (A and O as in Equation 6.21) which switch meaning when the polarization is flipped. For this experiment, the direction of positive polarization is approximately $+\hat{y}$. So it's reasonable to rename the 'adjacent' hemisphere for positive polarization as the 'top' hemisphere ($\phi = T$), and the 'opposite' hemisphere as the 'bottom' hemisphere ($\phi = B$), since they literally are. This relationship is flipped for the negative case.

$$
\begin{aligned}
N_{+x}(E,\theta,A) &= N_{+x}(E,\theta,T) \\
N_{+x}(E,\theta,O) &= N_{+x}(E,\theta,B) \\
N_{-x}(E,\theta,A) &= N_{-x}(E,\theta,B) \\
N_{-x}(E,\theta,O) &= N_{-x}(E,\theta,T)
\end{aligned}
$$

Taking Equation 6.28 for both positive and negative target polarizations, using the above substitutions, and utilizing the same steps used to arrive at it in the first place, the polarizations are added together resulting in

$$
\begin{aligned}
\Sigma_{2x}(E,\theta) = \frac{\pi}{2P_\gamma(E)} \big[& N^R_{+x}(E,\theta,T) - N^L_{+x}(E,\theta,T) + N^L_{+x}(E,\theta,B) - N^R_{+x}(E,\theta,B) \\
& + N^R_{-x}(E,\theta,B) - N^L_{-x}(E,\theta,B) + N^L_{-x}(E,\theta,T) - N^R_{-x}(E,\theta,T) \big] \\
\Big/ \Big\{ & P_{+x} \left[N^R_{+x}(E,\theta,T) + N^L_{+x}(E,\theta,T) + N^L_{+x}(E,\theta,B) + N^R_{+x}(E,\theta,B) \right] \\
& + P_{-x} \left[N^R_{-x}(E,\theta,B) + N^L_{-x}(E,\theta,B) + N^L_{-x}(E,\theta,T) + N^R_{-x}(E,\theta,T) \right] \Big\}
\end{aligned}
\tag{6.28}
$$

The missing mass distributions for the actual data (starting with Figure 4.14), already utilized this type of summation. What were called 'positive' and 'negative' sets are represented by N^P and N^N, respectively:

$$N^P(E,\theta) = N^R_{+x}(E,\theta,T) + N^L_{+x}(E,\theta,B) + N^R_{-x}(E,\theta,B) + N^L_{-x}(E,\theta,T) \quad (6.29)$$

$$N^N(E,\theta) = N^R_{+x}(E,\theta,B) + N^L_{+x}(E,\theta,T) + N^R_{-x}(E,\theta,T) + N^L_{-x}(E,\theta,B) \quad (6.30)$$

6.2 Pion Photoproduction Asymmetry

A useful test of the asymmetry construction is to also perform it for the π^0 photoproduction results. Given its much larger cross section, it's easier to check the validity of the method. The asymmetry is defined a bit differently for π^0 photoproduction however, and is in terms of the observables $F(E,\theta)$ and $T(E,\theta)$:

$$\frac{N^R_{+x}(E,\theta,\phi) - N^L_{+x}(E,\theta,\phi)}{N^R_{+x}(E,\theta,\phi) + N^L_{+x}(E,\theta,\phi)} = \frac{F(E,\theta)P_T P_\gamma(E)\cos(\phi_{+x}-\phi)}{1 + T(E,\theta)P_T \sin(\phi_{+x}-\phi)} \quad (6.31)$$

Examples of this are shown in Figure 6.3. The more complicated nature of the phi

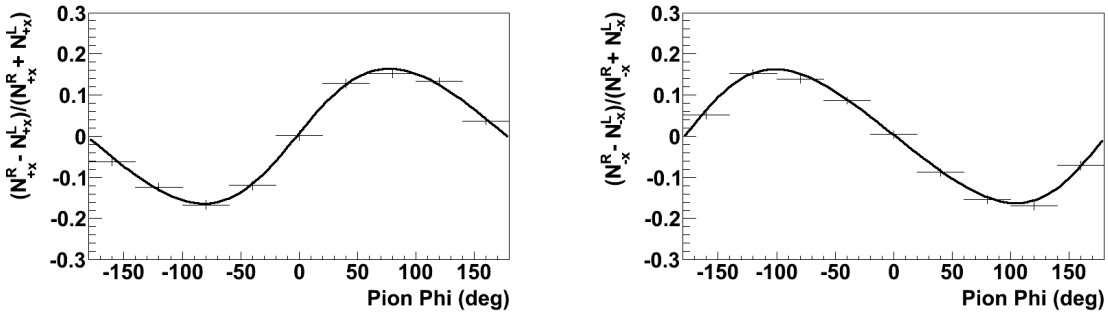

(a) Positive target (b) Negative target

Figure 6.3: Phi asymmetry distributions for π^0 photoproduction at 100-120°, with both a positive and negative target polarization

dependence is due to the fact that π^0 photoproduction has an intrinsic target asym-

metry $T(E,\theta)$ that is evident with a transversely polarized target and an unpolarized beam.

$$\frac{N_{+x}(E,\theta,\phi) - N_{-x}(E,\theta,\phi)}{N_{+x}(E,\theta,\phi) + N_{-x}(E,\theta,\phi)} = T(E,\theta) P_T \sin(\phi_{+x} - \phi) \tag{6.32}$$

For Compton scattering such an asymmetry is non-existent, so its version of $T(E,\theta)$ would be zero. This reduces Equation 6.31 to Equation 6.7, with its version of $F(E,\theta)$ being identical to $\Sigma_{2x}(E,\theta)$. An example for the π^0 photoproduction data, again at 100-120°, is shown in Figure 6.4, fitted with $\sin(\phi_0 - \phi)$.

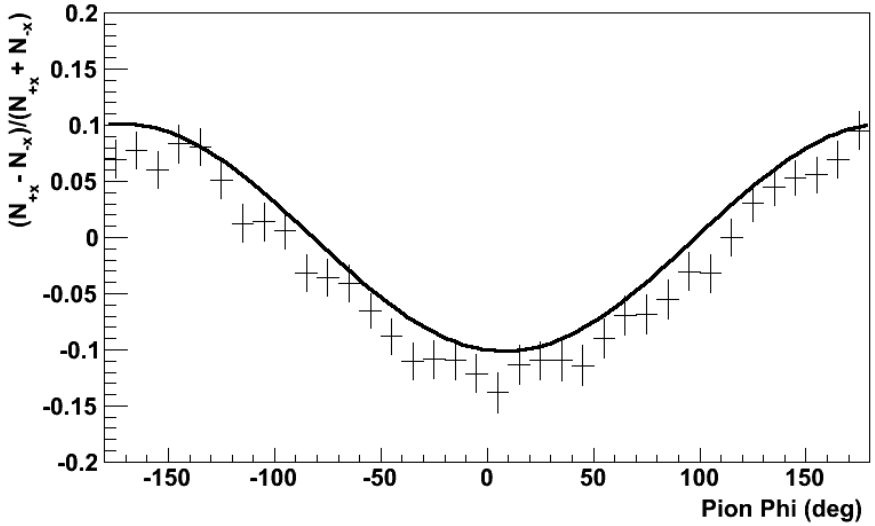

Figure 6.4: Phi asymmetry distributions for π^0 photoproduction at 100-120°, summing together both beam helicity states for each target polarization data sets

CHAPTER 7

RESULTS AND DISCUSSION

The results of the analysis outlined in this document are presented for two different energy ranges: one that is just below, and one that is just above, $\gamma p \rightarrow \pi^0\pi^0 p$ threshold (308.85 MeV). Specifically these ranges are 272.73-303.32 MeV and 315.25-345.94 MeV, respectively. Both energy ranges use data from the same experimental runs, which were broken into two main sets (one in September 2010 and one in February 2011), as well as subsets for positive and negative target polarization runs. These sets are listed with their run times and average target polarizations in Table 7.1, along with the total run time and an overall average of the absolute values of the target polarizations.

Set	Runs	Time (h)	Target Pol (%)
Neg. 1	26820-26853	12.2	-67.9 ± 3.6
Neg. 2	26859-27109	90.2	-75.2 ± 4.0
Pos. 1	27110-27367	84.6	+77.1 ± 4.1
Pos. 2	35532-35777	86.4	+89.0 ± 5.0
Pos. 3	35778-35885	41.5	+89.2 ± 5.1
Neg. 3	35887-36027	47.7	-77.0 ± 4.4
Neg. 4	36028-36303	96.0	-84.9 ± 4.8
Total/Aver.		459.6	81.6 ± 1.7

Table 7.1: Time and target polarization information for data sets

7.1 Below $\gamma p \rightarrow \pi^0\pi^0 p$ Threshold

While the parameters in Table 7.1 are energy independent, other important values in constructing the asymmetries are energy dependent. Two such variables are

the photon beam polarization and the carbon scaling factor used in subtracting out the carbon contribution to the missing mass spectra. The carbon scaling factor, as discussed in section 4.3, scales the separate experimental run on a carbon target to each of these runs on the polarized butanol target. Since the scaling factor is based on ratios of live time corrected tagger scaler hits, this factor is different for each polarization period, as well as for different regions of the tagger. In addition, as discussed in subsection 5.2.1, this base carbon scaling factor is insufficient to remove the background in π^0 photoproduction spectra. That result indicated an additional factor of 1.306 is needed in this energy bin to ideally match the background. For this energy bin these parameters are given in Table 7.2, along with total carbon to butanol scaling factors and an average photon beam polarization.

Set	Initial Scaling	Corrected Scaling	Photon Pol (%)
Neg. 1	0.156	0.203	67.9 ± 0.1
Neg. 2	1.239	1.618	67.9 ± 0.1
Pos. 1	1.020	1.333	68.7 ± 0.4
Pos. 2	1.244	1.624	66.5 ± 0.3
Pos. 3	0.610	0.797	66.5 ± 0.3
Neg. 3	0.762	0.996	64.8 ± 0.2
Neg. 4	1.392	1.818	64.5 ± 0.1
Total/Aver.	6.423	8.389	66.0 ± 0.1

Table 7.2: Carbon scaling factors before and after additional scaling factor, and photon polarization values for the lower energy bin

Calculating the asymmetry, using these parameters, through either the phi fitting method of Equation 6.25, or through the phi summing method of Equation 6.28, results in the asymmetries noted in Table 7.3.

Using the same method, discussed in section 1.2 and subsection A.6.3, that produced Figure 1.11 and Figure A.15, the asymmetry results are plotted with dispersion theory curves for a variety of values for γ_{M1M1} while holding γ_{E1E1} fixed at the HDPV[42] value of -4.3, as shown in Figure 7.1 and Figure 7.2. In both of these plots,

Angle	Fitted	Summed
90	-0.254 ± 0.110	-0.285 ± 0.131
110	-0.369 ± 0.080	-0.384 ± 0.091
130	-0.292 ± 0.153	-0.358 ± 0.166
150	-0.182 ± 0.148	-0.090 ± 0.155

Table 7.3: Asymmetry results using either the phi fitting method, or the phi summing method for the lower energy bin

as discussed previously, the various color bands represent different values for γ_{M1M1}, while the spread of each band is a result of allowing α, β, γ_0, and γ_π, to vary about their experimental errors. As depicted previously, Σ_{2x} exhibits a very weak sensitivity to γ_{M1M1}, allowing widely varying choices of this spin polarizability to adequately fit the data points, as shown in Figure 7.1 and Figure 7.2, which is itself encouraging as the data clearly follows the trend of these curves.

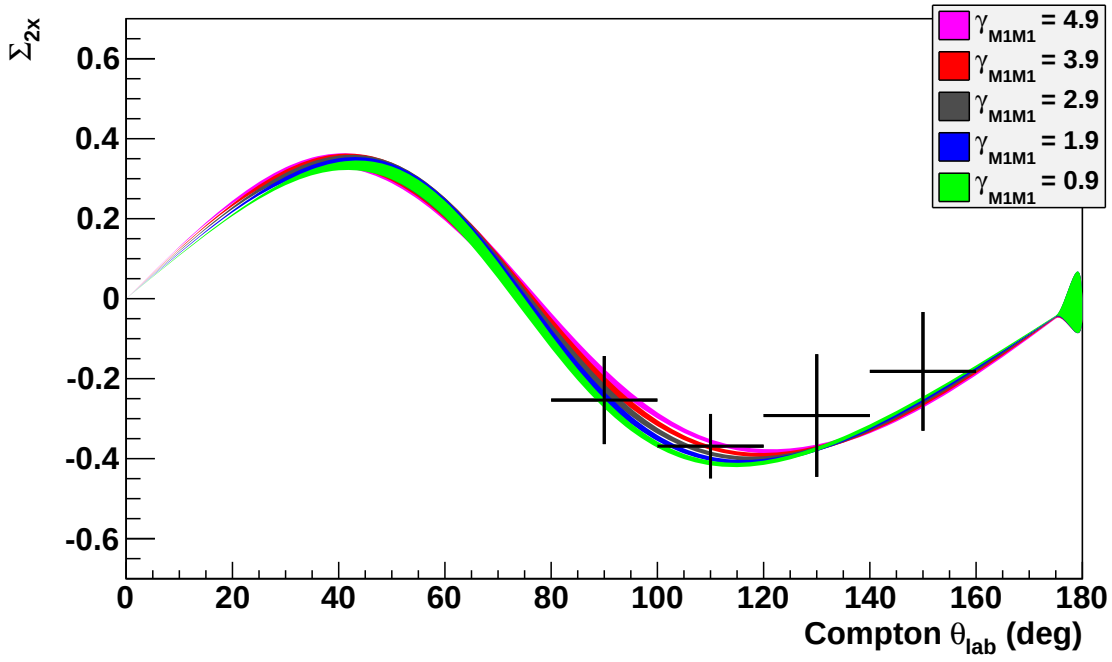

Figure 7.1: Σ_{2x} from phi fitting method, for 273-303 MeV, where γ_{M1M1} is varied while γ_{E1E1} is fixed at -4.3.

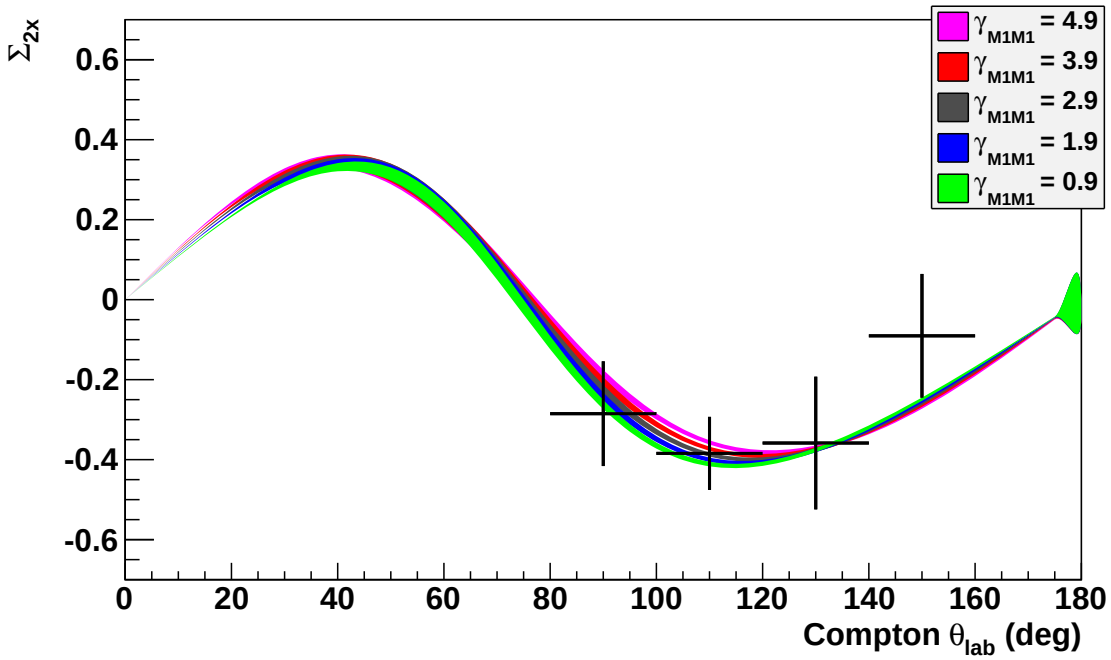

Figure 7.2: Σ_{2x} from phi summing method, for 273-303 MeV, where γ_{M1M1} is varied while γ_{E1E1} is fixed at -4.3.

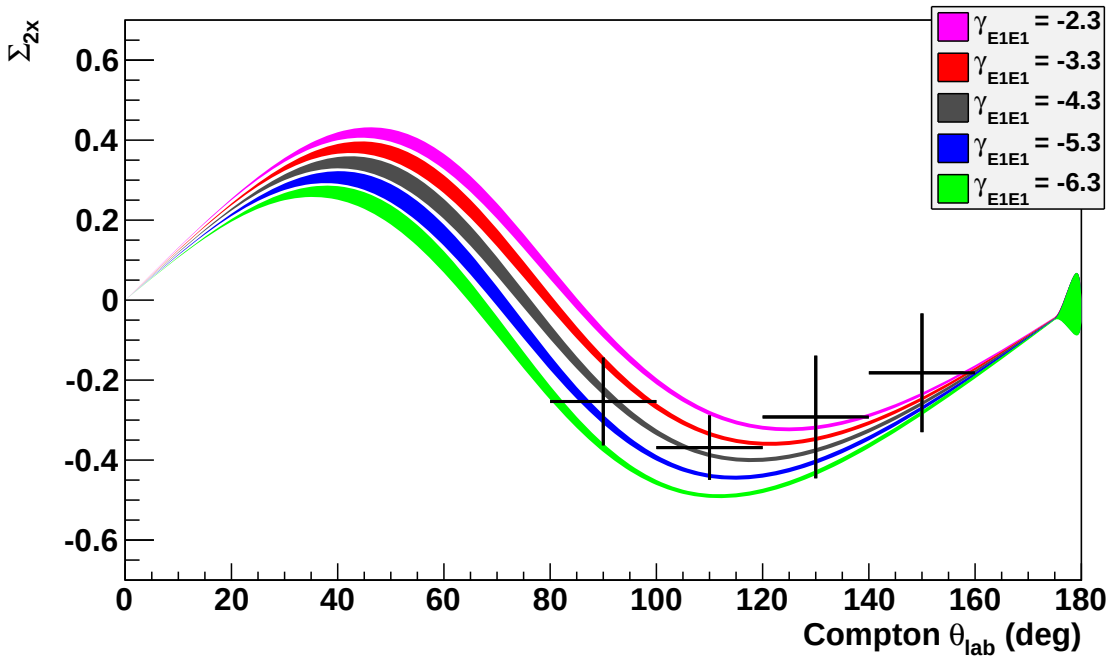

Figure 7.3: Σ_{2x} from phi fitting method, for 273-303 MeV, where γ_{E1E1} is varied while γ_{M1M1} is fixed at 2.9.

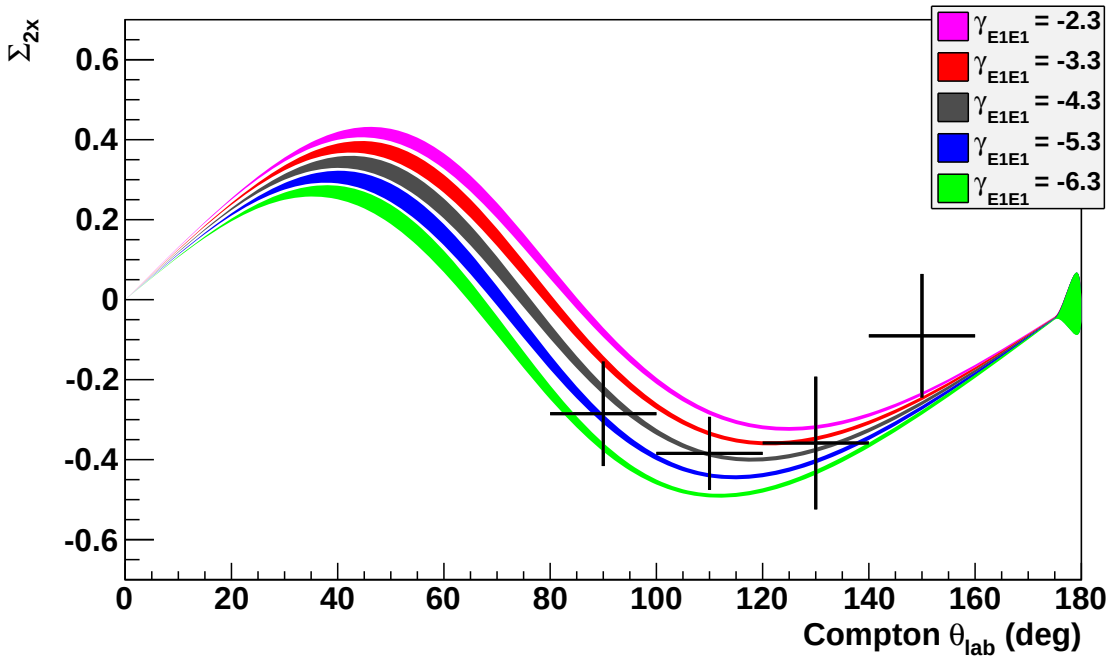

Figure 7.4: Σ_{2x} from phi summing method, for 273-303 MeV, where γ_{E1E1} is varied while γ_{M1M1} is fixed at 2.9.

The same data are also plotted with curves generated by varying γ_{E1E1} while holding γ_{M1M1} fixed at the HDPV[42] value of 2.9. These results are shown in Figure 7.3 and Figure 7.4 where, as also depicted previously, Σ_{2x} exhibits a very strong sensitivity to γ_{E1E1}. Now there is clearly a range of values for this spin polarizability that agrees with the data better than others. Even without a complicated χ^2 minimizing fit (which is underway), a rough 'eyeball fit' of $\gamma_{E1E1} = 4.3 \pm 1.5$ depicts the data well.

7.2 Above $\gamma p \to \pi^0\pi^0 p$ Threshold

Although the dispersion code, used in this analysis to produce theoretical asymmetries, is not valid above $\gamma p \to \pi^0\pi^0 p$ threshold, it's obviously still of interest to calculate these double polarized Compton asymmetries in this range for the first time. As with the previous case, the energy range has its own set of photon beam polariza-

tion as well as carbon scaling factors (including the additional carbon scaling factor of 1.234 noted in subsection 5.2.1). These are given in Table 7.4, along with total carbon to butanol scaling factors and an average photon beam polarization. With

Set	Initial Scaling	Corrected Scaling	Photon Pol (%)
Neg. 1	0.155	0.192	75.2 ± 0.1
Neg. 2	1.236	1.525	75.2 ± 0.1
Pos. 1	1.014	1.251	76.2 ± 0.4
Pos. 2	1.206	1.488	73.8 ± 0.3
Pos. 3	0.569	0.702	73.8 ± 0.3
Neg. 3	0.702	0.867	72.0 ± 0.2
Neg. 4	1.262	1.558	71.6 ± 0.1
Total/Aver.	6.144	7.582	73.2 ± 0.1

Table 7.4: Carbon scaling factors before and after additional scaling factor, and photon polarization for the higher energy bin

these parameters, and following the same methodology as the lower energy range, constructing the asymmetries with either the phi fitting method or the phi summing method produces Figure 7.5 or Figure 7.6, respectively. Since the dispersion code is not valid at this energy range, there are no theoretical curves plotted with these points. Of note however is the change in the scale of the asymmetry axis (from -0.7 to 0.7 before to -0.4 to 0.4 now). The numbers for the asymmetries are noted in Table 7.5.

Angle	Fitted	Summed
70	-0.106 ± 0.070	-0.160 ± 0.081
90	-0.153 ± 0.034	-0.168 ± 0.038
110	-0.222 ± 0.048	-0.202 ± 0.052
130	-0.229 ± 0.101	-0.308 ± 0.114
150	-0.056 ± 0.099	-0.074 ± 0.108

Table 7.5: Asymmetry results using either the phi fitting method, or the phi summing method for the higher energy bin

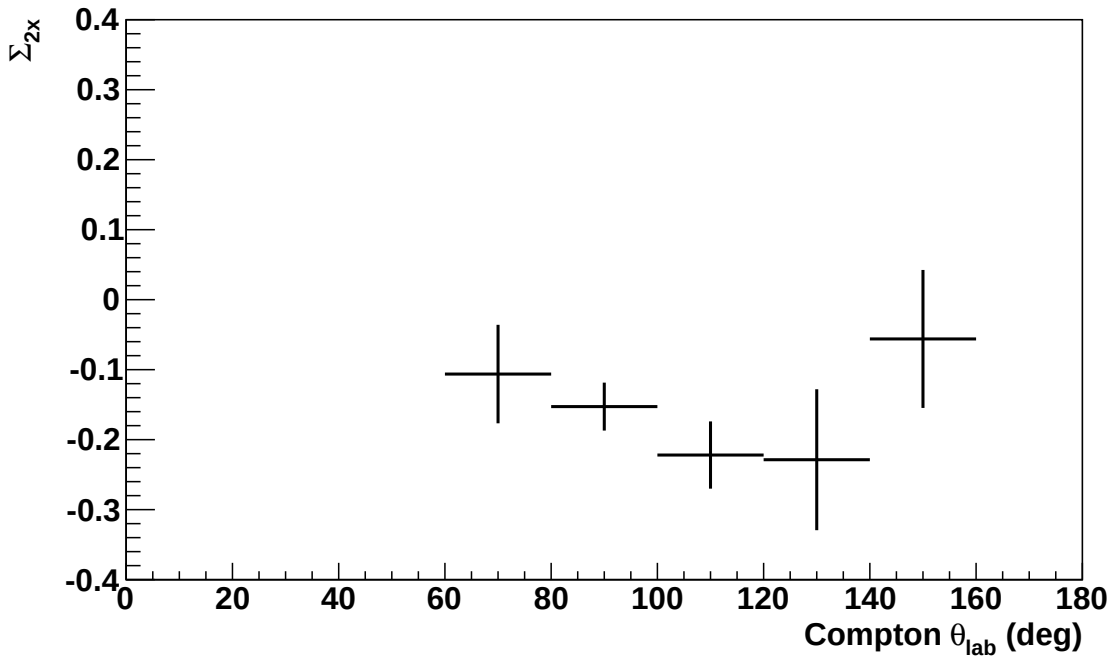

Figure 7.5: Σ_{2x} from phi fitting method, for 315-346 MeV

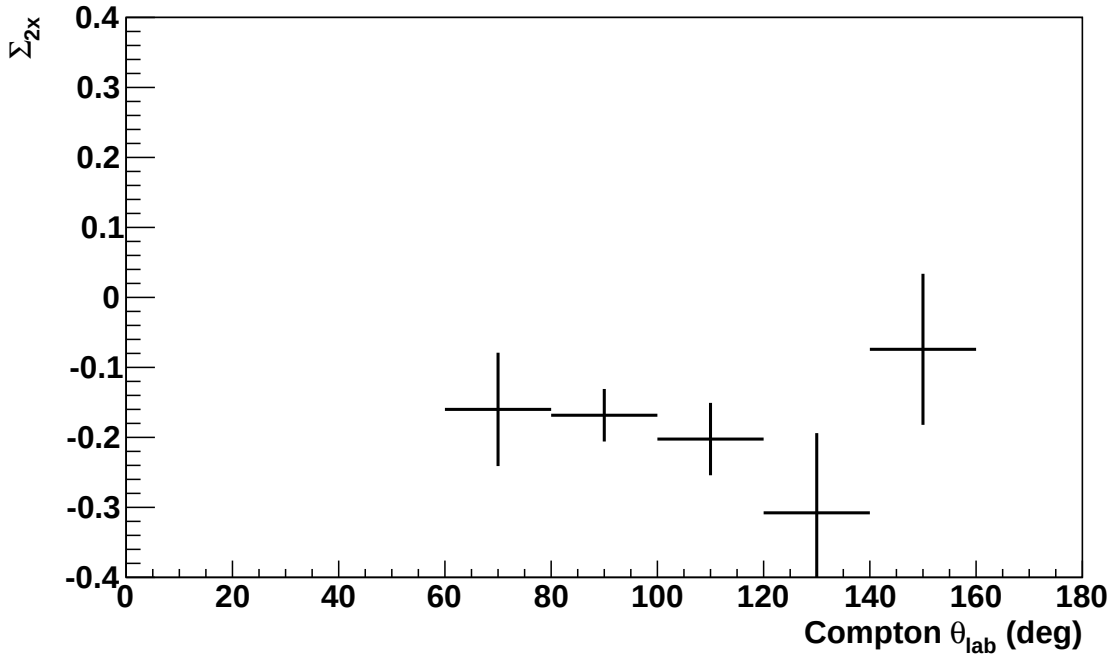

Figure 7.6: Σ_{2x} from phi summing method, for 315-346 MeV

7.3 Conclusion and Looking Forward

These asymmetries are certainly a significant achievement in their own right, being the first double polarized Compton scattering asymmetries ever measured. The uncertainty in these measurements are larger than initially anticipated due to several issues alluded to previously:

- Proton detection - With the need for distinguishing between a valid Compton event from a proton and coherent and incoherent processes on carbon and oxygen, the detection of a proton is vital to the analysis. Energy losses in the frozen spin target were considerably larger than expected (with a threshold of about 70 MeV, initially thought to have a threshold of about 40 MeV), and both the PID and MWPC suffered from efficiency losses during the beam-times.

- Pion background - Assuming the carbon subtraction is performed correctly, the remaining background in the analysis is neutral pion photoproduction off of the proton. Characterizing this background properly has been both more important and more difficult than expected. For this reason, as mentioned in subsection 4.5.4, the present asymmetries only utilize a simple integration of the missing mass peak up to 940 MeV (roughly the proton mass). The next steps in this analysis are to continue the investigation with simulation, and attempt to extract a larger portion of events by modeling the background more efficiently.

Even with the conservative upper integration limit on the missing mass spectra, a rough value for $\gamma_{E1E1} = 4.3 \pm 1.5$ can be 'eyeballed' from Figure 7.3 or Figure 7.4. Considering the spread in theoretical values for γ_{E1E1}, ranging from -1.4 to -5.7 as shown in Table 1.1, these asymmetries can already lend weight to the discussion of spin-polarizabilities. A more accurate value will also be extracted with a χ^2 fit utilizing the constraints provided by α, β, γ_0, and γ_π. This will be further improved by performing a global fit with other sets of Compton scattering data. Notably, the

A2 Collaboration at MAMI already have plans to perform a full run with a linearly polarized photon beam on an unpolarized proton target to measure Σ_3 later this year. After this, the installation of the Frozen Spin Target with a solenoidal holding coil, providing longitudinal target polarization, will allow for a measurement of Σ_{2z}.

These future runs will benefit from the experience of this experimental run, by noting a few of the lessons learned here:

- Ensure that all charged particle detection; through the PID, MWPC, and TAPS Veto; is as optimized as possible.

- A proper, pre-run calibration of the detectors would be very useful for characterizing all of the detectors before attempting the in-run calibration using π^0 photoproduction, as discussed in section 3.2.

- While the Cherenkov detector can be very useful in certain circumstances, the loss in efficiency for a crucial angular range of the recoil proton from Compton scattering was detrimental to this analysis. As such its removal is suggested for the future Compton runs.

- The inclusion of the $PbWO_4$, while not useful for Compton kinematics, could help in reducing some of the background. These have already been fixed, and are said to be fully working now.

- With the upgrade of the DAQ to FPGAs, there is now the possibility for implementing more advanced triggers, such as a coplanar trigger. Studies of this are underway and should help determine the feasibility and usefulness of such a trigger.

Once all three Compton scattering experiments have been completed a complete extraction of all four proton spin polarizabilities will be possible, providing a very important test of proton structure theories.

APPENDIX

SENSITIVITY STUDY

In preparing the proposal to the MAMI Peer Advisory Committee (PAC) for the set of three Compton scattering experiments, the following study investigated the sensitivities of the proton spin polarizabilities on the asymmetries, Σ_{2z}, Σ_{2x}, and Σ_3. A fixed-t dispersion analysis code was used to generate tables of cross sections for various values of the polarizabilities. These cross sections were turned into anticipated counts from which pseudo-data was created, and then fit to the polarizabilities using partial derivatives constructed from the code-produced tables. This was all done for the three experimental runs at two different energies of 240 MeV and 280 MeV. Four different constraints (γ_0, γ_π, $\alpha+\beta$, and $\alpha-\beta$) were potentially included in a chi-squared minimization routine, whose returned fitting errors are quoted here as the polarizability errors. The smallest errors returned were for the fully constrained 280 MeV data: 0.27, 0.60, 0.34, and 0.51×10^{-4} fm^4 for γ_{E1E1}, γ_{E1M2}, γ_{M1E2}, and γ_{M1M1} respectively. The largest errors returned were for the partially constrained 240 MeV data: 0.95, 2.12, 1.27, and 0.81×10^{-4} fm^4 for γ_{E1E1}, γ_{E1M2}, γ_{M1E2}, and γ_{M1M1} respectively.

A.1 Dispersion Code

This study used a fixed-t dispersion analysis code, courtesy of Barbara Pasquini[4], which used the 'nominal' (although adjustable) settings given in Table A.1. For Σ_{2z} and Σ_{2x} the program outputs polar lab scattering angle, unpolarized cross section (σ_{unpol}), polarized cross section with right helicity photons (σ^R), and polarized cross

	γ_{E1E1}	γ_{E1M2}	γ_{M1E2}	γ_{M1M1}	$\alpha+\beta$	$\alpha-\beta$
Value	-4.3	-0.01	2.1	2.9	13.82	10.5
Units	10^{-4} fm^4	10^{-4} fm^4	10^{-4} fm^4	10^{-4} fm^4	10^{-4} fm^3	10^{-4} fm^3

Table A.1: Nominal values for the scaler and vector polarizabilities used in the dispersion code

section with left helicity photons (σ^L). For Σ_3 it only outputs the polar lab scattering angle and the asymmetry, which was converted to cross sections (both parallel and perpendicular to the plane of beam polarization) using the same unpolarized cross sections given in Σ_{2z} and Σ_{2x}:

$$\sigma_{\parallel} = \sigma_{unpol}(1+\Sigma_3) \tag{A.1}$$

$$\sigma_{\perp} = \sigma_{unpol}(1-\Sigma_3) \tag{A.2}$$

The range of polar angles was selected from 0 to 180° in 1° steps for good flexibility.

To determine how the cross section is sensitive to the polarizabilities, the code was rerun after perturbing each polarizability, individually, about the nominal values by ±1.0 in the typical units. This whole process was also repeated for varied incident photon energies of ±10.0 MeV to average over the energy bin of the Bremsstrahlung beam.

A.2 Cross Sections and Partials

From these data sets, the energy bin averaged cross section was expressed by the following linear expansion:

$$< \sigma(k_{max}, k_{min}, \{\gamma_i\}) > = \sigma(k_o, \{\bar{\gamma}_i\}) + \sum_{i=1}^{6} \frac{\partial \sigma}{\partial \gamma_i}(k_o, \{\bar{\gamma}_i\}) \Delta\gamma_i + \left[\frac{\partial \sigma}{\partial k}(k_o, \{\bar{\gamma}_i\}) + \sum_{i=1}^{6} \frac{\partial^2 \sigma}{\partial \gamma_i \partial k}(k_o, \{\bar{\gamma}_i\}) \Delta\gamma_i \right] \times F(k_{max}, k_{min}) \tag{A.3}$$

where k_o is the energy bin centroid, $\bar{\gamma}_i$ is the nominal value for the polarizability, $\Delta\gamma_i = \gamma_i - \bar{\gamma}_i$ or the change in the polarizability from its nominal value (note that γ_i stands for any of the four spin polarizabilities, alpha, or beta, hence the summation from 1 to 6), and F is the flux factor given by:

$$F(k_{max}, k_{min}) = \frac{\left[(k_{max} - k_{min}) - k_o ln\left(\frac{k_{max}}{k_{min}}\right) \right]}{ln\left(\frac{k_{max}}{k_{min}}\right)} \tag{A.4}$$

The partials in Equation A.3 were approximated directly from the cross section data produced by the dispersion code, where each polarizability was individually perturbed. Taking γ_{E1E1} for example, and perturbing it up by 1.0 in the standard units:

$$\frac{\partial \sigma}{\partial \gamma_{E1E1}} \approx \frac{\sigma' - \bar{\sigma}}{\gamma'_{E1E1} - \bar{\gamma}_{E1E1}} = \frac{\sigma' - \bar{\sigma}}{-3.3 + 4.3} \tag{A.5}$$

With a little rearranging, Equation A.3 can be rewritten in the following form:

$$< \sigma(k_{max}, k_{min}, \{\gamma_i\}) > = < \sigma(k_{max}, k_{min}, \{\bar{\gamma}_i\}) > + \sum_{i=1}^{6} C_i(k_o, \{\bar{\gamma}_i\}) \Delta\gamma_i. \tag{A.6}$$

The first term is the energy bin averaged cross section with the nominal polarizability values, defined as:

$$< \sigma(k_{max}, k_{min}, \{\bar{\gamma}_i\}) > = \sigma(k_o, \{\bar{\gamma}_i\}) + \left[\frac{\partial \sigma}{\partial k}(k_o, \{\bar{\gamma}_i\}) \times F(k_{max}, k_{min}) \right] \tag{A.7}$$

The second term is the adjustment to the cross section for an alternate polarizability value, with the partial derivative expansion for each given by:

$$C_i(k_o, \{\bar{\gamma}_i\}) = \frac{\partial \sigma}{\partial \gamma_i}(k_o, \{\bar{\gamma}_i\}) + \left[\frac{\partial^2 \sigma}{\partial \gamma_i \partial k}(k_o, \{\bar{\gamma}_i\}) \times F(k_{max}, k_{min}) \right] \tag{A.8}$$

This separates the linear expansion into two parts. The first, Equation A.7, was calculated for a given energy bin and used to determine the 'nominal' data about which the pseudo-data was thrown. The second, Equation A.8, was calculated based on the perturbations put into the dispersion code, and used in the fitting process.

A.3 Simulating Data

This simulation was run prior to the actual data that now can be used to fit the polarizabilities. To test out these sensitivities, pseudo-data was produced by spreading out the expected number of counts by their statistical uncertainties. To calculate the expected counts, and the error, the details of the experimental setup were incorporated.

A.3.1 Solid Angle

As discussed in the actual analysis, this experiment was expected to be limited to events where the recoil proton had enough energy to reach the detector, allowing for tagging of the event. This minimum recoil energy was initially taken to be 40 MeV, which specified a forward angle cutoff of

$$\theta_{\min} = \cos^{-1}\left[1 - \frac{E_p M_p}{\left(E_\gamma^2 - E_p E_\gamma\right)} \right] \tag{A.9}$$

where E_p and M_p are the kinetic energy and mass, respectively, of the proton, and E_γ is the energy of the incident photon. From this angle backward to 160° the detector was divided into polar angle bins of 10° to have reasonable statistics in each bin. The

solid angle for a given bin was then determined by integrating over the azimuthal angle:

$$\Omega = \int_0^{2\pi} \int_{\theta_1}^{\theta_2} \sin\theta \, d\theta \, d\phi = 2\pi(\cos\theta_1 - \cos\theta_2) \tag{A.10}$$

The range for integration depends upon the experiment however. As described in subsection 6.1.3 and subsection 6.1.5, for the Σ_{2x} experiment, at a given helicity, one hemisphere of the detector sees a 'positive' target polarization while the other sees a 'negative' target polarization. However, the 'negative' target polarization can alternatively be thought of as a 'positive' target polarization with the opposite beam helicity. With an actual helicity flip, this situation is reversed. This leads to the solid angle being calculated over two bins, one for each hemisphere.

The situation for Σ_{2z} is much simpler, since the target is polarized along the beam axis (either parallel or anti-parallel to it). Because of this azimuthal symmetry, the solid angle can be calculated as one bin for the entire detector.

For the Σ_3 experiment, however, the beam is linearly polarized. At a given time two opposing quarters of the detector are considered to see the 'parallel' case and the other two opposing quarters see the 'perpendicular' case. To reduce systematics, the plane of polarization is typically rotated by 90°, thereby flipping the 'quarters'. For this situation then, the solid angle is calculated over four bins, although opposite bins are paired together in the end.

Regardless of how it's divided, the entire detector is effectively used with the time divided equally between right and left helicity (or parallel and perpendicular) states.

A.3.2 Polarization

All of the data produced by the dispersion code assumes 100% beam and target (if applicable) polarizations. This was corrected for to produce proper pseudo-data, which had a 'washing out' effect on the asymmetry. As noted in subsection 6.1.1,

real polarization was accounted for by adjusting the cross sections as given in Equation 6.3 and Equation 6.4. The magnitude of polarization $P(E,\phi)$ was given for Σ_{2x} in Equation 6.5. In the case of Σ_{2z}, this polarization is simply the product of the beam (P_γ) and target (P_T) polarizations. For Σ_3 it is

$$P(E,\phi) = P_\gamma(E)\,|\cos(\phi_0 - \phi)| \tag{A.11}$$

For this sensitivity study the variation was accounted for by treating the cross section as a constant over the portion of the detector being considered, and assigning an average effective polarization to that portion. The azimuthal ranges for determining the effective polarization are a hemisphere for Σ_{2x} and a quarter sphere for Σ_3, as discussed in the previous section.

$$\Sigma_{2x} \rightarrow \bar{P}(E) = \frac{1}{\pi}\int_{\phi_0-\frac{\pi}{2}}^{\phi_0+\frac{\pi}{2}} P_T P_\gamma(E)\cos(\phi_0-\phi)d\phi = \frac{2}{\pi}P_T P_\gamma(E) \tag{A.12}$$

$$\Sigma_{2z} \rightarrow \bar{P}(E) = P_T P_\gamma(E) \tag{A.13}$$

$$\Sigma_3 \rightarrow \bar{P}(E) = \frac{2}{\pi}\int_{\phi_0-\frac{\pi}{4}}^{\phi_0+\frac{\pi}{4}} P_\gamma(E)\,|\cos(\phi_0-\phi)|\,d\phi = \frac{2\sqrt{2}}{\pi}P_\gamma(E) \tag{A.14}$$

This resulted in the values for the effective polarizations shown in Table A.2, using the expected beam and target polarization values

Run	P_T (%)	P_γ (%)	P (%)
Σ_{2x}	70	70	31.2
Σ_{2z}	70	70	49.0
Σ_3	-	65	58.5

Table A.2: Effective polarizations expected for the different Compton scattering experiments

A.3.3 Asymmetries

With the effective polarization correction to the cross sections, the counts in each polar angle bin were determined using Equation 6.1, with the factors given in Table A.3.

	$\Phi\,(10^6\gamma/s)$	$\rho\,(10^{22}\text{nucleons/cm}^3)$	L (cm)	t (hours)
Σ_{2x}	1.0	4.5	2.0	300
Σ_{2z}	1.0	4.5	2.0	300
Σ_3	1.0	4.0	5.0	100

Table A.3: Factors used to convert theoretical cross sections to expected counts

The asymmetries were then constructed in the following way:

$$\Sigma_{2x} = \frac{\sigma^R_{+x} - \sigma^L_{+x}}{\sigma^R_{+x} + \sigma^L_{+x}} = \frac{N^R_{+x} - N^L_{+x}}{N^R_{+x} + N^L_{+x}} \tag{A.15}$$

$$\Sigma_{2z} = \frac{\sigma^R_{+z} - \sigma^L_{+z}}{\sigma^R_{+z} + \sigma^L_{+z}} = \frac{N^R_{+z} - N^L_{+z}}{N^R_{+z} + N^L_{+z}} \tag{A.16}$$

$$\Sigma_3 = \frac{\sigma_\parallel - \sigma_\perp}{\sigma_\parallel + \sigma_\perp} = \frac{N_\parallel - N_\perp}{N_\parallel + N_\perp} \tag{A.17}$$

Unlike in the real analysis, the effective polarization was not factored back out of these equations which left the asymmetries diluted. With the purpose of this study being to examine the sensitivity of the asymmetries to the polarizabilities, this does not matter. It was important to calculate the counts this way in order to properly determine the errors, propagate them, and throw the pseudo-data.

A.3.4 Errors

The error on the number of counts was determined simply as the statistical deviation:

$$\Delta N = \sqrt{N} \tag{A.18}$$

which then propagates into a generalized asymmetry measurement of

$$\Sigma = \frac{\sigma_1 - \sigma_2}{\sigma_1 + \sigma_2} = \frac{N_1 - N_2}{N_1 + N_2} \tag{A.19}$$

through

$$\Delta\Sigma = 2\sqrt{\frac{\left(N_2 \Delta N_1\right)^2 + \left(N_1 \Delta N_2\right)^2}{\left(N_1 + N_2\right)^4}} \tag{A.20}$$

A.4 Fitting

Using all of the previous equations, and the cross sections obtained through the dispersion code, the polarizabilities were fit to pseudo-data. The first step in this process was to produce the pseudo-data itself.

A.4.1 Throwing Pseudo-data

The procedure for producing a set of pseudo-data was as follows:

1. Turn dispersion code cross sections into real polarization cross sections (Equation 6.3 and Equation 6.4).

2. Account for energy bin width to determine 'nominal' cross sections (Equation A.7).

3. Turn cross sections into 'nominal' counts, N_{nom} (Equation 6.1).

4. Take square root of counts to obtain statistical errors (Equation A.18).

5. Throw counts over a Gaussian distribution with centroids of the 'nominal' counts and standard deviations equal to the statistical errors.

6. Call the new counts the 'experimental' counts, N_{ex}.

7. Take square root of N_{ex} to obtain 'experimental' error, N_{er}.

8. Construct 'experimental' asymmetries, Σ_{ex}, and asymmetry errors, Σ_{er} (Equation A.15 to Equation A.17 and Equation A.20).

The various partials, with respect to the different polarizabilities, described in section A.2 were also constructed. To optimize the processing time of the code, it was useful to actually describe the partials of counts, rather than the partials of cross sections. This avoided converting back to counts within the fitting function after every adjustment to the polarizabilities. The process for this alteration was identical to that described above, and gave variations on Equation A.6, Equation A.7, and Equation A.8 of:

$$< N(k_{max}, k_{min}, \{\gamma_i\}) > = < N(k_{max}, k_{min}, \{\bar{\gamma}_i\}) > + \sum_{i=1}^{6} C_i(k_o, \{\bar{\gamma}_i\}) \Delta\gamma_i \quad \text{(A.21)}$$

$$< N(k_{max}, k_{min}, \{\bar{\gamma}_i\}) > = N(k_o, \{\bar{\gamma}_i\}) + \left[\frac{\partial N}{\partial k}(k_o, \{\bar{\gamma}_i\}) \times F(k_{max}, k_{min}) \right] \quad \text{(A.22)}$$

$$C_i(k_o, \{\bar{\gamma}_i\}) = \frac{\partial N}{\partial \gamma_i}(k_o, \{\bar{\gamma}_i\}) + \left[\frac{\partial^2 N}{\partial \gamma_i \partial k}(k_o, \{\bar{\gamma}_i\}) \times F(k_{max}, k_{min}) \right] \quad \text{(A.23)}$$

Once all of this was complete a minimization class in ROOT, called Minuit, was run. Minuit takes, as input, the function to minimize and the parameters to adjust in order to minimize the function. The parameters passed to it were the desired polarizabilities to fit, and the function passed to it was a χ^2 function.

A.4.2 Construct Chi-squared

For each set of pseudo-data, theoretical values for the counts, N_{th}, were computed using Equation A.21. With the theoretical counts from the various experiments and helicity states, the theoretical asymmetries, Σ_{th}, were calculated using Equation A.15 to Equation A.17, and χ^2 was given by:

$$\chi^2 = \left(\frac{\Sigma_{ex} - \Sigma_{th}}{\Sigma_{er}} \right)^2 \quad \text{(A.24)}$$

χ^2 was constructed for each experiment, at each polar angle bin, and summed together to get an overall χ^2. In addition there were four selectable constraints on the minimization that could be added in, γ_0, γ_π, $\alpha+\beta$, and $\alpha-\beta$. The experimental values and errors used for these constraints were the currently accepted world values for them, as shown in Table A.4.

	γ_0	γ_π	$\alpha+\beta$	$\alpha-\beta$
Value	-1.0	8.0	13.82	10.5
Error	0.08	1.8	0.4	0.9
Units	10^{-4} fm^4	10^{-4} fm^4	10^{-4} fm^3	10^{-4} fm^3

Table A.4: Experimental values and errors for the various constraints[4]

A.4.3 Minimize Chi-squared

With all of the experiment and constraint components added in, χ^2 looks like:

$$\chi^2 = \sum_{\text{polar bins}} \left[\left(\frac{\Sigma_{ex} - \Sigma_{th}}{\Sigma_{er}} \right)^2_{2z} + \left(\frac{\Sigma_{ex} - \Sigma_{th}}{\Sigma_{er}} \right)^2_{2x} + \left(\frac{\Sigma_{ex} - \Sigma_{th}}{\Sigma_{er}} \right)^2_{3} \right] + \left(\frac{\gamma_{0_{ex}} - \gamma_{0_{th}}}{\gamma_{0_{er}}} \right)^2 + \left(\frac{\gamma_{\pi_{ex}} - \gamma_{\pi_{th}}}{\gamma_{\pi_{er}}} \right)^2 + \left[\frac{(\alpha+\beta)_{ex} - (\alpha+\beta)_{th}}{(\alpha+\beta)_{er}} \right]^2 + \left[\frac{(\alpha-\beta)_{ex} - (\alpha-\beta)_{th}}{(\alpha-\beta)_{er}} \right]^2 \tag{A.25}$$

The minimization program ran in a loop, adjusting the values of the parameters, recomputing the theoretical values of the asymmetries and then the value of χ^2, and finally determined where the minimum value of χ^2 occurred. The values of the parameters at this point were returned as the polarizability values for that pseudo-data set. Minuit also returned the error in each parameter fitting for that pseudo-data set. The polarizability errors reported by this study are the averages of each of these parameter errors over all the sets of pseudo-data (for the results here, 100,000 sets). To determine the errors in the four variables potentially used as constraints, each variable (γ_0, etc.) was constructed with the polarizabilities from an individual

pseudo-data set result. The values for these constraint variables were then plotted in histograms for all the pseudo-data sets, and the spreads in the histogram peaks give the errors in γ_0, etc.

A.5 Results

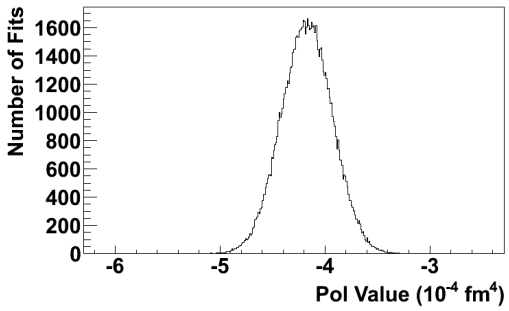

(a) γ_{E1E1}

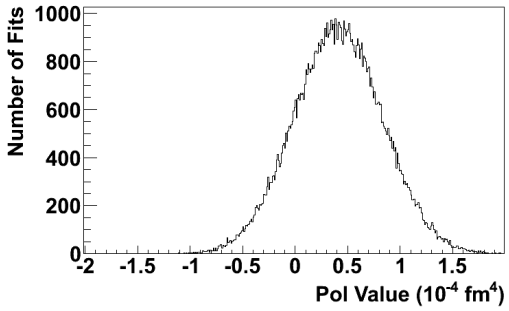

(b) γ_{E1M2}

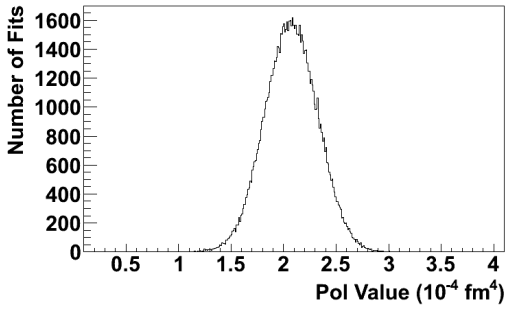

(c) γ_{M1E2}

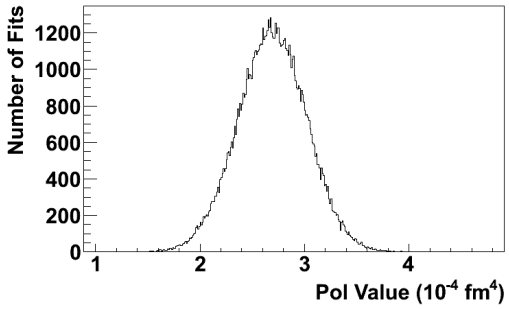

(d) γ_{M1M1}

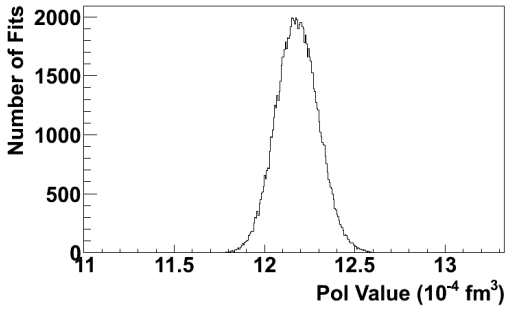

(e) α

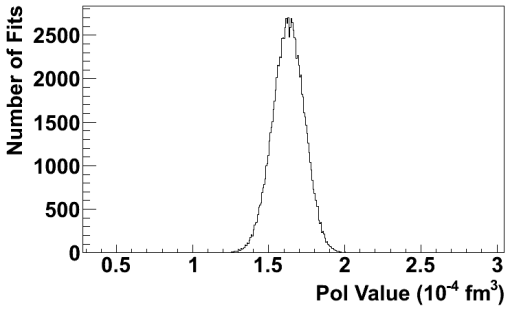

(f) β

Figure A.1: Sensitivity study polarizability fits at 240 MeV with all four constraints

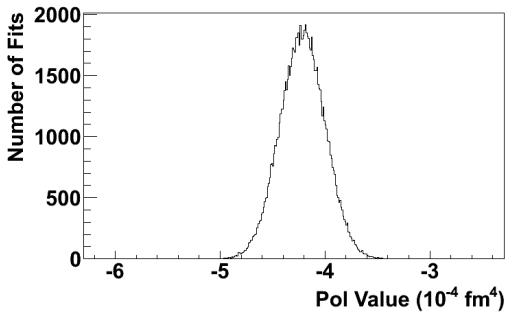

(a) γ_{E1E1}

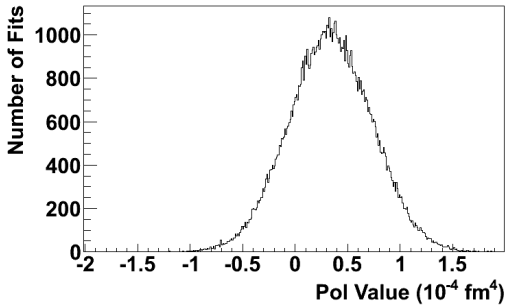

(b) γ_{E1M2}

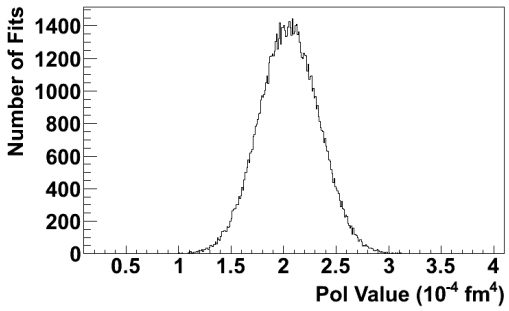

(c) γ_{M1E2}

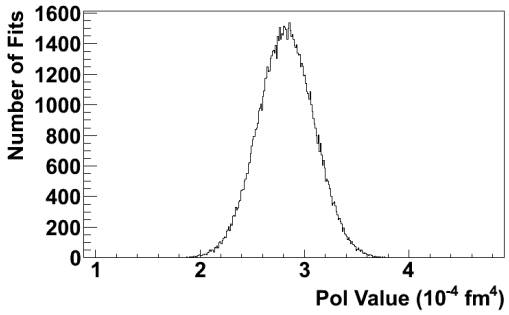

(d) γ_{M1M1}

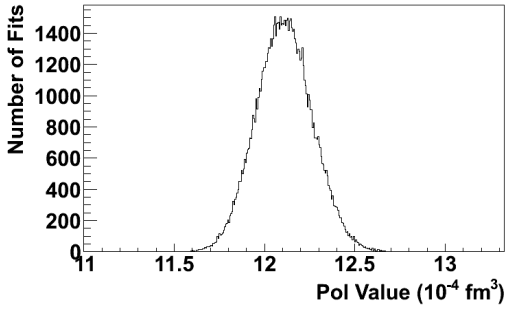

(e) α

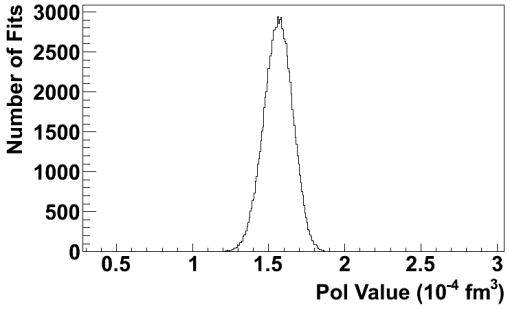

(f) β

Figure A.2: Sensitivity study polarizability fits at 280 MeV with all four constraints

The first study used all four constraints, γ_0, γ_π, $\alpha+\beta$, and $\alpha-\beta$, in the fitting subroutine. After minimization, the resulting values for each polarizability at 240 and 280 MeV were plotted in Figure A.1 and Figure A.2, respectively. The spread in each of those peaks, which again represents the error in the fitting of each polarizability, is given in Table A.5.

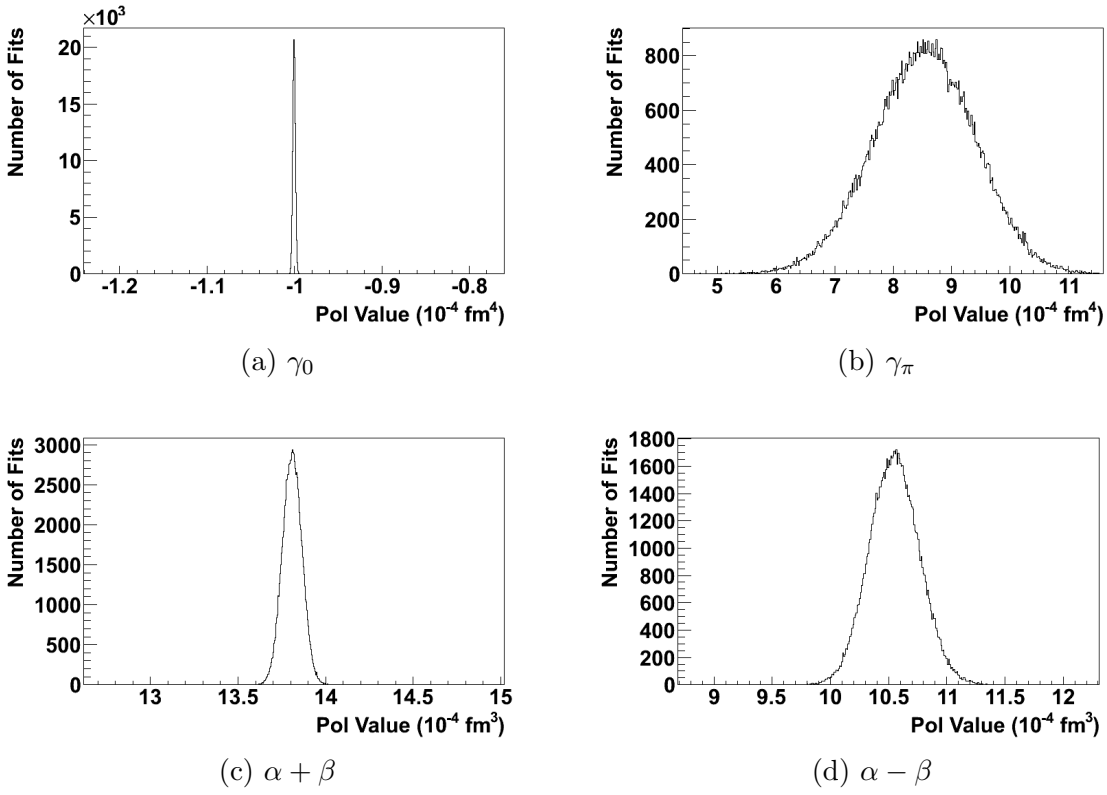

(a) γ_0 (b) γ_π

(c) $\alpha + \beta$ (d) $\alpha - \beta$

Figure A.3: Sensitivity study constraint fits at 240 MeV with all four constraints

E_γ	γ_{E1E1}	γ_{E1M2}	γ_{M1E2}	γ_{M1M1}	α	β
240	0.271	0.600	0.335	0.511	0.478	0.480
280	0.244	0.512	0.342	0.385	0.402	0.472

Table A.5: Polarizability errors when constrained with γ_0, γ_π, $\alpha + \beta$, and $\alpha - \beta$

For each of those fits, the resulting value for each of the four constraints was also calculated and plotted in Figure A.3 and Figure A.3, for 240 and 280 MeV, respectively. The spread in each of those distributions, which again represents the error in that constraint, is given in Table A.6.

E_γ	γ_0	γ_π	$\alpha + \beta$	$\alpha - \beta$
240	0.002	0.874	0.055	0.215
280	0.005	0.810	0.174	0.191

Table A.6: Constraint errors when constrained with γ_0, γ_π, $\alpha + \beta$, and $\alpha - \beta$

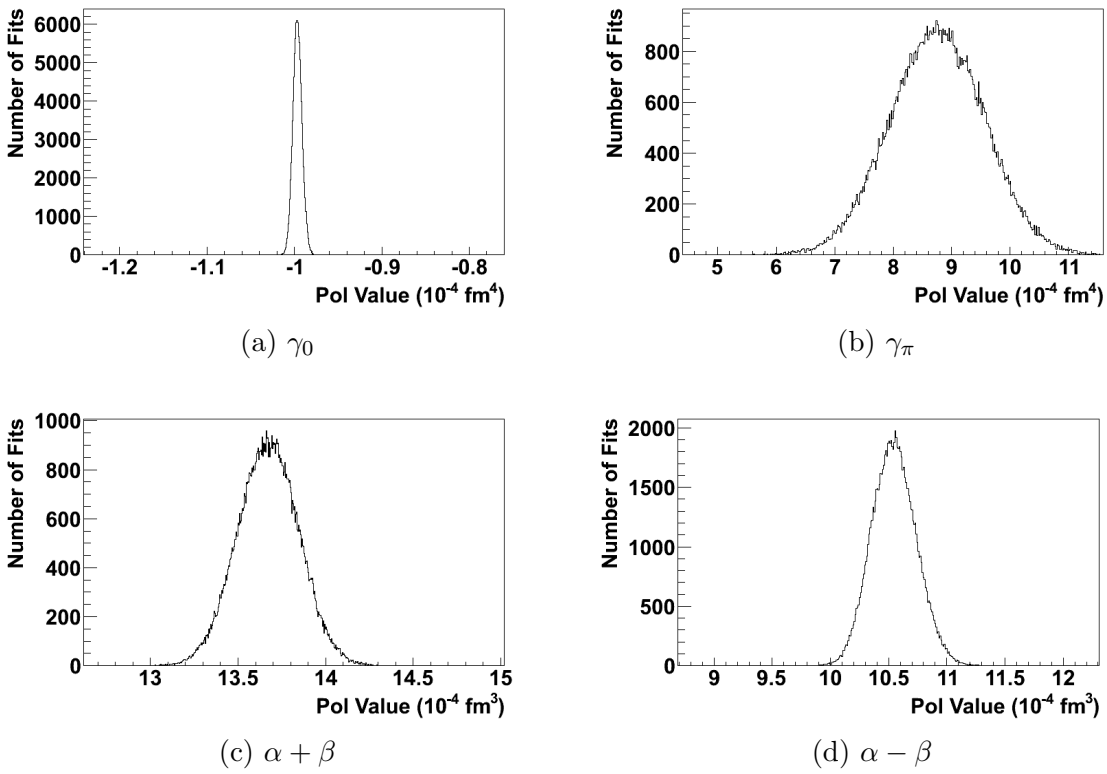

(a) γ_0 (b) γ_π

(c) $\alpha + \beta$ (d) $\alpha - \beta$

Figure A.4: Sensitivity study constraint fits at 280 MeV with all four constraints

A primary concern at this point was the very small error in γ_0, which was smaller by an order of magnitude than its experimental error. This may have been the result of a stepping size issue in the minimization program, where the already small experimental error for γ_0 perhaps appeared to be almost a delta function when compared to the other experimental errors. In the second study the γ_0 and γ_π constraints were turned off, leaving only $\alpha + \beta$ and $\alpha - \beta$ as constraints in the minimization. These results are also plotted for both 240 and 280 MeV in Figure A.5 and Figure A.6, respectively. The reconstructed constraint values for each fit are plotted in Figure A.5 and Figure A.6, for 240 and 280 MeV, respectively. As can be seen the above concern over γ_0 is removed, as it now floats almost uncontrolled. The resulting errors are given in Table A.7 and Table A.8. Even without the γ_0 and γ_π constraints, the spin polarizabilities do minimize near to the 'nominal' values. The errors are obviously

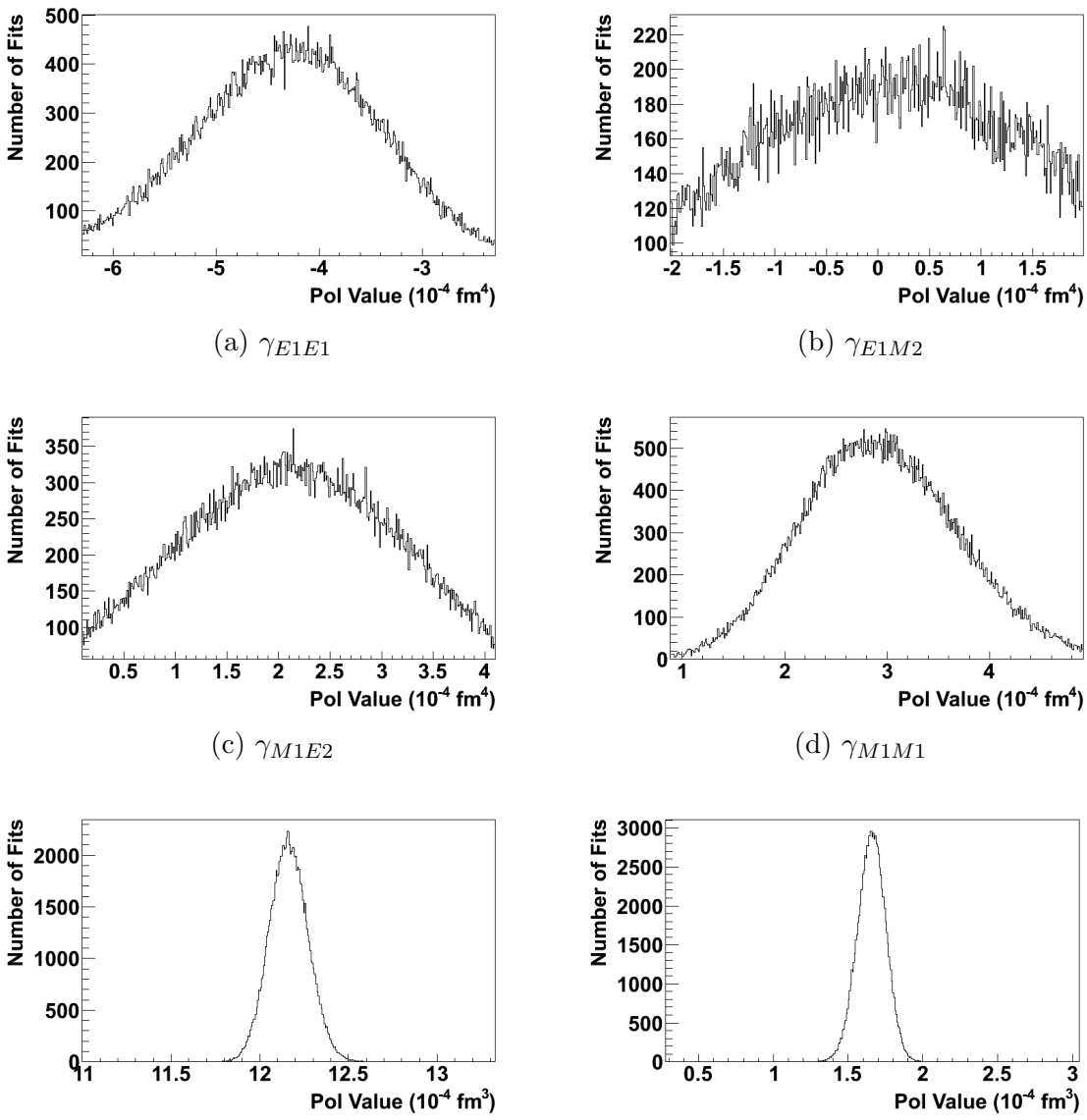

(a) γ_{E1E1} (b) γ_{E1M2}

(c) γ_{M1E2} (d) γ_{M1M1}

(e) α (f) β

Figure A.5: Sensitivity study polarizability fits at 240 MeV with only $\alpha+\beta$ and $\alpha-\beta$ constraints

larger, but still represent a significant measurement, especially in the light of being a rather unconstrained fit.

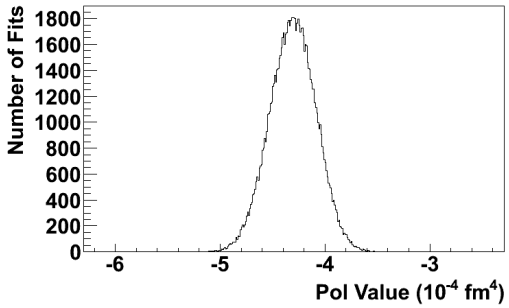

(a) γ_{E1E1}

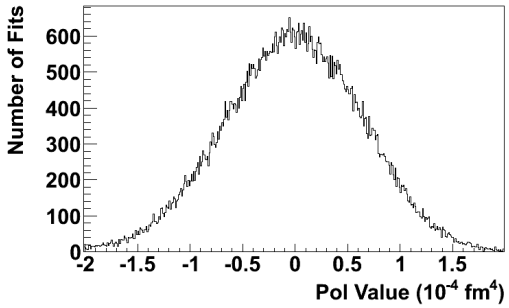

(b) γ_{E1M2}

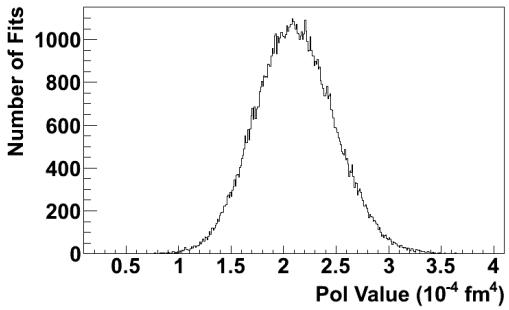

(c) γ_{M1E2}

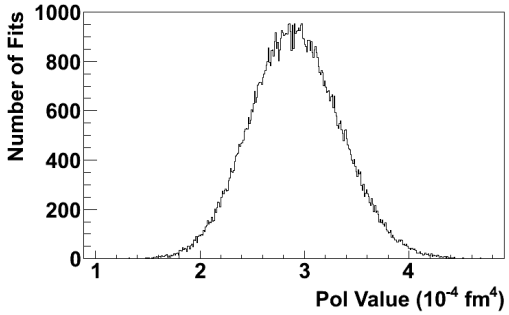

(d) γ_{M1M1}

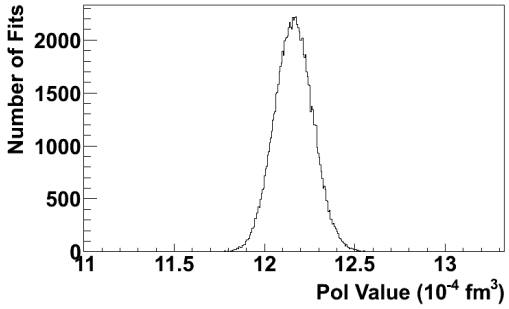

(e) α

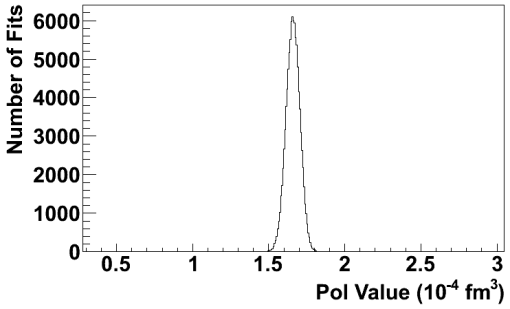

(f) β

Figure A.6: Sensitivity study polarizability fits at 280 MeV with only $\alpha+\beta$ and $\alpha-\beta$ constraints

E_γ	γ_{E1E1}	γ_{E1M2}	γ_{M1E2}	γ_{M1M1}	α	β
240	0.954	2.124	1.271	0.810	0.480	0.483
280	0.281	0.719	0.439	0.487	0.479	0.490

Table A.7: Polarizability errors when constrained with $\alpha+\beta$ and $\alpha-\beta$

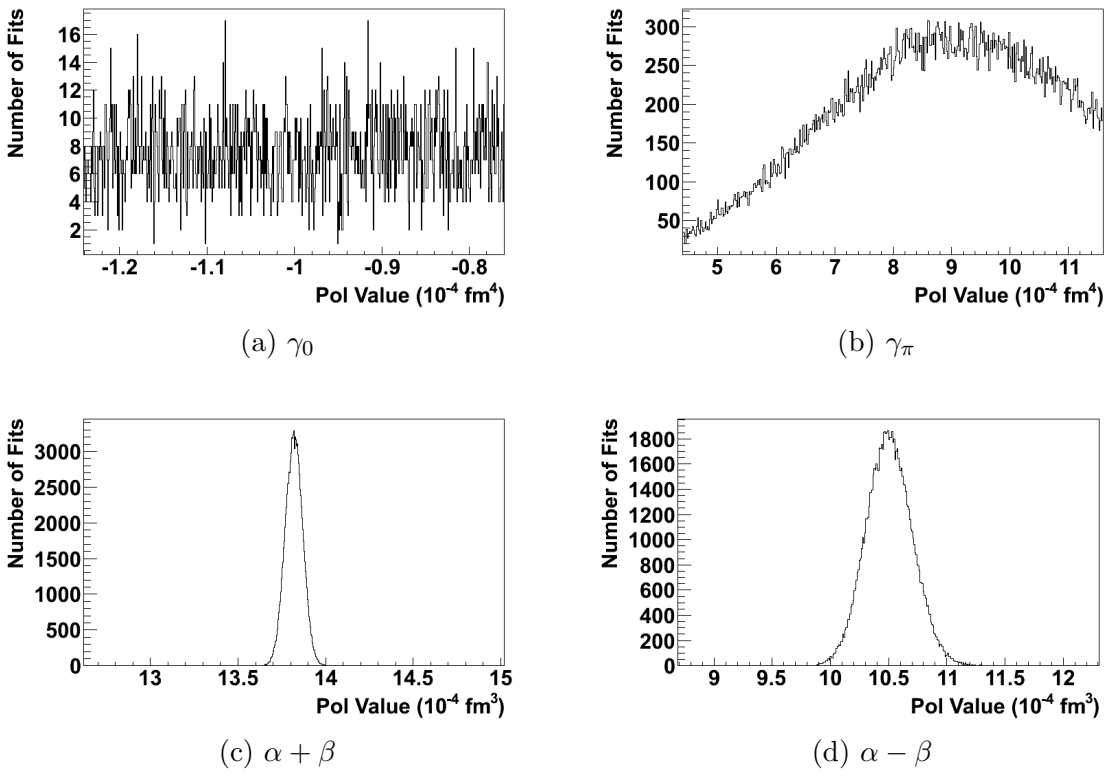

(a) γ_0 (b) γ_π

(c) $\alpha + \beta$ (d) $\alpha - \beta$

Figure A.7: Sensitivity study constraint fits at 240 MeV with only $\alpha + \beta$ and $\alpha - \beta$ constraints

E_γ	γ_0	γ_π	$\alpha + \beta$	$\alpha - \beta$
240	-	2.503	0.050	0.198
280	-	1.394	0.083	0.141

Table A.8: Constraint errors when constrained with $\alpha + \beta$ and $\alpha - \beta$

A.6 Visualizing the Sensitivities

While the study described so far was useful in demonstrating the ability to extract the spin polarizabilities from the combination of the three Compton scattering experiments, it did not adequately depict the sensitivity the asymmetries have to each polarizability. Three different ways to depict this were devised.

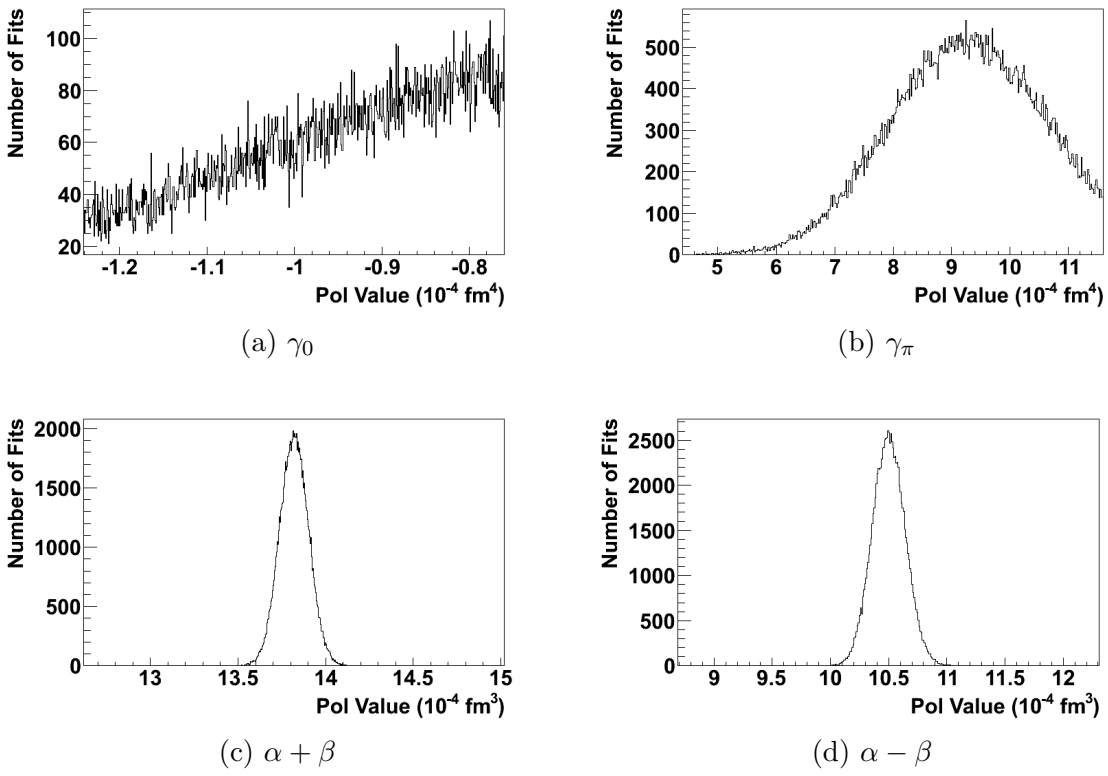

(a) γ_0 (b) γ_π

(c) $\alpha + \beta$ (d) $\alpha - \beta$

Figure A.8: Sensitivity study constraint fits at 280 MeV with only $\alpha + \beta$ and $\alpha - \beta$ constraints

A.6.1 Single Variation

The simplest way of visually inspecting the sensitivity to the spin polarizabilities is to plot the asymmetries for the nominal set of values, as well as for the set where one of the spin polarizabilities has been perturbed by $\pm 1.0 \times 10^{-4}$ fm^4 from its theoretical value. These results are shown in Figure A.9 to Figure A.11. From these it's clear that Σ_{2x} and Σ_{2z} show a larger sensitivity to γ_{E1E1} and γ_{M1M1} than to the two quadrupole polarizabilities in the multi-pole basis.

A.6.2 Multiple Variation

The concern was raised that the visualization of varying one polarizability at a time, does not depict the interplay between terms. Given that the fitting routine employed in this study assumed a linear dependence on the polarizabilities, ignoring

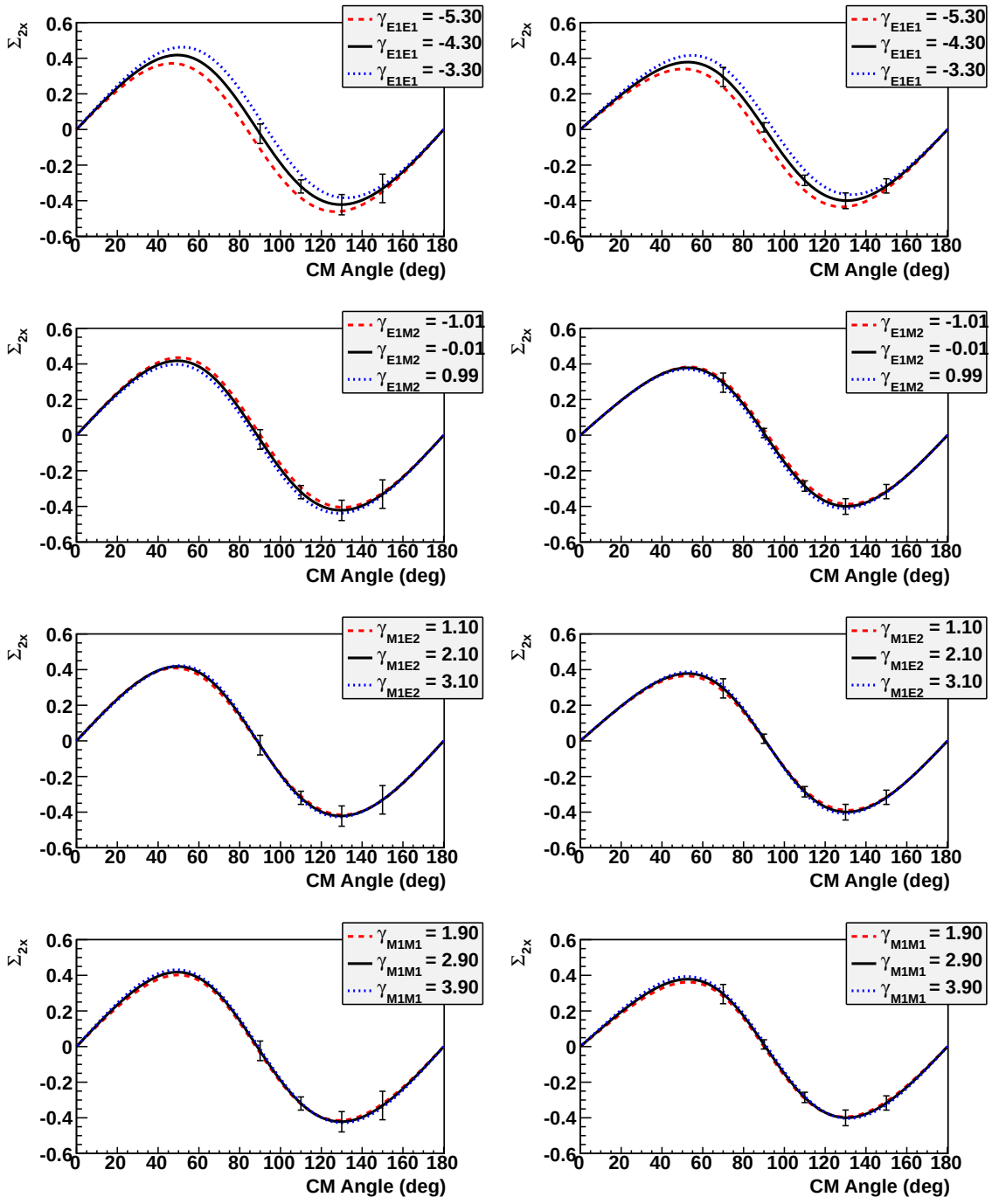

Figure A.9: Sensitivity of Σ_{2x} with single polarizability variations. Shown are E_γ = 240 MeV (left plots) or 280 MeV (right plots), varying either γ_{E1E1} (first row), γ_{E1M2} (second row), γ_{M1E2} (third row), or γ_{M1M1} (fourth row), by ± 1.0 in the standard units.

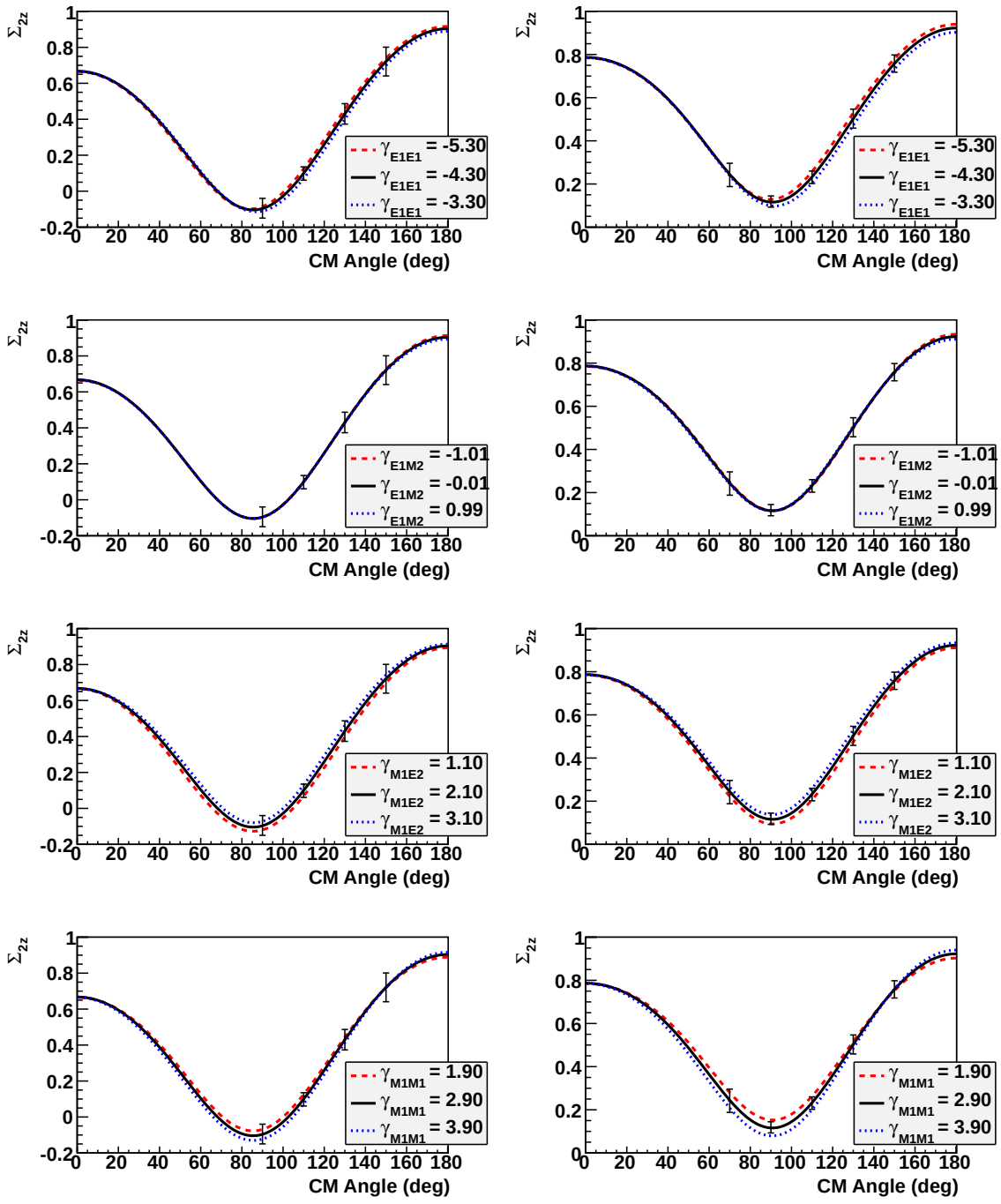

Figure A.10: Sensitivity of Σ_{2z} with single polarizability variations. Shown are E_γ = 240 MeV (left plots) or 280 MeV (right plots), varying either γ_{E1E1} (first row), γ_{E1M2} (second row), γ_{M1E2} (third row), or γ_{M1M1} (fourth row), by $\pm$ 1.0 in the standard units.

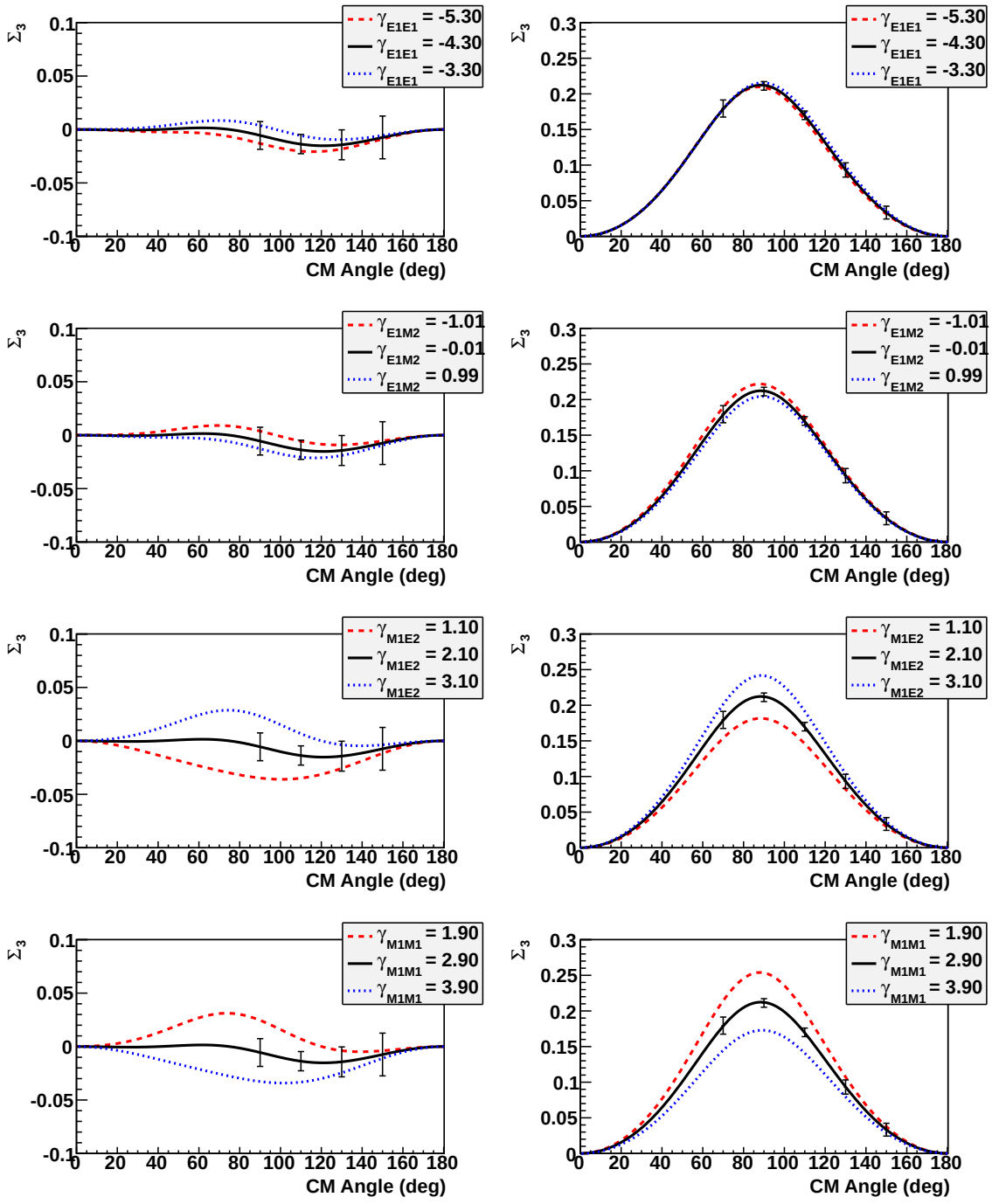

Figure A.11: Sensitivity of Σ_3 with single polarizability variations. Shown are E_γ = 240 MeV (left plots) or 280 MeV (right plots), varying either γ_{E1E1} (first row), γ_{E1M2} (second row), γ_{M1E2} (third row), or γ_{M1M1} (fourth row), by $\pm$ 1.0 in the standard units.

possible cross-terms, a study into multiple simultaneous variations was requested. Varying each polarizability by the same value, and then additionally varying a second term by the same value, some information regarding the interplay between them can be graphically conveyed. Figure A.12 to Figure A.14 show the results of this study. The dashed, and solid, lines represent the 'primary' polarizability being perturbed up, and down, respectively by 1.0×10^{-4} fm^4 from its theoretical value. The different colors represent a 'secondary' polarizability being perturbed up by 1.0×10^{-4} fm^4. In an instance where the sensitivity is solely dependent on the 'primary' polarizability in question, the various colors would be expected to group together, but with the group of solid lines and the group of dashed lines clearly separated. With this requirement it's observed (albeit more difficultly) that Σ_3 and Σ_{2z} are mostly sensitive to γ_{M1M1}, and Σ_{2x} is mostly sensitive to γ_{E1E1}.

A.6.3 Forward and Backward Polarizability Basis

Using the equations for γ_0 and γ_π, the spin polarizability basis can be rewritten in terms of γ_{E1E1}, γ_{M1M1}, γ_0, and γ_π. With the experimental values of γ_0 and γ_π, the values for γ_{E1E1} and γ_{M1M1} can be fitted without the quadrupole terms. These plots are produced here as Figure A.15 to Figure A.17. Allowing γ_0 or γ_π to vary about their experimental values by their experimental errors, with the variations from each are added in quadrature, provide the error bands to the plots. This gives an indication of how truly sensitive the asymmetries are to γ_{E1E1} and γ_{M1M1}. As before, Σ_{2x} is mostly sensitive to γ_{E1E1}, while Σ_3 and Σ_{2z} are mostly sensitive to γ_{M1M1}. Additionally it's clear that even with the 'smearing' provided by variations in γ_0 and γ_π, the quantities γ_{E1E1} and γ_{M1M1} are extractable.

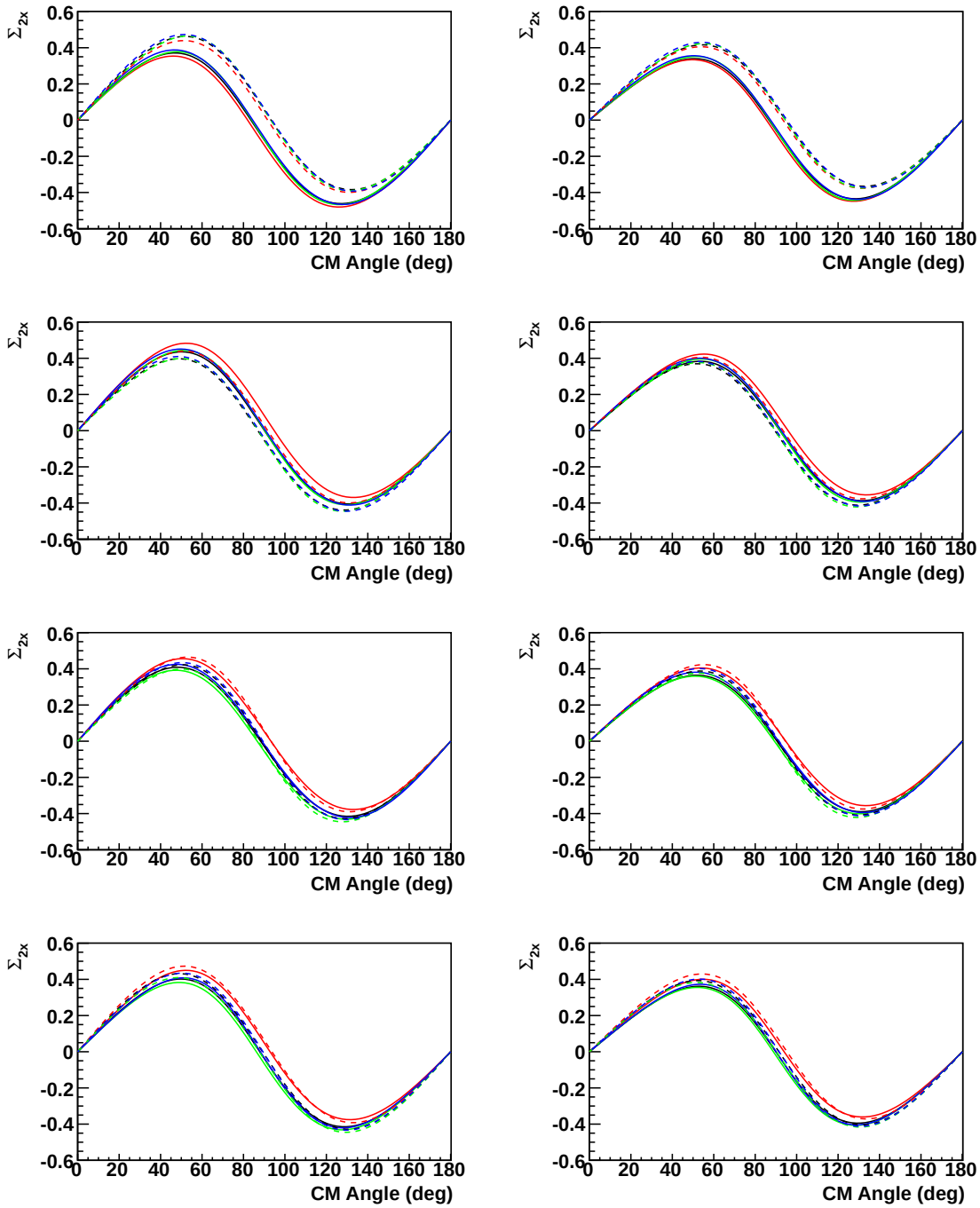

Figure A.12: Sensitivity of Σ_{2x} with multiple polarizability variations. Shown are $E_\gamma = 240$ MeV (left plots) or 280 MeV (right plots), varying either γ_{E1E1} (first row), γ_{E1M2} (second row), γ_{M1E2} (third row), or γ_{M1M1} (fourth row), by -1.0 (solid lines) or $+1.0$ (dashed lines) in the standard units. The black lines represent the other three spin polarizabilities remaining at their nominal values, while each color represents additionally varying one of them by $+1.0$ in the standard units.

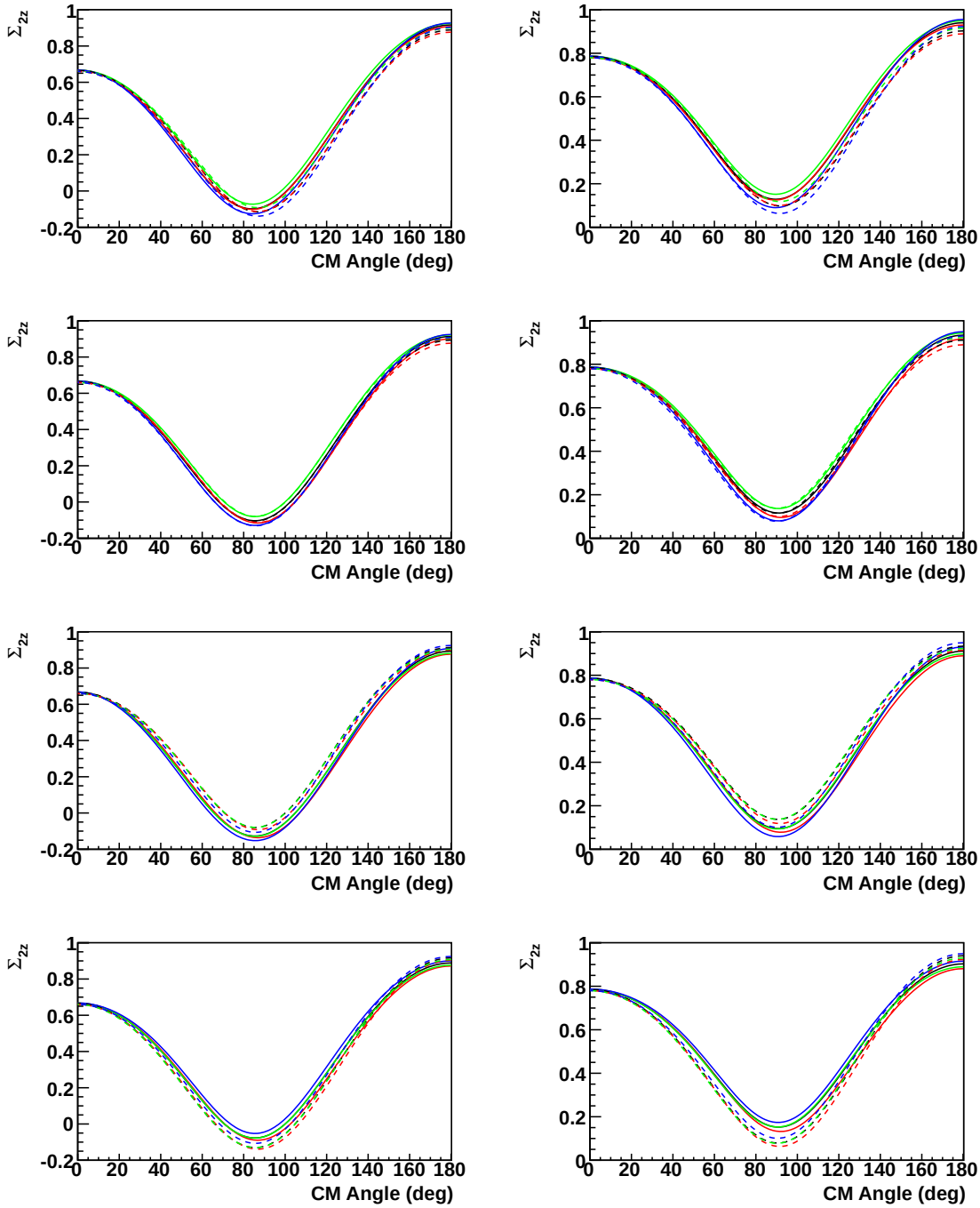

Figure A.13: Sensitivity of Σ_{2z} with multiple polarizability variations. Shown are $E_\gamma = 240$ MeV (left plots) or 280 MeV (right plots), varying either γ_{E1E1} (first row), γ_{E1M2} (second row), γ_{M1E2} (third row), or γ_{M1M1} (fourth row), by -1.0 (solid lines) or $+1.0$ (dashed lines) in the standard units. The black lines represent the other three spin polarizabilities remaining at their nominal values, while each color represents additionally varying one of them by $+1.0$ in the standard units.

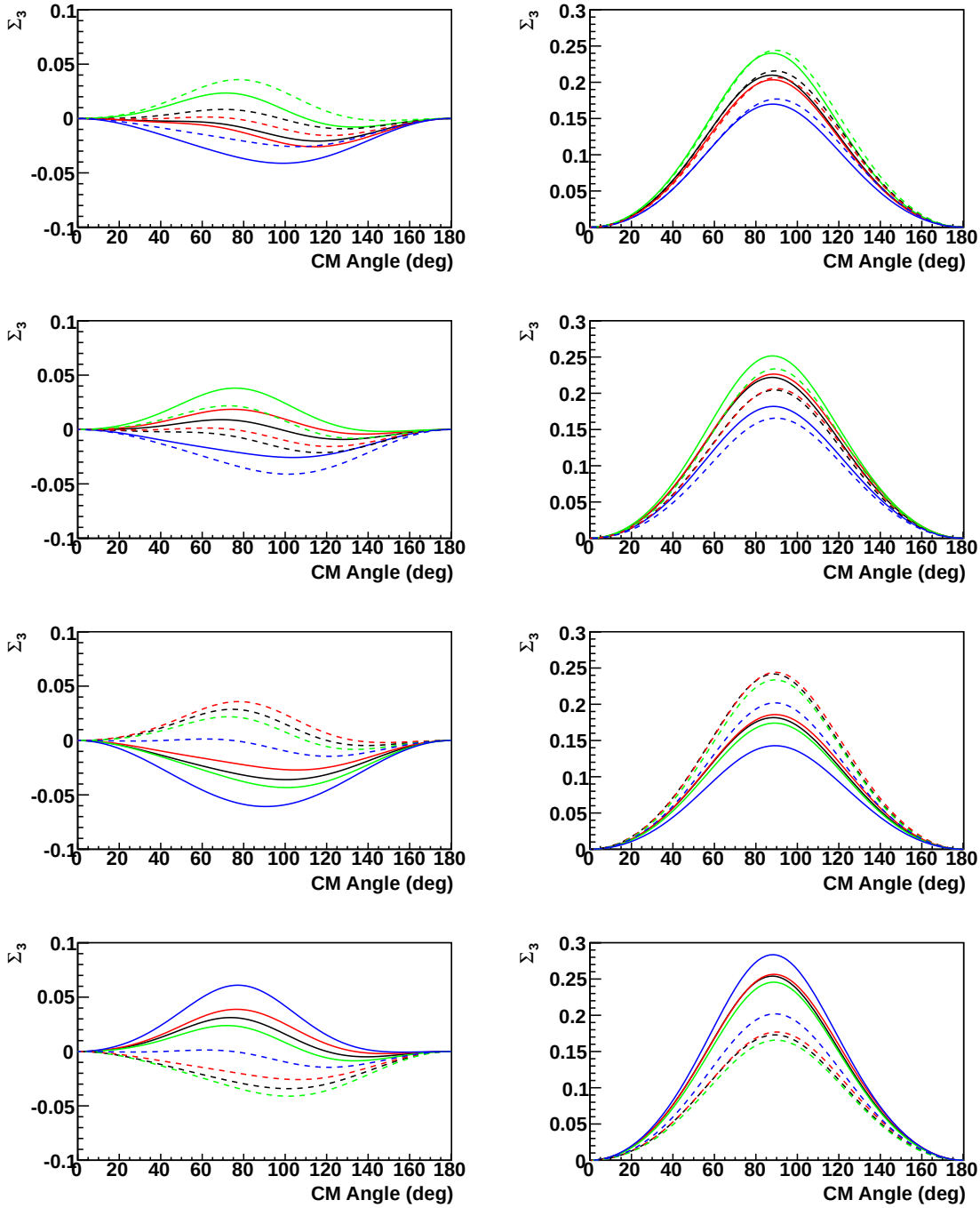

Figure A.14: Sensitivity of Σ_3 with multiple polarizability variations. Shown are $E_\gamma = 240$ MeV (left plots) or 280 MeV (right plots), varying either γ_{E1E1} (first row), γ_{E1M2} (second row), γ_{M1E2} (third row), or γ_{M1M1} (fourth row), by -1.0 (solid lines) or $+1.0$ (dashed lines) in the standard units. The black lines represent the other three spin polarizabilities remaining at their nominal values, while each color represents additionally varying one of them by $+1.0$ in the standard units.

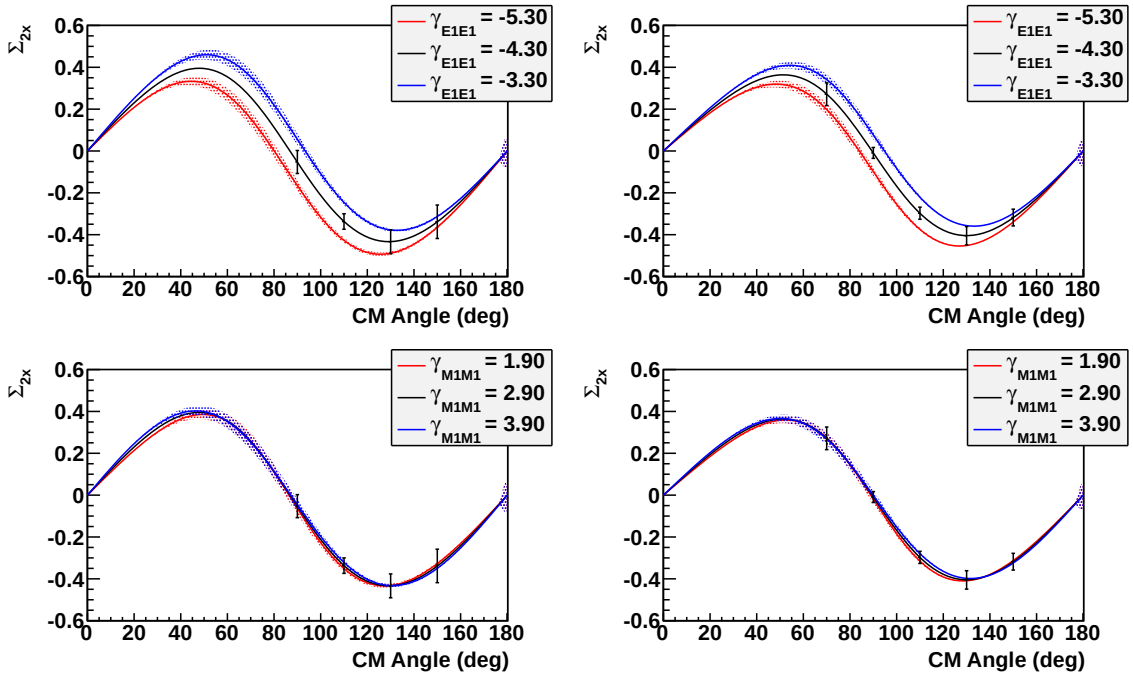

Figure A.15: Sensitivity of Σ_{2x} with forward and backward polarizability variations. Shown are $E_\gamma = 240$ MeV (left) or 280 MeV (right), varying either γ_{E1E1} (top) or γ_{M1M1} (bottom), with γ_0 and γ_π variation producing the band structure.

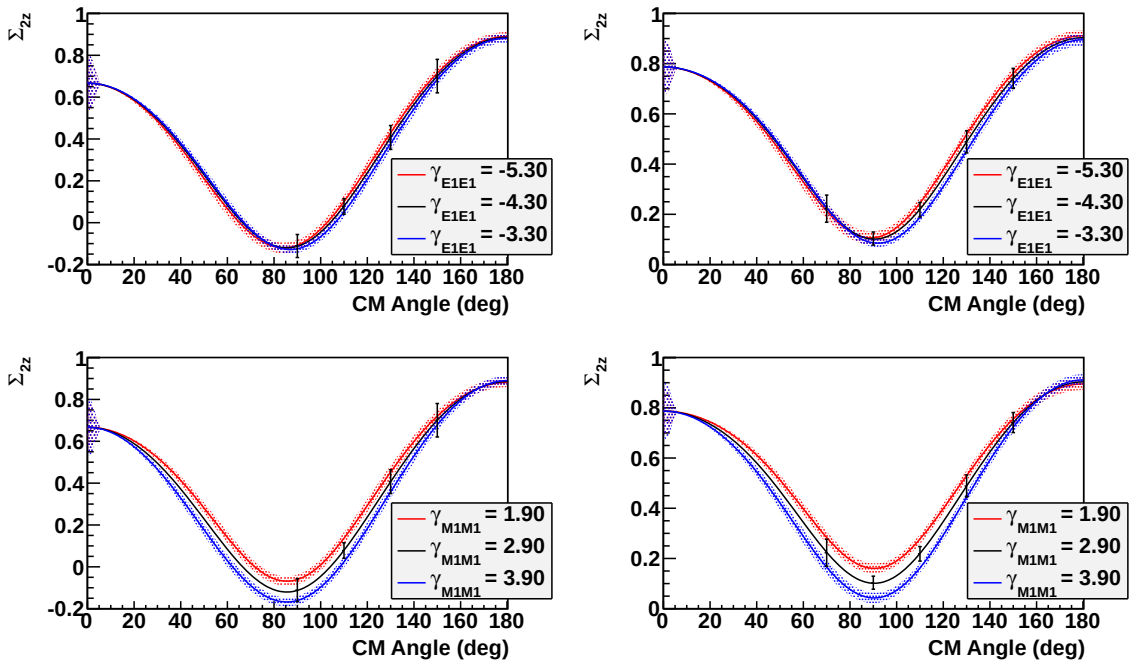

Figure A.16: Sensitivity of Σ_{2z} with forward and backward polarizability variations. Shown are $E_\gamma = 240$ MeV (left) or 280 MeV (right), varying either γ_{E1E1} (top) or γ_{M1M1} (bottom), with γ_0 and γ_π variation producing the band structure.

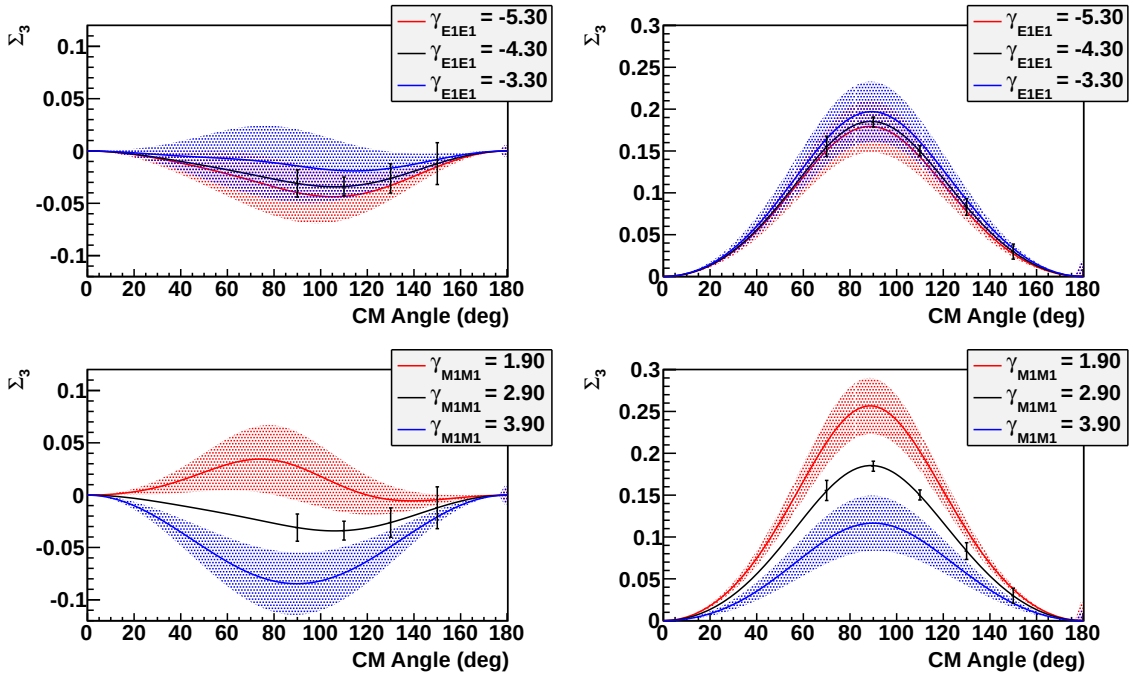

Figure A.17: Sensitivity of Σ_3 with forward and backward polarizability variations. Shown are $E_\gamma = 240$ MeV (left) or 280 MeV (right), varying either γ_{E1E1} (top) or γ_{M1M1} (bottom), with γ_0 and γ_π variation producing the band structure.

BIBLIOGRAPHY

[1] Berger, M.J., Hubbell, J.H., Seltzer, S.M., Chang, J., Coursey, J.S., Sukumar, R., Zucker, D.S., and Olsen, K. (2010), XCOM: Photon Cross Section Database (version 1.5). [Online] Available: `http://physics.nist.gov/xcom` [Tuesday, 31-May-2011 08:57:43 EDT]. National Institute of Standards and Technology, Gaithersburg, MD.

[2] Levchuk, M.I., and L'vov, A.I. Deuteron Compton scattering below pion photoproduction threshold. *Nucl. Phys. A 674* (2000), 449–492.

[3] Hütt, M.-Th., L'vov, A.I., Milstein, A.I., and Schumacher, M. Compton Scattering by Nuclei. *Physics Reports 323*, 6 (1999), 457–594.

[4] Pasquini, B., Drechsel, D., and Vanderhaeghen, M. Proton spin polarizabilities from polarized Compton scattering. *Phys. Rev. C 76*, 015203 (2007).

[5] Miskimen, R. Private communication.

[6] Grießhammer, Harald W., McGovern, Judith A., Phillips, Daniel R., and Feldman, Gerald. Using effective field theory to analyse low-energy Compton scattering data from protons and light nuclei. *Prog. Part. Nucl. Phys. 67* (2012), 841–897.

[7] Wissmann, F. *Springer Tracts in Modern Physics*. No. v. 200 in Springer Tracts in Modern Physics. Springer, 2004.

[8] Petrun'kin, V.A. *Sov. J. Part. Nucl. 12*, 278 (1981).

[9] Maximon, L. Scattering of polarized photons by protons. *Phys. Rev. C 39* (1989), 347–351.

[10] MacGibbon, B. E., Garino, G., Lucas, M. A., Nathan, A. M., Feldman, G., and Dolbilkin, B. Measurement of the electric and magnetic polarizabilities of the proton. *Phys. Rev. C 52* (Oct 1995), 2097–2109.

[11] Olmos de León, V., Wissmann, F., Achenbach, P., Ahrens, J., Arends, H.-J., Beck, R., Harty, P.D., Hejny, V., Jennewein, P., Kotulla, M., Krusche, B., Kuhr, V., Leukel, R., McGeorge, J.C., Metag, V., Novotny, R., Polonski, A., Rambo, F., Schmidt, A., Schumacher, M., Siodlaczek, U., Ströher, H., Thomas, A., Weiß, J., and Wolf, M. Low-energy Compton scattering and the polarizabilities of the proton. *Eur. Phys. J. A 10* (2001), 207–215.

[12] Federspiel, F. J., Eisenstein, R. A., Lucas, M. A., MacGibbon, B. E., Mellendorf, K., Nathan, A. M., O'Neill, A., and Wells, D. P. Proton Compton effect: A measurement of the electric and magnetic polarizabilities of the proton. *Phys. Rev. Lett. 67* (Sep 1991), 1511–1514.

[13] Zieger, A., de Vyver, R. Van, Christmann, D., Graeve, A. De, den Abeele, C. Van, and Ziegler, B. 180° Compton scattering by the proton below the pion threshold. *Phys. Lett. B 278*, 12 (1992), 34 – 38.

[14] Baldin, A.M. Polarizability of nucleons. *Nucl. Phys. 18* (1960), 310.

[15] Lapidus, L.I. Scattering of Gamma Quanta and Polarizability of Nuclei and Nucleons. *Sov. Phys. JETP 16* (1963), 964.

[16] Lensky, Vadim, and Pascalutsa, Vladimir. Predictive powers of chiral perturbation theory in Compton scattering off protons. *Eur. Phys. J. C 65* (2010), 195–209. 10.1140/epjc/s10052-009-1183-z.

[17] GDH and A2 Collaborations. First Measurement of the Gerasimov-Drell-Hearn Integral for ^{1}H from 200 to 800 MeV. *Phys. Rev. Lett. 87*, 2 (2001).

[18] Dutz, H., Helbing, K., Krimmer, J., Speckner, T., Zeitler, G., and GDH and A2 Collaborations. First Measurement of the Gerasimov-Drell-Hearn Integral for ^{1}H from 0.7 to 1.8 GeV at ELSA. *Phys. Rev. Lett. 91*, 19 (2003).

[19] Camen, M., Kossert, K., Wissmann, F., Ahrens, J., Arends, H.-J., Beck, R., Caselotti, G., Grabmayr, P., Harty, P.D., Jahn, O., Jennewein, P., Kondratiev, R., Levchuk, M.I., Lisin, V., L'vov, A.I., McGeorge, J.C., Natter, A., Olmos de León, V., Schumacher, M., Seitz, B., Smend, F., Thomas, A., Weihofen, W., and Zapadtka, F. Backward spin polarizability γ_π of the proton. *Phys. Rev. C 65*, 0302202 (2002).

[20] Schumacher, Martin. Polarizability of the nucleon and Compton scattering. *Prog. Part. Nucl. Phys. 55* (2005), 567–646.

[21] Helbing, K, Anton, G, Fausten, M, Menze, D, Michel, T, Nagel, A, Ryckbosch, D, Speckner, T, de Vyver, R Van, and Zeitler, G. The GDH-Detector. *Nucl. Instrum. Methods A 484*, 13 (2002), 129 – 139.

[22] Hallin, E. L., Amendt, D., Bergstrom, J. C., Caplan, H. S., Igarashi, R., Skopik, D. M., Booth, E. C., Delli Carpini, D., Miller, J. P., Federspiel, F. J., MacGibbon, B. E., and Nathan, A. M. Compton scattering from the proton. *Phys. Rev. C 48* (Oct 1993), 1497–1507.

[23] Blanpied, G., Blecher, M., Caracappa, A., Djalali, C., Giordano, G., Hicks, K., Hoblit, S., Khandaker, M., Kistner, O. C., Kuczewski, A., Lowry, M., Lucas, M., Matone, G., Miceli, L., Preedom, B., Rebreyend, D., Sandorfi, A. M., Schaerf, C., Sealock, R. M., Ströher, H., Thorn, C. E., Thornton, S. T., Tonnison, J., Whisnant, C. S., Zhang, H., and Zhao, X. $N \to \Delta$ Transition from Simultaneous Measurements of $p(\vec{\gamma},\pi)$ and $p(\vec{\gamma},\gamma)$. *Phys. Rev. Lett. 79* (Dec 1997), 4337–4340.

[24] Blanpied, G., Blecher, M., Caracappa, A., Deininger, R., Djalali, C., Giordano, G., Hicks, K., Hoblit, S., Khandaker, M., Kistner, O. C., Kuczewski, A., Lincoln, F., Lowry, M., Lucas, M., Matone, G., Miceli, L., Preedom, B. M., Rebreyend, D., Sandorfi, A. M., Schaerf, C., Sealock, R. M., Ströher, H., Thorn, C. E., Thornton, S. T., Tonnison, J., Whisnant, C. S., Zhang, H., and Zhao, X. $N \to \Delta$ transition and proton polarizabilities from measurements of $p(\vec{\gamma},\gamma)$, $p(\vec{\gamma},\pi^0)$, and $p(\vec{\gamma},\pi^+)$. *Phys. Rev. C 64* (Jul 2001), 025203.

[25] Galler, G., Lisin, V., Kondratiev, R., Massone, A.M., Wolf, S., Ahrens, J., Arends, H.-J., Beck, R., Camen, M., Capitani, G.P., Grabmayr, P., Hall, S.J., Hrter, F., Hehl, T., Jennewein, P., Kossert, K., L'vov, A.I., Molinari, C., Ottonello, P., Peise, J., Preobrajenski, I., Proff, S., Robbiano, A., Sanzone, M., Schumacher, M., Schmitz, M., and Wissmann, F. Compton scattering by the proton. *Phys. Lett. B 503*, 34 (2001), 245 – 255.

[26] Wolf, S., Lisin, V., Kondratiev, R., Massone, A.M., Galler, G., Ahrens, J., Arends, H.-J., Beck, R., Camen, M., Capitani, G.P., Grabmayr, P., Hrter, F., Hehl, T., Jennewein, P., Kossert, K., L'vov, A.I., Molinari, C., Ottonello, P., Owens, R.O., Peise, J., Preobrajenskij, I., Proff, S., Robbiano, A., Sanzone, M., Schumacher, M., Schmitz, M., and Wissmann, F. Compton scattering by the proton using a large-acceptance arrangement. *Eur. Phys. J. A 12* (2001), 231–252. 10.1007/s100500170031.

[27] Scherer, S. Introduction to chiral perturbation theory. *Adv. Nucl. Phys. 27* (2003), 277.

[28] Hildebrandt, R.P. *Elastic Compton Scattering from the Nucleon and Deuteron.* PhD thesis, Technischen Universität München, October 2005.

[29] Weinberg, S. Phenomenological Lagrangians. *Physica 96*, 327 (1979).

[30] Gasser, J., and Leutwyler, H. Chiral Perturbation Theory to One Loop. *Ann. Phys. 158* (1984), 142.

[31] Gasser, J., and Leutwyler, H. Chiral Perturbation Theory: Expansions in the Mass of the Strange Quark. *Nucl. Phys. B 250* (1985), 465.

[32] Hemmert, T.R., Holstein, B.R., and Kambor, J. *Delta*(1232) and the polarizabilities of the nucleon. *Phys. Rev. D 55*, 9 (1997), 5598–5612.

[33] Becher, T., and Leutwyler, H. Baryon chiral perturbation theory in manifestly Lorentz invariant form. *Eur. Phys. J. C 9* (1999), 643–671.

[34] Djukanovic, D. *Virtual Compton Scattering in Baryon Chiral Perturbation Theory*. PhD thesis, Johannes Gutenberg-Universität Mainz, Germany, June 2008.

[35] L'vov, A.I., Petrun'kin, V.A., and Schumacher, M. Dispersion theory of proton Compton scattering in the first and second resonance regions. *Phys. Rev. C 55*, 1 (1997), 359–377.

[36] Drechsel, D., Gorchtein, M., Pasquini, B., and Vanderhaeghen, M. Fixed-t subtracted dispersion relations for Compton scattering off the nucleon. *Phys. Rev. C 61* (1999), 015204.

[37] Drechsel, D., Pasquini, B., and Vanderhaeghen, M. Dispersion relations in real and virtual Compton scattering. *Phys. Rep. 378*, 015204 (2003).

[38] Hemmert, T.R., Holstein, B.R., Kambor, J., and Knöchlein, G. Compton scattering and the spin structure of the nucleon at low energies. *Phys. Rev. D 57*, 9 (1998), 5746–5754.

[39] Vijaya Kumar, K.B., McGovern, J.A., and Birse, M.C. Spin polarisabilities of the nucleon at NLO in the chiral expansion. *Phys. Lett. B 479* (2000), 167–172.

[40] Gellas, G.C., Hemmert, T.R., and Meißner, Ulf-G. Complete oneloop analysis of the nucleons spin polarizabilities. *Phys. Rev. Lett. 86*, 14 (2001).

[41] Babusci, D., Giordano, G., L'vov, A.I., Matone, G., and Nathan, A.M. Low-energy Compton scattering of polarized photons on polarized nucleons. *Phys. Rev. C 58*, 2 (1998), 1003–1041.

[42] Holstein, B.R., Drechsel, D., Pasquini, P., and Vanderhaeghen, M. Higher order polarizabilities of the proton. *Phys. Rev. C 61*, 034316 (2000).

[43] Kondratyuk, S., and Scholten, O. Compton scattering on the nucleon at intermediate energies and polarizabilities in a microscopic model. *Phys. Rev. C 64*, 024005 (2001).

[44] Jankowiak, A. The MAinzer MIcrotron MAMI: An cw Electron-Accelerator for Nuclear-Physics. [Online] Available: `http://wwwkph.kph.uni-mainz.de/B1//mamic.php` [Monday 23-May-2011 19:29:21 EDT]. Institut für Kernphysik, Mainz, Germany.

[45] Euteneuer, H., and Kreidel, H.-J. Mainz Microtron MAMI website. [Online] Available: `http://wwwkph.kph.uni-mainz.de/B1//params.php` [Wednesday, 18-May-2011 19:43:30 EDT]. Institut für Kernphysik, Mainz, Germany.

[46] Lampel, G. Nuclear Dynamic Polarization by Optical Electronic Saturation and Optical Pumping in Semiconductors. *Phys. Rev. Lett. 20* (1968), 491–493.

[47] Pierce, D.T., Meier, F., and Zürcher, P. Negative electron affinity GaAs: A new source of spinpolarized electrons. *Appl. Phys. Lett. 26*, 670 (1975).

[48] Pierce, D.T., and Meier, F. Photoemission of spin-polarized electrons from GaAs. *Phys. Rev. B 13*, 12 (1976).

[49] Aulenbacher, K., Nachtigall, Ch., Andresen, H.G., Bermuth, J., Dombo, Th., Drescher, P., Euteneuer, H., Fischer, H., Harrach, D.v., Hartmann, P., Hoffmann, J., Jennewein, P., Kaiser, K.H., Kbis, S., Kreidel, H.J., Langbein, J., Petri, M., Pltzer, S., Reichert, E., Schemies, M., Schpe, H.-J., Steffens, K.-H., Steigerwald, M., Trautner, H., and Weis, Th. The MAMI source of polarized electrons. *Nucl. Instrum. Methods A 391*, 3 (1997), 498–506.

[50] Tioukine, V., Aulenbacher, K., and Riehn, E. A Mott polarimeter operating at MeV electron beam energies. *Rev. Sci. Instrum. 82*, 033303 (2011).

[51] Tioukine, V. Mott polarimeter at MAMI. [Online] Available: `http://web.fe.infn.it/PST2009/body/talks/tioukine.pdf` [Sunday, 26-August-2012 19:10:00 EDT]. Istituto Nazionale di Fisica Nucleare, September 2009. XIIIth International Workshop on Polarized Sources, Targets and Polarimetry.

[52] Mott, N.F. The Scattering of Fast Electrons by Atomic Nuclei. *Proc. R. Soc. Long. A 123* (1929), 425–442.

[53] Tioukine, V., and Aulenbacher, K. Operation of the MAMI accelerator with a Wien filter based spin rotation system. *Nucl. Instrum. Methods A 568* (2006), 537–542.

[54] Jankowiak, A. The Mainz Microtron MAMI Past and future. *Eur. Phys. J. A 28*, s01 (2006), 149–160.

[55] Hornidge, D., Downie, E.J., Annand, J.R.M., and MacGregor, I.J.D. Measurement of the Proton Spin Polarizabilities. An A2 Collaboration Proposal for an Experiment at MAMI, 2009.

[56] Olsen, H., and Maximon, L.C. Photon and Electron Polarization in High-Energy Bremsstrahlung and Pair Production with Screening. *Phys. Rev. 114* (1959), 887–904.

[57] Downie, E.J. *Radiative π^0 photoproduction in the region of the $\Delta(1232)$ resonance*. PhD thesis, University of Glasgow, Scotland, December 2006.

[58] Crabb, D.G., and Meyer, W. Solid polarized targets for nuclear and particle physics experiments. *Annu. Rev. Nucl. Part. Sci. 47* (1997), 67–109.

[59] Farrar, C.T., Hall, D.A., Gerfen, G.J., Rosay, M., Ardenkjaer-Larsen, J.-H., and Griffin, R.G. High-Frequency Dynamic Nuclear Polarization in the Nuclear Rotating Frame. *J. Mag. Reson. 144* (2000), 134–141.

[60] Niinikoski, T.O., and Udo, F. "Frozen Spin" Polarized Target. *Nucl. Instrum. Methods 134* (1976), 219–233.

[61] Thomas, A. Overview installation of Polarized Target. [Online] Available: `http://wwwa2.kph.uni-mainz.de/A2/` [Wednesday, 25-May-2011 14:00:00 EDT]. Institut für Kernphysik, Mainz, Germany, September 2009. 14th Crystal Ball Meeting.

[62] Poco Graphite Website. [Online] Available: `http://www.poco.com/Portals/0/Literature/Semiconductor/78962v2PocoFoamFlyer.pdf` [Tuesday, 28-August-2012 09:00:00 EDT]. Poco Graphite, Inc., Decatur, TX, USA.

[63] A2 Collaboration Website. [Online] Available: `http://wwwa2.kph.uni-mainz.de/cb/pic_setup/cb4_k.jpg` [Wednesday, 25-May-2011 19:00:00 EDT]. Institut für Kernphysik, Mainz, Germany.

[64] Robinson, J. *Two Proton Knockout From Carbon Using Linearly Polarised Photons*. PhD thesis, University of Glasgow, Scotland, June 2010.

[65] Tarbert, C.M., Watts, D.P., et al. Incoherent Neutral Pion Photoproduction on ^{12}C. *Phys. Rev. Lett. 100*, 132301 (2008).

[66] Mushkarenkov, A. Private communication.

[67] Thiel, M. *In-medium properties of the ω-meson studied in photonuclear reactions near the production threshold*. PhD thesis, Justus-Liebig-Universität Gießen, Germany, November 2010.

[68] Krambrich, D. *Aufbau des Crystal Ball-Detektorsystems und Untersuchung der Helizitätsasymmetrie in $\gamma p \rightarrow \pi^0 \pi^0$*. PhD thesis, Johannes Gutenberg-Universität Mainz, Germany, January 2007.

[69] Knoll, G.F. *Radiation Detection and Measurement*. Wiley, 2000.

[70] MAID Website. [Online] Available: `http://wwwkph.kph.uni-mainz.de/MAID//maid2007/maid2007.html` [Monday, 3-September-2012 18:00:00 EDT]. Institut für Kernphysik, Mainz, Germany.

[71] Drechsel, D., Hanstein, O., Kamalov, S.S., and Tiator, L. A unitary isobar model for pion photo- and electroproduction on the proton up to 1 GeV. *Nucl. Phys. A 65* (1999), 145–174.

[72] Drechsel, D., Kamalov, S.S., and Tiator, L. Unitary isobar model - MAID2007. *Eur. Phys. J. A 34* (2007), 69–97.

[73] SAID Website. [Online] Available: `http://gwdac.phys.gwu.edu/` [Monday, 3-September-2012 18:00:00 EDT]. Center for Nuclear Studies, George Washington University, Washington, D.C.

[74] Geant4 Website. [Online] Available: http://geant4.cern.ch/ [Monday, 3-September-2012 18:00:00 EDT]. European Organization for Nuclear Research (CERN) Switzerland.

[75] Collaboration, Geant4. Geant4 - a simulation toolkit. *Nucl. Instrum. Methods A 506* (2003), 250–303.

[76] Collaboration, Geant4. Geant4 Developments and Applications. *IEEE Trans. Nucl. Sci. 53*, 1 (2006), 270–278.

[77] A2 Geant4 Simulation. [Online] Available: http://nuclear.physics.gla.ac.uk/~dglazier/A2/G4A2CBSimulation.pdf [Monday, 3-September-2012 18:00:00 EDT]. Nuclear Physics Research Group, University of Glasgow, Glasgow, Scotland.

[78] Baranov, P., Buinov, G., Godin, V., Kuznetzova, V., Petrunkin, V., Tatarinskaya, L., Shirthenko, V., Shtarkov, L., Yurtchenko, V., and Yanulis, Yu. New experimental data on the proton electromagnetic polarizabilities. *Phys. Lett. B 52*, 1 (1974), 122 – 124.

[79] Downie, E.J. Private communication.

[80] Gell-Mann, M., and Goldberger, M. L. Scattering of Low-Energy Photons by Particles of Spin 1/2. *Phys. Rev. 96* (Dec 1954), 1433–1438.

[81] Hildebrandt, R.P., Grießhammer, H.W., and Hemmert, T.R. Nucleon Polarizabilities from Deuteron Compton Scattering within a Green's-Function Hybrid Approach.

[82] Holstein, B.R. Blue skies and effective interactions. *Am. J. Phys. 67*, 5 (May 1999), 422.

[83] Hornidge, D. Private communication.

[84] Klein, Abraham. Low-Energy Theorems for Renormalizable Field Theories. *Phys. Rev. 99* (Aug 1955), 998–1008.

[85] Low, F. E. Scattering of Light of Very Low Frequency by Systems of Spin 1/2. *Phys. Rev. 96* (Dec 1954), 1428–1432.

[86] Petrun'kin, V.A. *Sov. Phys. JETP 13*, 808 (1961).

[87] Powell, John L. Note on the Bremsstrahlung Produced by Protons. *Phys. Rev. 75* (Jan 1949), 32–34.

[88] Wissmann, F., Kuhr, V., Jahn, O., Vorwerk, H., Achenbach, P., Ahrens, J., Arends, H.-J., Beck, R., Camen, M., Caselotti, G., Heid, E., Hejny, V., Jennewein, P., Kondratjev, R., Kossert, K., Kotulla, M., Krusche, B., Lang, M., Leukel, R., Levchuk, M.I., Lisin, V., Metag, V., Novotny, R., de Len, V. Olmos, Polonski, A., Preobrashenskij, I., Rambo, F., Rosenkranz, D., Schilling, E., Schmidt, A., Schumacher, M., Seitz, B., Siodlaczek, U., Strher, H., Thomas, A., Walcher, Th., Weiss, J., Wolf, M., and Zapadtka, F. Compton scattering from the free and bound proton at backward angles above π-threshold. *Nucl. Phys. A 660*, 2 (1999), 232 – 245.